Doctoral Dissertation

博士論文

The Statistical Properties of the Detailed Structures of
the Protoplanetary Disks in the Taurus Star-forming
Region with ALMA Super-resolution Imaging Technique
(ALMA 超解像度画像で探るおうし座星形成領域における原
始惑星系円盤の詳細構造)

A Dissertation Submitted for the Degree of Doctor of Philosophy
August 2021
令和3年8月博士（理学）申請

Department of Astronomy, Graduate School of Science,
The University of Tokyo
東京大学大学院理学系研究科天文学専攻

Masayuki Yamaguchi
山口 正行

Dissertation Advisor: Professor Ryohei Kawabe

Statistical Properties of the Detailed Structures of the Protoplanetary Disks in the Taurus Star-Forming Region with ALMA Super-resolution Imaging Technique

Masayuki Yamaguchi

Abstract

Planets are thought to originate from protoplanetary disks composed of cold gas and solid particles (dust) surrounding young stars. Such disks are a natural consequence of star formation, and several hundred have been confirmed with (sub)millimeter observation, such as the Submillimeter Array (SMA), in the low-mass star-forming regions at a distance of ~ 140 pc from the solar system. Owing to the advent of the Atacama Large Millimeter/submillimeter Array (ALMA), substructures, such as annular gaps and rings, of the disks have been discovered at a high spatial resolution. Several theories have attempted to explain the observational result, and some theories have proposed the planet origin of these substructures, that is, an idea that the interaction between the planet and disk is thought to have created these gaps in the disk. To investigate how and where planetary formation occurs in the disks or how the relationship between young planets in the disk and its stellar mass plays a role, high spatial resolution is one of the keys. However, a spatial resolution of $0''.02 - 0''.03$ (or $3 - 4$ au at $d = 140$ pc) is an ideal case, even for ALMA, which needs the observations using the longest baselines. Generally, ALMA observations have a spatial resolution of $0''.1$ due to the limited use of such longest baselines, becoming difficult to simultaneously image dozens of disks with a resolution on the scale of a few au. The application of so-called "super-resolution imaging techniques" has a potential to increase the number of spatially resolved disks on this scale even with originally 0".1 resolution data, and to achieve higher spatial resolution than ever. Here, I have focused on a new data science approach to image reconstruction in ALMA data, known as sparse modeling (SpM). This image reconstruction fits the observation data of both short and long baseline lengths by utilizing non-parametric imaging, which consists of the chi-square and penalty terms, and relying on the sparsity of the true solution. It thus has the potential to significantly improve the effective resolution of ALMA. Given this background, I study the following topics with a wealth of available ALMA observation data.

As the first step of the present work, SpM is applied for the first time to the observational data sets taken by ALMA. I chose two independent data sets observed with different array configurations at Band 7 (0.9 mm), targeting the protoplanetary disk around HD 142527; one in the shorter-baseline array configuration (~ 430 m), and the other in the longer-baseline array configuration (~ 1570 m). The image resolutions reconstructed from the two data sets are different by a factor of ~ 3. I confirm that the previously known disk structures appear on the images produced by both SpM and the conventional method, CLEAN, at the standard beam size. The image reconstructed from the shorter-baseline data using the SpM matches that obtained with the longer-baseline data using CLEAN, achieving a super-resolution image from

which a structure finer than the beam size can be reproduced. The results demonstrate that SpM can recover high-quality images even at the super-resolution regime.

Following the successful demonstration of SpM imaging of HD 142527, I focus on the case study targeting the T Tau system (T Tau N, Sa & Sb) located in the Taurus region. The previous ALMA observations have not revealed the detailed structure in the disk around T Tau due to insufficient spatial resolution: T T Tau N has a small disk with a radius of about 20 au, and the T Tau S system has a dwarf disk compared to T Tau N. To elucidate the detailed structure in the disks around T Tau, I carried out super-resolution imaging with SpM. I use the ALMA Band 6 (1.3 mm) continuum data and achieve an effective spatial resolution of $\sim 30\%$ (5 au) compared with the conventional CLEAN beam size of 17 au. The reconstructed image reveals a new annular gap structure at $r = 12$ au in the T Tau N compact disk with a disk radius of 24 au and resolves the T Tau Sa and Sb binary into two sources. If the observed gap structure in the T Tau N disk is caused by an embedded planet, we estimate a Saturn-mass planet when the viscous parameter of the disk is 10^{-3}.

I next present Taurus disk survey with the super-resolution imaging. I utilize ALMA 1.3 mm images for 40 Class II protoplanetary disks in the Taurus star-forming region. The target is selected from ALMA archival Band 6 (1.3 mm) data, which are observed with a nominal resolution less than $0''.1 - 0''.2$ and a relatively high signal-to-noise ratio (SNR > 30). The SpM imaging is applied to explore several au-scale substructures in compact and large disks with gaps and rings, which may evidence forming planets. The dust disk radius $r_{\rm d}$ is found to have a wide span ranging from 8 up to 200 au with a median of 45 au. Using the SpM images of 40 disk sources, such as achievable effective spatial resolution and limitation of its applicability has been investigated, As a result, SpM achieves better spatial resolution than CLEAN, i.e., $\sim 30 - 50\%$ of the CLEAN beam for half of the disk sample with more compact size and higher SNR. SpM images reveal 23 gaps, 29 rings, and 30 inflections (suggesting unresolved gaps or other features), and four disks with a ring alone. The gap locations $r_{\rm gap}$ of the target disks are located at $r_{\rm gap} = 5.5$ to 131 au; $r_{\rm gap}/r_{\rm d}$, the gap location normalized by their disk radius, is found to be around 0.1 or 0.4-0.7. Including several disks of the Disk Substructures at High Angular Resolution Project (DSHARP), I find the stellar mass dependence of the gap size and then estimate planetary masses assuming the gaps are due to forming planets and by applying the theoretical method of gap-formation, which connects the planetary mass and gap properties. If viscous parameters are taken over a wide range of $10^{-2} - 10^{-4}$, the stellar mass dependence of planetary mass in the outer disk regions ($r > 20$ au) can be observed for large disks. The majority of the inferred planets with a low-mass star (M–K type) is found to be Neptune-mass planets.

This thesis concludes that the new imaging technique using SpM is an attractive choice to provide a high-fidelity super-resolution image with ALMA, substructures such as gap and ring are found to be common for Class II disks in the low mass star-forming regions, and host stellar masses depend on gap size of their disks, suggesting that planetary masses inferred from the gap properties are related to the host stellar mass.

Contents

4   ALMA Disk Substructure Survey with Super-resolution Imaging (ALMA Disk-3S) in the Taurus Star-forming Region   **67**

Chapter 1

Introduction

How did the various planetary systems of the universe come into being? A planet formation hypothesis (or solar nebular hypothesis) was proposed by Kant and Laplace (Kant-Laplace nebular hypothesis; Kant 1755) long before astrophysicists suggested the presence of protoplanetary disks other stars and studied the formation of planets inside these disks. To answer this question, the diversity of the protoplanetary disks, i.e., birthplaces of planetary systems, must be understood. Planets are thought to originate from protoplanetary disks composed of cold gas and solid particles (dust) surrounding young star (Weidenschilling 1977; Hayashi 1981). Such disks are a natural consequence of star formation (Armitage 2011), and several hundred have been observed in the low-mass star-forming regions at a distance of ~ 140 pc from the solar system (Koepferl et al. 2013). Over the past two decades, spatial resolution has been dramatically improved, for example, by a factor of 40 between the Nobeyama Millimeter Array (NMA) and the Atacama Large Millimeter/submillimeter Array (ALMA) when observing the circumstellar disk around HL Tau (see Figure 1.1; Kitamura et al. 2002; Kwon et al. 2011; ALMA Partnership et al. 2015). Owing to the advent of ALMA, substructures, such as annular gaps and rings, of the HL Tau disk were finally discovered at a high spatial resolution of $0''.03$. Several theories have attempted to explain the observational result, and some of them have proposed the planet origin of these substructures, that is, an idea that the interaction between the planet and disk is thought to have created these gaps in the disk (e.g., Lin & Papaloizou 1986; Takeuchi et al. 1996; Pollack et al. 1996; Zhu et al. 2012; Pinilla et al. 2012). To investigate how and where planetary formation occurs in the disks, or how the relationship between young planets in the disk and its stellar mass plays a role, high spatial resolution is therefore vital.

A spatial resolution of $0''.02 - 0''.03$ (or $3 - 4$ au at $d = 140$ pc) is an ideal case even for ALMA, which needs the observations using the longest baselines. Generally, ALMA observations have a spatial resolution of $0''.1$ due to the limited use of such longest baselines. High spatial resolutions have been limited for bright and large disks with radii of $r = 50 - 260$ au (Andrews et al. 2018b; Cieza et al. 2020). It is thus difficult to simultaneously image dozens of disks with a resolution on the scale of a few au. The application of so-called "super-resolution imaging techniques" is desired to increase the number of spatially resolved disks on this scale and hence

understand the general properties of planet-forming disks and their diversity.

I have focused on a new statistical approach to image reconstruction, known as sparse modeling (SpM), which is one of the most promising super-resolution techniques. In radio interferometry, an image can be obtained from the Fourier transform of the observed data, so-called visibility data; however, numerous artifacts appear on the image because of insufficient sampling. To reconstruct the image from the visibility data, the CLEAN algorithm (hereafter referred to as the conventional method) has been widely used (Högbom 1974; Clark 1980; Schwab 1984; Cornwell 2008; Zhang et al. 2020). This technique iteratively identifies the point source in the image domain and subtracts the synthesized beam pattern (that is, the point-spread function) from the image. This process is repeated until a convergence requirement is met. The final image is obtained by convolving he point source model (i.e., a full set of identified point sources) with an idealized CLEAN beam (usually an elliptical Gaussian fitted to a synthesized beam). However, the beam convolution in the image domain cause a virtual "loss" in spatial resolution; i.e., a point source is expressed as a source with a CLEAN beam size. Image reconstruction based on SpM instead fits the observation data of both short and long baseline lengths by utilizing non-parametric imaging, which consists of the chi-square and penalty terms, and relying on the sparsity of the true solution. This reconstruction has been shown in mock observations to achieve spatial resolutions approximately three times higher than those of the conventional method without increasing the baseline length (Honma et al. 2014; Akiyama et al. 2018; Kuramochi et al. 2018), which has the potential to significantly improve the effective resolution of ALMA. The performance of this method has been mainly evaluated in simulations. Demonstrations using real observation data, for example, using ALMA, have never been performed, except for Event Horizon Telescope (EHT) observations (Event Horizon Telescope Collaboration et al. 2019).

With a wealth of available ALMA observation data, I investigate whether the new super-resolution imaging technique with SpM can achieve a 2–3 times higher spatial resolution than the conventional method (CLEAN) while maintaining high image fidelity. I applied this imaging technique to reveal the detailed structure of protoplanetary disks, which have not previously been spatially resolved, and explored the statistical nature of disk substructures from the Taurus disk survey that was revealed by super-resolution imaging. A general overview of our current knowledge on disk formation around young stellar sources and imaging synthesis using radio interferometer is provided in this introduction.

1.1 Evolutionary Schemes of Star Formation

The formation of a star is initiated by the gravitational collapse of a molecular cloud (Ward-Thompson & Whitworth 2011). The conservation of angular momentum ensures the spin-up of material, leading to a flattened, rotating structure around the star, known as a "disk" (Terebey et al. 1984). The early-phase disk is surrounded and fed by the protostellar envelope (e.g., Ohashi et al. 2014; Aso et al. 2015) and simultaneously deposits material onto the still-forming star for
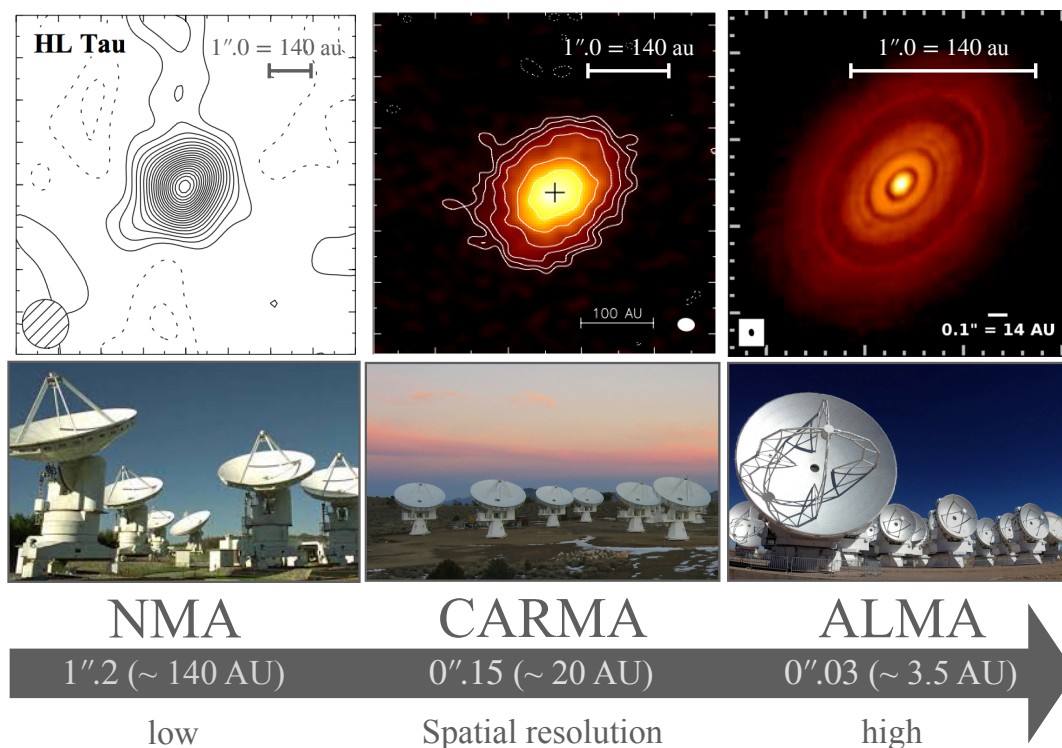
Figure 1.1: Observation history of the protoplanetary disk around HL Tau over the years. From left to right, mm source images from the NMA (Nobeyama millimeter array; Kitamura et al. 2002) , CARMA (Combined Array for Research in Millimeter-wave Astronom; Kwon et al. 2011), and ALMA (Atacama Large Millimeter/submillimeter Array; ALMA Partnership et al. 2015). The spatial resolution was improved by a factor of 40 between the NMA and ALMA. The credits for the radio interferometric images go to NAOJ and Caltech.

a period of a few 10^5 years (Dunham et al. 2014). Subsequently, the disk disperses its material through viscous accretion inside the disk and stellar winds at the disk surface (Hernández et al. 2007). Furthermore, the outflow from the disk removes a significant amount of gas from the envelope (Offner & Arce 2014). The disk gradually loses a fraction of its gas mass, and accretion onto the host star ceases; at this stage, several planets in the system begin to form. In such an environment, the dust, which has an initial size of $\sim 0.1 - 1$ μm (Mathis et al. 1977) and a size distribution of $n(a) \propto a^{-3.5}$, where $n(a)$ indicates the number of dust particles with size a, increases via repeated attachment to each other. The gravity of the central star causes dust to settle on the disk midplane, and the dust eventually grows to the planetary mass on the disk midplane (Chiang & Youdin 2010; Johansen et al. 2014). In the following subsections, we describe the evolutionary classification of protostars and characteristics of the circumstellar disk based on observational studies.
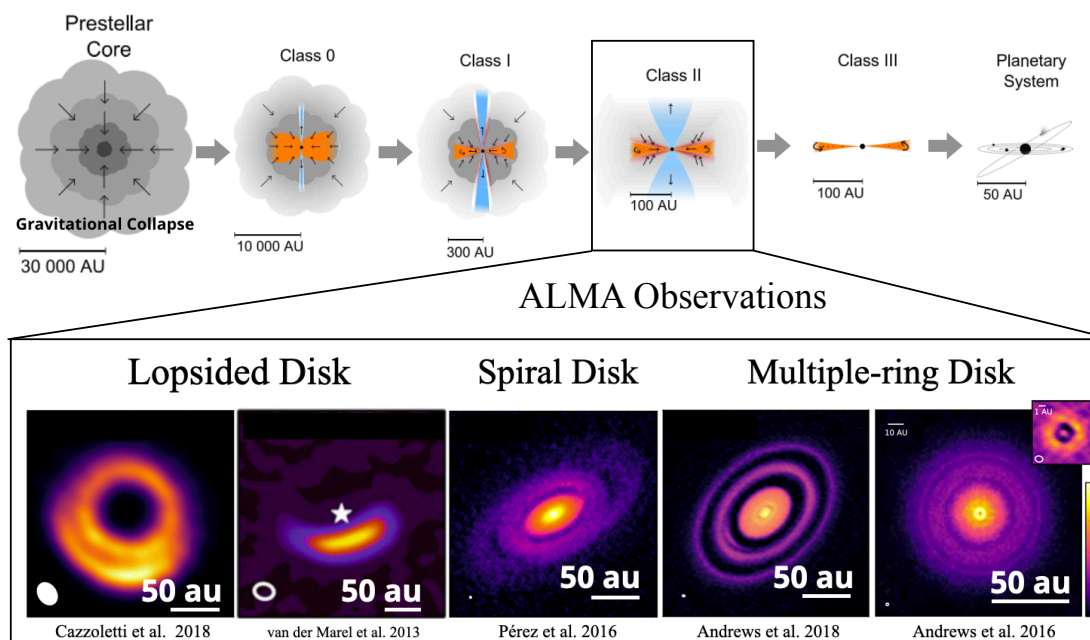
Figure 1.2: Top panel : The evolutionary process of star and planet formation. The prestellar core collapses into a protostar buried in the envelope. As the material falls, a Keplerian rotating disk forms around the young star. The disk evolves from a gas-rich disk to a debris disk, during which the gas is depleted, and eventually becomes a planetary system. The illustration of the evolutionary process was taken from Persson (2014). Bottom panel: The detailed substructure of the disks revealed by high-resolution ALMA observations. Lopsided, spiral, and multiple-ring disks have been confirmed (Cazzoletti et al. 2018; van der Marel et al. 2013; Pérez et al. 2016; Andrews et al. 2018b, 2016).

1.1.1 Evolutionary Classification of Protostars

Figure 1.3 shows the evolutionary sequence of planet formation. With the availability of infrared observations from the Infrared Astronomical Satellite (IRAS) and the Spitzer Space Telescope (Adams et al. 1987; Evans et al. 2009), the evolutionary sequence around protostars and pre-main-sequence (PMS) stars are grouped into four classes (that is, Class 0 $\sim$ III). The classification is based on the spectral slope (known as spectral index α) of their continuum spectra between 2 and 20 μm. The slope can be expressed as $\alpha = d\log(\lambda F_\lambda)/d\log(\lambda)$, where F_λ denotes the flux density.

Class 0 protostars are candidates for extremely young accreting protostars surrounded by a dense infalling envelope of gas and dust (Andre et al. 1993). The next youngest protostars detected in infrared are Class I sources and are characterized by $\alpha > 0$. They are less deeply embedded but still surrounded by an infalling envelope. The time scale of the protostellar phase (Class 0–I) is estimated to be $\sim$ 500 kyr, and the Class 0 phase itself is estimated to continue for $\sim$ 160 kyr (Dunham et al. 2014). Both the dust disk mass and radius decrease

in the protostellar phase (Tobin et al. 2020). The decrease in the disk mass is expected from disk evolution and accretion, and the decrease in the disk radius may suggest that the initial conditions of star formation do not lead to the systematic growth of the disk radius or that radial drift keeps the dust disk size small. Some of these observed disks have been confirmed to have a substructure using ALMA observations (that is, a gap or ring; Sheehan et al. 2020; Gulick et al. 2021). Although it is unclear whether the feature is related to planet formation, its presence so early in the lifetimes of disks raises interesting questions about how substructures are formed. Furthermore, the envelopes surrounding them are largely dissipated by the end of the Class I phase, resulting in disks surrounding the pre-main-sequence stars. These sources are known as Class II young stellar objects (YSOs) characterized by $-1.5 < \alpha < 0$. Most of these objects do not have envelopes but have disks (e.g., Ansdell et al. 2016; Cieza et al. 2019). This high disk occurrence rate in the later stages indicates that disk formation indicates a universal process in star formation. These disks around pre-main-sequence stars are commonly referred to as protoplanetary disks or Class II disks (see the next subsection for details). The final evolutionary stage of infrared PMS stars is known as Class III with $\alpha < -1.5$. These sources do not have envelopes but are surrounded by remnant protoplanetary disks (Hughes et al. 2018).

1.2 Protoplanetary Disks

Young stars surrounded protoplanetary disks are commonly identified through optical observations (e.g., Hubble Space Telescope in Bally et al. 1998). They can be subdivided by stellar mass as follows: T Tauri stars (Joy 1945) have masses in the range $0.2-2$ $M_\odot$ and luminosities in the range $0.1-20$ $L_\odot$ (Ward-Thompson & Whitworth 2011), and more massive stars ($2-12$ $M_\odot$) in the same evolutionary stage as T Tauri stars, which are known as Herbig Ae/Be stars (Herbig 1960; Waters & Waelkens 1998).

Protoplanetary disks are geometrically flattened structures consisting of a small quantity of dust (approximately 1% of the gap mass) suspended in molecular gas (Williams & Cieza 2011). Owing to the effects of thermal pressure, the density decreases with height from the disk midplane (e.g., Dubrulle et al. 1995). The disk temperatures are controlled by the passive irradiation of dust from the primary star (e.g., Dullemond et al. 2001). The dust disk radii of young stars have been measured using (sub)millimeter observations. Dust disk radii are in the range of $\sim 10-200$ au (Ansdell et al. 2016; Long et al. 2019; Cieza et al. 2019), whereas gas disk radii are estimated to be $\sim 100-1000$ au (Simon et al. 2017; Ansdell et al. 2018). Disks generally exhibit smaller dust continuum emissions than line emissions (Andrews 2020; Sanchis et al. 2021), and the difference in disk size is argued to be caused by both or either of the following two effects: the difference in optical depth between continuum and line emissions, or the radial drift of dust grains, which is an effect that the growing mm-sized grains experience owing to the drag force by abundant gas and they move toward the central star (Trapman et al. 2019).

Some of the observed disks around stars have been revealed to have substructures that

are lopsided, spiral, and exhibit (multiple) rings by ALMA high-resolution observations scaling down to $\sim 5-20$ au (see Figure 1.3; van der Marel et al. 2013; Pérez et al. 2016; Andrews et al. 2016; Cazzoletti et al. 2018; Andrews et al. 2018b). The gaps show axisymmetric patterns of alternating increases (rings) and decreases (gaps) in intensity distribution, which are often seen in the disks around low-mass (M-K type) stars detected in (sub)millimeter continuum observations (Andrews 2020). There are variations in this category, from cases where the entire disk is resolved into narrow gaps and rings are resolved into single gaps separating the central star from the outer rings. Asymmetric features, including the lopsided disk, are azimuthally resolved but radially narrow, which are often observed around intermediate (Herbig) mass stars (van der Marel et al. 2021; Stapper et al. 2021). It may represent gravitational instability due to its massive disk (Kratter & Lodato 2016).

1.3 Formation of Planets in Disk

An overview of the concepts of planet formation in disks are briefly introduced by focusing on two major models of core accretion (Mizuno 1980; Pollack et al. 1996) and gravitational instability (Cameron 1978; Boss 1998).

In the core accretion scenario, dust first accumulates in larger bodies via streaming instability (Youdin & Goodman 2005). Streaming instability is commonly accepted as a necessary step to form planetesimals in disks. We first consider a situation that consists of a local concentration of pebbles (mm/cm-sized particles) at the maximum gas pressure in the disk, which can stop their radial drift toward a central star (Pinilla et al. 2012). The local enhancement in the abundance of pebbles at such dust traps can then provide ideal conditions to trigger disk instability. For instance, it is thought that a concentration of the pebbles which is in state with the local gas-to-dust mass ratios smaller than ~ 30 triggers the instability (Carrera et al. 2015; Yang et al. 2017). This instability works as amplifying the maximum gas pressure and gathers more pebbles. As a result, The rapid formation of particle clumps can become self-gravitating and allows to grow to km-sized planetesimals (Simon et al. 2016; Abod et al. 2019). The annular gaps commonly observed in Class II disks could be interpreted as tentative evidence of particle trapping at the local gap pressure maxima generated by the inferred planet in the gap (e.g., Macías et al. 2021).

In gravitational instability scenario, a massive disk rapidly becomes gravitationally unstable and collapses with gas and dust to form a giant planet. The gravitational instability of the disk can be assessed using the Toomre Q parameter (Toomre 1964). This parameter can be calculated using the formula; $Q \equiv c_s \Omega_K / \pi G \Sigma_{gas}$, where c_s is sound speed, Ω_K is angular velocity, G is the gravitational constant, and Σ_{gas} is gas surface density. If the disks get close to unity, the disk is susceptible to gravitationally unstable, inducing a non-axisymmetric structure (Laughlin & Bodenheimer 1994). For Q to be near unity given optimistic constraints on disk temperature, we expect disk-star mass ratios M_d/M_* greater than 10^{-2} (Kratter & Lodato 2016). That is, the disks most likely to be gravitationally unstable are relatively massive compared with their

host star. For example, ALMA molecular line observations of the HL Tau disk have presented a disk-star mass ratio of 10^{-1} and Toomre Q of near unity ($r = 50 - 100$ au) (Booth & Ilee 2020), which suggests that this disk is affected from the gravitational instability. The region of instability coincides with the location of a proposed planet-carved gap in the dust disk (ALMA Partnership et al. 2015) and a spiral in the gas (Yen et al. 2019). If the origin of the gap is confirmed to be due to a forming giant planet, it is likely to have formed via the gravitational instability of the disk.

1.4 Observations of Dust Emissions from Disks
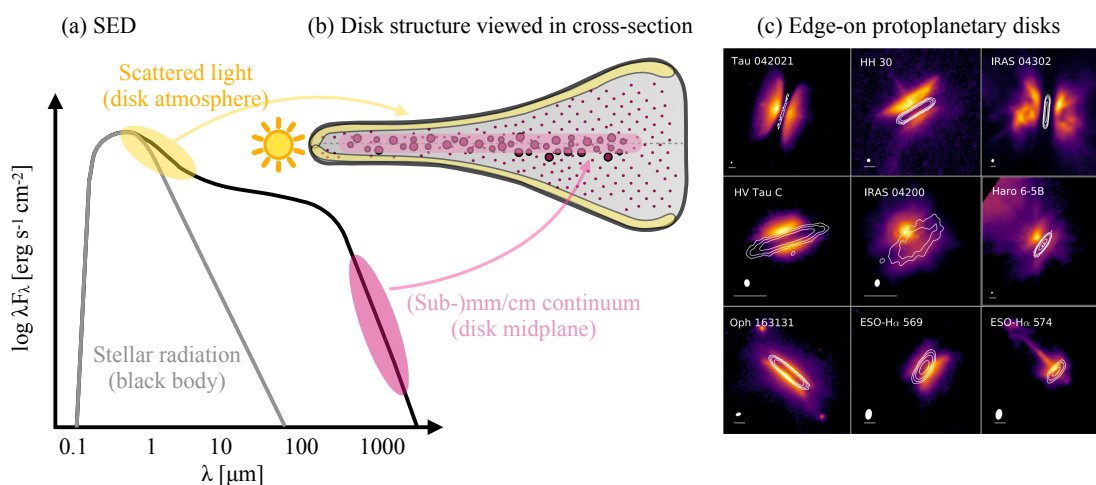
Figure 1.3: (a) Schematic view of the spectral energy distribution (SED) of a protoplanetary disk, ranging from optical to centimeter wavelengths. (b) Diagram of a disk structure viewed in cross-section. The gas is presented in grayscale, and the solids are marked with exaggerated sizes and colors. (c) Overlay of near-infrared Hubble Space Telescope scattered-light (colors, $\lambda = 0.4 - 2.2$ μm) and ALMA continuum images (contours, $\lambda = 0.8 - 1.3$ mm) for all sources in Villenave et al. (2020). For most sources, the millimeter continuum emission is found to be more compact than the scattered light, both in the vertical and radial directions.

Dust disks can be observed via continuum emission from dust and scattered light of dust reflected from stellar emission. Each emission and scattered light is sensitive to the properties of the disk and dust in the disk; hence, observational information from both emission and scattered light provides us with the properties of the dust itself and the dust disk. Figure 1.3 provides a guide to the characteristic regions of emission and scattered light at two representative wavelengths based on a spectral energy distribution (SED) model[1].

---

[1]Spectral energy distribution (SED) is a useful tool for interpreting source properties that characterize the radiative transfer of star light through the disk material over frequency or wavelength (Andrews 2015). The SED of the disk can be calculated by summing the local disk emission at each radius, weighted by the area. The host

Scattered light from the near-infrared wavelength ($\lambda \simeq 1-5~\mu$m) traces small ($\sim$ mm-sized) dust grains suspended in the gas vicinity of the surface disk (Andrews 2015, 2020), reflecting the radiation emitted by the central star (see panel (c) in Figure 1.3). The tracer is sensitive to the radial variation in the vertical height of the dust distribution and can detect flared disks (e.g., Avenhaus et al. 2018; Garufi et al. 2020). This tracer has the advantage of achieving high-spatial resolutions with adaptive optics systems operating near the diffraction limit in 8-m telescopes (such as the Subaru Telescope or the Very Large Telescope). It enables us to observe features in disks at $50-60$ mas scales (e.g., Muto et al. 2012; Avenhaus et al. 2018).

The (sub)millimeter continuum emission traces the dust thermal continuum ($\lambda \simeq 10^{-4}-10^{0}$ cm) originating from the disk midplane, that is, the site of planet formation, owing to the relatively low dust opacity at this long-wavelength (Dullemond et al. 2007). Using simplifications, a toy disk model that captures the essential features of thermal emission can be constructed from the radiative transfer equation (Rybicki & Lightman 1979). Assuming that dust scattering is negligible in a disk and the disk structure is vertically thin, the radiative transfer of the dust disk can be expressed as

$$I_\nu = B_\nu(T_\mathrm{d})\left(1 - e^{-\tau_\nu}\right) \tag{1.1}$$

where B_ν and T_d denote the full Planck function and dust temperature, respectively, and τ_ν is the optical depth, expressed as $\tau_\nu = \kappa_\nu \Sigma_\mathrm{d}$. Here, κ_ν and Σ_d denote the absorption dust opacity and dust surface density, respectively. In this model, the continuum simply provides black-body radiation B_ν weighted by the absorbing column ($1 - e^{-\tau_\nu}$). The optical depth τ_ν generally decreases with wavelength (e.g., Carrasco-González et al. 2019). The transition to optically thin regime ($\tau_\nu \leq 1$) is traditionally expected at (sub)millimeter wavelengths. In the regime, the intensity scales with the product of temperature, dust surface density, and opacity ($I_\nu \simeq \tau_\nu B_\nu = \kappa_\nu \Sigma_\mathrm{d} B_\nu$; Beckwith et al. 1990), whereas optically thick ($\tau_\nu > 1$) emissions play a role in a thermometer ($I_\nu \simeq B_\nu$) and trace the layer from the disk atmosphere (Andrews 2015).

1.5   Radio Interferometer

A (sub)millimeter interferometer can be used to observe through to a disk midplane owing to the relatively low dust opacity at such long wavelengths. It can be regarded as the best tool for observing the site of planet formation. In this section, we describe the method of obtaining the intensity I_ν emitted from the disk through observations with a radio interferometer based on interferometry theory.

First, the interferometer can be considered a single-segmented telescope (Thompson et al. 2017). It has the same angular resolution as a single telescope with a diameter equal to the

---

star dominates the SED at $\sim 1~\mu$m. Thermal emission from the disk begins to outshine the start at $\geq 2-5\mu$m (near-infrared). Broad spectral features ($\sim 10~\mu$m) provide insight into the properties of dust. The turnover in the infrared region marks the transition to optically thin emission. The millimeter SED slope can be used to investigate the shape of the opacity spectrum, which constrains the dust size in the disks (Ricci et al. 2010; Pinilla et al. 2014; Ribas et al. 2017; Zagaria et al. 2021).

largest separation between array elements but a lower sensitivity owing to the reduced collecting area. Moreover, there is a clear difference in imaging, that is, a single telescope focuses on the incoming signal to the focal plane directly imaged. In an interferometer, the signals are focused by a correlator, and the source is imaged indirectly. The basic unit of the synthesis array is a two-element interferometer consisting of a pair of antennas. Each two-element interferometer is defined by the distance between the pair of antennas, known as the baseline. An array of n antennas consists of $\frac{1}{2}n(n-1)$ such baselines. The power of an interferometer arises from its ability to image with a high spatial resolution, and the aim is to measure the two-dimensional brightness distribution of a radio source. A Fourier synthesis of the interferometer response pattern is the key to achieving it.

1.5.1 Interferometry Theory
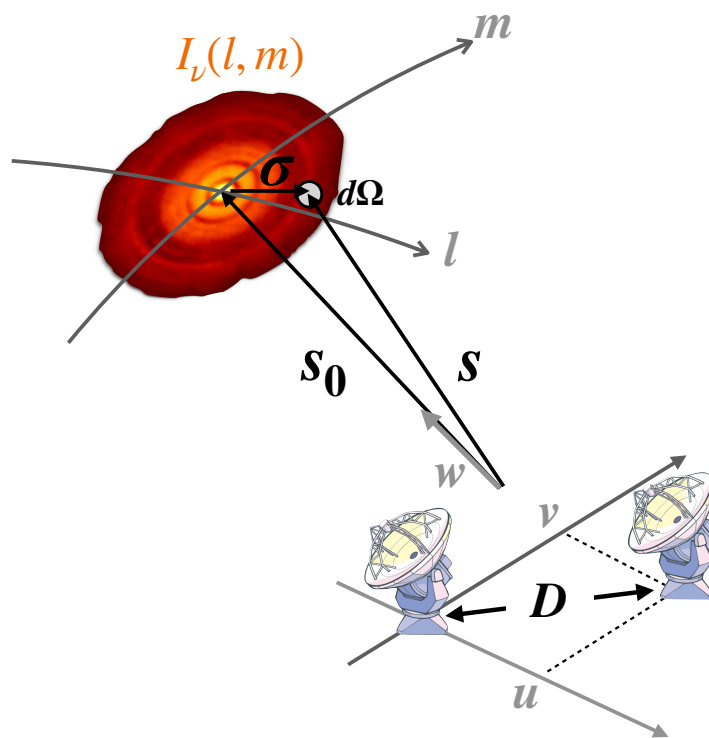
Figure 1.4: Schematic view of the fundamental relationships in interferometry theory for a two-element radio interferometer The antenna illustrations were taken from NAOJ.

Figure 1.4 shows the fundamental relationships in interferometry theory. The aim of synthesis imaging is to obtain the celestial brightness distribution $I_\nu(l, m)$ emitted from a radio source (e.g., a protoplanetary disk). Here, the radio source is observed in the relative direction $\boldsymbol{s}$ from the phase center $\boldsymbol{s}_0$ of the field of view. This is measured in terms of the angular extent of the source on the sky. The radiative intensity from the radio source $d\Omega$ in the frequency range $\Delta\nu$ can be expressed as $I_\nu(\boldsymbol{s})A(\boldsymbol{s})\Delta\nu d\Omega$, where $A(\boldsymbol{s})$ is a response pattern defined as the effective

collecting area. Given that the intensity extends over a small region compared with the response pattern, we can rewrite as $\boldsymbol{s} = \boldsymbol{s}_0 + \boldsymbol{\sigma}$, where $\boldsymbol{\sigma}$ is the vector connecting the phase center $\boldsymbol{s}_0$ and the relative direction $\boldsymbol{s}$. Given that the baseline vector $\boldsymbol{D}$ connects the two antennas on the ground, the response of the two-element interferometer to $I_v(\boldsymbol{\sigma})$ can be expressed in terms of visibility $V(\boldsymbol{D})$. Assuming the source is far from the interferometer, the visibility $V(\boldsymbol{D})$ can be expressed as

$$V(\boldsymbol{D}) = \int_{\Omega_{\text{size}}} \mathcal{A}(\boldsymbol{\sigma})I_v(\boldsymbol{\sigma})\mathrm{e}^{-2\pi\mathrm{i}\nu\boldsymbol{D}\cdot\boldsymbol{\sigma}/c} \, \mathrm{d}\Omega, \tag{1.2}$$

where Ω_{size} denotes the source-angle size. Next, we transform Equation 1.2 from a theoretical to practical formula. The relative direction $\boldsymbol{s}$ expands into three-dimensional coordinates on the celestial plane (l, m, n), and the baseline vector $\boldsymbol{D}$ expands into three-dimensional coordinates (u, v, w), where u and v point toward the east and north, respectively, and w is parallel to the direction of the source. The units of the coordinates (u, v, w) are the observed wavelengths λ. In other words, $(u, \nu, w) = \left(\frac{\boldsymbol{D}\cdot\mathbf{e}_l}{\lambda}, \frac{\boldsymbol{D}\cdot\mathbf{e}_m}{\lambda}, \frac{\boldsymbol{D}\cdot\mathbf{e}_n}{\lambda}\right)$, where $(\mathbf{e}_l, \mathbf{e}_m, \mathbf{e}_n)$ denote the unit vectors of the coordinates (l, m, n) . Thus, the coordinate (l, m) is the cosine direction with respect to u and v, which can be expressed as $\boldsymbol{D}\cdot\boldsymbol{s}/\lambda = ul + vm + wn$. In particular, the $(l,\ m)$ plane is commonly known as the image plane because the source intensity $I_\nu(l, m)$ is defined on the plane. With these definitions, we can describe the visibility in Equation 1.2 as

$$V(u, v) = \int_{-\infty}^{+\infty} \int_{-\infty}^{+\infty} \mathcal{A}(l, m)I_v(l, m)e^{-2\pi i(ul+vm)}\mathrm{d}l \, \mathrm{d}m. \tag{1.3}$$

Equation 1.3 is assumed in relation to the sky $l, m \ll 1$ in the case of small field imaging (that is, $\left|\left(l^2 + m^2\right)w\right| \ll 1$). In small-field imaging, the visibility $V(u, v)$ represents a Fourier transform component of the intensity distribution given by $\mathcal{A}(l, m)I_\nu(l, m)$. In other words, $\mathcal{A}(l, m)I_\nu(l, m)$ can be obtained by applying an inverse Fourier transform to the visibility data. The brightness distribution $I_\nu(l, m)$ is calculated through the correction of $\mathcal{A}(l, m)$. Equation 1.3 can be transformed into a set of linear equations:

$$\mathbf{V} = \mathbf{FI}, \tag{1.4}$$

where $\mathbf{V}$, $\mathbf{F}$, and $\mathbf{I}$ denote the observing vector (visibility), Fourier matrix consisting of the exponential components $(F_{u,v} = \exp^{-2\pi i(ul+vm)})$, and the solution vector (image), respectively. This equation represents the principle of operation in radio interferometry, which is generally known as the van Cittert–Zernike theorem.

1.6 Synthesis Imaging

Figure 1.5 illustrates image processing from the observed visibility data $V(u, v)$ to the resultant image (the dirty image, $DI(l, m)$). The integral in Equation 1.3 is mathematically performed
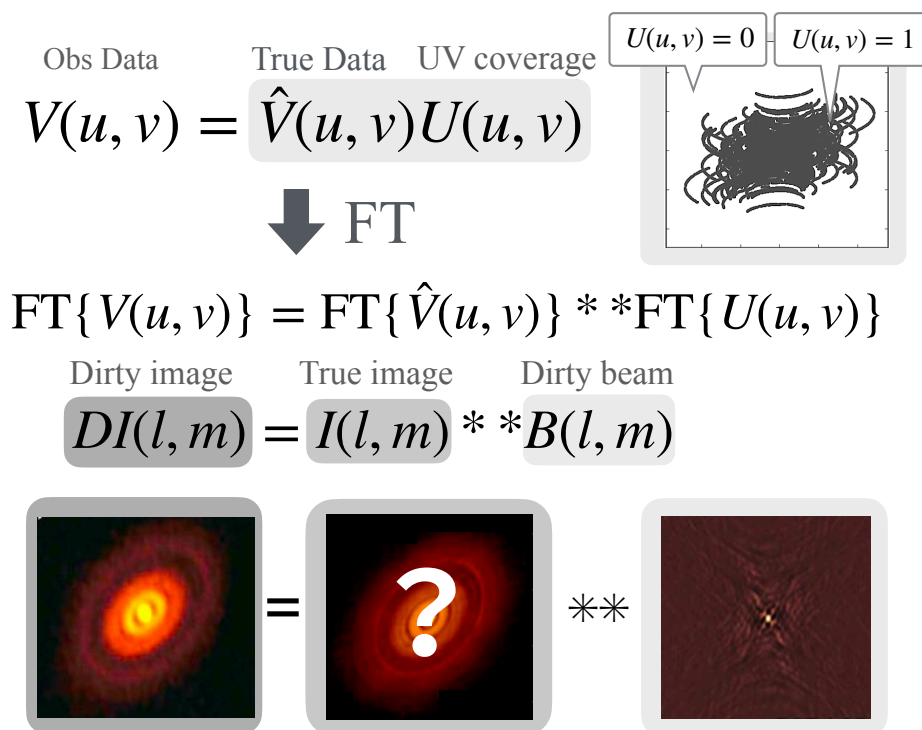
Figure 1.5: Image processing from the observed visibility data to the resultant image (the dirty image).

from $-\infty$ to $+\infty$; however, in practice, this is carried out over the limited range covered by the u and v values. There should be spaces between antennas, which causes unsampled "holes" in the $uv-$coverage. Such an incomplete (u, v) coverage causes an "underdetermined problem" in Equation 1.3 (Honma et al. 2014). For convenience, this problem can be solved by filling unsampled visibilities with zero, which is referred to as "zero-padding". Consequently, the observed visibility data $V(u, v)$ become the true data $\hat{V}(u, v)$ multiplied by $U(u, v)$, which equals 1 at (u, v) points where there is data and is 0 elsewhere. Thus, the convolution theorem indicates that the Fourier transform of the observed visibility data $V(u, v)$ is equal to the convolution of the Fourier transform of the true source visibility distribution (the true image, $I(l, m)$) and the Fourier transform of the $uv-$coverage (that is, the dirty beam, $B(l, m)$). Therefore, we obtain a Fourier transform of $V(u, v)$, known as the dirty image $DI(l, m)$, which suffers from dirty beam sidelobes. The relationship can be expressed as

$$DI(l, m) = I(l, m) * *B(l, m) \Leftrightarrow \hat{V}(u, v)U(u, v) \tag{1.5}$$

Because the $uv-$coverage is not fully sampled, the dirty beam has sidelobes that result in artifacts appearing in the dirty image. Therefore, it is essential to reconstruct the image. In the following subsection, several image reconstructions are introduced: the CLEAN algorithm, the maximum entropy method (MEM), and sparse modeling (SpM).

1.6.1 CLEAN algorithm
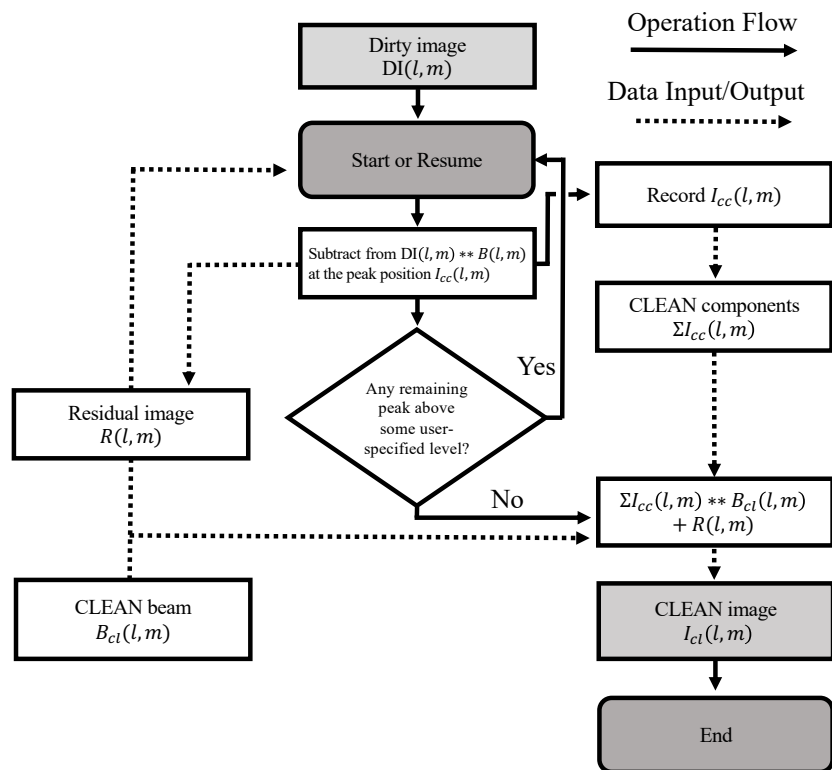
Figure 1.6: Flowchart of image processing using the CLEAN algorithm. The algorithm was introduced by Högbom (1974). $DI(l,m)$ is the dirty image directly obtained by the Fourier transform of the observed visibility data. $B(l,\ m)$ is the dirty beam consisting of fringe patterns. $l_{cc}(l,\ m)$ is the CLEAN component (delta function), the intensity of which is found by subtracting $DI(l,m)$ to obtain $B(l,m)$. B_{cl} is the CLEAN beam, which has an ideal beam shape composed of a Gaussian distribution using the FWHM of $B(l,\ m)$. $R(l,m)$ denotes the residual map. I_{cl} is the CLEAN image, which can be obtained through the beam convolution of $l_{cc}(l,\ m)$ with B_{cl}.

The CLEAN algorithm (e.g., Högbom 1974; Clark 1980; Schwab 1984; Cornwell 2008; Rau & Cornwell 2011) is the most standard deconvolution algorithm. Figure 1.6 presents a flowchart of image processing using the CLEAN algorithm. The CLEAN algorithm iteratively determines the point source in the image domain that best fits the observed visibilities, starting from the dirty image $DI(l,m)$. This process is repeated until a convergence requirement is met. The model image becomes a collection of point sources, known as the CLEAN components $l_{cc}(l,\ m)$. To suppress the extrapolation of the model to scale below $B(l,\ m)$, the final image $I_{cl}(l,m)$ is obtained by convolving the point source model $I_{cc}(l,m)$ (CLEAN components) with an idealized CLEAN beam $B_{cl}(l,m)$ (usually an elliptical Gaussian fitted to the dirty beam; Cornwell et al. 1999). It should be noted that the beam convolution in the image domain cause a virtual "loss" in spatial resolution; i.e., a point source is expressed as a source with a CLEAN beam size (e.g.,

Jennings et al. 2020).

1.6.2 Maximum Entropy Method (MEM)

The MEM is different from the CLEAN algorithm in the sense that this method dose not employ Fourier transformation with zero-padding but instead applies a priori information through regularization to solve the observational equation, $\mathbf{V} = \mathbf{FI}$ (Cornwell & Evans 1985; Narayan & Nityananda 1986; Chael et al. 2018; Cárcamo et al. 2018). This regularization is implemented by an entropy function that includes the information obtained from the dirty image. Numerous studies have discussed the construction of entropy functions from a theoretical and philosophical perspective, and these algorithms are based on Bayesian statistics. Here, the MEM imaging method proposed by Cárcamo et al. (2018) is briefly introduced. This imaging fits a model image to the observed data by minimizing the following objective function [2]:

$$\mathbf{I}_{\text{MEM}} = \underset{\mathbf{I}}{\operatorname{argmin}} \left(||\mathbf{W}(\mathbf{V} - \mathbf{FI})||_2^2 + \Lambda_{\text{mem}} \sum_i \sum_j \frac{I_{i,j}}{G} \log \frac{I_{i,j}}{G} \right), \text{ subject to } \mathbf{I} \geq G \qquad (1.6)$$

where $\mathbf{I} = \{I_{i,j}\}$ is the two-dimensional image reconstruction to be solved, the element in row i and column j is represented by $I_{i,j}$, $\mathbf{V}$ is the observed visibility data, $\mathbf{F}$ is the Fourier matrix, and $\mathbf{W} = \{\delta_{ij}/\sigma_{ij}^2\}$ is a diagonal matrix that normalizes the residual visibility ($\mathbf{V} - \mathbf{FI}$) in the first term. σ_{ij} [3] is the observational error on each data point, and δ_{ij} is the Kronecker delta. The MEM approach depends on four parameters that determine the properties of the resulting image, $\mathbf{I}_{\text{MEM}}$. These parameters are the entropy penalization factor Λ_{mem}, the minimum dimensionless intensity value G, the cell size, and the image size. G is set as the thermal noise on the dirty image $DI(l, m)$ (Casassus et al. 2018). The first term is the sum of the squared residuals between the observational data and the model, namely the traditional χ^2 term, which represents how well the reconstructed image reproduces the observational data. The second term is the entropy function, which adjusts the degree of disturbance of the brightness distribution. The balance of entropy is controlled by positive variables Λ_{mem}. When $\Lambda_{\text{mem}} = 0$, Equation 1.6 solves the least-squares optimization problem. In the case of a very small Λ_{mem}, the problem is nearly least-square with a lower bound constraint ($\mathbf{I} \geq G$). However, when Λ_{mem} increases, the fit to the data is less important, and the source structure on the image becomes smoother. Therefore, the

---

[2]argmin returns the value of $\mathbf{I}$ for which the objective function is the smallest. lp-norm $||\mathbf{x}||_\mathbf{p}$ is generally
$\quad\;\;\mathbf{I}$
defined as $||\mathbf{x}||_p = (\sum |x_i|^p)^{1/p}$ for $p > 0$

[3]σ_{ij} denotes the RMS noise of a given observed visibility for an antenna pair (i, j), such as $\sigma_{ij}(Jy) = (2k/\eta_q\eta_c A_{eff})\sqrt{(T_{sys,i}T_{sys,j}/2\Delta\nu_{ch}t_{ij})} \times 10^{26}$, where k is the Boltzmann constant. A_{eff} is the effective antenna area and is approximately 0.75 for ALMA dishes. η_q and η_c are the quantization and correlator efficiencies, respectively. For ALMA, these values are 0.88 and 096, respectively. T_{sys} denotes the system temperature of the antenna. $\Delta\nu_{ch}$ is the effective channel frequency width, and t_{ij} is the integration time per visibility; see the ALMA technical handbook.

MEM allows the exploration of smoother solutions by changing this single parameter (Cárcamo et al. 2018).

MEM imaging is known to reconstruct a super-resolution image by determining the effective angular resolution via a mock observation targeting a single spike (Cárcamo et al. 2018). This method has already been applied to the image reconstruction of protoplanetary disks observed by ALMA (Cieza et al. 2017; Casassus et al. 2018, 2019; Pérez et al. 2020) and has achieved a super-resolution that is greater than the resolution achieved using CLEAN by a factor of 2–3. A complete investigation on how the Λ_{mem} parameter affects image properties and how to determine the optimal parameter will be in the scope of future studies.

1.6.3   Sparse Modeling (SpM)

Sparse modeling (SpM) is another promising technique for achieving a high spatial resolution. This approach, like MEM, is a non-parametric image synthesis to derive a plausible solution (or a reconstructed image) that fits both short- and long-baseline data by applying appropriate a regularization(s) for the data. It instead estimates a plausible solution to the undetermined problem of synthesis imaging by assuming that the solution is sparse on some basis. Pioneering works (Wiaux et al. 2009; Li et al. 2011) discussed the application of this approach and demonstrated its effectiveness in radio interferometer imaging based on comparisons with standard CLEAN images. In the following, we introduce the least absolute shrinkage and selection operator (LASSO or ℓ_1 regularization) and ℓ_1+TSV regularization (our used approach in the research), which are applications of SpM.

LASSO (ℓ_1 regularization)

Figure 1.7: A gallery of LASSO images and visibility profiles of the protoplanetary disk around HD 142527. The image reconstruction is applied for 0.8-mm (Band 7) continuum data observed with compact array configurations of ALMA. Details on the ALMA data are presented in Chapter 2. The upper panel shows images controlled by the positive variables $_l$. The bottom panel shows the radial visibility profiles between the LASSO model (purple) and measured (black) visibility data.
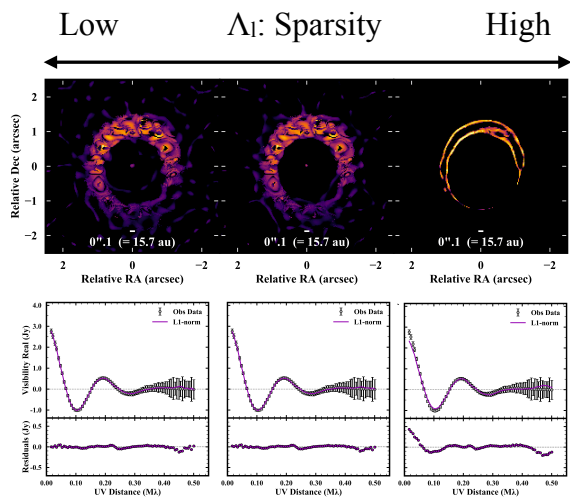
LASSO is a widely used method in SpM and was originally developed in the field of statistics (Tibshirani 1996). Honma et al. (2014) used LASSO to image a black-hole shallow in mock

observations with a radio interferometer. Imaging with LASSO is formulated as follows:

$$\mathbf{I}_{\mathrm{LASSO}} = \underset{\mathbf{I}}{\mathrm{argmin}} \left(||\mathbf{W}(\mathbf{V} - \mathbf{FI})||_2^2 + \Lambda_l \sum_i \sum_j |\mathrm{I}_{i,j}| \right), \text{ subject to } \mathbf{I} \geq \mathbf{0} \qquad (1.7)$$

The first term is the sum of the squared residuals between the observational data and the model, namely the traditional χ^2 term, which represents how well the reconstructed image reproduces the observational data. The second term, ℓ_1-norm, adjusts the sparsity of the brightness distribution. The balance of ℓ_1-norm is controlled by the positive variables Λ_l.

For reference, Figure 1.7 shows the LASSO images of the protoplanetary disk around HD 142527. The image reconstruction is used for 0.8 mm (Band 7) continuum data observed with compact array configurations of ALMA (details on the ALMA data are presented in Chapter 2). Although the structure of the HD 142527 disk originally formed a smooth crescent disk (e.g., Fukagawa et al. 2013), LASSO reproduces a sparsely distributed image owing to its underlying assumptions. The radio source, such as a protoplanetary disk, often represents a smooth structure on intensity distributions. It appears that regularization with LASSO is not a general-purpose constraint that works well for images. We should treat a non-sparse image with additional regularization instead of LASSO alone.

ℓ_1+TSV regularization
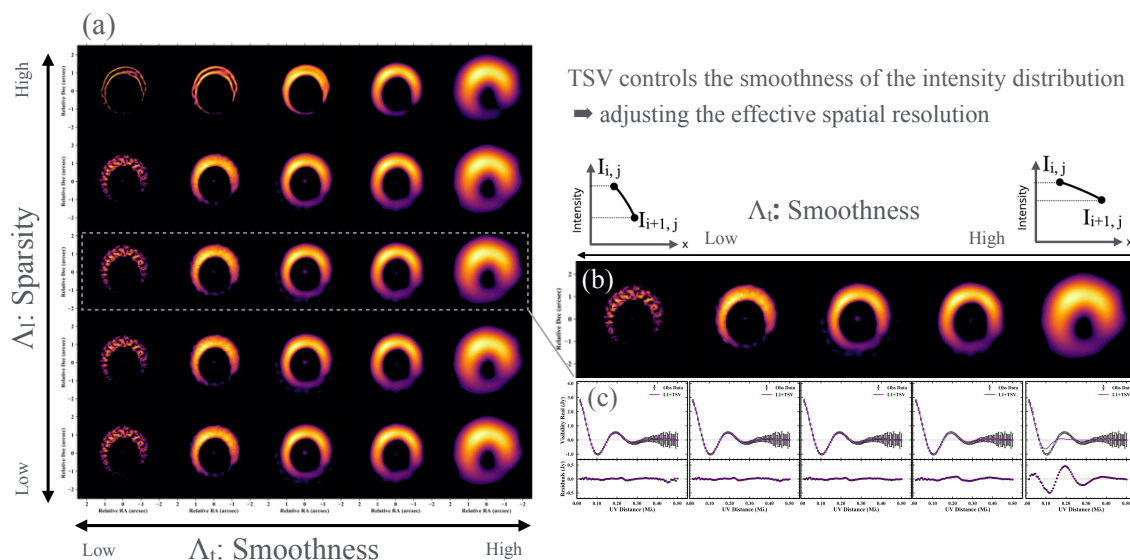
Figure 1.8: (a) A gallery of 25 SpM (ℓ_1+TSV) images of the protoplanetary disk around HD 142527. Image reconstruction is applied to the same data used in Figure 1.7. The images are controlled by the positive variables Λ_l (vertical line) and Λ_t (horizontal line). (b) Excerpted images controlled by TSV regularization. This shows that the TSV controls the smoothness of the intensity distribution and serves to adjust its effective spatial resolution on the image. (c) Visibility profiles of the SpM (ℓ_1+TSV) model (purple) and measured (black) visibility data.

Next, we introduce SpM with ℓ_1+TSV regularization (Kuramochi et al. 2018) and a procedure for generating the SpM image from visibility data owing to its application in this study. This latest imaging technique utilizes two convex regularization functions of the brightness distribution: ℓ_1-norm and the total squared variation (TSV), and these functions adjust the sparsity and smoothness of the brightness distribution, respectively. In particular, TSV has the property of selecting smooth images with no edges, which allows for the successful extraction of a radio source with smoothly-varying brightness distributions, and the reconstructed images are even more effective than those from LASSO. This approach has already been applied to EHT imaging (Event Horizon Telescope Collaboration et al. 2019). To date, the use of EHT mock observational data has confirmed that this technique achieves higher-fidelity images than the conventional CLEAN algorithm at an angular scale of $30\% - 40\%$ of the CLEAN beam (that is, super-resolution; Kuramochi et al. 2018). The imaging equation can be expressed as follows:

$$
\begin{aligned}
\mathbf{I}_{\mathrm{L1,TSV}} \quad = \quad & \underset{\mathbf{I}}{\mathrm{argmin}} \left(||\mathbf{W}(\mathbf{V} - \mathbf{FI})||_2^2 + \Lambda_l \sum_i \sum_j |\mathrm{I_{i,j}}| \right. \\
+ \quad & \left. \Lambda_t \sum_i \sum_j \left(|\mathrm{I_{i+1,j}} - \mathrm{I_{i,j}}|^2 + |\mathrm{I_{i,j+1}} - \mathrm{I_{i,j}}|^2 \right) \right), \text{ subject to } \mathbf{I} \geq \mathbf{0} \qquad (1.8)
\end{aligned}
$$

where the final term details the sparsity of the TSV in the gradient domain, which effectively controls the smoothness of the brightness distribution. The balance between these two regularization terms is controlled by two positive variables, Λ_l and Λ_t. Figure 1.8 shows that the effective resolution depends on the regularization parameters, especially on the TSV term; the smaller the value of Λ_t, the better the spatial resolution.

Procedure for Generating an SpM Image

Figure 1.9 shows a procedure for generating an SpM image from visibility data. The initial parameters required for SpM imaging are (1) the field of view, (2) pixel size of the reconstructed image, and (3) two regularization parameters for regularization functions, namely ℓ_1-norm and the TSV. Cross Validation (CV) is proposed (Geisser 1975) to select the optimal parameter set of (Λ_l, Λ_t). This approach evaluates the parameter sets and chooses a parameter set that offers the optimal goodness-of-fit for given uncertainties. CV is a statistical method that is used to choose the optimal regularization parameter values. In the process of N-fold CV, the dataset $\mathbf{V}$ is randomly divided into N subsets, and $N - 1$ sets are used for image reconstruction by employing the SpM imaging method with a fixed $(\Lambda_l, \Lambda_{tsv})$. The reconstructed image is then Fourier transformed, and the weighted chi-squared error, which is defined below, is computed for the remaining subset.

In the process of N-fold CV, the dataset $\mathbf{V}$ is randomly divided into N subsets, and $N - 1$ sets are used for image reconstruction by employing the SpM imaging method with a fixed $(\Lambda_l, \Lambda_{tsv})$. The reconstructed image is then Fourier transformed, and the weighted chi-squared error, which is defined below, is computed for the remaining subset.
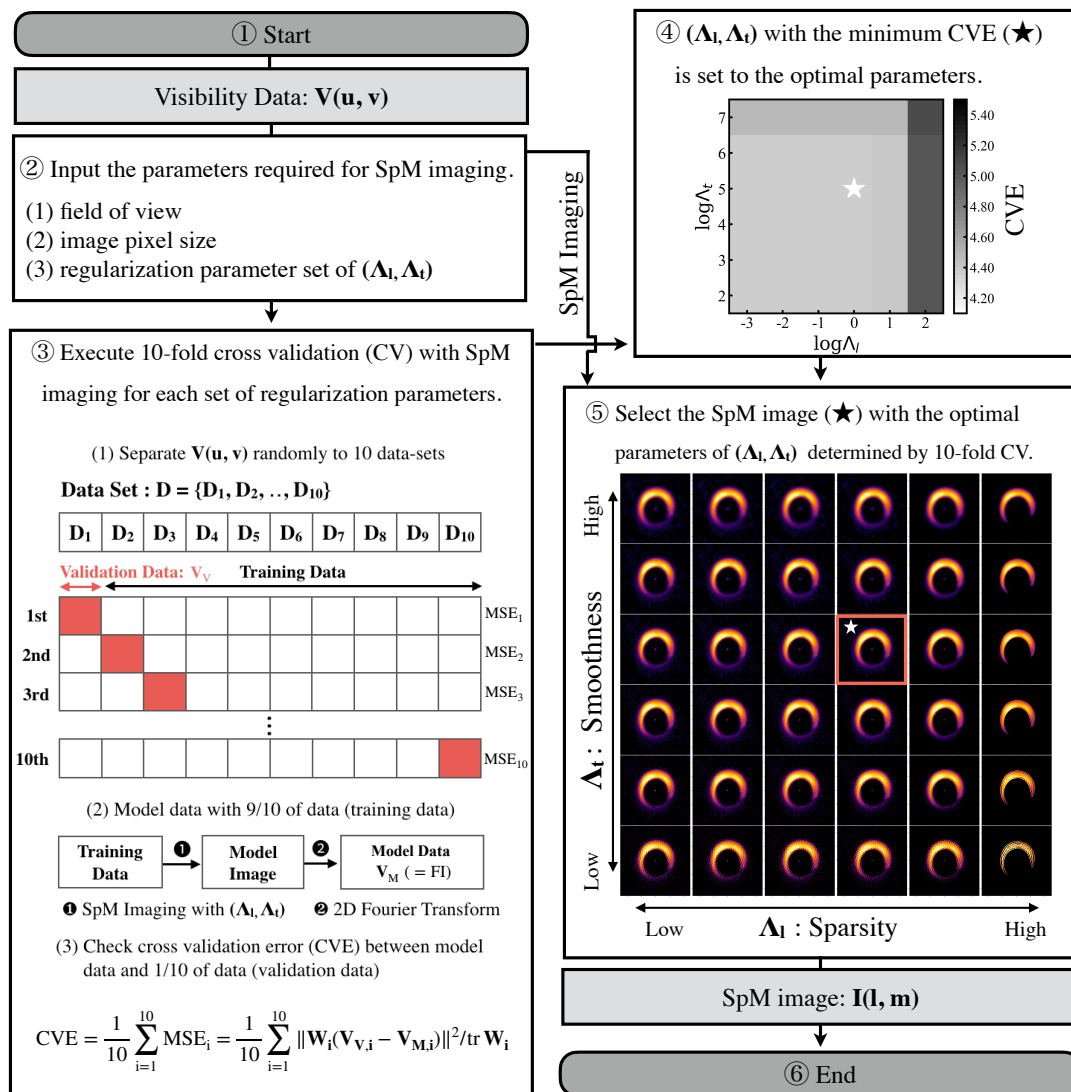
Figure 1.9: Flowchart of image processing using SpM (ℓ_1+TSV). The SpM image is automatically generated through 10-fold cross-validation (CV) after inputting a user-specified parameter set. Step 1: We prepare the visibility dataset (here, the self-calibrated visibilities of the dataset are used). Step 2: The user-specified parameters (that is, the field of view, image pixel size, and regularization parameter set of (Λ_l, Λ_t)) are set. Step 3: 10-fold cross validations with SpM imaging for each set of regularization parameters are executed, providing cross-validation error (CVE) results formulated in the Mean Squared Error (MSE). In the CVE equation, $\mathbf{W}$ ($= 1/\sigma^2$) is the weight of the observed visibilities. Step 4: (Λ_l, Λ_t) with the minimum CVE is set to the optimal regularization parameters. Step 5: SpM imaging is executed with a full dataset, and the SpM image with the optimal regularization parameters is finally selected.

$$\text{MSE} = \| \mathbf{W} \left(\mathbf{V} - \mathbf{FI} \right) \|^2 / \ tr\mathbf{W}, \tag{1.9}$$

where $tr\mathbf{W}$ is the trace of matrix $\mathbf{W}$. This process is iterated N times by taking different subsets and deriving the cross-validation error (CVE) formulated in the Mean Squared Error (MSE; $\Sigma_{i=1}^{N} MSE_i/N$) and standard deviation ($\Sigma_{i=1}^{N} \sqrt{(MSE_i - CVE)^2}/N\sqrt{N-1}$). In this study, the optimal parameter set of (Λ_l, Λ_t) is determined by 10-fold CV to evaluate the parameter sets. An image with the minimum CVE can be regarded as the optimal image (Akiyama et al. 2017a,b; Kuramochi et al. 2018).

How Can Sparse Modeling Achieve Super-resolution?

Figure 1.10 provides an interferometric theory-based probable explanation on how SpM imaging can achieve an approximately three times better spatial resolution than other methods. The usual diffraction-limited resolution is roughly the wavelength λ divided by the maximum baselines ($\lambda/D_{\max}$, where λ is the observed wavelength and $D_{\max}$ is the aperture size or longest baseline length in the interferometer). In interferometric synthesis observations, the synthesized beam $\text{B}(l,m)$ (that is, the response to a point-source or point spread function) can be expressed as a summation of each visibility fringe pattern given by a two-element interferometer (Cornwell et al. 1999).

$$\text{B}(l,m) = \sum_{k} W(u_k, v_k) \cos\left(u_k l + v_k m\right), \tag{1.10}$$

where (l,m) is the image coordinate, (u_k, v_k) is the sampling coordinate of the kth visibility, and $W(u_k, v_k)$ is the weighted sampling function. The (one-dimensional) visibility pattern produced by the longest baseline has a fringe spacing of $\sim \lambda/D_{\max}$. Furthermore, it exhibits a sharper spatial amplitude response with an FWHM of $1/3 \times \lambda/D_{\max}$ when only its positive side is considered to be contributing to the formation of the final beam. It is approximately three times smaller than the synthesized beam $\text{B}(l,m)$ with a size of $\lambda/D_{\max}$. SpM imaging is a regularized least-squares method in which the observed visibilities are directly used to retrieve the image and the long baselines can be utilized as much as possible in super-resolution imaging.

Conversely, the visibility amplitude distribution as a function of the uv-distance can be used to estimate the source sizes of compact objects. For a source with a Gaussian spatial distribution, the FWHM source size Θ_{FWHM} and the uv-distance, which provides the half-visibility amplitude $UV_{1/2}$, have a relation such that $\left(UV_{1/2}/100\ k\lambda\right) \cdot (\Theta_{\text{FWHM}}/1\ \text{arcsec}) = 0.91$ (Kawabe et al. 2018). If $UV_{1/2}$ is equal to $D_{\max}$, Θ_{FWHM} in units of radians is equal to $0.44 \times \lambda/D_{\max}$. This should be approximately $1/3 \times \theta_{\text{synth}}$ if $\theta_{\text{synth}} \simeq 1.22\lambda/D_{\max}$ (corresponding to the Rayleigh criterion for resolving two point sources; see the ALMA technical handbook). This expression indicates that interferometric imaging could utilize visibility amplitudes measured with high SNR even at long baselines to derive source structures much smaller than the synthesized beam.
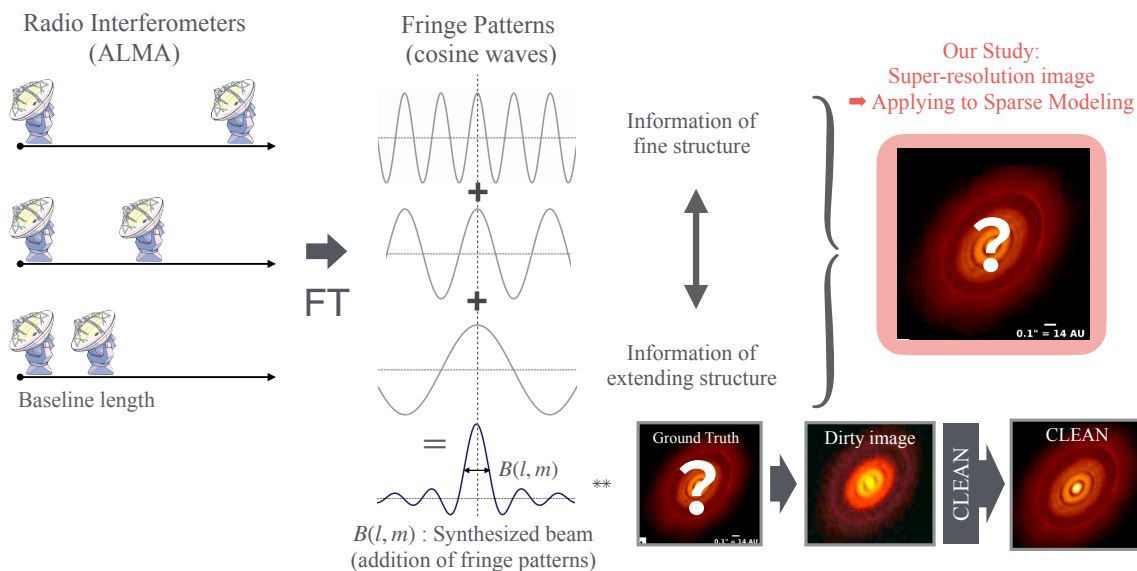
Figure 1.10: Flowchart of radio interferometry to imaging The baseline length of the two-element antenna is used to manipulate the spatial resolution. The Fourier transform of the observed data corresponding to this baseline length can be expressed as a component of the cos-wave known as the fringing pattern. The sum of these patterns represents the synthesized beam $B(l, m)$ (or dirty beam), which indicates the nominal resolution of the interferometer, and the spatial resolution of CLEAN can be manipulated using the beam size. However, higher-resolution (super-resolution) information on the fringe pattern of the long baseline has not been sufficiently extracted. In this study, SpM is applied to successfully reconstruct such information with super-resolution.

1.7 This Thesis

Given this background, this thesis presents the combined results of Yamaguchi et al. (2020), Yamaguchi et al. (2021), and Yamaguchi et al. (in preparation). The main objectives of this study are as follows: (1) to investigate whether the new super-resolution imaging technique, SpM, can achieve $2 - 3$ times higher spatial resolution than the conventional method (CLEAN algorithm) while maintaining high image fidelity in actual observations; (2) to apply this imaging technique to reveal the detailed structure of protoplanetary disks, which are yet to be spatially resolved; and (3) to investigate the statistical nature of disk substructures, especially the gap structure expected to be the planetary origin, and to explore planetary system formation in comparison with corresponding theories.

In this thesis, Chapter 2 investigates whether the new super-resolution imaging technique, SpM, can achieve $2 - 3$ times higher spatial resolution than the conventional method (CLEAN algorithm) while maintaining high image fidelity in actual observations. Chapter 3 describes the application of the imaging technique to reveal the detailed structure of the protoplanetary disks of the T Tau system, which are yet to be spatially resolved. Chapter 4 explores the nature of

disk substructures (that is, gaps and rings) using archival data from the Taurus disk survey by super-resolution imaging. Additionally, planetary masses and the stellar-mass tendency of the inferred planetary masses are investigated by assuming that the discovered gaps are a result of forming planets. Finally, Chapter 5 summarizes and concludes the study.

Chapter 2

Super-resolution Imaging of the Protoplanetary Disk HD 142527 Using Sparse Modeling

2.1 Chapter Overview

With an emphasis on improving the fidelity even in super-resolution regimes, new imaging techniques have been intensively developed over the last several years, which may provide substantial improvements to the interferometric observation of protoplanetary disks. In this study, sparse modeling (SpM) is applied for the first time to observational data sets taken by the Atacama Large Millimeter/submillimeter Array (ALMA). The two data sets used in this study were taken independently using different array configurations at Band 7 (330 GHz), targeting the protoplanetary disk around HD 142527; one in the shorter-baseline array configuration ($\sim$ 430 m), and the other in the longer-baseline array configuration ($\sim$ 1570 m). The image resolutions reconstructed from the two data sets are different by a factor of $\sim$ 3. We confirm that the previously known disk structures appear on the images produced by both SpM and CLEAN at the standard beam size. The image reconstructed from the shorter-baseline data using the SpM matches that obtained with the longer-baseline data using CLEAN, achieving a super-resolution image from which a structure finer than the beam size can be reproduced. Our results demonstrate that on-going intensive development in the SpM imaging technique is beneficial to imaging

with ALMA.

2.2 Introduction

In this study, for the first time, SpM imaging is applied to an ALMA observational data set
of the protoplanetary disk around HD 142527. The target object hosts one of the most well-
studied transition disks. It is a binary system at a distance of 156 ± 7.5 pc (Gaia Collaboration
et al. 2016a). The primary star is a Herbig Ae/Be with spectral type F6 III, having a mass of
2.2 $M_\odot$ while the secondary has a mass of 0.1-0.4 $M_\odot$ (Verhoeff et al. 2011; Biller et al. 2012).
Several observations of the object have so far been carried out with ALMA. The results show
that the brightness distribution is strongly lopsided and that the radius of the cavity is ~ 150
au (Casassus et al. 2013; Fukagawa et al. 2013; Boehler et al. 2017; Ohashi et al. 2018; Soon
et al. 2019). An observational data set covering several different angular resolutions therefore
exists in the same frequency band. It is possible to evaluate the performance of SpM imaging
by comparing the resulting images with those derived using the CLEAN algorithm.

Two sets of ALMA archive data at Band 7 ($\sim$330GHz) were used to investigate the proto-
planetary disk around HD 142527, one of which was taken with the compact array configuration,
and the other with the extended array configuration. The maximum baseline lengths between
the two data sets are different by a factor of $\sim 3 - 4$. Images were constructed from the data
sets using the SpM and the popular multi-scale Cotton-Schwab CLEAN algorithm (hereafter
MS-CLEAN; Cornwell 2008; Rau & Cornwell 2011) to evaluate whether the previously seen
disk structures appear on the images made by both the SpM and MS-CLEAN at the angular
resolutions taken by each data set. The fidelity of the SpM image was also compared with the
image from MS-CLEAN by changing the angular resolution for both images. The detailed outer
disk structure of the SpM image seen in the super-resolution regime is also discussed.

This study provides the first opportunity to evaluate the performance of the SpM imaging
using real observational data at different angular resolutions. The chapter is organized as follows.
The observations, calibrations, and imaging procedures are introduced in Section 2.3, the images
from both data sets are then evaluated based on a general image fidelity metric in Section 2.4.
The disk substructure inferred from the SpM image at the super-resolution regime and the
remaining technical issues are discussed in Section 2.5. The conclusion of this study is presented
in Section 2.6.

2.3 Data Reductions and Imaging

2.3.1 ALMA Data Set used for Imaging

Two data sets of ALMA observations of the protoplanetary disk around HD 142527 at a fre-
quency of ~ 330 GHz (ALMA Band 7) are used in our investigation. One uses a compact antenna
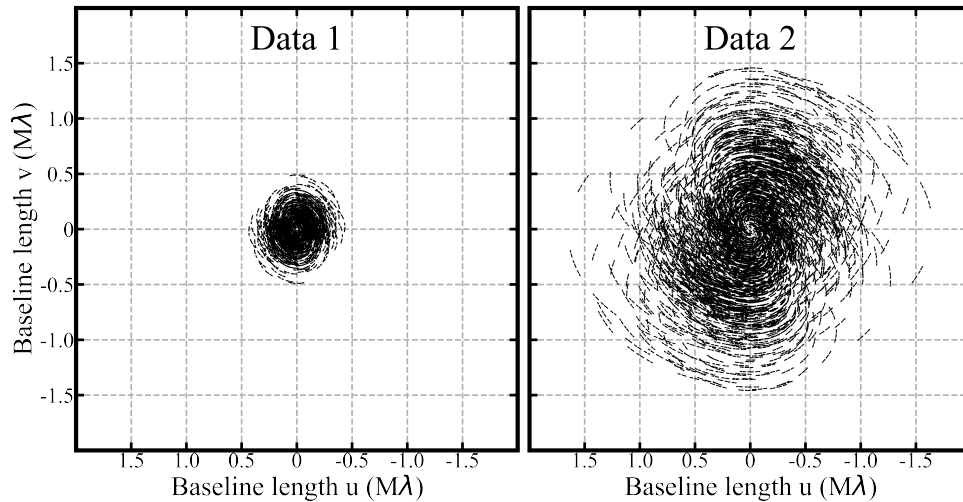
Figure 2.1: *uv*-coverage of two data sets of ALMA observations toward HD 142527 adopted in this work. The left panel shows Data 1 obtained with the more compact array configuration, while the right panel shows Data 2 from the more extended array configuration.

configuration, and the other uses extended. Figure 2.1 shows the *uv*-coverage of the two data sets. The maximum extensions of the baseline lengths differ by a factor of $\sim$3-4, leading to the same difference in the size of the synthesized beams. The calibrations used for each data set are summarized below.

The data set obtained with the compact array configuration with a maximum baseline length of 430 m was labeled as *Data 1*. Data 1 were obtained as part of the project 2015.1.00425.S, which has already been published in Kataoka et al. (2016). The corresponding observations were carried out on March 11, 2015, at 343 GHz (0.87 mm) to detect the full polarization of the continuum emission. The observing array consisted of thirty-eight 12 m antennas. The data were taken over a total bandwidth of 8 GHz, consisting of four 2 GHz spectral windows centered at 336, 338, 348, and 350 GHz. The on-source time of HD 142527 was 1.2 h, and observations were carried out for 3.4 h in total.

The data set obtained with the extended array with a maximum baseline length of 1570 m was labeled as *Data 2*. Data 2 were obtained as part of the project 2012.1.00631.S, which was carried out on July 17, 2015, at 322 GHz (0.93 mm) with the correlator configuration for dual-polarization. The observations made use of forty 12 m antennas. The total observing time was 22.5 h with an on-source time of 1.9 h. The total bandwidth of 4.8 GHz was separated into two 0.5 GHz spectral windows centered at 314 and 329 GHz and two 1.9 GHz spectral windows centered at 315 and 328 GHz.

2.3.2   Data Reduction and Imaging with MS-CLEAN

Data 1 were calibrated using version 4.7.2 of the Common Astronomy Software Applications
package (CASA; McMullin et al. 2007), in the same manner as Kataoka et al. (2016). The initial
calibration was performed using the ALMA pipeline. In the pipeline, the complex gains and
bandpass were calibrated with J1604-4441 and J1427-4206, respectively, while the instrumental
polarization was calibrated with J1512-0905. To improve the fidelity of the image, we performed
the self-calibration technique for the corrected data. First, we constructed Stokes I model of
HD 142527 using MS-CLEAN performed with scale parameters of [0, 0.3, 0.9] asec ("asec" is an
abbreviation for "arcsecond") by adopting Briggs weighting of robust parameter 0.5. Next, using
the MS-CLEAN model, we performed iterative self-calibration of the visibility phase (calmode
= p). The interval time used to solve the complex gain varied from 420 to 30 s. The resultant
image (= MS-CLEAN model convolved with CLEAN beam + residual map) after self-calibration
provided the beam size of 0.51×0.44 asec with position angle (P.A.) of $58.7°$. The RMS noise
level of the resultant image was 0.32 mJy beam^{-1}.

Data 2 were calibrated in the same manner as Data 1. The data were initially calibrated
with the same version of the ALMA pipeline. In the pipeline, Pallas, Ceres, and J1427-4206
were used for the flux calibration, while the complex gains and bandpass were calibrated with
J1604-4228 and J1517-2422, respectively. The corrected data were imaged using MS-CLEAN
performed with scale parameters of [0, 0.3, 0.9] asec by adopting Briggs weighting of robust
parameters 0.5. The corrected data were then further calibrated iteratively with MS-CLEAN
and self-calibration in phase (`calmode = p`). The interval of time used to solve the complex gain
varied from 360 to 50 s. The resultant image (= MS-CLEAN model convolved with CLEAN
beam + residual map) after self-calibration provided the beam size of 0.20×0.14 asec at P.A.
of $78.1°$. The RMS noise level of the resultant image was 0.07 mJy beam^{-1}.

We note that the ratio of the central frequencies of the two data sets is ~ 0.9. In the (sub)
millimeter continuum emissions of protoplanetary disks, the ratio may cause a difference of
$\sim 10 - 20\,\%$ in the source intensity based on the typical value of the spectral index ($\alpha_{\mathrm{mm}} \sim 2 - 3$
given by $F_\nu \propto \nu^{\alpha_{mm}}$), such as that typically seen in the (Beckwith & Sargent 1991; Mannings
& Emerson 1994; Andrews & Williams 2005, 2007). With a typical flux calibration error of up
to 10 % in ALMA observations (see ALMA technical hand book), the source intensity of the
two data sets may differ by a total of $\lesssim 30\,\%$. To check the difference in intensity between the
two data sets, the total fluxes are estimated by measuring the maximum value of the visibility
amplitude. The resultant total fluxes of Data 1 and 2 are derived to be 3.3 Jy and 3.2 Jy,
respectively, indicating a total difference of $\sim 3\,\%$. The two data sets therefore satisfy the
assumptions.

2.3.3   Imaging with Sparse Modeling

We used the self-calibrated visibilities of both data sets to reconstruct the images with SpM
utilizing ℓ_1+TSV regularization (see Chapter 1). This latest imaging technique utilizes two con-

vex regularization functions of the brightness distribution: ℓ_1-norm and TSV. These regularizers adjust sparsity and smoothness in the brightness distribution, respectively. This technique can be used to achieve resolutions as high as $\sim 30 - 40\%$ of the angular resolution while maintaining image fidelity (Kuramochi et al. 2018).

For generating an SpM image from visibility data, the parameters first required for SpM imaging are (1) field of view, (2) pixel size of the reconstructed image, and (3) two regularization parameters for regularization functions, namely ℓ_1-norm and TSV. A pixel size of 0.05×0.05 asec was used for Data 1 and 0.025×0.025 asec for Data 2, which were both at least 7 times smaller than the synthesized beam of MS-CLEAN, and 5.0×5.0 asec for the field of view, which is large enough to cover the entire region where the continuum emission has been detected. Note that this pixel size does not significantly affect the resultant images as it is small enough to trace the structure on the spatial scales constrained by the longest-baseline visibilities, because we utilize the TSV which supports multi-resolution reconstruction by regularizing the gradient function of the image. The TSV can reconstruct an edge-smoothed image (Kuramochi et al. 2018).

We adopt 16×9 sets of regularization parameters for Data 1, consisting of $(1 \times 10^2, 2 \times 10^2, ..., 9 \times 10^2)$ for Λ_l and $(3 \times 10^4, 4 \times 10^4, ..., 9 \times 10^5)$ for Λ_t, and 6×6 sets of regularization parameters for Data 2, consisting of $(10^2, 10^3, ..., 10^7)$ for Λ_l and $(10^{-3}, 10^{-2}, ..., 10^2)$ for Λ_t. The optimal parameter set of (Λ_l, Λ_t) was determined by 10-fold cross validation (CV) that evaluates the parameter sets and chooses a parameter set providing the optimal goodness-of-fit for given uncertainties. The cross validation error (CVE) of these parameter sets was then evaluated using 10-fold CV, and the parameter set and corresponding image were selected, minimizing the CVE for each spectral window of each set of data.

For the self-calibrated visibilities, the imaging equation becomes a convex optimization, guaranteeing the convergence to a unique solution regardless of the initial conditions (e.g., Akiyama et al. 2017b; Kuramochi et al. 2018). The fast iterative shrinking threshing algorithm (FISTA; Beck & Teboulle 2009a,b) is a popular and efficient algorithm for solving optimization; therefore a monotonic variant of FISTA (MFISTA) was used, that is especially designed for the regularization of ℓ_1-norm with another convex function (see Akiyama et al. 2017b, for details). Prior to imaging, the self-calibrated visibilities were gridded using cell-averaging (e.g., see Thompson et al. 2017). Images were reconstructed for both data sets at each spectral window to evaluate the noise levels in the reconstructed images, and also to minimize the potential effects caused by frequency-dependent residual gains in the visibility amplitudes. As a result, four images were reconstructed for each data set and then averaged into a final image.

It is worth noting that because the self-calibrated visibilities that were iteratively calibrated with MS-CLEAN imaging and self-calibrations in phase were used, the SpM images will be affected by residual gains in the visibility amplitude, as well as the residual phase errors induced by the use of self-calibration with MS-CLEAN, which may cause additional errors and artifacts on the reconstructed images. The effects of these residual complex gains are discussed in Section 2.5.2 in detail, although it will not significantly affect the main results of this chapter described in Section 2.4.
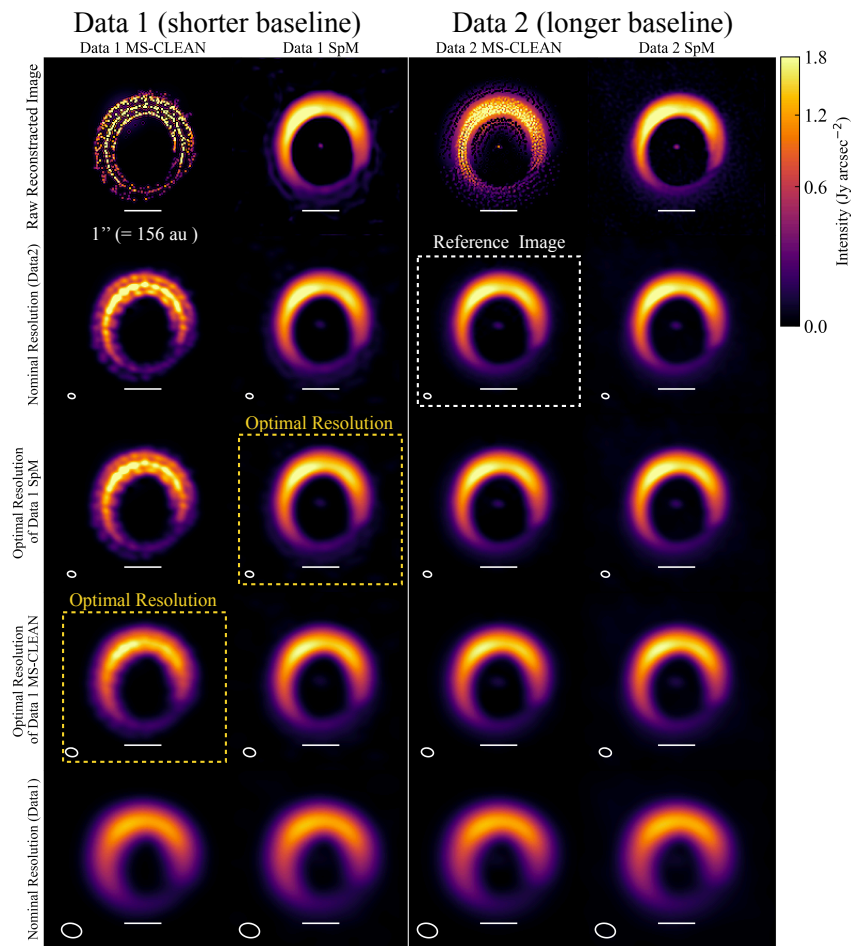
Figure 2.2: Images of HD 142527 constructed with two data sets from ALMA observations taken at 322 and 343 GHz as reconstructed using SpM and MS-CLEAN. The same color scale given by a power law with a scaling exponent of 0.6 and field of view of 5.0 × 5.0 asec are adopted for all images. The left two columns show images from Data 1 reconstructed with SpM and MS-CLEAN, respectively, while the right two columns show images from Data 2. The raw reconstructed images or those restored with an elliptical Gaussian beam are given for each row of images, for which the FWHM shape is shown in a white ellipse in each panel. The axial ratio and P.A. of the beam are fixed to those of the synthesized beam size of Data 2 for Briggs weighting with a robust parameter of 0.5 adopted for use with MS-CLEAN. (Top panels): The raw reconstructed images without any Gaussian convolution. (2nd panel): Reconstructed images convolved with the nominal resolution of Data 2. (3rd panel): Reconstructed images convolved with the optimal resolution of Data 1 for SpM, respectively, determined by NRMSE analysis (see Section 2.4.2 and Figure 2.3). (4th panel): Reconstructed images convolved with the optimal resolution of Data 1 for MS-CLEAN, determined by NRMSE analysis. (5th panels): Reconstructed images convolved with the nominal resolution of Data 1

2.4   Results

2.4.1   Images at Different Angular Resolutions

The images reconstructed by SpM and MS-CLEAN are compared and evaluated to ascertain
whether the previously known disk structures appear on both images. The image fidelity of SpM
in comparison with MS-CLEAN is also examined with regards to the super-resolution regime.
Figure 2.2 shows the reconstructed images from the two data sets of the ALMA observations at
322 and 343 GHz using SpM and MS-CLEAN. The images are either not convolved (top panels)
or convolved (lower panels) with different sizes of elliptical Gaussian beams. Nominal resolutions
are defined as synthesized beams of the MS-CLEAN images for Data 1 and 2. Meanwhile, in
both the SpM and MS-CLEAN images, optimal resolutions are determined using normalized
root mean square error (NRMSE) analysis by regarding the Data 2 MS-CLEAN image as the
reference image (see Section 2.4.2). For the NRMSE analysis, the beam and P.A. of the images
has to be matched to that of the reference image. In this analysis, the nominal resolution of
Data 1 is therefore modified to 0.57×0.40 asec with a P.A. of $78.1°$, which is determined to
have the same solid angle of the beam as the original one.

We define that the beam size ratio for the nominal resolution of Data 1 (labeled by R) has
a range of $0\ \% \leq R \leq 100\ \%$. The lowest angular resolution shown in the bottom panels of
Figure 2.2 corresponds to the nominal resolution of Data 1 (0.57×0.40 asec, R = 100 %). It is
apparent that the source intensity is consistent within $\lesssim 6$ % between the four images, which
may be accounted for by the differences in the central frequencies and the flux calibration errors
between Data 1 and 2. All the four images show a lopsided structure in the outer disk and
the thermal dust emission that is brighter in the northeastern side, as seen in previous studies
(Casassus et al. 2013; Fukagawa et al. 2013; Casassus et al. 2015; Boehler et al. 2017; Ohashi
et al. 2018).

The disk structures in the SpM and MS-CLEAN images start to deviate at the optimal
resolution of Data 1 MS-CLEAN (0.34×0.24 asec, R = 60 %). Blobby structures appear in the
MS-CLEAN image, while those are blurred. The blobby structures become more apparent in
the MS-CLEAN image at the optimal resolution of Data 1 SpM (0.23×0.16 asec, R = 41 %). On
the other hand, the Data 1 SpM image is still consistent with the Data 2 MS-CLEAN image at
these resolutions, even in a super-resolution regime (i.e., the nominal resolution of MS-CLEAN
for Data 2, R = 35 %). This fact is consistent with previous works based on imaging simulations
(e.g., Chael et al. 2016; Akiyama et al. 2017a,b; Kuramochi et al. 2018).

It is worth noting that the differences between SpM and MS-CLEAN are also remarkable
in the raw reconstructed images which present the original images before Gaussian convolution
(top panels of Figure 2.2, R = 0 %). The raw SpM images from the two data sets with different
array configurations consistently show a smooth distribution of brightness in the outer disk. In
comparison, the outer disk in the raw MS-CLEAN images, in which the map of clean components
is shown, consists of more compact point-like features, which are not consistent with each other
or with any of the other images, suggesting that these features can be presumed artificial.

2.4.2 Fidelity at Multi-resolution

For more quantitative analysis, we evaluate the normalized root mean square error (NRMSE) between the images with different angular resolutions (Chael et al. 2016; Akiyama et al. 2017a; Kuramochi et al. 2018). The NRMSE is defined as:

$$\text{NRMSE}(\mathbf{I}, \mathbf{K})_{\text{image}} = \sqrt{\frac{\sum_i \sum_j |\text{I}_{i,j} - \text{K}_{i,j}|}{\sum_i \sum_j |\text{K}_{i,j}|}}. \tag{2.1}$$

where $\mathbf{I} = \{\text{I}_{i,j}\}$ is the input image and $\mathbf{K} = \{\text{K}_{i,j}\}$ is the reference image. The NRMSE is calculated by changing a beam size (i.e., a spatial resolution). The beam size providing the minimum NRMSE may be considered as an optimal resolution (Chael et al. 2016). Previous studies (e.g., Akiyama et al. 2017a; Kuramochi et al. 2018) suggest that the NRMSE is often dominated by errors in excessively bright pixels, and therefore may not represent the fidelity of some other properties such as the smoothness of the image and the size of the emission region. Hence, the NRMSE of the gradient-domain brightness distribution was also evaluated using the Prewitt filter (Kuramochi et al. 2018). The metric for the fidelity of the image is evaluated by taking the gradients of the image, given by

$$|\nabla\text{I}(\text{x}, \text{y})| = \sqrt{\left|\frac{\partial\text{I}}{\partial\text{x}}\right|^2 + \left|\frac{\partial\text{I}}{\partial\text{y}}\right|^2} \tag{2.2}$$

as a continuous distribution of the brightness. Errors in the image gradients can be evaluated using equation (2.1),

$$\text{NRMSE}_{\text{grad}}(\mathbf{I}, \mathbf{K}) \equiv \text{NRMSE}_{\text{image}}(\nabla\mathbf{I}, \nabla\mathbf{K}) \tag{2.3}$$

To calculate NRMSE, it is necessary to choose a reference image. The risk of intrinsic bias becomes lower when the reference image is chosen to be a method that is well known to and trusted by the community. The Data 2 MS-CLEAN at its nominal resolution is therefore the best choice as the reference image. With this reference image, the NRMSEs of the beam-convolved MS-CLEAN and SpM images of Data 1 are evaluated.

Figure 2.3 shows the results of NRMSE analysis on both the image and gradient domains. Each image is convolved with an elliptical beam size, whose axial ratio and P.A. are the same as that of the Data 2 MS-CLEAN image. The nominal resolution of Data 1 normalizes the convolving beam size. The solid green line shows the ideal NRMSE curves between the non-convolved and the convolved reference images, effectively quantifying the best-case scenario in which the difference from the original input is due to a loss of resolution. The other lines show the NRMSEs between the reference image and the other three images.

Table 2.1 summarizes the optimal resolutions as determined by the NRMSE. For each image, the worst optimal resolution was selected from the results of two NRMSE analyses (for the image and gradient domains) and defined as the optimal resolution. In the 3rd and 4th rows of Figure 2.2, we show all four images convolved with the optimal resolutions of the SpM and MS-CLEAN images, respectively. In the following paragraphs, we describe in more detail the characteristics of each curve (image and gradient domain) and their relation to the corresponding images.

Table 2.1:: Optimal Resolutions determined by NRMSE analysis

Angular Resolution (mas)	SpM (Data 1)	MS-CLEAN (Data 1)	Ref: MS-CLEAN (Data 2)
Nominal Res	NaN	57×40 (100 %)	20×14 (35 %)
Optimal Res on Image	23×16 (41 %)	31×22 (55 %)	NaN
Optimal Res on Gradient	22×15 (39 %)	34×24 (60 %)	NaN

Note. — The axial ratio and the P.A. of the beams for Data 1 are fixed to those of the synthesized beam size of the MS-CLEAN image for Data 2. The percentages indicate the beam size ratio for the nominal resolution of Data 1. "mas" is an abbreviation for "milliarcsecond"

The Data 1 MS-CLEAN image achieves the optimal resolution at R = 60 % and sharply increases the NRMSEs at finer resolutions. The compact artifacts created in MS-CLEAN dominate the deviations from the other lines for NRMSE. The Data 1 MS-CLEAN image at its optimal resolution (4th row of Figure 2.2) already shows blobby-like structures, which can be attributed to the underlying assumption used in the production of the image.

In general, the original image of MS-CLEAN is composed of an ensemble of point sources and Gaussian sources with appropriate sizes, i.e., CLEAN components (top row of Figure 2.2). The final CLEAN image is reconstructed by convolving the CLEAN components with an idealized CLEAN beam corresponding to the nominal resolution of Data 1. With a finer spatial resolution than the nominal resolution, the MS-CLEAN image gets close to the CLEAN components itself, making the image blobby. Since NRMSE is more weighted at brighter pixels than lower-intensity skirts of the emission, the optimal resolution would be slightly finer than the nominal resolution, causing the blobby structures. These results are consistent with previous work on imaging simulations (Chael et al. 2016; Akiyama et al. 2017a,b; Kuramochi et al. 2018).

In contrast, the Data 1 SpM image follows the curves of the reference image until at R = 45 − 50 % in both the image and in the gradient domains. The optimal resolution reaches R = 41 %, which is better than that of the Data 1 MS-CLEAN. At resolutions finer than R = 41 %, the NRMSE of the Data 1 SpM shows flat curves until at the nominal resolution of Data 2 (R = 35 %), with typical ranges of 5 − 10 % in the image domain and 10 − 15 % in the gradient domain. Although this resolution is better than the nominal resolution for Data 1 by a factor of ∼ 3 (i.e., a super-resolution), the Data 1 SpM image is consistent with the Data 2 MS-CLEAN at the same resolution, while the Data 1 MS-CLEAN image is significantly affected by compact structures that can be attributed to underlying assumption used in the production of these images.
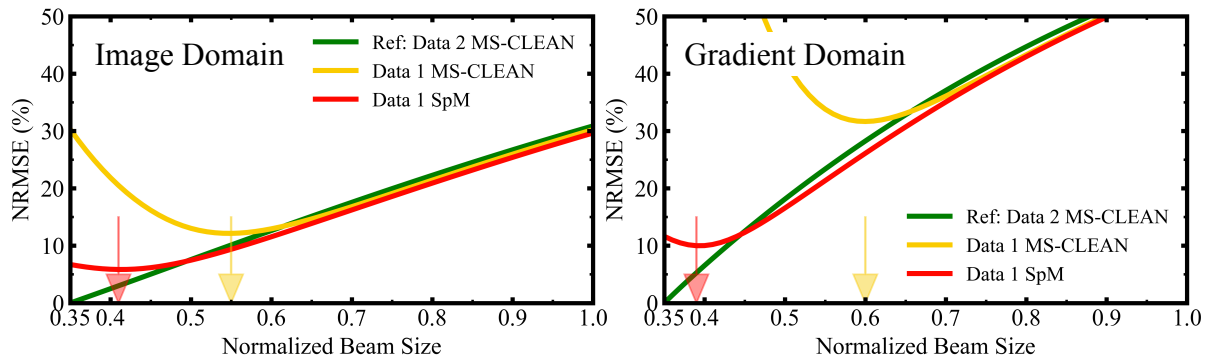
Figure 2.3: NRMSEs of the four reconstructed images as a function of the normalized beam size, on the image domain (the left panel), and the gradient domain (the right panel). The Data 2 MS-CLEAN image is adopted as the reference image (green line) for the NRMSE analysis in both panels. Each image is convolved with an elliptical beam size, with the same axial ratio and P.A. as the nominal resolution of Data 2. The nominal resolution of Data 1 normalizes the size of the convolving beam shown in the horizontal axis. The nominal resolution of Data 2 indicates 35 % ($= 20 \times 14$ mas) of Data 1.

2.4.3 Evaluation of Radial and Azimuthal Structure of the Outer Disk

The NRMSE analysis described in Section 2.4.2 evaluates the image fidelity by compressing two-dimensional information into a single value. In this section, we investigate source-specific quantities to evaluate the reconstructed images.

Interesting metrics would be based on the radial and azimuthal structure of the outer disk, with the origin set to the location of the central star. Considering that each radial structure would form a Gaussian distribution, Figure 2.4 shows the peak and the FWHM of the radial surface brightness profiles at position angles for the Data 1 SpM and Data 2 MS-CLEAN images convolved with the nominal resolution of Data 2. The data points of the physical parameters of the outer disk, each within $10°$ along the P.A. are thus collected, deriving the mean values as a measurement set on the P.A. profiles. The shaded regions in Figure 2.4 indicate the standard deviations σ_i derived by the calculation. The total flux of the Data 1 SpM image is scaled to that of the Data 2 MS-CLEAN image to minimize the effects of errors in the flux calibration.

Table 2.2 summarizes the residual statistics for the physical parameters of the P.A. profiles, as shown in Figure 2.4. The residual parameters are subtracted from the two images on each P.A. profile. The radial locations of the peak and its halves (outer/inner half peak) and the radial FWHMs are mostly consistent within nearly 10% of the nominal angular resolution of Data 2, which is close to the pixel size of the image. The peak and integrated intensity are also consistent; the mean and standard deviation are comparable to the noise levels on the residual maps estimated in Section 2.5.2. Therefore, Figure 2.4 indicates that each profile is in good agreement in terms of the radial and azimuthal structure of the outer disk.

Table 2.2:: Residual Statistics of P.A. profiles

Quantities (unit)	SpM (D1) - MS-CLEAN (D2)		
	Mean	Std	Abs.Max
Radial Peak (mas)	1.14	14.82	27.00
Outer Half Peak (mas)	1.38	12.58	24.00
Inner Half Peak (mas)	-5.92	22.30	27.00
FWHM (mas)	-7.30	21.93	36.00
Peak I (mJy asec^{-2})	-2.77	49.37	46.23
Integr. I (mJy asec^{-1})	-1.20	8.05	5.51
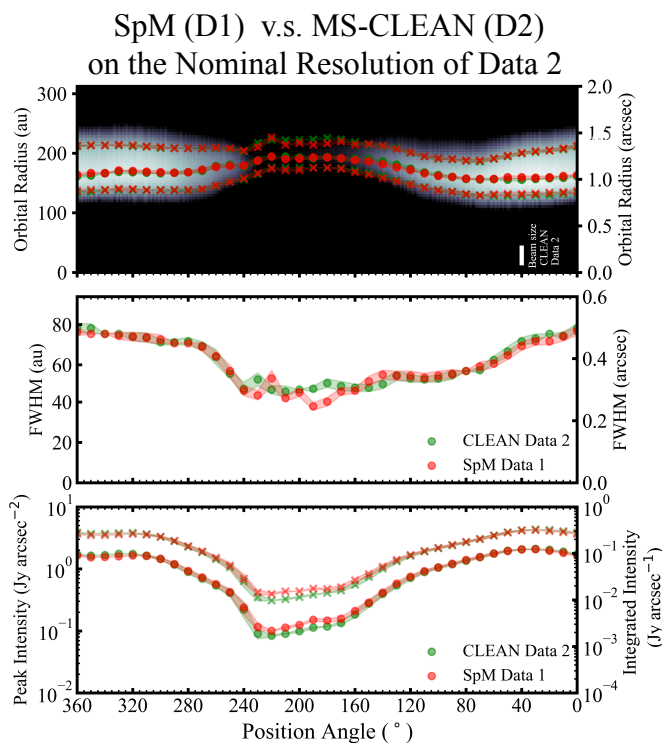
Figure 2.4: The position angle (P.A.) profile for the Data 1 SpM (red color) and the Data 2 MS-CLEAN (green color) images convolved with the Data 2 MS-CLEAN nominal resolution. The top panel shows the radial location of the peak (circle points) and its 50% (i.e., FWHM; cross points) of the intensity distribution of the outer disk overlaid by the Data 2 MS-CLEAN image. The middle panel shows the radial FWHM sizes of the intensity distribution for the outer disk. Bottom panel shows the peak (circle points) and radially integrated (cross points) intensities.

2.5   Discussion

2.5.1   Investigations of Raw Reconstructed Images

In Section 2.4, we have demonstrated that the application of SpM to Data 1 is possible to provide a high fidelity image in the super-resolution regime. Following the successful experimental application of the SpM, in this section, we discuss the SpM image reconstructed from especially Data 2.

We focus on the raw SpM image. Figure 2.2 shows that the raw SpM image from Data 2 is similar to the image that has undergone post-imaging beam convolution at the nominal resolution of Data 2. Kuramochi et al. (2018) pointed out that the raw reconstructed image can keep a

high fidelity and thereby the traditional method of the Gaussian convolution with a restoring beam in interferometric imaging would no longer be required for the ℓ_1+TSV regularization. It is thus instructive to investigate whether the substructures of the emission are seen in the raw reconstructed image of SpM. In the following subsections, we first introduce the noise term of the raw reconstructed image of SpM to evaluate the detection threshold, and the substructures seen in the image are discussed.

2.5.2   Noise Terms in Reconstructed Images

Figure 2.5: Histograms of artificial emissions outside the outer disk (i.e., off-source area) on the raw (i.e., non-convolved) SpM images for Data 1 (top panel) and Data 2 (bottom panel). The vertical dashed lines denote the 99.7% intensity ($I_{99.7}$) and the maximum (100%) intensity (I_{100}) of the off-source area.
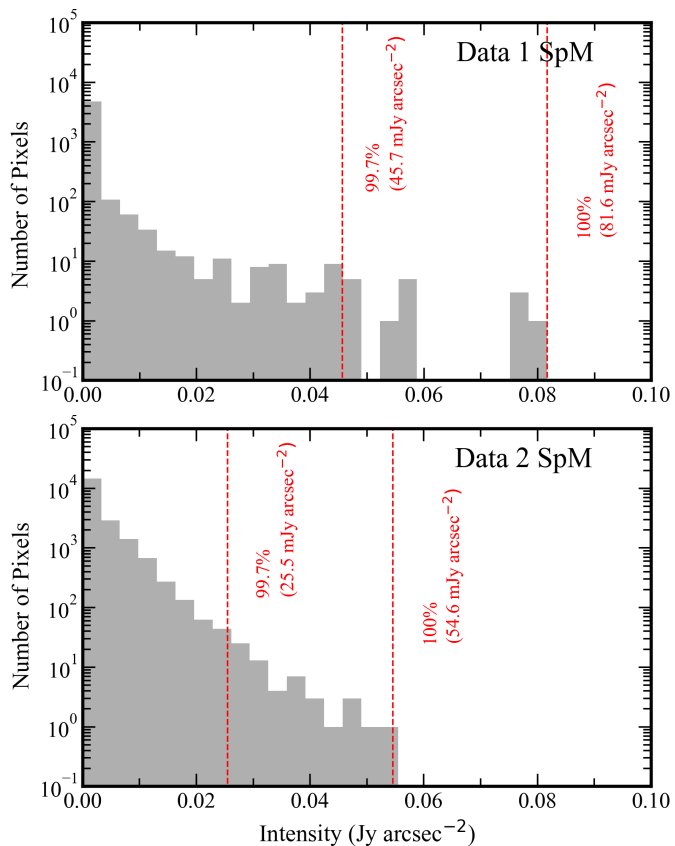
We evaluate the noise level of the raw reconstructed images for Data 1 and 2, respectively. Figure 2.5 shows a histogram that details the artificial emission outside the outer disk, 2.0 asec from the phase center (hereafter, the off-source area). Due to both systematic errors and thermal noise, both raw SpM images suffer from artificial emissions in the off-source area. Because of the non-negative constraints in the imaging algorithm, as described in Section 2.3.3, the histogram is on the positive side and has a longer tail than that of a Gaussian distribution. A maximum intensity (I_{100}) of 81.6 and 54.5 mJy asec^{-2} is apparent for Data 1 and 2, respectively.

Another way to estimate the noise levels is to measure the standard deviation of the residual map, which can be obtained by two-dimensional Fourier transform of the residual visibilities between the model data (which can be obtained by inverse two-dimensional Fourier transform
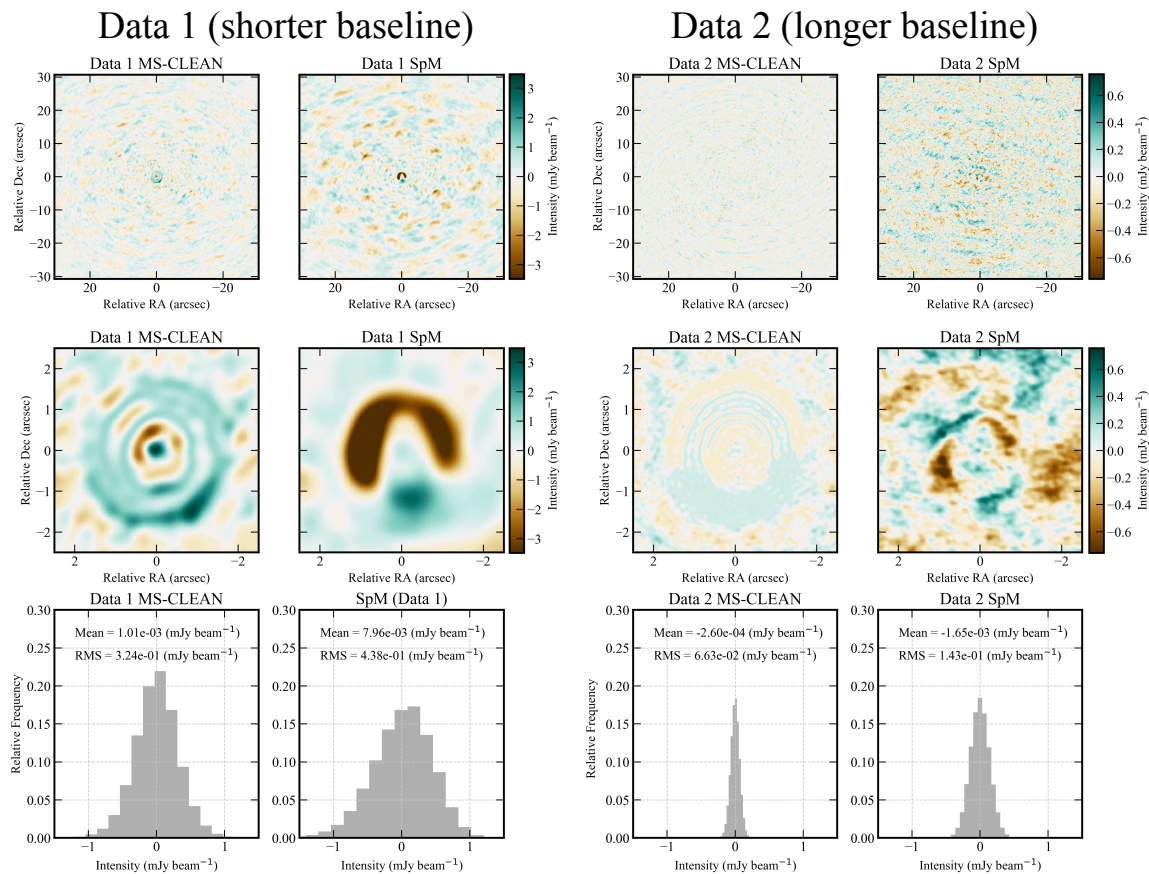
Figure 2.6: Residual maps of the four reconstructed images produced by SpM and MS-CLEAN. The field of view of 61.44×61.44 asec and 5.0×5.0 asec are adopted for the four images in the top and middle panels, respectively. The lower panels show that the off-source regions, which are outside a radius of 2.0 asec from the center coordinates, are extracted from the noise histograms in these images and count pixel values comparable to noise levels in the image domain. The residual maps with MS-CLEAN for Data 1 and Data 2 are convolved with a synthesized beam of 0.51×0.44 asec (P.A. $= 59°$) and 0.20×0.14 asec (P.A. $= 78°$), respectively (see Section 2.3.2 for details). The residual maps with SpM for Data 1 and Data 2 are convolved with a synthesized beam of 0.57×0.49 asec (P.A. $= 63°$) and 0.22×0.16 asec (P.A. $= 80°$), respectively (see Section 2.5.2 for details).

of the reconstructed image) and the observed data.

The residual maps of SpM were reconstructed from the residual visibilities using the DIFMAP software (Shepherd et al. 1994). To minimize the effects caused by frequency-dependent residual gains in the visibility amplitudes, we first made the residual visibilities from the SpM image reconstructed at each spectral window. Then, the residual maps were created through two-dimensional Fourier transform adopting a natural weighting, providing synthesized beams of 0.57×0.49 asec with a P.A. $= 63°$ and 0.22×0.16 asec with a P.A. $= 80°$ for Data 1 and 2, respectively. Finally, we combined the residual maps of all the spectral windows to obtain

a final image. The residual maps of MS-CLEAN were generated on the process of the image reconstruction as described in the Section 2.3.2. The degree of difference of the beam size on the residual map between the SpM and MS-CLEAN was derived to be 12 %.

The top and middle panels of Figure 2.6 show the residual maps of MS-CLEAN and SpM for Data 1 and 2. In the on-source area, MS-CLEAN images have a near symmetrical distribution of the residuals, while SpM images have asymmetric and more residuals. This can also be seen in the off-source area; the SpM residual images have RMS noise of 0.44 and 0.14 mJy beam^{-1} for Data 1 and 2, respectively, while the MS-CLEAN residual maps show smaller RMS noise of 0.32 and 0.07 mJy beam^{-1}. This is primary because SpM imaging is performed on self-calibrated data for the MS-CLEAN images, and the gains are not precisely solved for SpM images. This is because the SpM imaging solves the observational data by assuming that a modeled object is composed of various smooth scale sizes, while the self-calibration solves gains by assuming that a model is a collection of point sources, adopting a multi-scale approach with the MS-CLEAN algorithm. The processing may lead to both artificial emissions and higher residuals on the SpM image than on the MS-CLEAN image of almost the same resolution.

We regard higher intensity than detection threshold ($> I_{100}$) as the dust emissions from the disk. When we take the beam-convolution into account, I_{100} are comparable to 7 times higher than the RMS noise level in the residual map of Data 1 and 2.7 times for Data 2. Therefore, the emissions above the I_{100} level is likely able to capture the previously known disk structure around HD 142527.

2.5.3   Double Ridge-line shown in the Outer Disk

Figure 2.7 shows the raw reconstructed SpM images of Data 1 and 2 with contours starting at I_{100}. Only in the Data 2 SpM image, we found there is a break area of the emission, where the I_{100} contour twists and connects to the bright region toward the north. Moreover, the intensity distribution at P.A. of $265° − 270°$ shows a double ridge-like structure. Figure 2.8 shows the radial profiles along the specific position angles of the raw reconstructed SpM images as well as those of the Data 2 MS-CLEAN image. The radial profile of the raw Data 2 SpM image only shows a double ridge-like structure at P.A.$= 265° − 270°$, which might indicate the presence of substructure in the horseshoe dust distribution.

We caution that there is so far no clear evidence to present the robust degree of the super-resolution of Data 2 for SpM. The degree of super-resolution that we can achieve for Data 2 varies depending on the signal-to-noise ratio, as well as the *uv*-coverage. Figure 2.1 actually shows that the higher spatial frequency components of *uv*-coverage for Data 2 are relatively sparse. Due to the lower density of the high spatial frequency components, the shorter-baseline data are more weighted in the minimization of the SpM equation. Such a data set could at least prevent the factor 3 improvement of the spatial resolution with SpM imaging. To assess the consistency of the SpM imaging and definitely confirm the existence of this disk substructure, the observations at higher spatial resolution and deeper sensitivity comparable to DSHARP
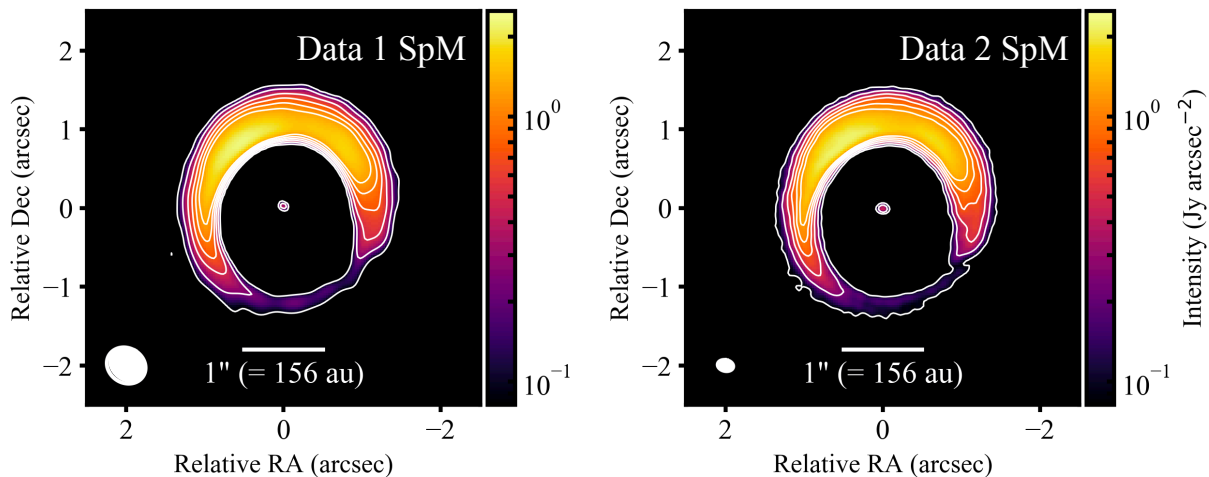
Figure 2.7: SpM images of protoplanetary disk HD 142527 from Data 1 (*left panel*) and Data 2 (*right panel*). The same logarithmic color scale and field of view of 5.0×5.0 asec are adopted for images. A white bar of 1 asec ($= 156$ au) is provided for reference to the angular scales. Each contour corresponds to $(1, 3, 6, 9, 12, 15) \times \mathrm{I}_{100}$ for Data 1 and I_{100} for Data 1 is 81.6 mJy asec^{-2}, as derived in Figure 2.5. I_{100} for Data 2 is 54.6 mJy asec^{-2}. The total flux of the Data 2 SpM image is scaled to that of the Data 1 SpM image to minimize the effects from flux calibration errors, and these images are not convolved with the Gaussian beam. The beam sizes of nominal resolution of Data 1 and 2 are plotted on its panels respectively to compare the degree of the spatial resolution between the nominal resolution domain and the raw image domain.
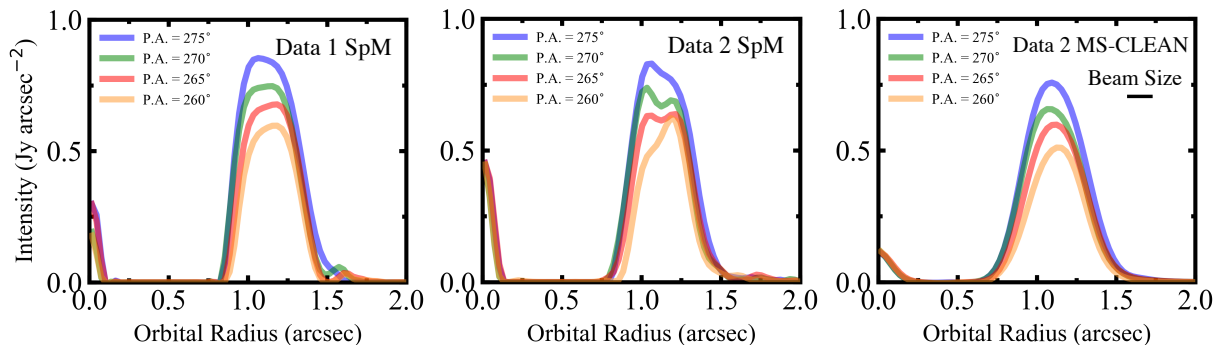
Figure 2.8: The radial profiles along the specified position angles near the break area (P.A. $= 260°, 265°, 270°, 275°$) for the raw (i.e. non-convolved) reconstructed SpM images for Data 1 and Data 2 (left and middle panels) and the Data 2 MS-CLEAN image (right panel). The horizontal axis indicates the orbital radius starting from the phase center (corresponding to the position of the central star). The vertical axis indicates the intensities of dust emissions. The total flux of the SpM image and MS-CLEAN image for Data 2 are scaled to that of the Data 1 SpM image to minimize the effects from flux calibration errors.

(Andrews et al. 2018c) should be conducted. We also note that more source-specific modeling of brightness distribution on the sky and observational simulations may be necessary to verify

the presence of very small scale structures, in a similar manner as Event Horizon Telescope
Collaboration et al. (2019).

2.5.4   Future Prospects for Imaging

In Section 2.4, we have demonstrated that the application of SpM provides high-fidelity super-
resolution images. The major structures are in good agreement with a factor of ~ 3 times the
nominal resolution used in MS-CLEAN imaging. Although this factor is broadly consistent with
previous research (Honma et al. 2014; Akiyama et al. 2017a,b; Kuramochi et al. 2018), it could
be profoundly different for other data sets with different intensity distributions, uv-coverages,
and/or sensitivities. In future work, we will investigate how to determine the effective resolution
for this technique.

We next describe several issues which can be further explored in future work, to improve the
signal-noise ratio (SNR) further and the fidelity of reconstructed images. Primary features that
limit the SNR of both SpM images are the compact noises seen on the off-source area. Because
the locations of these compact noises are broadly consistent with those within the MS-CLEAN
components, this could predominantly be due to the miscalibration of the complex gains caused
by the self-calibration with MS-CLEAN images. A straightforward way to reduce these compact
noises is iterative SpM imaging involving self-calibration. Recent work in Chael et al. (2018)
has suggested that self-calibration with images from new imaging techniques may significantly
reduce such artifacts. Event Horizon Telescope Collaboration et al. (2019) has also adopted this
strategy using the SpM imaging produced during this study.

Another factor, which is less important but which can limit the fidelity of our SpM images,
are errors coming from the uv-gridding. Because the SpM images are produced from uv-gridded
visibilities, our imaging process is equivalent to a single minor cycle in the Cotton-Schwab
CLEAN (Schwab 1984). This issue can be mitigated by switching the Fourier transform algo-
rithm to non-uniform FFT (NuFFT) algorithms, which may adopt an image from uv-gridded
data as the initial model to minimize the number of iterations and NuFFT operations. The ma-
jor cycle could also be included to reduce the number of NuFFT operations further. This can be
achieved by (1) computing residual visibilities on the original uv-coordinates with NuFFT using
the previous minor-cycle image, (2) deriving uv-gridded visibilities by adding uv-gridded resid-
ual visibilities to the model visibilities from the minor-cycle image, (3) imaging with uv-gridded
visibilities, and (4) repeating (1-3).

we note that for the community to use such new imaging techniques, the implementation of
these algorithms in a major software package is essential. The SpM imaging algorithms presented
in this chapter are currently being implemented as an external module of `CASA` (`PRIISM`; Nakazato
et al. 2019), with many improvements to the core imaging code such as the use of FFT/NuFFT
algorithms and with further acceleration of the numerical codes.

2.6   Conclusion

We present images of the protoplanetary disk around HD 142527 obtained with ALMA using SpM, which is a new high-fidelity super-resolution imaging technique for radio interferometry. We summarize our main conclusions as follows.

(1) SpM drastically improves the image fidelity of observations of the disk structure around HD 142527 in the super-resolution regime. The Data 1 SpM image achieves an optimal beam size of $35 - 40$ % of the nominal resolution for Data 1 by using NRMSE analysis regarding the Data 2 MS-CLEAN image as the reference image. This result means that the Data 1 SpM image achieves ~ 3 times the higher angular resolution with respect to the nominal resolution of Data 1.

(2) To evaluate the raw (i.e., not convolved) SpM image, we conservatively introduce the detection threshold I_{100}, which is the maximum intensity in the emission-free area. With this threshold, we found that new substructures in the horseshoe dust disk are inferred. There is a break area at P.A. of $\sim 230°$, where the I_{100} contour twists and connects to the bright region toward the north. Moreover, the intensity distribution at P.A. of $265° - 270°$ shows a double ridge-like structure. To confirm these notable substructures, the HD 142527 disk deserves a follow-up observation at higher spatial resolution and deeper sensitivity.

(3) SpM images have more asymmetric and larger residuals, while MS-CLEAN images have nearly symmetric residuals distributions. This is predominantly caused by the miscalibration of the complex gains due to the self-calibration with MS-CLEAN. A straightforward of mitigating this problem is iterative SpM imaging involving self-calibration. By combining the implementation of the NuFFT algorithm, SpM imaging will lead to further improvements in the fidelity and SNR of the reconstructed images of protoplanetary disks observed with ALMA. We plan to investigate this in the near future further.

Our results demonstrate that on-going intensive developments of new imaging techniques using SpM is an attractive choice to provide a high-fidelity super-resolution image with ALMA.

(KT). This paper makes use of the following ALMA data: ADS/JAO.ALMA#2012.1.00631.S, ADS/JAO.ALMA#2015.100425.S. ALMA is a partnership of ESO (representing its member states), NSF (USA) and NINS (Japan), together with NRC (Canada), MOST and ASIAA (Taiwan), and KASI (Republic of Korea), in cooperation to the Republic of Chile. The Joint ALMA Observatory is operated by ESO, AUI/NRAO, and NAOJ." The data analysis was in part carried out on the Multi-wavelength Data Analysis System operated by the Astronomy Data Center (ADC), National Astronomical Observatory of Japan.

Software: AnalysisUtilities (`https://casaguides.nrao.edu/index.php?title=Analysis_Utilities`), Astropy (Astropy Collaboration et al. 2013), CASA (McMullin et al. 2007), DIFMAP (Shepherd et al. 1994), matplotlib (Hunter 2007)

Chapter 3

ALMA Super-resolution Imaging of T Tau: r = 12 au Gap in the Compact Dust Disk around T Tau N

3.1   Chapter Overview

Based on Atacama Large Millimeter/submillimeter Array (ALMA) observations, compact protoplanetary disks with dust radii of $r \lesssim 20-40$ au were found to be dominant in nearby low-mass star formation regions. However, their substructures have not been investigated because of the limited spatial resolution achieved so far. We apply a newly developed super-resolution imaging technique utilizing sparse modeling (SpM) to explore several au-scale structures in such compact disks. SpM imaging can directly solve for the incomplete sampling of visibilities in the spatial frequency and potentially improve the fidelity and effective spatial resolution of ALMA images. Here, we present the results of the application to the T Tau system. We use the ALMA 1.3 mm continuum data and achieve an effective spatial resolution of $\sim 30\%$ (5 au) compared with the conventional CLEAN beam size at a resolution of 17 au. The reconstructed image reveals a new annular gap structure at $r = 12$ au in the T Tau N compact disk with a dust radius of 24 au, and resolves the T Tau Sa and Sb binary into two sources. If the observed gap structure in the T Tau N disk is caused by an embedded planet, we estimate a Saturn-mass planet when the viscous parameter of the disk is 10^{-3}. Ultimately, ALMA observations with enough angular resolution and sensitivity should be able to verify the consistency of the super-resolution imaging

and definitely confirm the existence of this disk substructure.

3.2   Introduction

The advent of the Atacama Large Millimeter/submillimeter Array (ALMA) has enabled us to observe PPDs with high spatial resolution, and transformational images or analysis (e.g., interferometric modeling) of disks have been produced. For instance, the disk substructures at the High Angular Resolution Project (DSHARP) and the Ophiuchus DIsc Survey Employing ALMA (ODISEA) provided ALMA images for bright and large disks with radii of $r = 50 - 260$ au with angular resolutions down to $2 - 5$ au (for consistency, we always refer to "dust disk" as "disk"; Andrews et al. 2018b; Cieza et al. 2020). These results reveal an annular gap structure, which are likely carved by a planet with Neptune-Jupiter mass (Zhang et al. 2018). However, disks of small sizes ($r \lesssim 20 - 40$ au) of PPDs were found to be dominant in the fraction ($\sim 70 - 90\%$) in low-mass star-forming regions (Cieza et al. 2019; Long et al. 2019; Ansdell et al. 2016), but their substructures have not been well investigated. Small disks are typically less massive in terms of the disk mass compared with large disks, and will be key to investigating the missing link between PPD substructures such as gaps and their locations. There is the need for extensive research on such a major PPD population to investigate the inner $r = 5 - 40$ au region in such PPDs as a possible location for the formation of giant planets (e.g., Bate 2018; Lodato et al. 2019)

To explore a few au-scale gap structures in such compact disks in nearby low-mass star formation regions, a high spatial resolution of $\lesssim 0''.035$ is required to resolve, e.g., a gap formed by a Jupiter-mass planet orbiting around a low-mass star ($0.5\ M_\odot$, $d = 140$ pc) where the gap width is assumed to be roughly 5 au and calculated to be 5.5 times of Hill radius at $r = 10$ au (Lodato et al. 2019). The highest angular resolution in ALMA Band 6 observations achieved thus far is $\sim 0''.02 - 0''.05$ (e.g., DSHARP and ODISEA). ALMA high-resolution observations potentially resolve the compact disk's substructure as well with sufficient $uv-$coverage by longer observing time (e.g., SR 4, DoAr 33, and WSB 52; Huang et al. 2018). Sparse modeling (SpM) is another approach, i.e., a promising technique that can achieve such a high spatial resolution, even in the lower frequency ALMA Band 4 and 6. This technique has already been applied to the imaging of the event horizon telescope (EHT) (Event Horizon Telescope Collaboration et al. 2019) and ALMA (see Chapter 2). To date, the use of EHT mock observational data (Honma et al. 2014; Akiyama et al. 2017a,b; Kuramochi et al. 2018) and ALMA actual observational data (in Chapter 2) has confirmed that this technique achieves a higher-fidelity image than the conventional CLEAN algorithm at the angular scale of $30\% - 40\%$ of the CLEAN beam (i.e., super-resolution). Furthermore, with an emphasis on improving the fidelity even in super-resolution regimes and at the calculation speeds, a new SpM imaging software intended for ALMA observational data has been developed over the last several years (Nakazato & Ikeda 2020).

Here, we focus on the PPD around the T Tau triple star system. T Tau is a triple star that

became an eponymous member of the class of low-mass, pre-main sequence stars (Joy 1945).
This system consists of a star (T Tau N) in the north and a close binary (T Tau Sa and Sb)
in the south (Dyck et al. 1982; Koresko 2000), located in the Taurus star-forming region at a
distance of 143.7 ± 1.2 pc, as measured by Gaia DR2 (Gaia Collaboration et al. 2016b, 2018).
Both T Tau N and T Tau S (Sa + Sb) are embedded in an infalling envelop (Momose et al.
1996), jets have been found to associated with both sources (Beck et al. 2020). T Tau N is
classified as Class II, while T Tau S is a Class I system (Furlan et al. 2006; Luhman et al. 2010).
The mass of T Tau Sa and Sb are 2.1 $M_\odot$ and 0.4 $M_\odot$, respectively (Schaefer et al. 2020). T
Tau N is one of the brightest classical T Tauri stars in Taurus. The stellar properties of T Tau
N have been calculated using optical spectral types combined with stellar evolutionary models
in several studies, and we adopted a stellar bolometric luminosity of 6.82 $L_\odot$ and a stellar mass
of 2.19 $M_\odot$ (Herczeg & Hillenbrand 2014).

Previous ALMA continuum observations targeted the dust disk around the T Tau system,
but were unable to spatially resolve them on the CLEAN image because of the insufficient
spatial resolution of $0''.12$ (or 17 au) (Long et al. 2019). The T Tau Sa/Sb disk is only seen
as a single Gaussian-like distribution. The T Tau N disk was found to be a bright disk with
a total flux of ~ 180 mJy at 1.3 mm, but is only seen as a flat compact disk with a radius of
~ 20 au. Similarly, neither ground-based near-infrared adaptive optics observations nor space-
based optical observations can resolve the disk around T Tau N and T Tau Sa/Sb well with
a resolution of $\sim 0''.07$ or 10 au (e.g., Yang et al. 2018). Intriguingly, Manara et al. (2019)
pointed out that significance residuals ($\sim 3\sigma$) were found both at the T Tau N and T Tau S
after subtracting axisymmetric models of the two sources from the ALMA continuum image. It
can be interpreted as tentative evidence of disk substructures around the T Tau system. Such
bright and compact disks around T Tau system would be most suitable for exploring several
au-scale structures using SpM imaging.

In this study, by using super-resolution imaging with SpM, which is an approach that has
been proven in previous studies, we present a high-resolution (5 au or $0''.03$) image of the T Tau
system. We find an annular gap at $r = 12$ au in the disk around T Tau N and two separate
point-like dust continuum emissions, which are located at positions corresponding to T Tau Sa
and Sb. In Section 3.3, we describe the data reduction and imaging with both CLEAN and
SpM. In Section 4.5, we show the resulting images of a 1.3 mm continuum emission, and present
the findings of the substructure of the T Tau N disk and the two disks originating from T Tau
Sa and Sb on the SpM image. In section 4.6, we discuss the expected origins of the annular gap
found in the T Tau N disk.

3.3 Data Reduction and Imaging

3.3.1 Data Reduction and Imaging with CLEAN

We reanalyzed the ALMA archival data obtained for T Tau on August 18, 2017, as part of the project 2016.1.01164.S (PI: Herczeg), including the continuum at 225.5 GHz and ^{13}CO (J = 2−1) and C^{18}O (J = 2 − 1) line data. Continuum data have already been published in Long et al. (2019); Manara et al. (2019); Beck et al. (2020). The observations were performed with a 12-m array consisting of forty-three 12-m antennas (C40-7 antenna configuration with the baseline length extending from 21.0 m to 3637.7 m) and the on-source time of the target source was 8 min.

The data consisted of four spectral windows (spws). Two of the spws were used for the continuum observations and had center frequencies of 218 and 233 GHz. The average observation frequency was 225.5 GHz (wavelength of 1.3 mm). The other spws were used to cover ^{13}CO and C^{18}O with a velocity resolution of 0.16 km s^{-1}. In this study, we used continuum spws to reconstruct images by employing two different techniques, namely CLEAN and SpM. The ^{13}CO and C^{18}O data were analyzed, but emissions associated with T Tau S and N were not identified in the two lines.

The raw data were calibrated using the Common Astronomy Software Applications package (`CASA; McMullin et al. 2007`), version 5.1.1. The initial calibration was performed using the ALMA pipeline on `CASA`. In the pipeline, J0423 − 0120 was used for the flux and bandpass calibration, and J0431 + 1731 was used for phase calibration. The positional offset between the phase (map) center and the emission peak of the T Tau N disk was adjusted using the `CASA` task `fixvis`.

The data were firstly imaged with the `tclean` task (hereafter CLEAN) by adopting Briggs weighting (`robust = 0.5`). The CLEAN is the most standard image reconstruction algorithm and also one of the nonlinear deconvolution technique (e.g., Högbom 1974; Clark 1980; Schwab 1984; Cornwell 2008; Zhang et al. 2020). The technique iteratively determines the point source on the image domain that best fits the observed visibilities, starting from a dirty image, which is obtained by the Fourier transform of the observed visibility with non-observed data filled with zero. This process is repeated until some convergence requirement is met. The final image is obtained by convolving the point-source model (CLEAN model) with an idealized CLEAN beam (usually an elliptical Gaussian fitted to a synthesized beam). We note that the beam-convolution in the image domain corresponds to multiplication in the visibility domain, which causes a loss in spatial resolution in the visibility domain via an underestimate of the observed visibility amplitudes (see Appendix.A).

Next, to improve the signal-to-noise ratio (SNR) of the image by correcting a systematic gain error (e.g., antenna-based and baseline-based errors), we performed two rounds of phase (longer at the 1st (98 s) and down to the integration time at the 2nd (49 s) with `calmode = p`) and one round of amplitude and phase (integration time of 98 s with `calmode = ap`) self-

calibrations. We obtained the final CLEAN image (= CLEAN model convolved with CLEAN beam + residual map) after self-calibration with the signal-to-noise ratio improved by a factor of 3.8, compared with the initial one. The CLEAN beam size θ_{CLEAN} was $0''.14 \times 0''.10$ at PA of $34°.1$, and its peak intensity and RMS noise level (collected noise values for $r > 3''.0$ from the phase center) were 63.81 mJy beam^{-1} and 41 μJy beam^{-1}, respectively. These values are in relatively good agreement with those reported previously in Long et al. (2019) (i.e., peak intensity = 64.56 mJy beam^{-1}, RMS noise = 52 μJy beam^{-1}).

3.3.2 Imaging with Sparse Modeling

We performed the SpM (ℓ_1+TSV) imaging. Here we briefly describe the outline of the SpM imaging and the cross validation (CV), which were used for the imaging. The self-calibrated visibility data were adopted for the image reconstruction with the latest SpM imaging task, `PRIISM` (Python Module for Radio Interferometry Imaging with Sparse Modeling), ver.0.3.0 (Nakazato & Ikeda 2020) working with `CASA`. `PRIISM` is an imaging tool for ALMA based on the SpM technique. The image is reconstructed by minimizing a cost function in which two convex regularization terms of the brightness distribution, ℓ_1-norm and total squared variation (TSV), were utilized with the chi-squared error term (Kuramochi et al. 2018). We used the 10-fold CV implemented in `PRIISM` and searched for the optimal parameter set with 5×5 sets of regularization parameters, which are $\Lambda_l = (10^3, 10^4, ..., 10^7)$ and $\Lambda_{tsv} = (10^7, 10^8, ..., 10^{11})$. In the imaging using `PRIISM`, we used non-uniform fast Fourier transform (NuFFT) algorithms to compute the Fourier transform and perform iterative fitting of the model to visibility data ($N_{\mathrm{iter}} = 1000$) until the iteration algorithm converges.

We obtained 25 images corresponding to 25 different sets of (Λ_l and Λ_{tsv}). The wide range of parameter space is selected via pre-tuning so that we do not miss the optimal image and so that it is possible to find it near the center of the image matrix. In this pre-tuning, Λ_l is first fixed, and an optimal Λ_{tsv} with the minimum cross-validation error (CVE) is searched in a wide range via SpM imaging. Next, the obtained optimal Λ_{tsv} is fixed, and an optimal Λ_l is similarly searched in a wide range for Λ_l. The values and ranges can be tuned according to the target source properties in `PRIISM`. Figure B.1 shows the reconstructed images together with the calculated values of CVE. As demonstrated in Chapter 2, an image with the minimum CVE can be regarded as the optimal image (see Appendix. B). In other words, the image of (Λ_l, Λ_{tsv}) = $(10^5, 10^9)$ is selected as the optimal one.

In order to quantify the effective resolution θ_{eff} of the technique, we have performed the following evaluation. We injected an artificial point source to the observed data in the visibility domain. We then performed the SpM imaging with the same regularization parameters of the optimal image as well as other sets of parameters. In the SpM images, effective resolution was evaluated with an elliptical Gaussian fit to the point source (see Figure C.1). In these simulation, we refer to an evaluation of an effective spatial resolution from the non-parametric image modeling with the maximum entropy method (MEM; Cárcamo et al. 2018; Pérez et al. 2020). The input flux density of the point source is 7.1 mJy, which is comparable with that

of the emission around T Tau Sa (see Table 3.1). The reconstructed image for the optimal
parameter provides the FWHM size (i.e., effective spatial resolution) of the point source, $\theta_{\mathrm{eff}} =$
$0''.038 \times 0''.027$ (or 5×4 au) with a PA of $45.3°$ and recovers a total flux of 7.9 mJy ($\sim 10\%$
higher than the input value). The obtained effective resolution is roughly consistent with the
empirical values of $\sim 30\%$ of CLEAN beams θ_{CLEAN} (Akiyama et al. 2017a,b; Kuramochi et al.
2018), which is $\theta_{\mathrm{CLEAN}} = 0''.14 \times 0.''10$ with a PA of $34.1°$. The derived θ_{eff} is comparable to
those in high-resolution observations ($\theta_{\mathrm{CLEAN}} \sim 0.''02 - 0''.05$) such as DSHARP and ODISEA
even though the maximum baseline length of our data (~ 4 km) is $3 - 4$ times shorter than
that of those high-resolution data ($\sim 13 - 16$ km; Andrews et al. 2018b; Cieza et al. 2020). The
effective resolution depends on the regularization parameters, especially on the TSV term. The
simulation results for other sets of regularization parameters (mainly for different Λ_{tsv}) are given
in Appendix.C.

3.4   Results

3.4.1   SpM image and evaluation of its noise levels

We evaluated the noise and significance levels of the optimal SpM image. As described in Chapter
2, owing to both thermal and systematic noise, an SpM image suffers from (unexpected) positive
emissions in its off-source area (i.e., outside the target source area). This is because non-negative
constraints have been adopted in the SpM imaging algorithm, and artificial emissions with
positive intensity may be present in the off-source area. Here, we define a detection threshold
(DT) in the target source area as the maximum intensity (I_{DT}) of such artificial emissions (note
that I_{DT} is the same definition as I_{100} in Chapter 2). I_{DT} was found to be 272 mJy asec^{-2} by
analyzing noise statistics at the pixel scale ($0''.05$) outside the source ($r > 0''.8$).

For direct comparison with the noise level in the CLEAN image, we convolved the optimal
SpM image with the same beam size as that used for the RMS noise estimate of the CLEAN
image (`robust = 0.5`). We found that the beam-convolved I_{DT} is 152 μJy beam^{-1} for the
optimal SpM image and was approximately 3.7 times higher than the RMS noise of the CLEAN
image (see Figure C.2).

Another way of estimating the detection threshold is the usage of image simulation of an
injected artificial point source, as described in Appendix.C. We changed the flux density of the
input point source from 1000 μJy to 100 μJy in increments of 100 μJy in the SpM simulation
and judged the detection of the point source in the image. In the optimal image case ((Λ_l, Λ_{tsv})
$= (10^5, 10^9)$), the detection threshold is 300 μJy beam^{-1} (see Figure C.2), which is two times
higher than I_{DT}. This value would provide not accurate but some reference to the threshold
if we consider that the increment of the flux density is rough and the selection of the source
position is not so optimized for evaluating the detection threshold precisely.

It would also be possible to estimate the noise levels with measuring the RMS noise of
a residual map, which can be obtained by performing the 2D Fourier transform of residual
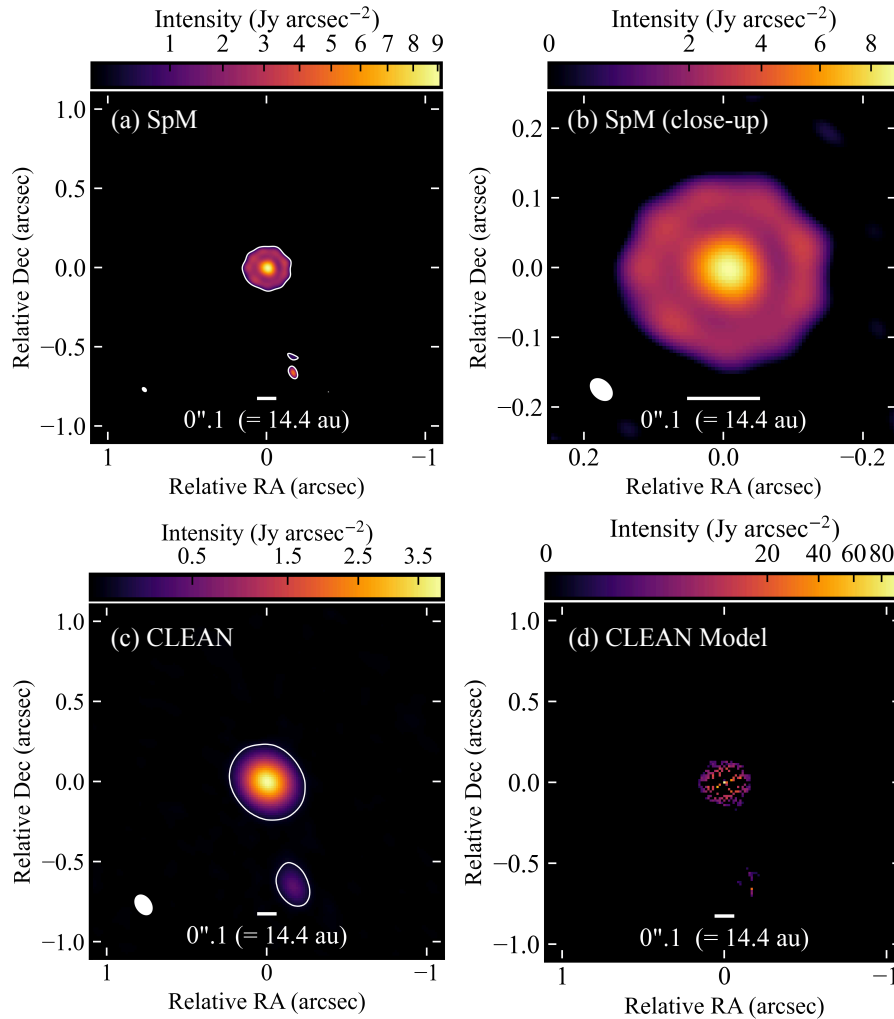
Figure 3.1: Gallery of ALMA continuum images at 1.3 mm (Band 6) of PPD T Tau system. The same color scale given by a power law with a scaling exponent of $\gamma = 0.6$ was adopted, except for the CLEAN model image ($\gamma = 0.3$). A white bar of $0.''1$ ($=14.4$ au) is provided for reference to the angular scales. (a) SpM image. The filled white ellipse denotes the effective spatial resolution with a size of $0''.038 \times 0''.027$ for a PA of $45°.3$ in the bottom left corner. The resolution is estimated from an artificial point source simulation. The contour corresponds to $I_{\rm DT}$, where $I_{\rm DT}$ is the detection threshold of 272 mJy asec^{-2}. Note that the SpM image is not processed by a synthesized beam-convolution as a CLEAN image is done, and the unit of the SpM image is not Jy beam^{-1}. The unit of the SpM image that was initially obtained from the imaging is Jy pixel^{-1}, and we convert it to Jy arcsec^{-2}. (b) Close-up view centered on T Tau N of SpM image. A field of view of $0.''5 \times 0.''5$ is adopted. (c): CLEAN image with Briggs weighting with a robust parameter of 0.5. The filled white ellipse denotes the synthesized beam with a size of $0''.14 \times 0''.10$ for a PA of $34°.1$ in the bottom left corner. The contour corresponds to $20\sigma_I$, where σ_I is the RMS noise of 2.58 mJy asec^{-2} ($= 41$ μJy beam^{-1}). (d) CLEAN model image before convolution with the CLEAN beam.

Figure 3.2: Comparison of positions of T Tau
Sa and Sb between the peak emission on the
SpM image and the stellar orbit model on the
date of the ALMA observations (2017 August
18 UTC, Köhler et al. 2016). The positions of
the sub-mm emission peaks are marked with
stars, and the predicted positions of T Tau
Sa and Sb are marked with crosses. These
marked positions were superimposed on the
SpM image. The image contours correspond
to $(1, 2, 3, 6, 9, 12, 15) \times I_{\mathrm{DT}}$. Black bars are
provided for reference to angular scales.
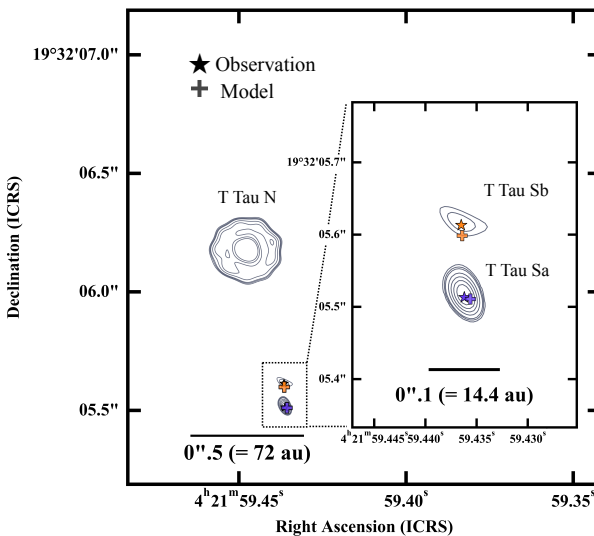
visibilities between the SpM model data (which can be obtained by the inverse 2D Fourier
transform of the SpM image) and the observed data. The residual map was reconstructed from
the residual visibilities using `DIFMAP` (Shepherd et al. 1994). The residual map was created by
adopting a natural uv weighting, providing synthesized beams of $0''.17 \times 0''.12$ with a PA =
$36.8°$ and an RMS noise of 31 μJy beam^{-1}. This is smaller than that in the CLEAN image,
and this could be because the SpM model image retrieves positive noises. For comparison, we
convolved the optimal SpM image with the same beam size as that used for the RMS noise
estimate. We found that the beam-convolved $I_{\mathrm{DT}}(= 152~\mu$Jy beam^{-1}) was approximately five
times higher than the RMS. Based on the above evaluations, emission features above I_{DT} are
considered significant in the SpM image.

Figure 3.1 shows the SpM and CLEAN images of the T Tau system. The SpM image
spatially resolves the disk structure around T Tau N, and an annular gap structure has been
newly found. The emission around the T Tau S system is spatially resolved into two sources,
although the CLEAN image does not resolve them. Table 3.1 shows that the total fluxes of
these sources obtained from the SpM image above the I_{DT} level are generally consistent with
the values obtained from the CLEAN image above 5σ levels. SpM reproduces a high fidelity
image that better fits the observed visibilities than the CLEAN image, but it provides similar
results in visibility domain to the CLEAN model (see Appendix.A). We consider that the
SpM image better reconstructs the disk surface brightness distribution while the CLEAN model
reconstructs an image with a sum of a number of point sources as shown in Figure 3.1 (d), which
do not reflect the disk structures precisely. Therefore, in the following sections, we adopt the
SpM image to derive the physical properties of T Tau system.

3.4.2   Dust Emissions from T Tau Sa and Sb

As described in Section 3.4.1, two separate emissions were found around T Tau Sa and Sb.
Figure 3.2 presents a close-up view of the Tau Sa and Sb regions. Two-dimensional Gaussian

fitting was applied to each of them using the `CASA` task `imfit`. The results are listed in Table
3.2.

To confirm whether each of the two emissions originated from T Tau Sa or Sb, Figure
3.2 compares the image with stellar positions predicted by the stellar orbit model of the T
Tau S binary in Köhler et al. (2016), based on observational data spanning approximately 18
years. The coordinate systems of the binary were derived for the date of the ALMA observation
(August 18, 2017). The offsets between the emission peaks and predicted stellar positions are
calculated to be 9.3 mas (1.3 au) and 14.6 mas (2.1 au) for Sa and Sb, respectively, and will
be roughly within errors involved in the calculations; e.g., the uncertainties of the model, a few
mas (Köhler et al. 2016, priv. comm) and 1σ positional errors for T Tau Sa and Sb in the SpM
image, $\sim$1 and 5 mas, respectively. In addition, each total flux roughly fits each spectral energy
distribution (SED) predicted by an accretion disk model (Ratzka et al. 2009). Hence, it can
explain that the two emissions originate from T Tau Sa or Sb.

As shown in Table 3.2, the best-fit sizes (i.e., the FWHM of the semi-major/semi-minor
axes from the Gaussian fitting) of T Tau Sa and Sb were found to be 6×4 au and 7×3 au,
respectively. These disk sizes are slightly larger than the effective spatial resolution of the SpM
image ($\theta_{\mathrm{eff}} = 5 \times 4$ au) and not resolved sufficiently. Hence, these sizes should be considered to
be the conservative upper limits. The total flux density of T Tau Sb is a factor of seven smaller
than T Tau Sa, which is in good agreement with a factor of eight given in Beck et al. (2020).
This implies that the actual disk size of T Tau Sb would be about three times smaller than that
of T Tau Sa when we consider the scaling relation between the mm-continuum disk radii R_{mm}
and luminosities L_{mm}; $L_{\mathrm{mm}} \propto R_{\mathrm{mm}}^2$ (Tripathi et al. 2017; Andrews et al. 2018a; Hendler et al.
2020).

3.4.3   Disk Structure of T Tau N

Here, we investigate the global disk properties of T Tau N derived from the SpM image and
compare them with previous studies based on mid-infrared and millimeter observations. The
T Tau N disk is known to be viewed as nearly face-on (Akeson et al. 1998; Ratzka et al. 2009;
Long et al. 2019; Manara et al. 2019; Beck et al. 2020). We derived the inclination and PA of
the disk on the image by fitting an ellipse to the outer ring, as described in Appendix.D. As
shown in Table 3.3, the measured inclination of $25.2 \pm 1.1°$ agrees well with $< 30°$ derived from
mid-infrared interferometric observations with very large telescope interferometer (VLTI) and
SED simulations (Ratzka et al. 2009) as well as with $\simeq 28°$ from visibility fitting using the same
ALMA data (Manara et al. 2019; Beck et al. 2020).

Next, we derive a disk radius r_{d} using a curve-of-growth method similar to that described in
Ansdell et al. (2016). The disk radius is measured with successively larger photometric apertures
on a deprojected image until the measured flux reaches 95% of the total flux. As a result, r_{d} was
calculated to be 24 ± 4 au. The error on r_{d} is calculated by taking the range of radii within the
uncertainties of the 95% flux measurement. The obtained effective radius is in good agreement

with the one ($r_d \simeq 21$ au) from Manara et al. (2019) in the same definition of the measurement. Most populated Taurus disks (spectral type earlier than M3) are known to be faint and compact (Total flux of < 100 mJy at 1.3 mm, dust radii of < 40 au; Long et al. 2019). Thus, the T Tau N disk can be regarded as a bright compact disk.

Table 3.1:: Properties of dust disks in T Tau system.

Source	CLEAN		Sparse Modeling (SpM)		
	$F_\nu(> 5\sigma)$	Peak I_ν	$F_\nu(> I_{\mathrm{DT}})$	Peak I_ν	Peak I_ν Position
	(mJy)	(Jy asec^{-2})	(mJy)	(Jy asec^{-2})	(RA, Dec)
T Tau N	175.0	4.0	174.4	9.1	($04^h21^m59^s.4475$, $+19^d32^m06^s.1731$)
T Tau S (Sa+Sb)	8.0	0.4	7.9	–	–
T Tau Sa	–	–	7.1	5.1	($04^h21^m59^s.4362$, $+19^d.32^m.05^s.5131$)
T Tau Sb	–	–	0.8	0.8	($04^h21^m59^s.4365$, $+19^d.32^m.05^s.6131$)

Note. — The first column lists the total flux (F_ν) above $5\sigma(= 13$ mJy asec^{-2}) level and peak intensity (Peak I_ν) on the CLEAN image. The last three columns list the total flux (F_ν) above the $I_{\mathrm{DT}}(= 272$ mJy asec^{-2}) level , peak intensity (Peak I_ν), and its position (RA, Dec) on the SpM image..

Table 3.2:: Results of 2D Gaussian Fits to T Tau Sa and Sb.

Source	θ_{maj}	θ_{maj}	θ_{min}	θ_{min}	PA	inclination	Peak I_ν	F_ν
	(mas)	(au)	(mas)	(au)	(°)	(°)	(Jy/asec^2)	(mJy)
T Tau Sa	44.7 ± 0.7	6.4 ± 0.1	27.1 ± 0.4	3.9 ± 0.1	25.2 ± 1.1	52.8 ± 0.6	5.6 ± 0.1	7.7 ± 0.1
T Tau Sb	49.7 ± 5.0	7.2 ± 0.7	22.4 ± 2.3	3.2 ± 0.3	64.9 ± 4.6	63.2 ± 2.9	0.9 ± 0.1	1.1 ± 0.1

Note. — Disk properties for T Tau Sa and Sb obtained using the `imfit` task in `CASA` to fit a 2D Gaussian on the SpM image. The task returns the total flux density (F_ν) of the source along with the statistical uncertainty, the full width at half maximum (FWHM) along the semi-major (θ_{maj}) and semi-minor (θ_{min}) axes, and the position angle (PA). The inclination is derived from θ_{maj} to θ_{min} ratio, assuming a perfect circle disk. Estimates of the uncertainties derived from `imfit` are based on Condon (1997) and that of the inclination is derived from error propagation.Note that θ_{maj} and θ_{min} give upper limits, and these uncertainties in astronomical units do not account for the uncertainty in the distance to the source.

3.4.4 Gap structure in the T Tau N disk

Figure 3.3 shows the deprojected and azimuthally averaged radial intensity profile $I_\nu(r)$ where $r = 0$ au is set to the peak intensity of the T Tau N disk. The uncertainty of the radial profile is evaluated as the error of the mean at each radius where we consider the effective spatial resolution of the major axis ($\theta_{\mathrm{eff,maj}}$) as the smallest independent unit. That is, the error is the standard deviation of each elliptical bin divided by the square root of the number of $\theta_{\mathrm{eff,maj}}$ spanning the whole azimuthal angle at each radial bin. For comparison, a standard deviation at each radius is also potted in the radial profile in Figure 3.3.

Table 3.3:: Physical properties of T Tau N disk.

Parameters	Measurements
Position angle	91.4 ± 3.0 (°)
Inclination	25.2 ± 1.1 (°)
Disk radius: r_d	166 ± 25 (mas), 24 ± 4 (au)
Outer ring peak: r_peak	109 ± 1 (mas), 15.7 ± 0.1 (au)
Gap location: r_gap	81 ± 2 (mas), 11.6 ± 0.3 (au)
Gap width: Δ_I	0.28 ± 0.02
Gap depth: δ_I	1.22 ± 0.06

Note. — The physical parameters of the T Tau N disk are calculated from the SpM image and the radial intensity profile. These uncertainties in astronomical units do not account for the uncertainty in the distance to the source.
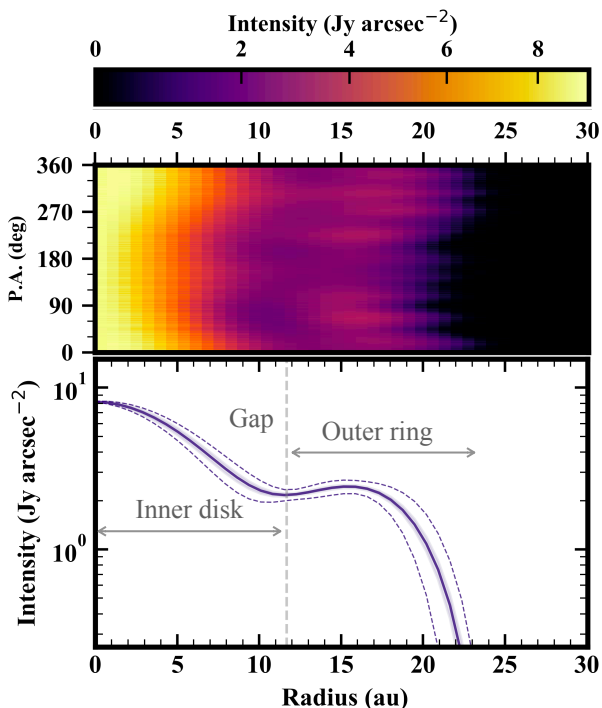
Figure 3.3: Top panel: SpM image of T Tau N, which is deprojected into a map in polar coordinates to more clearly view the disk substructure. Bottom panel: Radial profiles of the intensity averaged over the full azimuthal angle on a logarithmic scale. The profile is linearly interpolated onto radial grid points spaced by 0.1 au with `interpolate.interp1d` in the `SciPy` module. The light purple ribbon shows the error of the mean at each radius, while the purple dashed lines show the standard deviation for comparison. For reference, the vertical dashed line marks the position of the gap, which correspond to the distance of 12 au.

We identify an annular gap (local minimum in $I_\nu(r)$ at $r_\mathrm{gap} = 11.6 \pm 0.3$ au) and an outer peak (the local maximum in $I_\nu(r)$ at $r_\mathrm{peak} = 15.7 \pm 0.1$ au) as well as in the radial intensity profile. We then adopt the same approach as in Zhang et al. (2018) to measure the gap depth δ_I and the gap width Δ_I. The gap depth is defined as $\delta_\mathrm{I} = I_\nu(r_\mathrm{peak})/I_\nu(r_\mathrm{gap})$. The gap width is defined as $\Delta_\mathrm{I} = (r_\mathrm{out} - r_\mathrm{in})/r_\mathrm{out}$, where r_out and r_in are the inner edges of the outer ring and the outer edge of the inner disk, respectively. The relationship between $I_\mathrm{edge} \equiv 0.5\{I_\nu(r_\mathrm{peak}) + I_\nu(r_\mathrm{gap})\}$ defines the edge locations. The edge location r_in is defined as the smallest value r satisfying the criteria $I_\mathrm{edge} = I_\nu(r_\mathrm{in})$ and $r < r_\mathrm{gap}$. Another edge location r_out is defined as the largest value

Figure 3.4: Top panel: the radial profiles of the brightness temperature $T_{br}(r)$ (purple line). The disk temperature model $T_d(r)$ denotes the gray line. Middle panel: optical depth $\tau_\nu(r)$ (purple line). The horizontal dashed gray line in the middle panel shows the threshold for the optical depth $\tau_\nu = 1$. Bottom panel: the dust surface densities $\Sigma_d(r)$ for the two dust opacity models, compared to the Hayashi (1981) dust surface density model for the MMSN (gray line). In the middle and bottom panels, the interior radii of 8 au are shaded because the optical thickness steepens by more than several orders of magnitude ($\tau_\nu \gg 1$) at the threshold ($r = 8$ au). The light colored ribbons show the error of the mean at each radius, while the dashed lines show the standard deviation for comparison. For reference, the vertical gray dashed lines indicate the annular gap location ($r = 12$ au) obtained from the radial intensity profile.
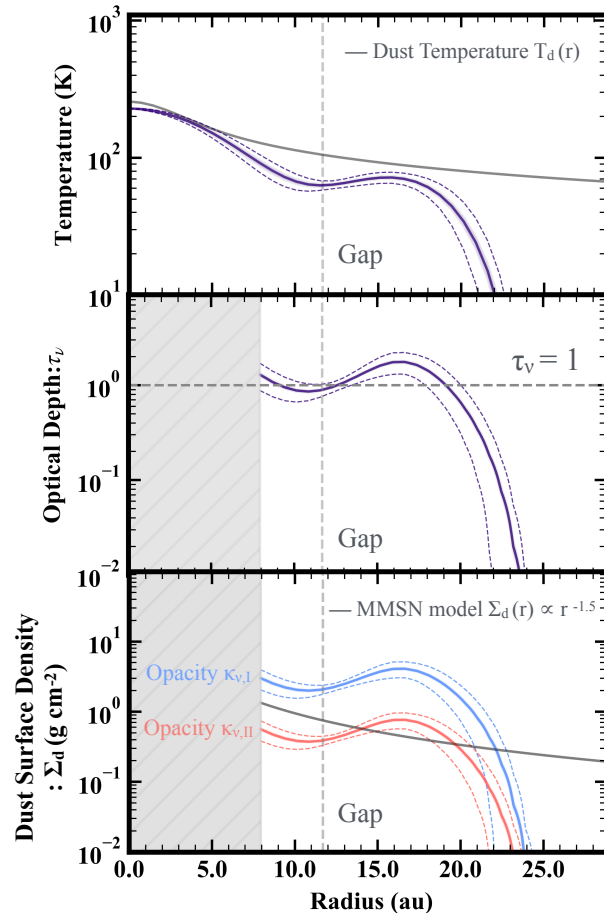
satisfying the criteria $I_{edge} = I_\nu(r_{out})$ and $r_{gap} < r < r_{peak}$. The measured parameters are listed in Table 3.3. In Section 4.6.3, the measured $\Delta_I (= 0.28 \pm 0.02)$ and $\delta_I (= 1.22 \pm 0.06)$ are used to estimate the planetary mass under the hypothesis of planet-induced gap.

3.4.5 Physical Properties of T Tau N Disk

Here, we derive the disk temperature $T_d(r)$, optical depth $\tau_\nu(r)$, and dust surface density $\Sigma_d(r)$ of the T Tau N disk based on the SpM image to characterize the disk and substructure. We employ the radiative transfer equation expressed as

$$I_\nu(r) = B_\nu \left(T_d(r) \right) \left(1 - e^{-\tau_\nu} \right), \tag{3.1}$$

where $B_\nu(r)$ and $T_d(r)$ denote the full Planck function, and the dust temperature, respectively, and $\tau_\nu(r)$ is the optical depth expressed as $\tau_\nu(r) = \kappa_\nu \Sigma_d(r)$. Here, κ_ν and $\Sigma_d(r)$ denote the absorption dust opacity and the dust surface density, respectively. The brightness temperature $T_{br}(r)$ can be calculated from Equation 3.1 such as

$$T_{br}(r) = \frac{h\nu}{k} \left[\ln \left(\frac{2h\nu^3}{c^2 I_\nu(r)} + 1 \right) \right]^{-1}, \tag{3.2}$$

where c, h, and k denote the speed of light, the Planck's constant, and the Boltzmann constant, respectively. Figure 3.4 (top panel) shows that $T_{\mathrm{br}}(r)$ reaches 257 ± 1 K at the peak, and the average $T_{\mathrm{br}}(r)$ over the disk ($= \int T_{\mathrm{br}}(r) r dr / \int r dr$, where $r \leq 24$ au) is calculated to be 97 ± 1 K. The average $T_{\mathrm{br}}(r)$ predominantly exceeds that predicted from the dust temperature model ($T_d \simeq 30 - 40$ K) which are simply scaled using the stellar luminosity (Andrews et al. 2013; van der Plas et al. 2016).

We should point out that the peak T_{br} is much higher than standard peak values ($\sim 20 - 100$ K) of other PPDs in the same observational wavelength and similar resolutions (see Fig.4 in Facchini et al. 2019). Moreover, the average spectral index over the disk is estimated to be $\alpha_{\mathrm{mm}} = 1.9 \pm 0.1$ (see Appendix.E).

From the high brightness temperature and the low spectral index described above, the disk tends to be optically thick overall ($\tau_\nu \geq 1$), and the measured $T_{\mathrm{br}}(r)$ should represent the temperature of the emitting layer from the disk atmosphere. The innermost region ($r < 5$ au) seems to be thicker than the outer ring, and the brightness temperature should be close to the dust temperature near the disk surface in such a case. Therefore, we assume that $T_{\mathrm{d}}(r)$ is equal to $T_{\mathrm{br}}(r)$ at the optically thick region with $\tau_\nu \geq 1$. The disk temperature profile can be obtained as $T_{\mathrm{d}}(r) = 360 (r/1 \text{ au})^{-0.5}$ [K] by assuming $T_{\mathrm{d}}(r)$ has a power-law form, such as $T_{\mathrm{d}}(r) \propto r^{-0.5}$ (Kenyon & Hartmann 1987). In this fitting, $T_{\mathrm{d}}(r)$ is smoothed with θ_{eff} to match the $T_{\mathrm{br}}(r)$ profile. It should be noted that a disk midplane temperature will generally be lower than $T_{\mathrm{br}}(r)$ at optically thick regions. Thus, dust surface densities (and dust masses) estimated in what follows would be lower limits in such a case.

We have estimated $\tau_\nu(r)$ and $\Sigma_d(r)$ by adopting $T_{\mathrm{d}}(r)$ derived above as the disk temperature. The optical depth $\tau_\nu(r)$ is calculated using the radiative transfer calculation of Equation 3.1 as:

$$\tau_\nu(r) = -\ln \left(1 - \frac{I_\nu(r)}{B_\nu(T_{\mathrm{d}}(r))} \right). \tag{3.3}$$

Figure 3.4 shows the derived $\tau_\nu(r)$ profile. $\Sigma_d(r)$ is also expressed as:

$$\Sigma_d(r) = \frac{\tau_\nu(r)}{\kappa_\nu}. \tag{3.4}$$

If we fix the disk temperature, another uncertainty in $\Sigma_d(r)$ comes from assumption of the dust opacity κ_ν, which usually depends on the grain size and many other factors. Here, we consider two independent dust opacity models (but keep not claiming which opacity model reproduces a "better" nature of the T Tau N). One is DSHARP opacity model $\kappa_{\nu,\mathrm{I}}$ ($= 0.43$ cm^2 g^{-1}; Birnstiel et al. 2018) assuming a maximum grain size of 0.1 mm supported by recent (sub)mm polarization measurements of other Class II PPDs in the Taurus region (Bacciotti et al. 2018). The model value is constrained by dust size distribution with reference to its measurements from (sub)mm observations. Another is a conventional model $\kappa_{\nu,\mathrm{II}}$ ($= 2.3$ cm^2 g^{-1}; Beckwith & Sargent 1991), which can be expressed as $\kappa_\nu = 2.3(\nu/230 \text{ GHz})^{0.4}$[cm^2 g^{-1}] and being simply parameterized because of the large uncertainties in the opacity. $\kappa_{\nu,\mathrm{II}}$ has been widely used for PPDs (e.g.,

Williams & Cieza 2011) and being supported by spatially resolved multi-wavelength continuum observations of other PPD (Lin et al. 2021).

The final results of $\Sigma_d(r)$ using $\kappa_{\nu,\mathrm{I}}$ and $\kappa_{\nu,\mathrm{II}}$ are plotted in Figure 3.4 together with that of the minimum mass solar nebula (MMSN; $\Sigma_d(r) = 30~(r/1~\mathrm{au})^{-1.5}$ [g cm^{-2}]; Weidenschilling 1977; Hayashi 1981). We found that the dust surface density profiles of the T Tau N disk are locally more massive than the MMSN by a factor of 15 for $\kappa_{\nu,\mathrm{I}}$ and 3 for $\kappa_{\nu,\mathrm{II}}$ around the outer ring, but it sharply decreases at the disk edge. For comparison, the dust surface density profiles of the disks in Ophiuchus, Taurus-Auriga (Andrews 2015), and Lupus (Tazzari et al. 2017) generally appear less massive than the MMSN, while only a few of them have a comparable or larger mass. The T Tau N disk, despite being a small dust disk, would be regarded to be more massive than typical disks in the low-mass star-forming regions.

The mm-dust mass M_{dust} of the outer ring ($r_{\mathrm{gap}} \leq r \leq r_{\mathrm{d}}$) can be computed using the obtained $\Sigma_d(r)$, which is defined as $M_{\mathrm{dust}} = \int_{r_{\mathrm{gap}}}^{r_d} \Sigma_d(r) 2\pi r dr$. The dust ring mass results in a wide range of values depending on the dust opacity; $\sim 104~M_\oplus$ for $\kappa_{\nu,\mathrm{I}}$ and $\sim 20~M_\oplus$ for $\kappa_{\nu,\mathrm{II}}$. We note that these dust ring masses should be considered as lower limit due to the uncertainty of midplane temperature. In the range of the inferred dust masses, the outer ring of T Tau N is roughly as massive as the outer ring (at a location of ~ 100 au, $M_{\mathrm{dust}} \sim 67~M_\oplus$) in Herbig Ae star MWC 480, as located in the Taurus region (Liu et al. 2019).

To check whether the T Tau N disk is gravitationally stable, Toomre Q (Toomre 1964) was calculated using the formula; $Q \equiv c_s \Omega_\mathrm{K} / \pi G \Sigma_{\mathrm{gas}}$, where c_s is sound speed, Ω_K is angular velocity, G is the gravitational constant, and Σ_{gas} is gas surface density. If the disk follows the criterion $Q \lesssim 1.5$, the disk is gravitationally unstable and grows spiral arms (Laughlin & Bodenheimer 1994). Here, we employed the Toomre Q under the standard assumption of $\Sigma_{\mathrm{gas}}/\Sigma_{\mathrm{dust}} = 100$ (Bohlin et al. 1978). In both $\kappa_{\nu,\mathrm{I}}$ and $\kappa_{\nu,\mathrm{II}}$, the Toomre Q values exceed the unity around the outer ring area; $Q \gtrsim 3$ for $\kappa_{\nu,\mathrm{I}}$ and $Q \gtrsim 10$ for $\kappa_{\nu,\mathrm{II}}$. The T Tau N disk thus appears to be gravitationally stable. It should be noted that a secular gravitational instability (requiring high gas-to-dust ratios < 100 and low viscous parameter $\alpha \lesssim 10^{-3}$) can generate a ring-like structure in the disk (Takahashi & Inutsuka 2014, 2016). That being said, the required physical parameters remain highly uncertain at this stage, and it cannot conclude the possibility of secular gravitational instability as the origin of the rings yet.

3.5   Discussion

3.5.1   Origins of Gap in the T Tau N Disk

Recent high-resolution observations have revealed multiple annular gap structures in bright giant disks (e.g., Andrews et al. 2018b; Cieza et al. 2020). Several detections of gaps or cavities in compact disks have also been reported so far; the transitional disks around XZ Tau B (disk radius of 3 au, cavity radius of 1.3 au, Osorio et al. 2016) and around several candidates (see Pinilla et al. 2018, for details), and the annular gap structure in the disks around a single star

SR 4 ($r_{\mathrm{gap}} = 11$ au, $r_{\mathrm{d}} = 31$ au; Huang et al. 2018), DoAr 33 ($r_{\mathrm{gap}} = 9$ au, $r_{\mathrm{d}} = 27$ au; Huang
et al. 2018), WSB 52 ($r_{\mathrm{gap}} = 21$ au, $r_{\mathrm{d}} = 32$ au; Huang et al. 2018), CIDA 1 ($r_{\mathrm{gap}} = 8$ au,
$r_{\mathrm{d}} = 40$ au; Pinilla et al. 2021), J0433 ($r_{\mathrm{gap}} = 15$ au, $r_{\mathrm{d}} = 46$ au; Kurtovic et al. 2021), and one
of a binary system GQ Lup A ($r_{\mathrm{gap}} = 8$ au, $r_{\mathrm{d}} = 20$ au; Long et al. 2020). The T Tau N case
is very similar to SR 4, DoAr 33, and GQ Lup A in terms of the radius of the disk and gap
location. In previous studies on gap origins in disks (e.g., Huang et al. 2018; Long et al. 2018),
two main possibilities have been investigated, that is, snow line and planet origins.

The snow line, which is also referred to as an ice sublimation front, is the location in the
disk midplane where dust opacity and collisional growth are expected to change, producing
features such as ring-like substructures seen in continuum images (Zhang et al. 2015; Okuzumi
et al. 2016). An estimate of the snowline location inferred from disk midplane temperature
models (e.g., Dullemond et al. 2001) should be calculated and is confirmed by comparing the
gap location. However, the brightness temperature of the T Tau N disk is much higher than that
of the regular disk, and this disk appears optically thick at 1.3 mm. It can be thus challenging
to find a reasonable disk midplane temperature model that matches observations. This problem
would be solved by observing the optically thin disk at lower wavelengths to determine an
adequate model.

3.5.2   Planetary Origin and Planet Mass Estimates

Another possible origin of this gap is the planet clearing of the disk material. Below, we estimate
planetary masses by applying two different methods that connect the planetary mass and gap
shape (Kanagawa et al. 2015, 2016; Zhang et al. 2018).

We first apply the relationship between the planet mass and the width and depth of the
gaseous gap according to the theory proposed by Kanagawa et al. (2015, 2016). The gap depth
and width are defined as the difference between the initial and gap-formed surface density profiles
in the theory, but this definition cannot be adopted in our case as the initial model cannot be
set because of a lack of complete information of $\Sigma_d(r)$. Instead of the original definition, we
adopt the gap width Δ_Σ and depth δ_Σ given in the dust surface density $\Sigma_d(r)$. As shown in
Equation 3.4, $\Sigma_d(r)$ is simply calculated by dividing the optical depth $\tau_\nu(r)$ by the constant
opacity models ($\kappa_{\nu,\mathrm{I}}$ or $\kappa_{\nu,\mathrm{II}}$). Therefore, the gap width and depth of the dust surface density
profile would not change regardless of which of the two opacities are used. Here, we apply a
Gaussian fit to $\Sigma_d(r)$ at the gap area ($r = 8 - 16$ au) in a similar manner with Segura-Cox
et al. (2020), by using the least-squares method implemented in `optimize.leastsq` from `SciPy`
(Jones et al. 2001). The uncertainties are the statistical uncertainties from the Gaussian fitting.
The FWHM gap width Δ_Σ is derived as 8.3 ± 0.1 au at a gap location of $r_{\Sigma,\mathrm{gap}} = 10.89 \pm 0.02$
au. We define the gap depth $\delta_\Sigma = \Sigma_{\mathrm{peak}}/\Sigma_{\mathrm{gap}}$, where Σ_{peak} is the local peak of the outer ring,
and Σ_{gap} is the local minimum at $r_{\Sigma,\mathrm{gap}}$. The gap depth was calculated to be $\delta_\Sigma = 2.1 \pm 0.3$.

Here, we assume that the dust is well coupled to the gas content of the disk, and the radial
location of the planet is at $r_{\Sigma,\mathrm{gap}}$. Note that our defined gap depth may be underestimated

Figure 3.5: Schematic view of the conserva-
tion relation with the gap width and depth in
radial intensity (or surface density) profile for
the T Tau N disk.
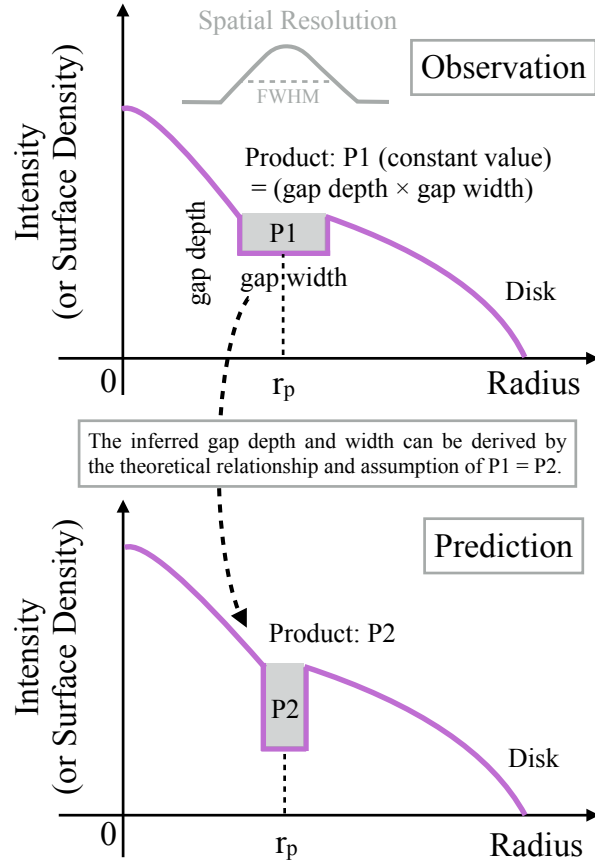
because it may be shallower than the original one. We use the relationship between the planetary
mass M_p and the gap depth δ_Σ as follows (Eq.7 in Kanagawa et al. 2015):

$$\frac{M_p}{M_*} = 0.16(\delta_\Sigma - 1)^{0.5} \left(\frac{h_{\Sigma,\text{gap}}}{r_{\Sigma,\text{gap}}}\right)^{2.5} \left(\frac{\alpha_\text{vis}}{10^{-3}}\right)^{0.5}, \tag{3.5}$$

where $h_{\Sigma,\text{gap}}$ is the scale height at $r_{\Sigma,\text{gap}}$, and α_vis is the viscous parameter (Shakura & Sunyaev
1973). We also use the relation with the gap width Δ_Σ as follows (Eq.5 in Kanagawa et al.
2016):

$$\frac{M_p}{M_*} = 0.19 \left(\frac{\Delta_\Sigma}{r_{\Sigma,\text{gap}}}\right)^2 \left(\frac{h_{\Sigma,\text{gap}}}{r_{\Sigma,\text{gap}}}\right)^{1.5} \left(\frac{\alpha_\text{vis}}{10^{-3}}\right)^{0.5}. \tag{3.6}$$

By eliminating the planetary mass in the above two equations, Eq.3.5 and Eq.3.6, the relationship
between δ_Σ and Δ_Σ can be obtained as follows:

$$\Delta_\Sigma = 0.92(\delta_\Sigma - 1)^{0.25} \left(\frac{r_{\Sigma,\text{gap}}}{1 \text{ au}}\right) \left(\frac{h_{\Sigma,\text{gap}}}{r_{\Sigma,\text{gap}}}\right)^{0.5} \text{ au} \tag{3.7}$$
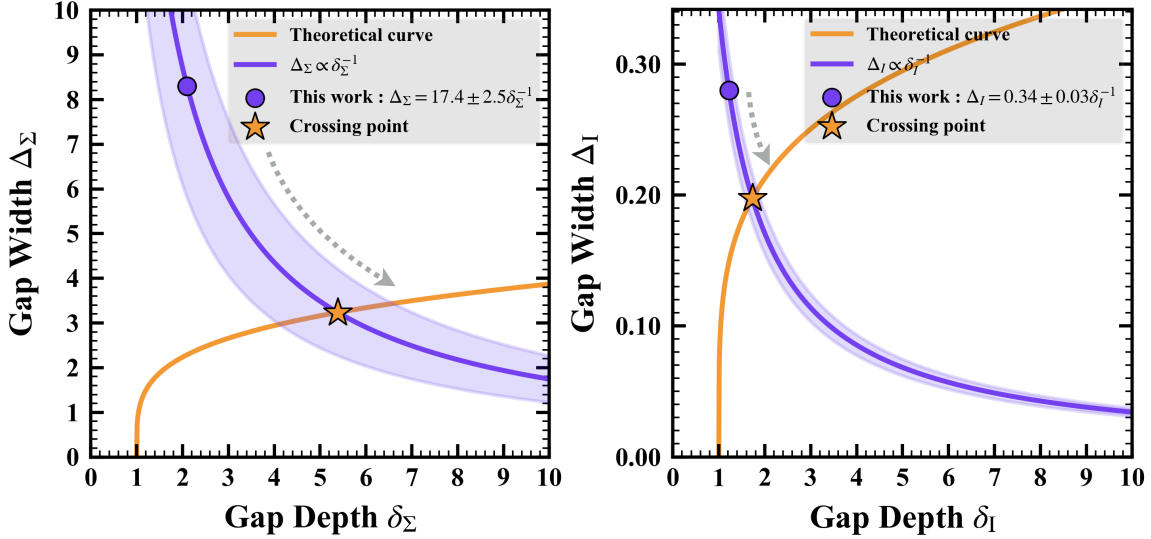
Figure 3.6: Relationships between the gap width and depth controlled by the planetary mass using Eq.3.7 (orange curve in the left panel) and Eq.4.4 (orange curve in the right panel). In each panel, the blue circle denotes the measured values obtained from the observation, the blue curve denotes the relationship that the gap depth times the gap width retains the values ($\Delta_\Sigma \propto \delta_\Sigma^{-1}$, or $\Delta_I \propto \delta_I^{-1}$) derived from the observation, and the star mark shows the cross point between the blue curve and the orange curve indicating the prediction of a set of the gap width and depth. The light blue ribbons show the uncertainties of the gap width due to 1σ errors in both the measured gap depth and width.

Using $T_d(r)$, the aspect ratio $h_{\Sigma,gap}/r_{\Sigma,gap}$ was calculated to be 0.05, and the viscous parameter is set to be 10^{-3} for the T Tau N disk, as in Kanagawa et al. (2015). We found that the derived depth and width are too shallow and too wide compared to the theoretical curve. Nomura et al. (2016) reported that owing to beam smearing, the derived measurements, δ_Σ and Δ_Σ give a lower limit and upper limit, respectively. Following the discussion by Nomura et al. (2016), we assume that the gap depth times the gap width conserves the value derived from the observations (i.e., $\Delta_\Sigma \propto \delta_\Sigma^{-1}$) and r_p remains fixed, as illustrated in Figure 3.5. The conservation has been confirmed in the case of TW Hya (Tsukagoshi et al. 2016, priv. comm). Thus, the relation can be plotted in the left panel of Figure 3.6. The crossing point between the two curves is located at the width and depth of $\Delta_\Sigma = 3.2 \pm 0.3$ au and $\delta_\Sigma = 5.4 \pm 1.3$ under the condition of $\Delta_\Sigma = 17.4 \pm 2.5 \, \delta_\Sigma$ au. The crossing point and the use of Eq.3.5 and Eq.3.6 give the planetary mass of 1.4 ± 0.2 M_{Saturn}. The error range of the planetary mass results from the uncertainty of the product, which can change the location of the crossing point.

Next, we consider another relationship in Zhang et al. (2018). This approach defines the gap depth δ_I and width Δ_I in $I_\nu(r)$ in Section 3.4.4 without assuming a functional form for the substructures or an initial surface density; it has the relationships to derive the planet mass from the measured δ_I and Δ_I in Section 3.4.4. We now use the relationship between the planet mass and the gap depth δ_I (Eq.24 in Zhang et al. 2018):

$$\frac{M_{\rm p}}{M_*} = 0.073 \left(\frac{\delta_{\rm I} - 1}{C}\right)^{1/D} \left(\frac{h_{\rm gap}}{r_{\rm gap}}\right)^{2.81} \left(\frac{\alpha_{\rm vis}}{10^{-3}}\right)^{0.38} \tag{3.8}$$

We also used the one with the gap width $\Delta_{\rm I}$ (Eq.22 in Zhang et al. 2018):

$$\frac{M_{\rm p}}{M_*} = 0.115 \left(\frac{\Delta_{\rm I}}{A}\right)^{1/B} \left(\frac{h_{\rm gap}}{r_{\rm gap}}\right)^{0.18} \left(\frac{\alpha_{\rm vis}}{10^{-3}}\right)^{0.31} \tag{3.9}$$

By eliminating the planetary mass in the two equations, Eq.4.2 and Eq.4.3, the relationship
between $\Delta_{\rm I}$ and $\delta_{\rm I}$ can be obtained as follows.

$$\Delta_{\rm I} = A \left[0.635 \left(\frac{\delta_{\rm I} - 1}{C}\right)^{1/D} \times \left(\frac{h_{\rm gap}}{r_{\rm gap}}\right)^{2.63} \left(\frac{\alpha_{\rm vis}}{10^{-3}}\right)^{0.07}\right]^{B} \tag{3.10}$$

where A, B, C, and D are constant parameters introduced by Zhang et al. (2018), and depend
on the gas surface density $\Sigma_{\rm g}$ and the maximum grain size ($s_{\rm max} = 0.1 \sim 10$ mm). Figure 18 of
Zhang et al. (2018) shows the relationship between a gas surface density and an averaged dust
surface density $\Sigma_{\rm d}$ at an outer disk (or ring) for hydrodynamical simulations. We can then use
their Figure 18 to estimate the gas surface density $\Sigma_{\rm g}$ based on the average $\Sigma_{\rm d}(= 3.4$ g cm$^{-2})$ at
the outer ring of T Tau N and the aspect ratio $h_{\rm gap}/r_{\rm gap}(= 0.05)$. Finally, the four parameters
($A = 1.11$, $B = 0.29$, $C = 0.0478$, and $D = 1.23$) are selected from Table 1 and 2 of Zhang et al.
(2018), when considering the estimated $\Sigma_{\rm g}(> 100$ g cm$^{-2})$ and the maximum dust particle size
($s_{\rm max} = 0.1$ mm; Bacciotti et al. 2018) in the disk.

$\Delta_{\rm I}$ is calculated as a function of $\delta_{\rm I}$, as shown in Figure 3.6, where we used the obtained
parameters for (A, B, C, and D), the aspect ratio ($h_{\rm gap}/r_{\rm gap}$) of 0.05, and the viscous parameter
of $\alpha_{\rm vis} = 10^{-3}$. A conservation relation derived from the measured $\Delta_{\rm I}$ and $\delta_{\rm I}$ can also be
obtained by assuming that the product of the gap depth and width conserves on the radial
intensity profile (i.e., $\Delta_{\rm I} \propto \delta_{\rm I}^{-1}$), as shown in the right panel of Figure 3.6. We obtain the
relation $\Delta_{\rm I} = 0.34 \pm 0.03 \, \delta_{\rm I}$ for $\Delta_{\rm I} = 0.19 \pm 0.01$ and $\delta_{\rm I} = 1.78 \pm 0.11$. The crossing point
between the two curves gives a planetary mass of 1.2 ± 0.1 M$_{\rm Saturn}$, which agrees well with
1.4 ± 0.2 M$_{\rm Saturn}$ derived from the analytic formula by Kanagawa et al. (2015, 2016) within the
uncertainties involved.

We assumed the viscous parameter, $\alpha_{\rm vis} = 10^{-3}$ for the above estimate. If we take $\alpha_{\rm vis}$ over
a wide range of $\alpha_{\rm vis} = 10^{-2} - 10^{-4}$, the derived planetary masses vary by a factor of ~ 3, and
are calculated to be $0.5 - 4.5$ M$_{\rm Saturn}$ for the analytic formula by Kanagawa et al. (2015, 2016)
and $0.5 - 2.7$ M$_{\rm Saturn}$ for the analytic formula by Zhang et al. (2018). Even considering the wide
range of $\alpha_{\rm vis}$, the planet mass is still similar to Saturn's mass. In addition, the gap location
($r = 12$ au) is close to Saturn's orbit, and T Tau N is an interesting example that is analogous
to the solar planetary system.

There are two other cases of gaps at $r \simeq 10$ au in the compact disks, indicating the presence
of planets: SR 4 (Zhang et al. 2018) and GQ Lup A (Long et al. 2020). Both cases indicate
upper limits of planet masses of $M_p \lesssim 7.2 \ M_{\mathrm{Saturn}}$ for SR 4 ($F_\nu = 69$ mJy at 1.3 mm; Andrews
et al. 2018a) and $M_p \lesssim 0.1 \ M_{\mathrm{Saturn}}$ for GQ Lup A ($F_\nu = 28$ mJy at 1.3 mm; Wu et al. 2017), by
using the the same manner as Zhang et al. (2018) taken from a gap width alone for $\alpha_{\mathrm{vis}} = 10^{-3}$
and $s_{\mathrm{max}} = 0.1$ mm. While there are a few samples of the inferred planet mass for the compact
disks at this stage, it could be a correlation between planet mass and (sub)millimeter disk flux
(or disk mass) in such disks, suggesting that more massive disks tend to produce more massive
planets (Lodato et al. 2019). Planets inferred to be forming in the larger DSHARP disks are
roughly in a Neptune mass group at the outer disk ($r > 10$ au) and in a Saturn-Jupiter mass
group at the inner disk ($r \simeq 10$ au) (see Fig.21 in Zhang et al. 2018), i.e., the planet mass could
be higher at smaller radii. Thus, investigating further the tendency for compact disks versus
large disks would lead to an intriguing study for understanding planet mass induced by disk
size.

According to the core accretion model of giant planets in a minimal mass solar nebula,
the optimal formation site is believed to be $r = 5 - 10$ au (Helled et al. 2014), although the
distance at which a giant gas planet can form could be greater than 10 au on the assumption of
pebble accretion (Lambrechts & Johansen 2012) or the maximum rate of planetesimal accretion
(Rafikov 2011). Investigations of such an inner $5 - 10$ au region for compact disk sources,
including our target with higher spatial resolution, is also of great interest, and could be very
valuable for comparing theoretical and observational studies.

3.6 Conclusions

By using the super-resolution imaging with sparse modeling, we investigated a young triple
system T Tau using ALMA 1.3 mm archival data. A summary of our findings is as follows:

1. The imaging drastically improves the spatial resolution on the continuum image of the T
   Tau system. We then find an annular emission gap in the T Tau N disk and two new
   emissions around T Tau Sa and Sb.

2. The effective spatial resolution of the image achieves $\sim 30\%$ (38×27 mas or 5×4 au)
   compared with the CLEAN beam size confirmed by tests evaluating the response to ar-
   tificial point source injections. This result is in good agreement with the prediction that
   interferometric imaging can use visibility amplitudes at maximum baselines for deriving
   source structures by $\sim 30\%$ (or 1/3) of the synthesized beam size.

3. Each position of the separated two emissions around T Tau Sa and Sb is in good agreement
   within their uncertainties, with each one predicted by the stellar orbital model in Köhler
   et al. (2016). In addition, each total flux roughly fits each SED predicted by an accretion
   disk model (Ratzka et al. 2009). The two emissions can thus be regarded as dust emissions
   originating from the circumstellar disks of T Tau Sa and Sb. The dust disk sizes of T Tau

Sa and Sb are smaller than 6×4 au (45×27 mas) and 7×3 au (50×22 mas), respectively. The total flux density of T Tau Sb is about seven times lower than T Tau Sa. This ratio implies that the actual disk size of T Tau Sb would be smaller than that of T Tau Sa when considering general scaling relations between disk properties (Tripathi et al. 2017; Andrews et al. 2018a; Hendler et al. 2020).

4. The T Tau N disk has a radius of 24 ± 4 au radius enclosing 95% of the total flux and has an annular gap at $r = 11.6 \pm 0.3$ au. Its total flux is as large as 174 mJy, comparable with that of much larger disks. The disk then shows the high brightness temperature of 257 ± 1 K at the peak and the low spectral index of 1.9 ± 0.1, suggesting the optically thick at 1.3 mm. The lower-limited dust surface density appears higher than the MMSN case locally at the outer ring, even though a majority of disks in the low mass star-forming regions generally appear less massive than the MMSN (Andrews 2015; Tazzari et al. 2017). The T Tau N disk, despite being a small dust disk, would be regarded to be more massive than regular disks. Meanwhile, given the relatively high values of Toomre Q parameter ($Q > 3$) at the outer ring, it appears to be gravitationally stable.

5. We considered a possibility for the origin of the gap in the T Tau N disk by using two different methods that connect the planetary mass and gap shape. If we take a viscous parameter over a wide range of $10^{-2} - 10^{4}$, the derived planetary masses are similar to Saturn's mass; $0.5 - 4.5$ M_{Saturn} for the analytic formula by Kanagawa et al. (2015, 2016) and $0.5 - 2.7$ M_{Saturn} for the analytic formula by Zhang et al. (2018).

participating in the *Gaia* Multilateral Agreement.

Software: AnalysisUtilities (`https://casaguides.nrao.edu/index.php?title=Analysis_Utilities`), Astropy (Astropy Collaboration et al. 2013), CASA (McMullin et al. 2007), DIFMAP (Shepherd et al. 1994), Matplotlib (Hunter 2007), PRIISM (Nakazato & Ikeda 2020), SciPy (Jones et al. 2001), least-squares fitting (Hammel & Sullivan-Molina 2020)

Appendix

A   Comparison between CLEAN and SpM Images
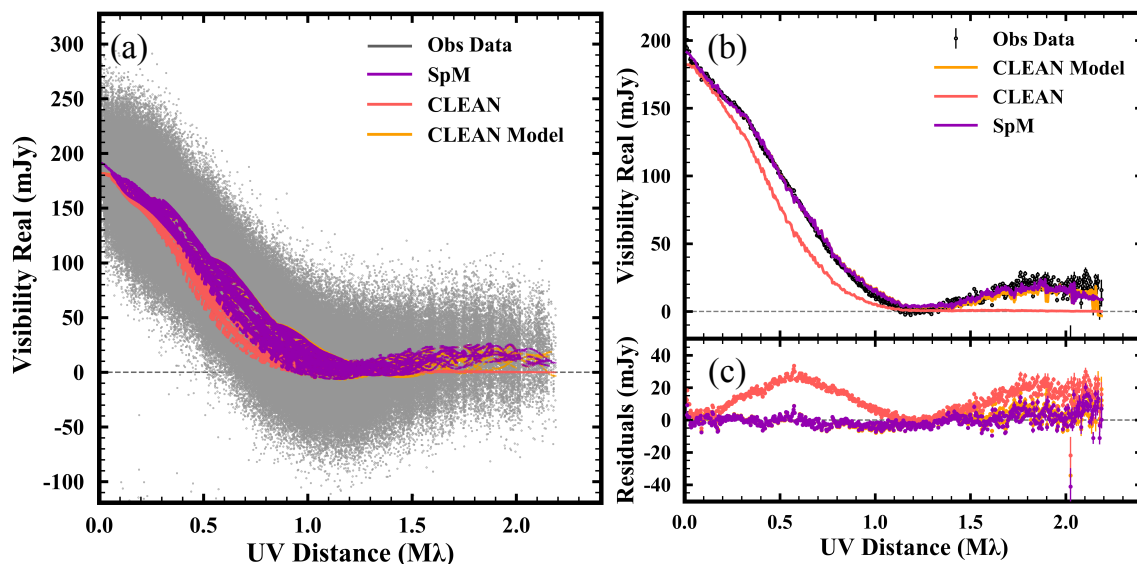
Figure A.1: (a) radial visibility profile gathered from radial visibilities in each azimuthal angle after deprojection in the $uv-$plane. This panel shows real parts of the visibilities for the SpM image (purple), the CLEAN image (rad), and the CLEAN model image (orange) together with the observational data (gray). (b) Binned and deprojected visibility profile in 3 kλ bins. (c) Residual visibilities between each model and the observations.

As shown in Fig.3.1, we have three images for the T Tau system: the beam-convolved CLEAN image (Fig. 3.1(c)), the CLEAN components or CLEAN model (Fig. 3.1(d)), and SpM (Fig. 3.1(b)). Here, we compare the three images in visibility domain and discuss which image can be the best used for image analyses.

Figure A.1 shows radial visibility profiles of the T Tau system calculated from the SpM image, the CLEAN model, and the beam-convolved CLEAN image together with the real part of observed visibilities. Here, the visibility of the beam-convolved CLEAN image is obtained from the Fourier transform of the final CLEAN image (see Fig.3.1(c)) by extracting the Fourier component that corresponds to the observed uv-sampling. The observed visibilities O and

modeled M are deprojected in the uv-plane using the following equations: $u' = (u \cos \mathrm{PA} - v \sin \mathrm{PA}) \times \cos i, v' = (u \cos \mathrm{PA} + v \cos \mathrm{PA})$, where i and PA denote the inclination and position angle derived from an ellipse fit to the outer ring of the T Tau N disk (see Appendix.D).

To evaluate the goodness of fits between the models and the observation, we calculated the reduced-χ^2. The formula is given by $\chi^2_{red} = N^{-1} \sum_{i=1}^{N} fW_i |O_i - M_i|^2$, where N is the total number of the visibilities and W_i is the weight of the $i-$th observed visibility O_i. The values of W_i are obtained in the measurement set of ALMA data. The factor f is the ratio between the weight and the standard deviation (stddev) of the visibility ($f = $stddev^{-2}/weight), which is reported to be $\sim 0.2 - 0.3$ in other disk observations (Hashimoto et al. 2021a,b). To estimate f of the T Tau data, we calculated the standard deviation of the real part of visibility in every 3 $k\lambda$ bins along the uv distance. We have obtained that $f = 0.29$. Finally, all the visibility models corresponding to the three images (CLEAN image, CLEAN model, and SpM) have resulted in the reduced χ^2 of around unity: 1.31 for the CLEAN image, 1.18 for the CLEAN model, and 1.18 for the SpM, respectively. Therefore, all the three images equally reproduces the visibility distribution in 2D uv-plane.

However, the situation changes when we consider azimuthally averaged visibility profiles. We have binned the visibility data every 3 $k\lambda$ of the uv-distance and have taken average in each bin (Figure A.1 (b, c)). The noise of the azimuthally averaged visibility is much smaller than the original 2D visibility. As a result, we found following two features; (1) The CLEAN model and the SpM image reproduce the observed visibility even after azimuthal average. (2) The visibility profile obtained from the CLEAN image significantly deviates from the observed visibility at $0.2 - 1.1$ Mλ and at $1.5 - 2.2$ Mλ. We expect that the deviation of the CLEAN image is caused by the convolution by the restoring beam. We therefore consider that either the CLEAN model or the SpM image better reproduces observations compared to the CLEAN image.

It is not possible to distinguish the CLEAN model and SpM image from the goodness of fit measured by the reduced-χ^2 values. However, we consider that the SpM image better reconstructs the disk surface brightness distribution. The CLEAN model reconstructs an image with a sum of a number of point sources (CLEAN components; Högbom 1974; Clark 1980). As a result, we see a patchy pattern in the CLEAN model image, which we consider irrelevant for disk structures. The SpM image shows more smooth structures than the CLEAN model and therefore seems more reasonable. Therefore, in this chapter, we mainly use the SpM image for image analyses. We do not yet have more quantitative measurements that can distinguish the SpM image from the CLEAN model image , and the bias that the SpM image may have is still an open question.

B   Selection of Optimum Image in SpM Imaging of T Tau N Disk

Figure B.1 shows 25 SpM images ($1''.6 \times 1''.6$) of the T Tau system and a closeup of T Tau N ($0''.5 \times 0''.5$), each of which corresponds to two sets of 25 SpM images of T Tau sys-

tem corresponding to 25 combinations of regularization parameters $(\Lambda_l, \Lambda_{tsv})$. We observe that the reconstructed disk structures change depending on the combination. We also show the visibility (real and imaginary parts) plots and calculated cross-validation error (CVE) with 1σ uncertainty. The optimal image is selected as one for $(\Lambda_l = 10^5, \Lambda_{tsv} = 10^9)$, giving the minimal CVE ($100.0000 \pm 0.13\%$). It is clearly seen that images with larger CVEs, i.e., $(\Lambda_l = 10^7, \Lambda_{tsv} = 10^7...10^{11})$ and $(\Lambda_l = 10^3...10^7, \Lambda_{tsv} = 10^{11})$ also show large deviations of model visibilities compared with observed data, especially at higher spatial frequencies. It should be noted that the annular gap structure of the T Tau N disk and the two separated emissions around T Tau Sa/Sb are commonly seen in images with a CVE of approximately 100.0%, for example, $(\Lambda_l = 10^4, \Lambda_{tsv} = 10^9)$ and $(\Lambda_l = 10^5, \Lambda_{tsv} = 10^8)$. This indicates that the presence of these structures is quite robust.

In contrast, the image for $(\Lambda_l = 10^5, \Lambda_{tsv} = 10^7)$ also yields a low CVE ($100.0012 \pm 0.13\%$), and the inner disk is likely to be more resolved than other images. As described in Section 4.4.2, the effective spatial resolution θ_{eff} is $0''.03$. The ratio of the T Tau Sa disk size to the CLEAN beam was obtained as $\sim 19\%$ for the image with $(\Lambda_l = 10^5, \Lambda_{tsv} = 10^7)$, which is smaller than θ_{eff} ($\sim 30\%$ of the CLEAN beam) for the optimal image with $(\Lambda_l = 10^5, \Lambda_{tsv} = 10^9)$. In a previous study, the SpM image allowed us to achieve a smaller beam size, that is, typically $\sim 30 - 40\%$ (Akiyama et al. 2017a,b; Kuramochi et al. 2018) compared to the corresponding CLEAN image (also see Chapter 2). The SpM image with such a "hyper" spatial resolution (i.e., beam smaller than 20% of the CLEAN beam) may reflect the presence of a small substructure in the inner disk, but it appears difficult to evaluate the feasibility. Therefore, we conclude that the optimal image selected from the cross-validation (CV) would be the best among the images in Figure B.1 in terms of spatial resolution improvement, and it is also the best for quantitative analysis.

C   Effective Spatial Resolution and Detection Threshold of SpM image

We performed two kinds of SpM imaging simulations. One is for estimating effective spatial resolution in the SpM imaging, and another is for evaluating the detection threshold. For both, we injected an artificial point source at $0''.4$ north in the observed data. We made the SpM images for $\Lambda_{tsv} = 10^7, 10^8, 10^9, 10^{10}$, and 10^{11} and fixed $\Lambda_l = 10^5$. For the effective spatial resolution purpose, we injected the point source with a flux density of 7.1 mJy (which corresponds to the total flux of the T Tau Sa disk). We fitted a two-dimensional Gaussian to the retrieved image of the point source. The obtained geometric mean of the source size of major and minor axis for each regularization parameter is plotted in Figure C.1. For detection threshold estimate, we change the flux density of the point sources, from 100 μJy to 1000 μJy in an increment of 100 μJy. We judged the detection in the image according to the criterion that the point source can be seen at the injected position with having a single source with roughly more than 90 % of the input flux density. The results are summarized in Figure C.2 together with I_{DT} estimated
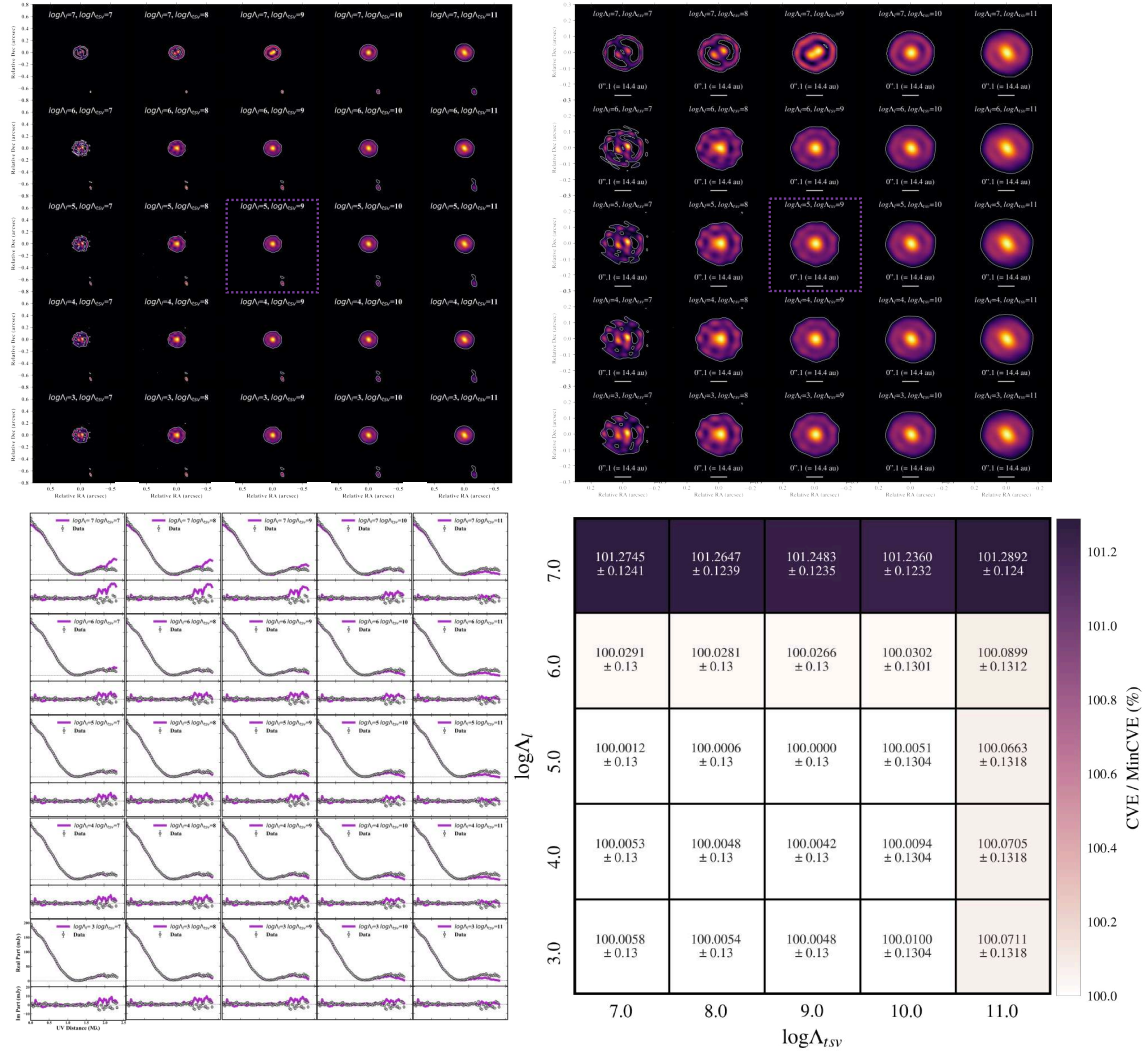
Figure B.1: SpM imaging of PPD T Tau system. Each panel corresponds to a gallery of 20 images with a combination of Λ_l and Λ_{tsv}. (upper left): SpM images. A wide field of view of $1''.6 \times 1''.6$ is adopted. The dashed line box indicates the optimal image $\left(\Lambda_l = 10^5, \ \Lambda_{tsv} = 10^9\right)$ selected by CV. (upper right): Close-up view of SpM images. A field of view of $0''.5 \times 0''.5$ is adopted. (lower left): Radial-visibility profile The upper and lower panels indicate the real and imaginary parts obtained from the observed data (gray color) and the Fourier transform of the SpM images (purple color). (lower right): CV errors (CVEs) and 1σ uncertainties. The CVEs are the residual values between the observed data and SpM data using the mean squared error. Outputs denote the CVEs normalized to the minimum value.

from beam-convolved image (Jy/beam, beam size; $\theta = 0''.14 \times 0''.10$). The RMS noise σ and CLEAN beam size for each robust parameter are summarized for comparison (see Figure C.2). The values of detection threshold for simulation in different Λ_{tsv} or I_{DT} can be compared with CLEAN cases, and we found that those correspond to roughly 4σ of the CLEAN image for `robust = 0.5` and are lower than 4σ level for `robust = −2` or $−1$. These results show that
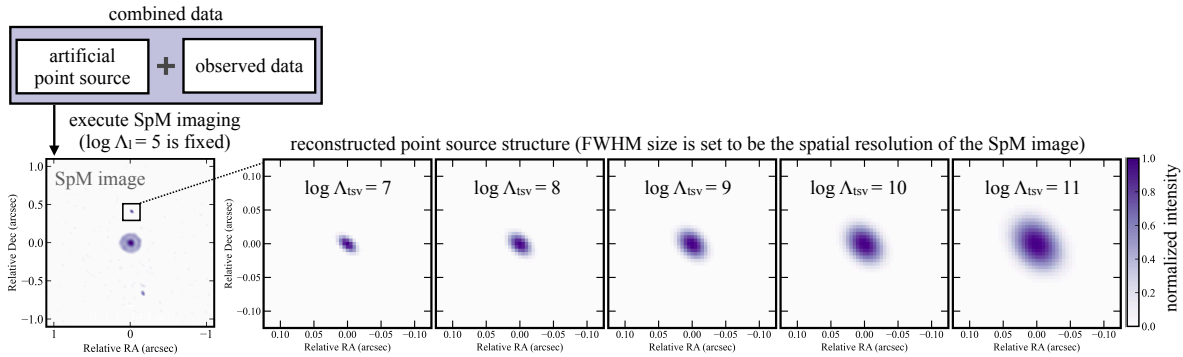
Figure C.1: Evaluation of effective spatial resolutions of the SpM images. The effective spatial resolution of the SpM image is evaluated in the way of an elliptical Gaussian fit to an artificial point source injected into $0''.4$ north in the observed data. Each resolution is tuned by the regularization parameter of Λ_{tsv} while the regularization parameter of Λ_l is fixed to be log $\Lambda_l = 5$.
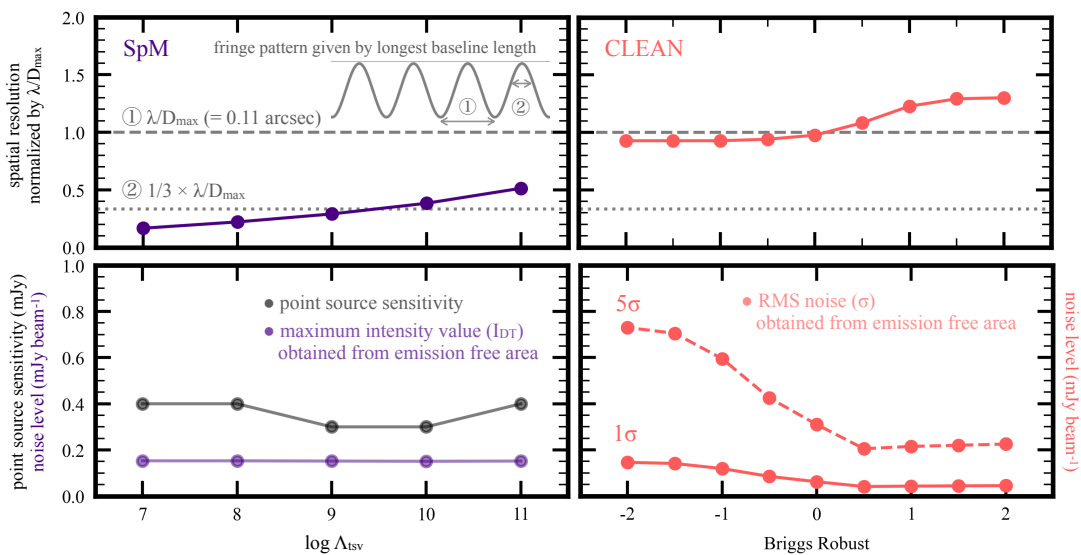
Figure C.2: Comparison of spatial resolutions and noise levels on the SpM (left side) and CLEAN (right side) images. Each resolution is plotted in the top panel as the geometric mean of the major and minor axes of beam (or point source, see Fig C.1) normalized by the diffraction-limited resolution $(\lambda/D_{max} = 0''.11)$ given by the maximum baseline length D_{max}. The left bottom panel indicates the point source sensitivity (gray color) in the SpM image set to be the threshold that the point source can be seen at the injected position with having a single peak with roughly more than 90 % of the input flux density. The results are summarized in the panel together with I_{DT} (purple color) estimated from beam-convolved image (Jy/beam, beam size; $\theta = 0''.14 \times 0''.10$). The right bottom panel shows the RMS noise σ of the CLEAN image for each `Brigss robust` parameter.

the SpM imaging can achieve super-resolution without significant degradation of point-source
sensitivity.

D   Disk Inclination and Position Angle of T Tau N

Figure D.1: Result of the best-fit ellipse to the
outer ring overlaid on the SpM image. The
black ellipse shows the best-fit model. The
purple curves show the distribution of solu-
tions considering the estimated 1σ error, while
the purple dots along the outer ring indicate
the radial averaged peak positions with an az-
imuthal angle spacing of $20°$. The outer peak
in the range of PA $= 165° \sim 220°$ cannot
be identified because of an insufficient angular
resolution or low signal-to-noise ratio, and it
was excluded from the fitting. To clearly iden-
tify the silhouette of the outer ring, the image
contour levels of $[1, 8, 9, 10, 12, 14, 16, 18, 20] \times$
I_{DT} were adopted.
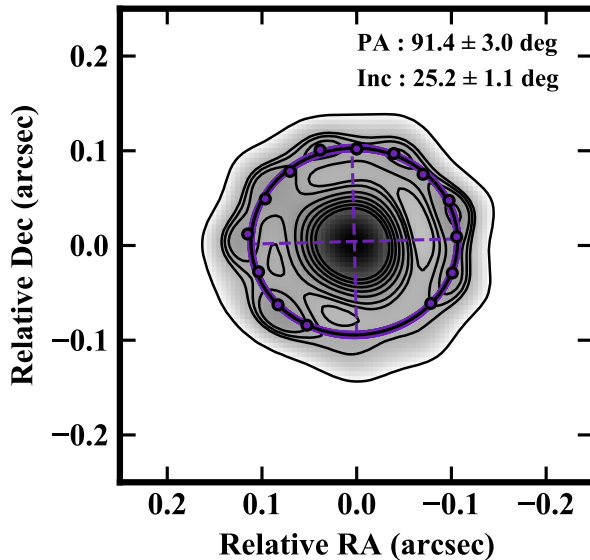
To derive the position angle (PA) and inclination of the T Tau N disk using the SpM image,
we performed an ellipse fit to the outer ring of the disk using least-squares fitting (Hammel &
Sullivan-Molina 2020) together with the Monte Carlo routine, as shown in Figure D.1. Here, we
assume that the outer ring is a perfect circle in face-on, and we estimated the inclination angle
from the aspect ratio of the ellipse.

First, we sampled the radial peak position of the outer ring on the PA profile every $1°$ in the
azimuthal angle θ. We averaged the peak position $r_{\mathrm{peak}}(\theta)$ and derived its standard deviation
$\sigma_{\mathrm{r}}(\theta)$ from the measurements within the azimuthal angle spacing $\Delta\theta$, and used them for the
ellipse fit. $\Delta\theta$ is set to be of the order of the major axis of the spatial resolution element $\theta_{\mathrm{eff,maj}}$
$(= 0''.038)$ in Section 3.4.1. Given that the radial peak positions are roughly located at a radius
of $r = 0''.1$ (estimated from visual inspection), the azimuthal angle spacing in degrees is thus
derived as $\Delta\theta \sim \theta_{\mathrm{eff,maj}} \times 360°/2\pi r \simeq 20°$.

Because the radial peak positions in the range of PA $= 165°-220°$ cannot be identified owing
to an insufficient angular resolution or low signal-to-noise ratio, these samples are excluded from
the use of the ellipse fit. To calculate the error of the fit, a Monte Carlo routine was performed
by randomly sampling the $\sigma_{\mathrm{r}}(\theta)$ deviation, and then $r_{\mathrm{peak}}(\theta)$ were added to them. 5000 iterative
calculations were performed, and the best-fit ellipse can be obtained from the average values of
the iterations. Uncertainties in each parameter of the ellipse fit were calculated by taking the
standard deviation found with the iterations. The best-fit results of the PA and inclination are

$91.4 \pm 3.0°$ and $25.2 \pm 1.1°$, respectively, as summarized in Table 3.3.

E   Spectral Index of T Tau N Disk

The spectral index α of the T Tau N disk was estimated using two spectral windows (spws) that were used for the continuum observations at Band 6, with center frequencies at $\nu_1 = 218$ GHz and $\nu_2 = 233$ GHz. Two CLEAN images were restored with the same beam size identical to that obtained at a lower frequency. Using the CLEAN maps, we obtained the total flux densities, F_1 and F_2 for $\nu_1 = 218$ GHz and $\nu_2 = 233$ GHz, respectively. The spectral index was calculated as $\alpha = \ln(F_1/F_2) \, / \, \ln(\nu_1/\nu_2)$, and was obtained as $\alpha = 1.9 \pm 0.1$. For the optically thick emission, the Rayleigh-Jeans limit gives $\alpha = 2$. For other PPDs in the Taurus, the typical α_{mm} values are below 3.0 and several of them are even below 2.0, as in the case of the T Tau N disk (e.g., Ricci et al. 2010; Akeson & Jensen 2014; Pinilla et al. 2014; Ribas et al. 2017; Zagaria et al. 2021). The obtained spectral index lower than the limit can be explained by considering the additional effect of dust self-scattering (Liu 2019; Zhu et al. 2019).

Chapter 4

ALMA Disk Substructure Survey with Super-resolution Imaging (ALMA Disk-3S) in the Taurus Star-forming Region

This work presented in this Chapter is a collaboration with Ryohei Kawabe, Takashi Tsukagoshi, Takayuki Muto, and Hideko Nomura. A publication is currently in preparation.

4.1   Chapter Overview

We present 1.3-mm sparse modeling (SpM) super-resolution images for 40 Class II protoplanetary disks in the Taurus star-forming region. The target disk sample is based on the Atacama Large Millimeter/Submillimeter Array (ALMA) archival Band 6 (1.3 mm) data, which were observed with a nominal resolution of less than $0''.1 - 0''.2$ and a relatively high signal-to-noise ratio (SNR). Here, we apply the SpM imaging technique to explore several au-scale substructures in compact and large disks with gaps and rings, which may evidence forming planets. The dust disk radii r_d widely range from 8 up to 200 au with a median of 45 au. Using the SpM images of the 40 disk sources, the statistical nature of this method, including the achievable effective spatial resolution and limitations on its applicability, was investigated, and SpM was found to achieve a better spatial resolution than the conventional CLEAN algorithm (i.e., $\sim 30 - 50\%$ of the CLEAN beam in size for half of the disk sample with a compact size and high SNR). This method drastically improves the spatial resolution of the images. The SpM images reveal 23 gaps, 29 rings, 30 inflections (suggesting unresolved gaps or other features), and four disks with a ring alone. The gap locations r_gap of the collected disks are at 5.5 to 131 au; the $r_\mathrm{gap}/r_\mathrm{d}$ value, which is the gap location normalized by the disk radius, is found to be approximately

0.1 and 0.4–0.7. Including disks of the Disk Substructures at High Angular Resolution Project (DSHARP), we find the stellar mass dependence of the gap size and then estimate planetary masses assuming the gaps are due to forming planets and by applying the theoretical method of gap-formation, which connects the planetary mass and gap properties. If we consider a viscous parameter over a wide range of $10^{-2} - 10^{-4}$, the stellar mass dependence of planetary mass in the outer disk regions ($r > 20$ au) can be observed for large disks. The majority of the inferred planets with a low-mass star (M–K type) appear to be Neptune-mass planets. Substructures, such as gaps and rings, are found to be common, even for compact Class II disks in the low-mass star-forming regions, and planetary masses inferred from gap properties are related to the stellar mass.

4.2   Introduction

Planets are formed in protoplanetary disks (PPDs) around young stars, which are composed of gas and dust (e.g., Hayashi et al. 1985). The structure and evolution of PPDs are thought to be closely linked to the formation process of planets in both core accretion and disk instability models (e.g., Johansen et al. 2007; Ida et al. 2013). Protoplanets with a sufficiently large mass can induce the formation of a gap in the disks (e.g., Lin & Papaloizou 1986; Takeuchi et al. 1996; Zhu et al. 2012; Pinilla et al. 2012). The minimum gap-opening mass depends on the viscosity and scale-height of the disk, and super-Earth-mass planets ($\sim 10\ M_\oplus$) can ideally produce detectable gaps in the (sub)millimeter regime (Rosotti et al. 2016; Zhang et al. 2018). Once the gap is spatially resolved, its width and depth can be used to estimate the mass of a growing planet (e.g., Kanagawa et al. 2015, 2016; Zhang et al. 2018). Meanwhile, several alternative explanations have been proposed for the origin of the gap; for instance, the effect of the snowlines of major volatiles (e.g., Zhang et al. 2015; Okuzumi et al. 2016), magneto-hydrodynamic effects (e.g., Flock et al. 2015), secular gravitational instability (e.g., Youdin 2011; Takahashi & Inutsuka 2014, 2016), and thermal wave instability (e.g., Watanabe & Lin 2008; Siebenmorgen & Heymann 2012; Ueda et al. 2019, 2021). The effectiveness of each proposed mechanism depends on the physical and chemical properties of the disks; the different mechanisms may work together in certain disks, or a dominant mechanism may differ among disks. Understanding the origin of substructures, such as gaps and rings, and their links to planet formation is currently a popular topic in this field.

In this study, using super-resolution imaging with sparse modeling (SpM), we present 1.3-mm SpM super-resolution images for 40 Class II protoplanetary disks in the Taurus star-forming region. The target disk sample is based on Atacama Large Millimeter/Submillimeter Array (ALMA) archival Band 6 (1.3 mm) data, which were observed with a nominal resolution of less than $0''.1 - 0''.2$ and a relatively high signal-to-noise ratio (SNR). Here, we apply the SpM imaging technique to explore several au-scale substructures, such as gaps and rings, in compact and large disks, which may evidence forming planets.

4.3   Source Selection
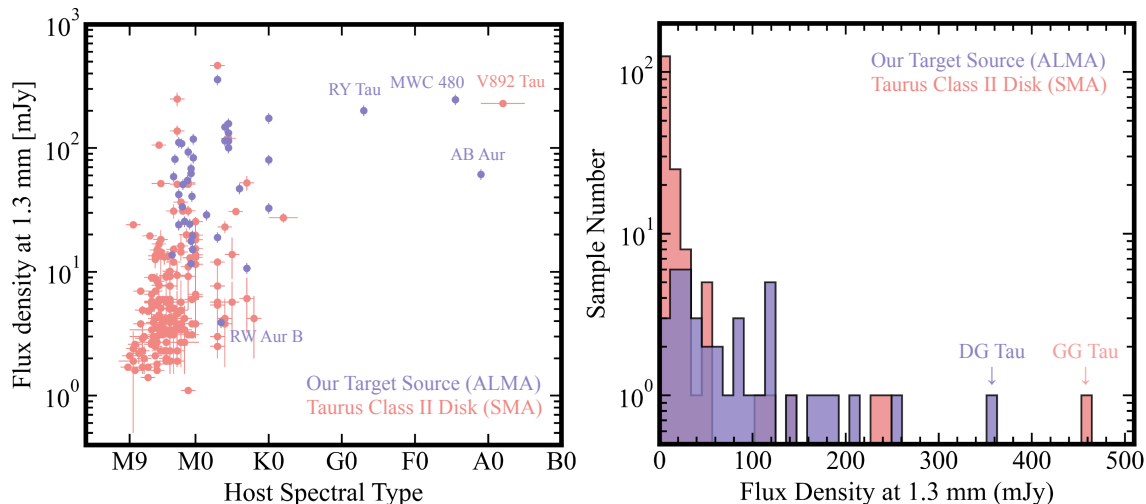
Figure 4.3.1: Left panel: Diagram of 1.3-mm flux density taken from Class II Taurus disks versus the spectral types of their stellar hosts in the Taurus low-mass star-forming region. Right panel: Histogram of 1.3-mm flux density taken from Class II Taurus disks. Our target sample (purple circles) is given by the total flux on the SpM image. For comparison, the flux densities of other Taurus Class II disks (gray circles) taken from Submillimeter Array (SMA) observations (Andrews et al. 2013) are also given. Our sample shows a bias toward disks with relatively high flux densities relative to the disks in total.

Our sample of 40 Class-II disks is based on the ALMA archival data with spatial resolutions higher than $0''.2$, in which the majority are disks observed in the survey by Long et al. (2019). Hence, our source selection mostly follows this survey. The initial source list was obtained from Class II disks in Andrews et al. (2013), which were selected from a sample of Class II disks identified in Spitzer observations by Rebull et al. (2010) and Luhman et al. (2010). Using this list, we first selected sources around stars with spectral types classified between M3 and A1 identified from Herczeg & Hillenbrand (2014). Although the excluded source list with types $M9 - M4$ is abundant in Taurus Class II disks, most of them were not observed with ALMA because their 1.3-mm emissions are faint (less than 10 mJy) (Andrews et al. 2013). Binaries with small separations of $0''.1-0''.5$ (White & Ghez 2001) were excluded because, at those separations, the binary interactions are expected to significantly decrease the disk size (e.g., Machida et al. 2008). However, two spectroscopic binaries (UZ Tau E and DQ Tau) were included in this sample because their closed spatial separations are not expected to affect the large-scale of disk structures (e.g., UZ Tau E is a binary with an ~ 0.03 au separation in Prato et al. (2002) and DQ Tau is a binary with a period of ~ 16 days in Tofflemire et al. (2017)). We also excluded stars with high extinction magnitudes $A_v > 3$ and stars with faint J-band magnitudes (e.g., V892 Tau; Long et al. 2021). This is because such stars appear to have inner edge-on disks, blocking the light from the central star. From these criteria, 51 stellar systems were listed. Subsequently, we gathered these systems as single and multiple stars from ALMA archival Band

6 data, excluding the following systems: nine systems observed with spatial resolutions lower than $0''.2$ (i.e., CW Tau, DE Tau, DP Tau, FX Tau, Haro 6–28, IS Tau, SU Aur, V955 Tau, and VY Tau), and three systems with SNRs of less than 30 (i.e., CX Tau, HQ Tau, and GK Tau) on the CLEAN images (it should be noted that these objects were imaged using SpM; however, the expected disk structure (ellipse-like structure), as observed in a CLEAN image, could not be reproduced). We finally selected 27 single stars, 12 primaries, and one companion star in binary or multiple systems; the companion star of the binary systems, RW Aur B, is included because this disk reveals an inner hole a few au in scale on the continuum image (see Section 4.5.1). The full list of 40 targets and their respective observed wavelengths and spatial resolutions are given in Table 4.4.1.

Figure 4.3.1 shows the 1.3-mm total flux density of Class II disks versus the spectral types of their stellar hosts in the Taurus region and a histogram of the total flux density. The relatively higher-mass stars ($M_* \simeq 1.5 - 2.5\ M_\odot$, G-F-A types) are rare, and their parent number was identified as merely four. In this study, three were obtained (RY Tau, MWC 480, and AB Aur). In contrast, lower-mass stars ($M_* \simeq 0.3 - 1.5\ M_\odot$, M-K type stars) dominate in the Taurus region, and more than 200 have been identified. Of these, 37 have been used in our sample. Note that the initial source list for M–K-type stars has a flux density lower than 10 mJy and our sample is biased to disks with higher flux densities ($F_\nu > 10$ mJy) relative to them.

4.4   Data Deduction and Imaging

4.4.1   Data Reduction and Imaging with CLEAN

All data were calibrated, and each image was constructed in the same unified manner. The data were initially calibrated with the ALMA pipeline reduction scripts taken from the ALMA archive. Note that several images created from long-baseline data alone can be affected by resolving dust emission around the largest scales of the disk. Thus, long-baseline observations were combined with more compact configuration ALMA data from other projects to avoid this problem and maximize sensitivity to the extended emission scale (a list of combined datasets is presented in Table 4.4.1). Before combining data from different observations (i.e., data with a different ALMA "project" code/codes), the positional offset between the phase (map) center and emission peak of the target source was adjusted using the `CASA` task `fixvis`. After the coordinates of each dataset were centered, the fluxes of two datasets (i.e., the long and short baselines) were re-scaled by following a similar procedure to Andrews et al. (2018b): we compared two overlapping datasets on the deprojected visibility profile and calculated a re-scaling factor. One of the two datasets was then re-scaled using the task `gencal`. After re-scaling the flux, the different executions were combined into a single dataset.

First, the data were imaged with the `tclean` task (hereafter referred to as CLEAN) by adopting Briggs' weighting (`robust = 0.5`) in version 6.1.0 of the Common Astronomy Software Applications package (`CASA`; McMullin et al. 2007). Here, two CLEAN algorithms were

applied depending on the disk structure. On the initial CLEAN image, the Cotton–Schwab algorithm (Schwab 1984) was applied to the compact disk in which no substructure (i.e., a gap or inner hole) was confirmed, whereas a multi-scale multi-frequency deconvolution algorithm (Rau & Cornwell 2011) was applied to the large disk in which substructures were detected.

To improve the SNR of the image by correcting a systematic gain error (e.g., antenna-based and baseline-based errors), we performed self-calibration for all datasets except for DM Tau. Kudo et al. (2018) identified that the phase root mean square (RMS) of the shorter-baseline data of DM Tau is relatively low, and gain phase self-calibration does not significantly improve. For targets with initial SNR $>$ 100 in the CLEAN image, we performed two rounds of phase (down to the integration time, `calmode = p`) and one round of amplitude&phase (`calmode = ap`) self-calibration. For targets with an initial SNR $<$ 100, we applied one round of phase and one round of amplitude & phase self-calibration. Finally, we obtained the CLEAN image (= CLEAN model convolved with CLEAN beam + residual map) after self-calibration with the SNR improved by several times compared with the initial image. Each CLEAN beam size $\theta_{\rm cl}$, peak intensity, and RMS noise level $\sigma_{\rm cl}$ (collected noise value from the dust emission-free area) is listed in Table 4.4.1.

4.4.2   Imaging using Sparse Modeling

We briefly describe the performed SpM (ℓ_1+TSV) imaging and the cross validation (CV) scheme, which was used to select the most feasible SpM image. In this study, the self-calibrated visibility data were adopted for image reconstruction using the latest SpM imaging task, `PRIISM`, ver.0.3.0 and 0.7.2 (Nakazato & Ikeda 2020) in conjunction with `CASA`. The image was reconstructed by minimizing a cost function in which two convex regularization terms of the brightness distribution, ℓ_1-norm and the total squared variation (TSV), were utilized with the chi-squared error term. The two regularizers adjust the sparsity and smoothness of the reconstructed image, as controlled by the positive variables Λ_l and Λ_{tsv}, respectively. The effective resolution mainly depends on the regularization parameters, especially the TSV term; the smaller the value of Λ_{tsv}, the better the spatial resolution.

In this study, we used 10-fold CV implemented in `PRIISM` and searched for the optimal parameter set of two regularization parameters, Λ_l and Λ_{tsv}. In imaging using `PRIISM`, we used non-uniform fast Fourier transform (NuFFT) algorithms to compute the Fourier transform and iteratively fit the model to visibility data ($N_{\rm iter} = 1000$) until the iteration algorithm converges. Finally, we obtained 25 images corresponding to 25 different sets of (Λ_l and Λ_{tsv}) with different parameter values for each order of magnitude. The wide range of parameter space was selected via pre-tuning to avoid missing the optimal image and ensure it can be found near the center of the image matrix. The values and ranges can be tuned according to the target source properties in `PRIISM`. In previous studies, an image with the minimum CVE (or its surroundings) was favored as the optimal image (Akiyama et al. 2017a,b; Kuramochi et al. 2018). Therefore, we adopted images with the minimum CVE for most of the datasets. Meanwhile, for datasets with relatively lower SNRs ($\sim 100 - 200$), CV tends to select blobby

disk structures in images of V409 Tau, HO Tau, DN Tau, GO Tau, HP Tau, CIDA 9A, DS Tau, and IP Tau. Therefore, we did not adopt those images and instead used images that increase $\log \Lambda_{\mathrm{tsv}}$ to $1-2$ (corresponding to degradation of the spatial resolution). Note that each CVE on the adopted parameter is within the 1σ error on each parameter of the minimum CVE. For the dataset of HP Tau with an SNR that is relatively higher (SNR $= 460$) on the CLEAN image, an annular gap structure was detected in $(\log \Lambda_{\mathrm{l}} = 6, \log \Lambda_{\mathrm{tsv}} = 9)$ near the parameter selected by the minimum cross validation error (CVE) $(\log \Lambda_{\mathrm{l}} = 5, \log \Lambda_{\mathrm{tsv}} = 10)$. We adopted the images of $(\log \Lambda_{\mathrm{l}} = 6, \log \Lambda_{\mathrm{tsv}} = 9)$ as an optimal image because the CVE of this parameter fits within the 1σ error of the parameter selected by the minimum CVE.

Next, we evaluated the effective spatial resolution θ_{eff} of the optimal SpM image. In the same manner as in Chapter 3, we injected an artificial point source into the observed data in the visibility domain. We performed SpM imaging with the same regularization parameters as the optimal image and other sets of parameters. The SpM images evaluated the effective resolution with an elliptical Gaussian fit to the point source. Each input flux density of the point source is 5% or 10% of the total flux of each target source, and each reconstructed image for the optimal parameter provides the FWHM size (i.e., the effective spatial resolution) of the point source θ_{eff} and recovers a total flux within a $10-30\%$ error compared with the input value. The injection of the point source was performed within the maximum recoverable scale in the emission-free region and was conducted from the phase center to the north. We trialed the injection of sources to the east, west, and south to ensure that each FWHM size of the reconstructed source was within an error of a few percent compared with that in the north direction.

Table 4.4.1:: Disks Sample and CLEAN/SpM Image Properties.

Name (1)	ALMA Project IDs (2)	Frequency (GHz) (3)	CLEAN Beam θ_{cl} (mas, PA) (4)	SpM Beam θ_{eff} (mas, PA) (5)	CLEAN RMS σ_{cl} (mJy asec^{-2}) (6)	SpM I_{DT} (mJy asec^{-2}) (7)	Peak I_c (CLEAN, SpM) (mJy asec^{-2}), (8)	F_ν (CLEAN, SpM) (mJy) (9)	$\log\Lambda$, $\log\Lambda_{tsv}$ (10)
AB Aur	2015.1.00889.S, 2019.1.00579.S	225	49 × 24 (22.3°)	63 × 38 (18.9°)	8.81	14.44	727.85, 314.03	46.7, 61.3	4, 15
GM Aur	2017.1.01151.S, 2018.1.01230.S	260	52 × 30 (3.3°)	27 × 18 (3.2°)	8.84	108.38	634.42, 726.99	188.2, 148.4	5, 13
CI Tau	2016.1.01164.S, 2016.1.01370.S	229	58 × 45 (14.1°)	40 × 30 (18.3°)	5.11	32.52	1300.94, 1529.69	118.0, 100.8	5, 14
LkCa 15	2018.1.01255.S, 2018.1.00945.S	224	54 × 42 (7.9°)	38 × 32 (3.9°)	6.41	31.88	250.83, 275.4	114.4, 113.8	4, 12
DL Tau	2016.1.01164.S	225	140 × 121 (9.6°)	93 × 83 (12.8°)	2.62	18.34	702.6, 1069.87	159.1, 157.5	4, 12
Haro 6-37 C	2013.1.00105.S	237	184 × 159 (7.8°)	110 × 97 (−3.4°)	3.19	31.02	561.9, 1072.36	99.5, 93.0	4, 10
AA Tau	2013.1.01070.S, 2016.1.01205.S	241	101 × 67 (40.3°)	85 × 64 (36.2°)	2.85	21.59	231.46, 244.78	76.0, 68.2	5, 14
GO Tau	2016.1.01164.S	225	143 × 103 (−15.5°)	130 × 109 (−24.5°)	3.11	11.97	452.3, 504.47	37.6, 42.2	5, 13
MWC 480	2016.1.01164.S	225	163 × 104 (22.2°)	80 × 58 (30.9°)	2.83	41.83	1529.74, 2415.1	251.5, 246.2	4, 11
IQ Tau	2016.1.01164.S	225	192 × 160 (−4.4°)	132 × 114 (−13.8°)	2.97	18.61	267.57, 344.9	59.3, 54.9	4, 12
DM Tau	2013.1.00498.S, 2017.1.01460.S	224	35 × 23 (24.7°)	43 × 35 (7.1°)	13.27	23.92	405.44, 340.36	361, 58.9	5, 15
UZ Tau E	2016.1.01164.S	225	133 × 123 (3.1°)	62 × 59 (−11.2°)	2.64	30.6	520.1, 786.21	122.9, 109.1	5, 11
DS Tau	2016.1.01164.S	225	163 × 98 (−18.8°)	110 × 69 (−23.4°)	2.65	14.42	173.56, 321.85	19.7, 19.6	5, 12
CY Tau	2013.1.00498.S	224	239 × 64 (−0.9°)	104 × 89 (−5.8°)	1.71	30.62	490.78, 869.1	111.5, 111.3	4, 10
CIDA 9 A	2016.1.01164.S	225	130 × 114 (4.3°)	91 × 83 (8.1°)	2.81	21.8	177.88, 266.16	33.7, 33.6	5, 12
RY Tau	2016.1.01164.S, 2017.1.01460.S	225	51 × 30 (20.5°)	34 × 22 (23.5°)	22.16	117.26	1595.05, 1864.24	204.2, 200.7	5, 13
DN Tau	2016.1.01164.S	225	137 × 114 (3.1°)	91 × 80 (10.0°)	2.83	12.66	747.62, 1240.68	83.8, 83.3	5, 12
DR Tau	2016.1.01164.S	225	132 × 101 (41.7°)	51 × 41 (43.7°)	3.15	120.97	1369.86, 2678.85	117.7, 114.6	5, 10
DG Tau	2015.1.01268.S, 2016.1.00846.S	232	36 × 27 (−5.7°)	20 × 16 (1.6°)	11.31	124.65	5877.71, 8773.88	360.2, 357.2	6, 13
UX Tau A	2013.1.00105.S	237	181 × 158 (3.1°)	76 × 71 (−33.7°)	3.43	84.69	337.74, 743.42	82.6, 80.2	4, 9
V710 Tau A	2016.1.01164.S	225	163 × 132 (44.5°)	76 × 60 (38.5°)	2.15	40.46	423.22, 723.06	51.7, 51.0	5, 11
FT Tau	2016.1.01164.S	225	149 × 129 (−17.8°)	67 × 58 (21.9°)	2.55	28.47	617.47, 1093.16	83.2, 81.4	5, 11
DQ Tau	2016.1.01164.S	225	131 × 99 (42.3°)	50 × 39 (48.8°)	3.13	101.73	1509.73, 3452.9	64.7, 62.4	5, 10
V409 Tau	2016.1.01164.S	225	181 × 139 (35.1°)	117 × 90 (43.2°)	2.11	9.83	232.61, 406.9	18.4, 17.7	5, 12
BP Tau	2016.1.01164.S	225	184 × 125 (−34.0°)	105 × 73 (−26.5°)	1.95	10.89	271.65, 304.99	41.4, 40.8	5, 12
IP Tau	2016.1.01164.S	225	147 × 116 (−19.7°)	80 × 76 (−6.8°)	2.16	17.41	75.69, 139.81	11.2, 11.7	5, 12
DO Tau	2016.1.01164.S	225	144 × 106 (−21.5°)	69 × 59 (−20.9°)	2.97	41.54	1321.45, 1940.07	119.5, 118.3	5, 11
Haro 6-13	2016.1.01164.S	225	139 × 112 (−4.4°)	53 × 44 (−4.0°)	2.86	129.91	1898.27, 4008.4	137.2, 132.4	5, 10
HO Tau	2016.1.01164.S	225	191 × 135 (−55.2°)	55 × 42 (−53.4°)	1.86	0.0	218.48, 501.6	16.4, 13.7	6, 11
V836 Tau	2016.1.01164.S	225	168 × 127 (−27.6°)	67 × 53 (−17.0°)	2.4	7.08	425.52, 639.98	25.0, 24.4	5, 11
HK Tau A	2016.1.01164.S	225	132 × 115 (−2.2°)	66 × 60 (7.7°)	2.84	214.46	698.09, 1470.62	31.8, 25.5	5, 11
G1 Tau	2016.1.01164.S	225	145 × 128 (−12.2°)	78 × 60 (−12.5°)	2.38	22.31	250.98, 364.11	15.3, 15.1	5, 11
RW Aur A	2016.1.01164.S, 2017.1.01631.S	224	40 × 22 (14.6°)	20 × 14 (14.0°)	9.24	66.79	3573.07, 6295.08	33.0, 32.7	6, 13
T Tau N	2016.1.01164.S	225	140 × 100 (34.1°)	38 × 27 (45.3°)	2.56	272.2	3952.76, 9145.97	175.0, 174.4	5, 9
HP Tau	2016.1.01164.S	225	138 × 112 (−4.1°)	29 × 25 (−7.2°)	2.89	0.0	1324.81, 3790.23	49.0, 47.0	6, 9
DH Tau A	2016.1.01164.S	225	146 × 118 (−30.7°)	73 × 61 (−20.9°)	2.7	42.46	508.33, 800.86	24.2, 24.0	5, 11
HN Tau A	2016.1.01164.S	225	150 × 110 (43.4°)	36 × 27 (50.1°)	2.34	0.0	378.87, 1429.93	11.5, 10.7	6, 10
DK Tau A	2016.1.01164.S	225	137 × 115 (7.0°)	46 × 42 (17.9°)	2.63	116.03	747.64, 1520.14	29.0, 28.8	5, 10
RW Aur B	2016.1.01164.S, 2017.1.01631.S	224	40 × 22 (14.6°)	20 × 14 (14.0°)	9.24	39.47	505.23, 754.8	4.0, 3.9	6, 13
UY Aur A	2016.1.01164.S	225	154 × 100 (−16.3°)	45 × 31 (−14.4°)	2.72	76.22	932.55, 5490.32	18.7, 19.0	5, 9

Note. — Column description: (1) Name of host star. The names are ordered by the au-scale size of the dust disks from top to bottom. (2) Observed frequency. All target sources are taken from Band 6 observations. (4) CLEAN beam θ_{cl}. **Brigss robust** parameter was set as 0.5. (5) SpM beam θ_{eff}. The beam size (effective spatial resolution) of each image is taken from a point source simulation. (6) RMS noise σ_{cl} of the CLEAN image. The value is derived from the emission-free area. (7) Detection threshold I_{DT} of the SpM image. The value is derived from the peak value in the emission-free area. (8) Peak intensity of each CLEAN and SpM image. (9) Total flux F_ν of each CLEAN and SpM image. The flux is taken from the total value above $5\sigma_{cl}$ for CLEAN or I_{DT} for SpM. (10) Two regularization parameters ($\log\Lambda_l$, $\log\Lambda_{tsv}$) adopted for each SpM image.

4.5   Results

4.5.1   Reconstructed Images in CLEAN and SpM

Figure 4.5.1 and 4.5.2 show 40 images from Taurus Class II disks, reconstructed using CLEAN
and SpM, respectively. Table 4.4.1 lists the image properties of sample disks. As shown in
Table 4.4.1, the total fluxes of the sources obtained from the SpM image above the I_{DT} level
are generally consistent with the values obtained from the CLEAN image above $5\sigma_{\mathrm{cl}}$ levels. The
effective resolution values of the SpM images are given in Table 4.4.1, which achieves $30-50\%$
of CLEAN beams for half of the datasets (see Section 4.5.3 in details). The SpM image spatially
resolves the disk structure for all target sources, and annular gap structures (UZ Tau E, RY Tau,
DR Tau, FT Tau, T Tau N, and HP Tau) and inner holes (RW Aur B) have been found in several
sources, although the CLEAN images do not resolve them. In Chapter 3, we demonstrated that
SpM reproduces a high-fidelity image that better fits the observed visibilities than the CLEAN
image for the T Tau system. The SpM images of other sources also appear to better reconstruct
the disk surface brightness distribution than the CLEAN images. Therefore, in the following
sections, we use the SpM image to derive the physical properties of the disks.

4.5.2   Dust Disk Size

We derived the dust disk radius r_{d} in each SpM image using a curve-of-growth method similar
to Ansdell et al. (2016); Huang et al. (2018). First, we derived the inclination (i) and position
angle (PA) of each disk in the image domain by fitting two methods: an ellipse-fitting to the
outer ring for disks with an outer ring, and a two-dimensional (2-D) Gaussian-fitting for disks
with no clear outer ring. The Gaussian-fitting was applied for disks that were incompatible with
the ellipse-fitting due to lower SNRs, not exhibiting a ring, or an insufficient spatial resolution
along the projected minor axis. The measurements and used method for all disks are listed in
Table 4.5.1. The disk radius was measured with successively larger photometric apertures on
a deprojected image and settled on the point where the slope of the curve on the relationship
between the measured aperture radius and flux becomes constant. Figure 4.5.3 shows a list of
the dust disk radii in our sample, which indicates that there is no bias in the disk size.

The minimum disk radius of UY Aur A is 8 au, and the maximum disk radius AB Aur
extends to 214 au. Using our sample, we derived a median disk radius of 45 au and set this
value to be the boundary between "compact" and "large" disks for later analysis of the difference
between the two types of disks (see Section 4.5.3 and 4.5.4). Note that faint disks with 1.3-mm
fluxes below 10 mJy, which are excluded from our sample but are dominant in the Taurus region,
should have a dust radius smaller than $30-40$ au owing to the mm flux versus disk radius scaling
relation ($L_{\mathrm{mm}} \propto r_d^2$; Tripathi et al. 2017; Andrews et al. 2018a). Note that our sample selection
takes a measurement bias, and the inclusion of faint compact disks in our sample should decrease
the median disk radius.
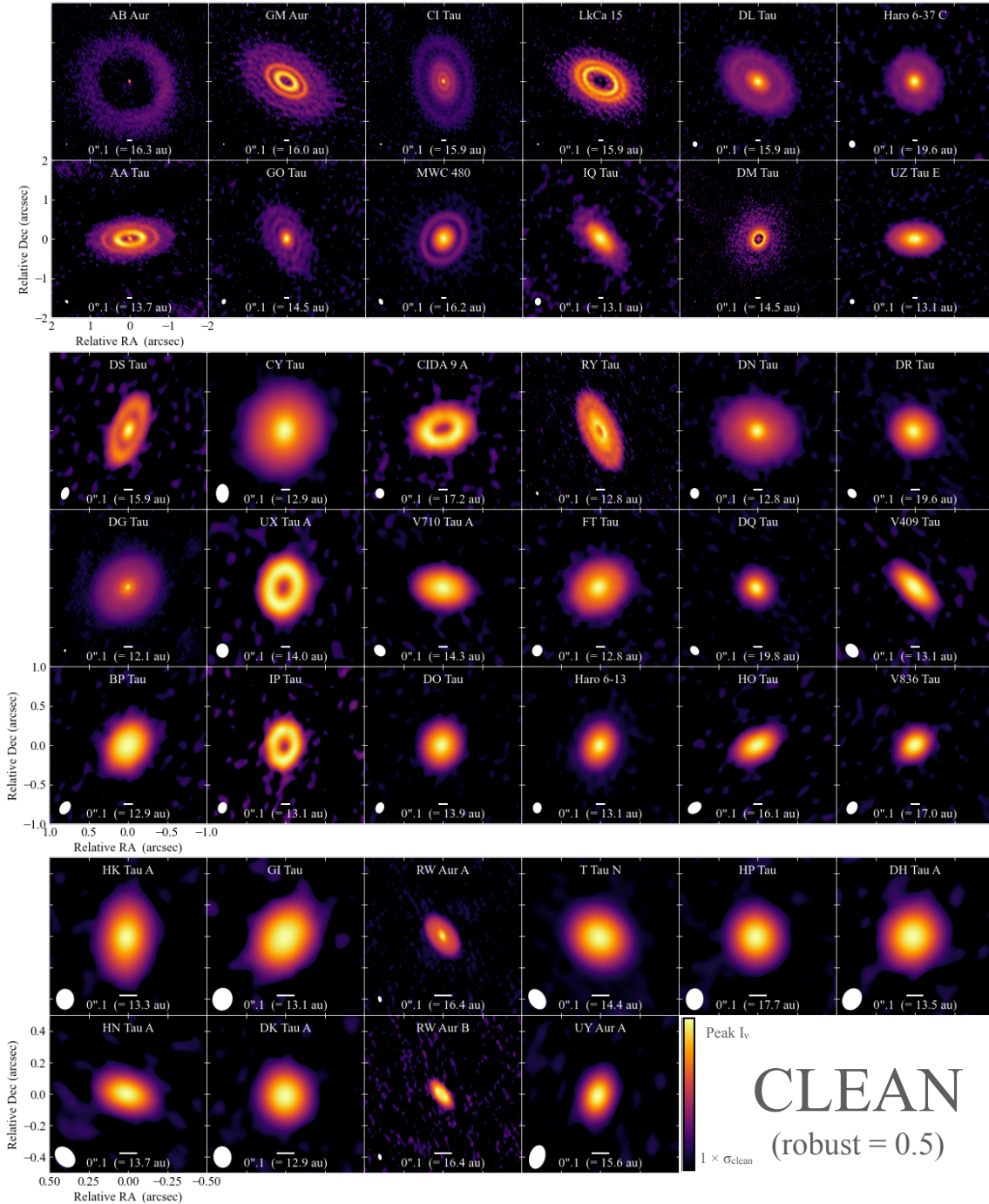
Figure 4.5.1: Gallery of CLEAN images for 40 disks in our sample. Briggs weighting with a robust parameter of 0.5 was adopted for all images. These images are ordered by decreasing dust disk size from left to right and top to bottom. The same color scale given by a power law with a scaling exponent of $\gamma = 0.45$ is adopted. The maximum and minimum color scales for each image are the peak value and RMS noise (σ_{cl}), respectively. A white bar of $0.''1$ is provided as reference to angular scales. The white filled ellipse in the bottom left corner denotes the synthesized beam.
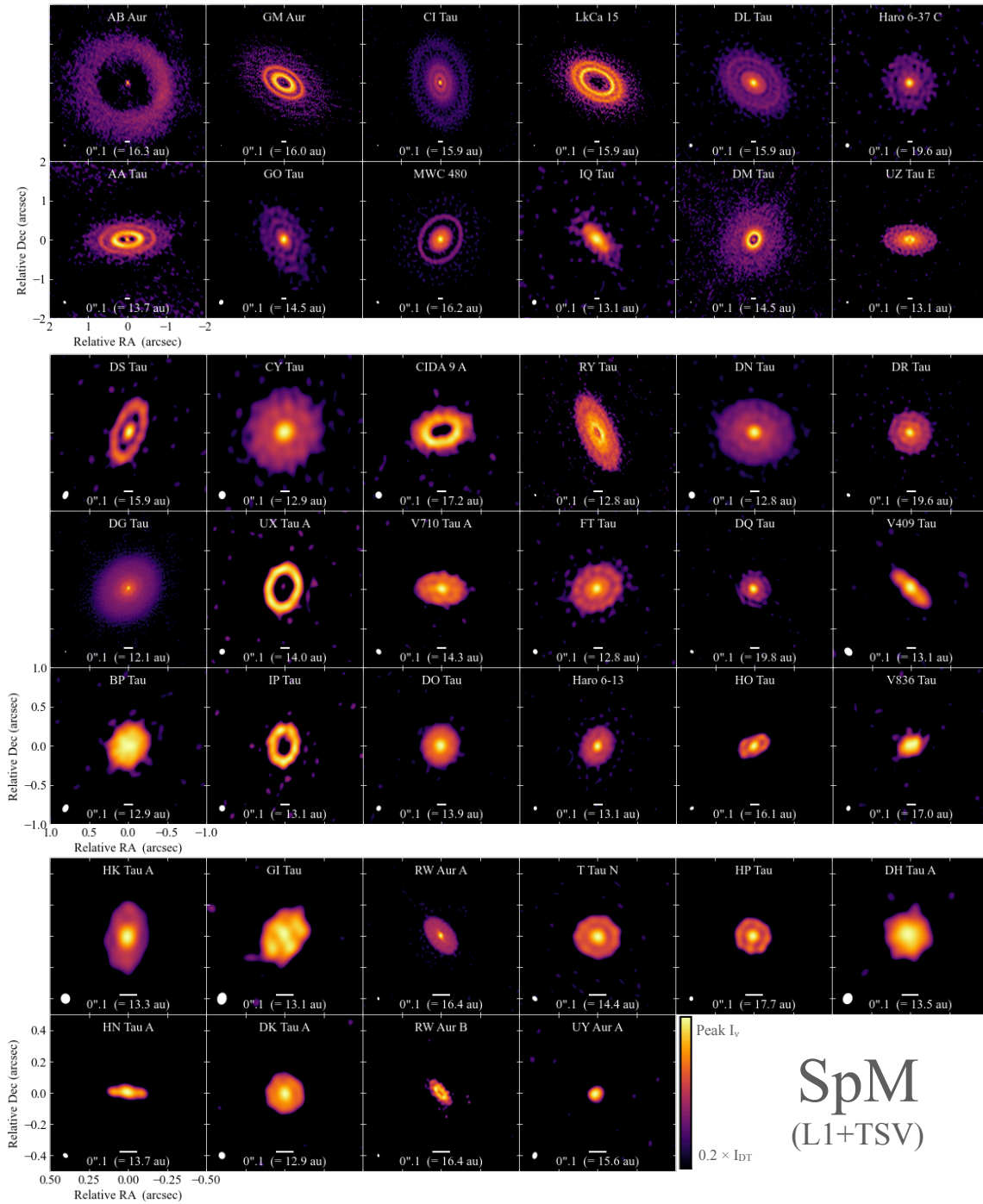
Figure 4.5.2: Gallery of SpM images for 40 disks in our sample. The same color scale given by a power law with a scaling exponent of $\gamma = 0.45$ is adopted. These images are ordered by decreasing dust disk size from left to right and top to bottom. The maximum and minimum color scales for each image are the peak value and 0.2 times detection threshold (σ_{DT}), respectively. A white bar of $0.''1$ is provided as reference to the angular scales. The white filled ellipse in the bottom left corner denotes the effective spatial resolution.

Table 4.5.1. Disks Sample and CLEAN/SpM Image Properties.

| Name	d (pc)	SpT	Luminosity ($L_\odot$)	Stellar Mass ($M_\odot$)	Disk Radius (au, arcsec)	Inc (deg)	P.A. (deg)	Method
(1)	(2)	(3)	(4)	(5)	(6)	(7)	(8)	(9)
AB Aur	162.9	A1.0	33.20	1.84	214 (1.31)	23.2	-36.0	Ref
GM Aur	159.6	K6.0	0.64	0.84	183 (1.14)	53.8	57.8	E
CI Tau	158.7	K5.5	0.81	0.89	178 (1.12)	50.1	11.8	E
LkCa 15	158.9	K5.5	0.79	0.97	168 (1.06)	50.6	61.8	E
DL Tau	159.3	K5.5	0.65	0.98	141 (0.89)	43.7	52.5	E
Haro 6-37 C	195.7	M1.0	0.56	0.45	138 (0.71)	21.5	18.6	E
AA Tau	137.2	M0.6	0.42	0.45	138 (1.0)	60.0	94.0	E
GO Tau	144.6	M2.3	0.21	0.34	129 (0.89)	54.5	24.8	E
MWC 480	161.8	A4.5	17.38	1.91	121 (0.75)	36.6	-31.4	E
IQ Tau	131.3	M1.1	0.22	0.50	99 (0.76)	61.0	42.8	G
DM Tau	145.1	M3.0	0.14	0.35	92 (0.63)	37.0	-22.2	E
UZ Tau E	131.2	M1.9	0.35	1.23	85 (0.65)	55.6	90.4	E
DS Tau	159.1	M0.4	0.25	0.58	69 (0.43)	63.4	-19.5	E
CY Tau	128.9	M2.3	0.25	0.38	67 (0.52)	26.8	151.4	G
CIDA 9 A	171.9	M1.8	0.20	0.43	63 (0.37)	44.0	105.0	E
RY Tau	128.2	F7	12.30	2.04	62 (0.48)	65.4	23.5	E
DN Tau	128.2	M0.3	0.70	0.52	59 (0.46)	32.2	83.2	E
DR Tau	195.7	K6	0.63	0.93	51 (0.26)	6.4	161.9	G
DG Tau	121.2	K7.0	0.38	0.64	51 (0.42)	33.5	135.6	G
UX Tau A	139.9	K0.0	0.51	1.30	45 (0.32)	42.9	-13.8	E
V710 Tau A	142.9	M1.7	0.26	0.42	45 (0.32)	52.2	0.2	G
FT Tau	127.8	M2.8	0.15	0.34	44 (0.35)	34.2	124.7	E
DQ Tau	197.7	M0.6	1.17	1.61	41 (0.21)	20.5	4.4	G
V409 Tau	131.4	M0.6	0.66	0.50	40 (0.31)	68.9	44.8	E
BP Tau	129.1	M0.5	0.40	0.52	38 (0.3)	38.0	151.7	E
IP Tau	130.6	M0.6	0.34	0.52	36 (0.27)	45.0	-5.5	E
DO Tau	139.4	M0.3	0.23	0.59	36 (0.26)	27.3	170.3	E
Haro 6-13	130.5	K5.5	0.79	0.91	34 (0.26)	42.4	151.5	G
HO Tau	161.4	M3.2	0.14	0.30	32 (0.2)	54.9	118.6	G
V836 Tau	169.6	M0.8	0.44	0.48	31 (0.18)	43.0	117.4	E
HK Tau A	133.3	M1.5	0.27	0.44	27 (0.21)	53.8	175.0	G
GI Tau	130.5	M0.4	0.49	0.52	24 (0.18)	43.9	142.6	E
RW Aur A	163.5	K0	0.99	1.20	22 (0.14)	55.2	38.6	G
T Tau N	143.7	K0	6.82	2.19	20 (0.14)	25.6	91.0	E
HP Tau	177.1	K4.0	1.30	1.20	20 (0.11)	22.1	61.7	E
DH Tau A	135.4	M2.3	0.20	0.37	19 (0.14)	13.6	22.4	G
HN Tau A	136.6	K3	0.16	1.53	16 (0.11)	71.3	85.4	G
DK Tau A	128.5	K8.5	0.45	0.60	15 (0.12)	17.1	176.2	G
RW Aur B	163.5	K6.5	0.60	0.81	14 (0.09)	64.6	43.4	E
UY Aur A	155.6	K7.0	1.05	0.65	8 (0.05)	28.6	127.4	G

Note. — Column description: (1) Name of host star. The names are ordered by the au-scale size of the dust disks from top to bottom. (2) The distance of individual stars is adopted from *Gaia* DR2 parallax (Gaia Collaboration et al. 2018). Long et al. (2019) evaluated the Gaia parallaxes of the 29 closest Taurus members to RY Tau, computing an average Gaia distance of 128.2 pc. We adopted this distance for RY Tau. (3), (4) The spectral type and stellar luminosity are adopted from Herczeg & Hillenbrand (2014), and the luminosity is updated to the *Gaia* distance. (5) Stellar mass is taken from Long et al. (2019); Wallace et al. (2020). (6) The disk radius is derived from the SpM image for each disk. (7) Inclination of each disk. 0° is face-on, and 90° is edge-on. (8) Position angle (P.A.) of each disk (east of north). (9) Method used to deproject the disk structure: "E" indicates ellipse-fitting of the outer ring on the SpM image using the same manner as in Chapter 3, and "G" indicates the two-dimensional Gaussian fitting on the SpM image using the `imfit` task in `CASA`. "Ref": the inclination and P.A. of AB Aur are taken from Keplerian rotation derived from ^{12}CO(J = 2 − 1) observations (Tang et al. 2017). Note that Haro 6-37 C is one of multiple stellar systems and we adopted its stellar mass, luminosity, and spectral type from Akeson et al. (2019).
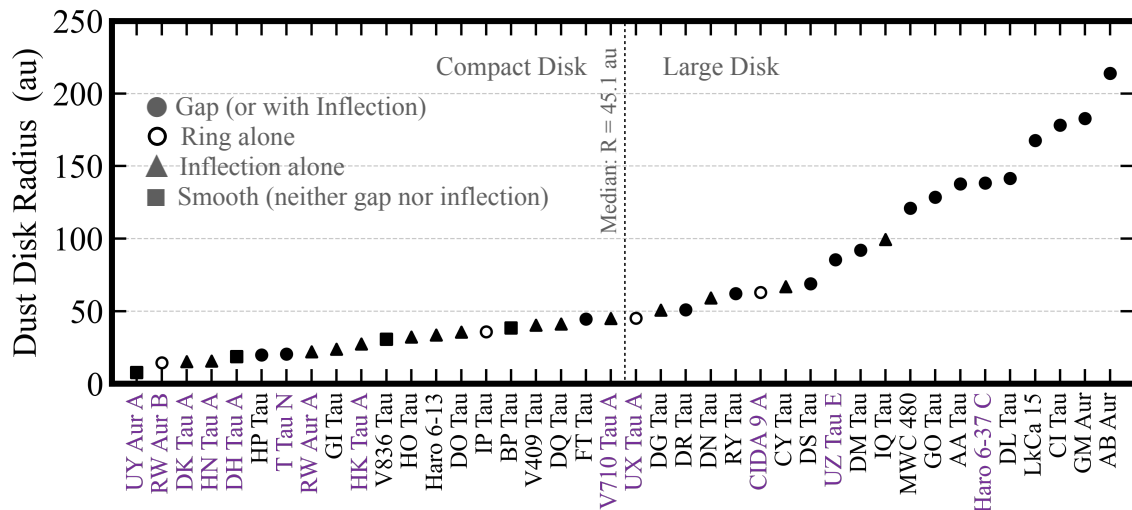
Figure 4.5.3: The dust disk radii in our sample are lined-up in order of size from small to large using the SpM images. The disk radius r_d was measured using aperture photometry (integrated flux density in a circle area with the radius). Binary and multiple stars are indicated in purple in the source names. The disk features can be identified by the shape of the markers, as presented in Table 4.5.2; a gap (or with inflection), ring alone, inflection alone, and smooth (neither gap nor inflection) are indicated by a circle, ring, triangle, and square, respectively. The vertical dashed line indicates the median disk radius ($r_\mathrm{d} = 45$ au) for this sample. With this line as a boundary, we define large and compact disks for convenience.

4.5.3 Performance and Features of SpM Imaging

Figure 4.5.4 shows the spatial resolutions of SpM and CLEAN images for the compact and large disk groups in 40 disks, in order of resolution. As a reference, Figure 4.5.5 also presents the spatial resolution ratios of each image. The spatial resolutions of each image are taken from Table 4.4.1. The statistical nature of this method, such as the achievable effective spatial resolution and limitations on it applicability, was investigated, and we found that SpM achieves a better spatial resolution than the conventional CLEAN algorithm (i.e., $\sim 30 - 50\%$ of the CLEAN beam in size for half of the disk sample with a more compact size). In particular, most of the resolutions are higher than $0''.1$, and the highest resolution is $0''.02$ for the compact disk around RW Aur AB.

Here, we focus on evaluating the performance of SpM imaging, including how notably the spatial resolution can be improved, and whether there are any advantages or disadvantages in reconstructing the disk structure. First we consider how the spatial resolution can be improved by investigating the relationship between spatial resolution and the SNR. Figure 4.5.6 shows the spatial resolution ratio of SpM to CLEAN and the SNR of the CLEAN image for our sample. Interestingly, a correlation can be observed between the two variables, and smaller ratios are achieved for more compact disks. To formulate the correlation, we derived the equation with a least-squares method as $\log_{10} Y = -0.26 \log_{10} X + 2.3$, where Y and X indicate the
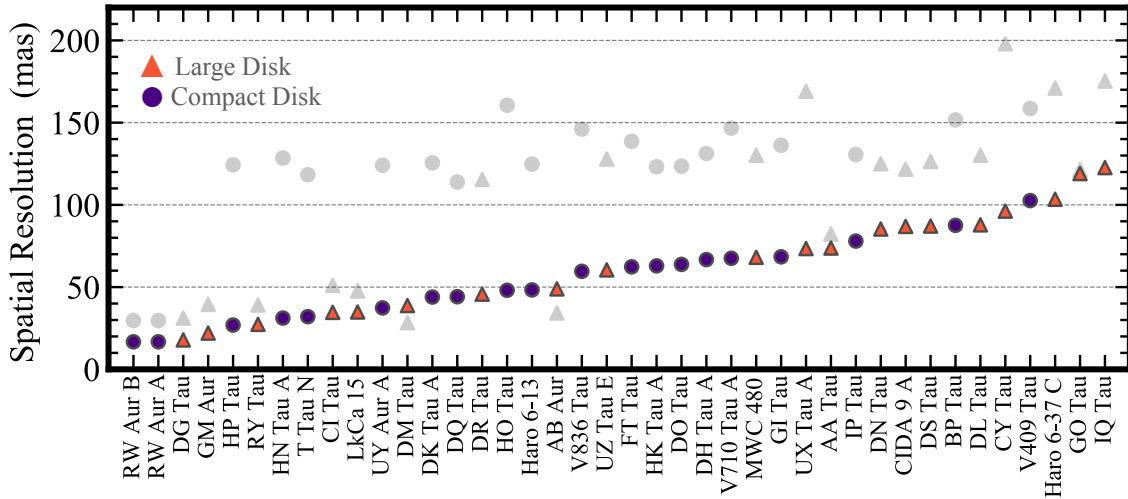
Figure 4.5.4: Resolutions of the CLEAN (light gray) and SpM (two colors: red and purple) images in our sample. The spatial resolutions of each image are taken from Table 4.4.1. The shape of the marker differs between compact disks (circle) and large disks (triangular), as defined in Figure 4.5.3. Although most CLEAN images have a spatial resolution of $0''.1 - 0''.2$, SpM images achieve a spatial resolution of $0''.02 - 0''.1$.

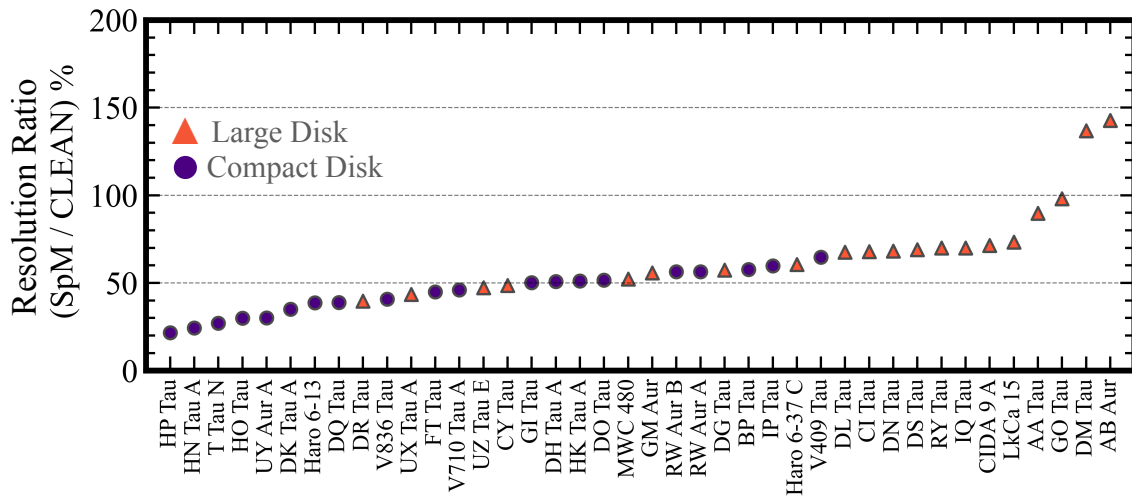**Figure 4.5.5**: Resolution ratios of the CLEAN to SpM images in our sample. The spatial resolutions of each image are taken from Table 4.4.1. The shape of the marker differs between compact disks (circle) and large disks (triangular), as defined in Figure 4.5.3. Half of the samples achieve $30 - 50\%$ of the CLEAN beam, and most of them are compact disks.

Figure 4.5.6: Relationship between the res-
olution ratio (SpM/CLEAN) and signal-to-
noise ratio (CLEAN) in our sample. The
shape of the marker differs between com-
pact disks (circle) and large disks (triangu-
lar), as defined in Figure 4.5.3. Using this
sample, we derived the equation, $\log_{10} Y =
-0.26 \log_{10} X + 2.3$, with the least-squares
method (linear regression), where Y indicates
the resolution ratio and X indicates the signal-
to-noise ratio. The gray ribbon denotes the
95% confidence interval for the regression.
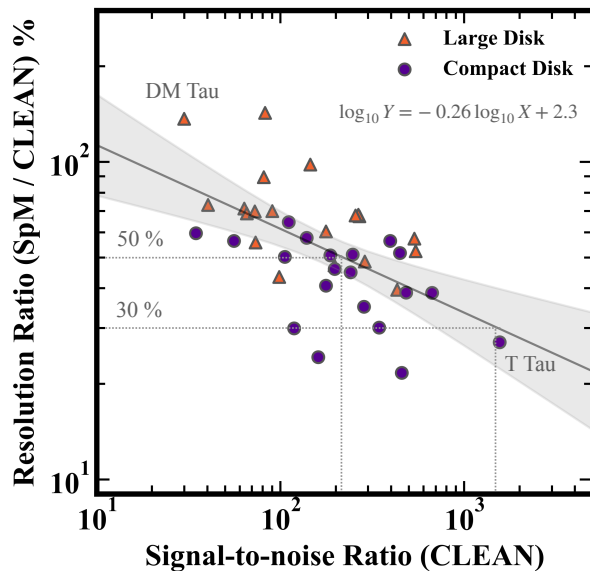
resolution ratio and the SNR, respectively. Given the empirical relationship, SpM achieves a
spatial resolution of $\sim 30\%$ of the nominal resolution when the SNR reaches the value of $\sim 10^3$.
Our results suggest that its performance mainly depends on the disk size. For disks with a similar
SNR, compact disks, which are $2-5$ times larger than the nominal beam size of CLEAN, are
likely to achieve a better resolution than large disks. Large disks are generally brighter in the
central region but less intense in the broadened region in our sample. SpM tends to ignore the
fitting of the weak intensity distribution owing to its lower SNR and adjusts the bright intensity
distribution to the observed visibility data (which dominates the short-baseline length). For
such disks, this conservatively suppresses the improvement of the effective resolution.

To evaluate the reliability of the reconstructed disk structures for the 40 Taurus disks,
we investigated the performance of SpM using three disks for which higher spatial resolution
data ($\sim 0''.03$) are available: DG Tau, RY Tau, and CI Tau. The RY Tau and DG Tau
disks are uniformly bright (i.e., low-contrast intensity) at a 1.3-mm emission and exhibit various
substructures (Francis & van der Marel 2020; Podio et al. 2020). The CI Tau disk was confirmed
to have a high-contrast intensity distribution and multiple gaps (Clarke et al. 2018). In the same
manner as in Chapter 2, we investigate the performance of SpM using two baseline datasets for
each source. The baseline lengths differ by a factor of three between the short-baseline used for
SpM and the long-baseline data used for reference (as a CLEAN image). The detailed procedure
is described in Appendix A. We confirm that a substructure (i.e., a gap and inner hole) seen
in the reconstructed SpM images are in good agreements with the reference owing to improving
spatial resolution by up to $2-3$ times. In addition, we found that SpM exhibits a favorable source
of reconstructing a high-fidelity image, such as the low-contrast intensity distribution observed
in the disks of DG Tau and RY Tau. This behavior can be explained by the fact that it works
with a bias to weight higher intensity areas, whereas the fitting weights are generally ignored in
weaker areas. In other words, if the gradient of the disk intensity is relatively low on the image
and its image has a high SNR, SpM should work well. Therefore, the low-contrast intensity

distributions like the RY Tau and DG Tau disks are suitable for reconstructing the high-fidelity
images. In the case of the CI Tau disk, which has a high-contrast intensity distribution, fidelity
can be improved by azimuthally averaging the images into a radial intensity profile (see the case
of the CI Tau disk in Figure A.2). Based on our results, we extract the physical quantities of
the disk from the radial intensity profile in the following section.

4.5.4   Radial Intensity Profile
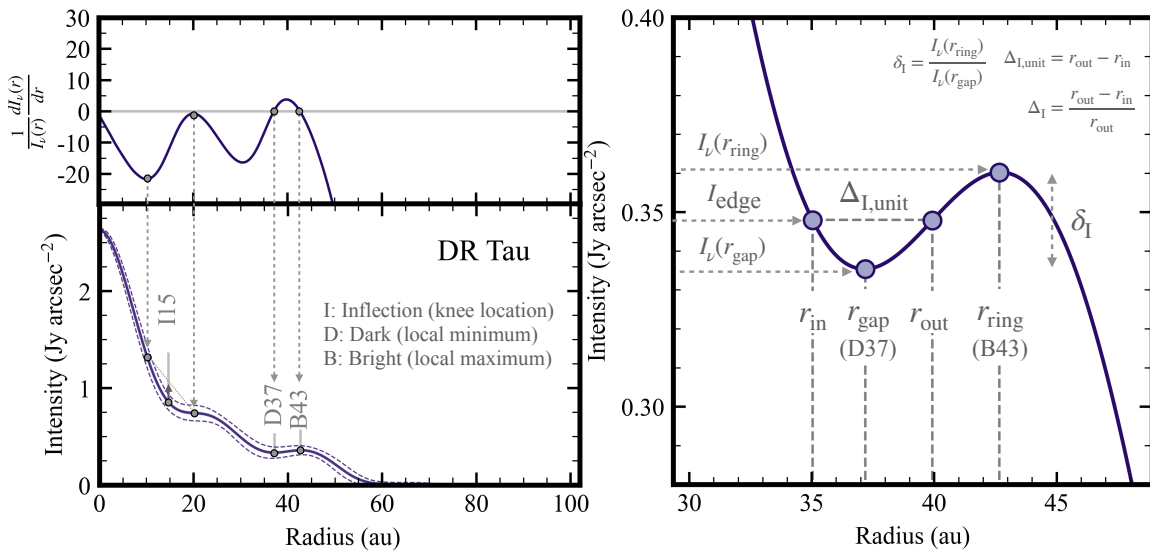
Figure 4.5.7: Example of our definition of the inflection position (marked by I), gap (marked
by D), and ring (marked by B). The three features are identified through the slope, using the
same method in Section 4.5.4. This example is taken from DR Tau. Left top panel: The slope
of the radial intensity profile divided by the radial intensity, $\frac{1}{I_\nu(r)}\frac{dI_\nu(r)}{dr}$. Left bottom panel:
The radial intensity profile averaged over the full azimuthal angle on a linear scale. The light
purple ribbon shows the mean error on each radius, while the purple dashed lines show the
standard deviation for comparison. Right panel: Close-up view of the radial intensity profile.
The definitions of gap width $\Delta_{I,unit}$, normalized gap depth Δ_I, and gap depth δ_I are given on
the profile with reference to Huang et al. (2018); Zhang et al. (2018).

Radial intensity profiles were generated to explore the statistical nature of the dust disk
structure revealed by our super-resolution imaging, including a comparison with previous studies.
Figure 4.5.8 and 4.5.9 show the deprojected and azimuthally averaged radial intensity profiles
$I_\nu(r)$ from analyzing 40 disks. The radial intensity profiles were calculated for each disk after
deprojection using the derived geometries (i.e., the inclination and PA) in Section 4.5.2. With
reference to Pinilla et al. (2021), the uncertainty of the radial profile is evaluated as the error of
the mean at each radius, where we consider the geometric mean of the effective spatial resolution
θ_{eff} to be the smallest independent unit. That is, the error is the standard deviation of each
elliptical bin divided by the square root of the number of θ_{eff} spanning the entire azimuthal
angle at each radial bin.
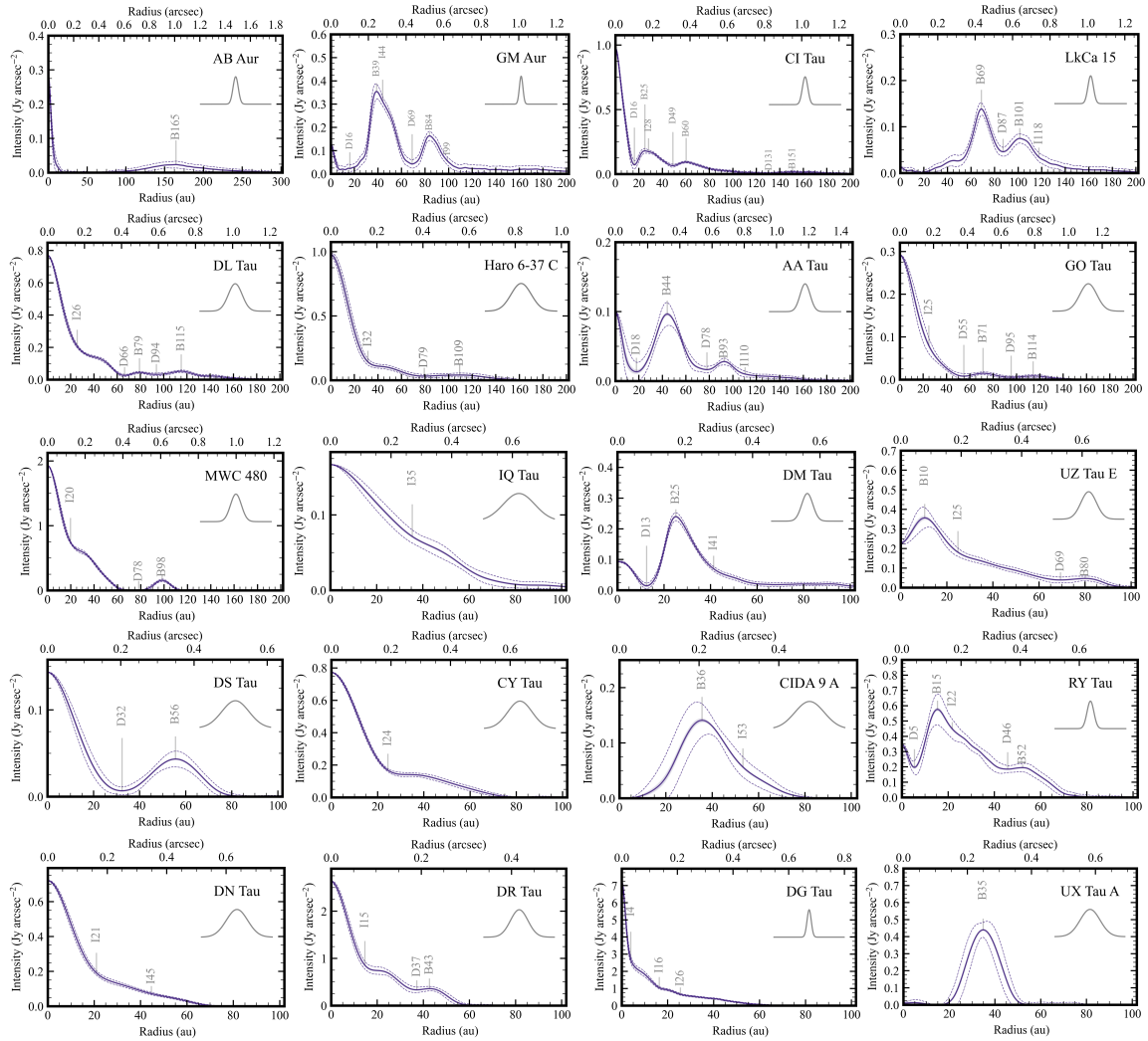
Figure 4.5.8: Deprojected and azimuthally-averaged radial intensity profiles taken from
SpM images. These profiles are ordered by decreasing dust disk size from left to right and
top to bottom. Each profile is interpolated onto radial grid points spaced by 0.1 au with
`interpolate.interp1d` in the `SciPy` module. The light purple ribbon shows the error on the
mean at each radius, while the purple dashed lines show the standard deviation for comparison.
Solid gray lines mark inflection I, gap D, and ring B listed in Table 4.5.2. The top right insets
show the geometric mean of the effective spatial resolution of each image.
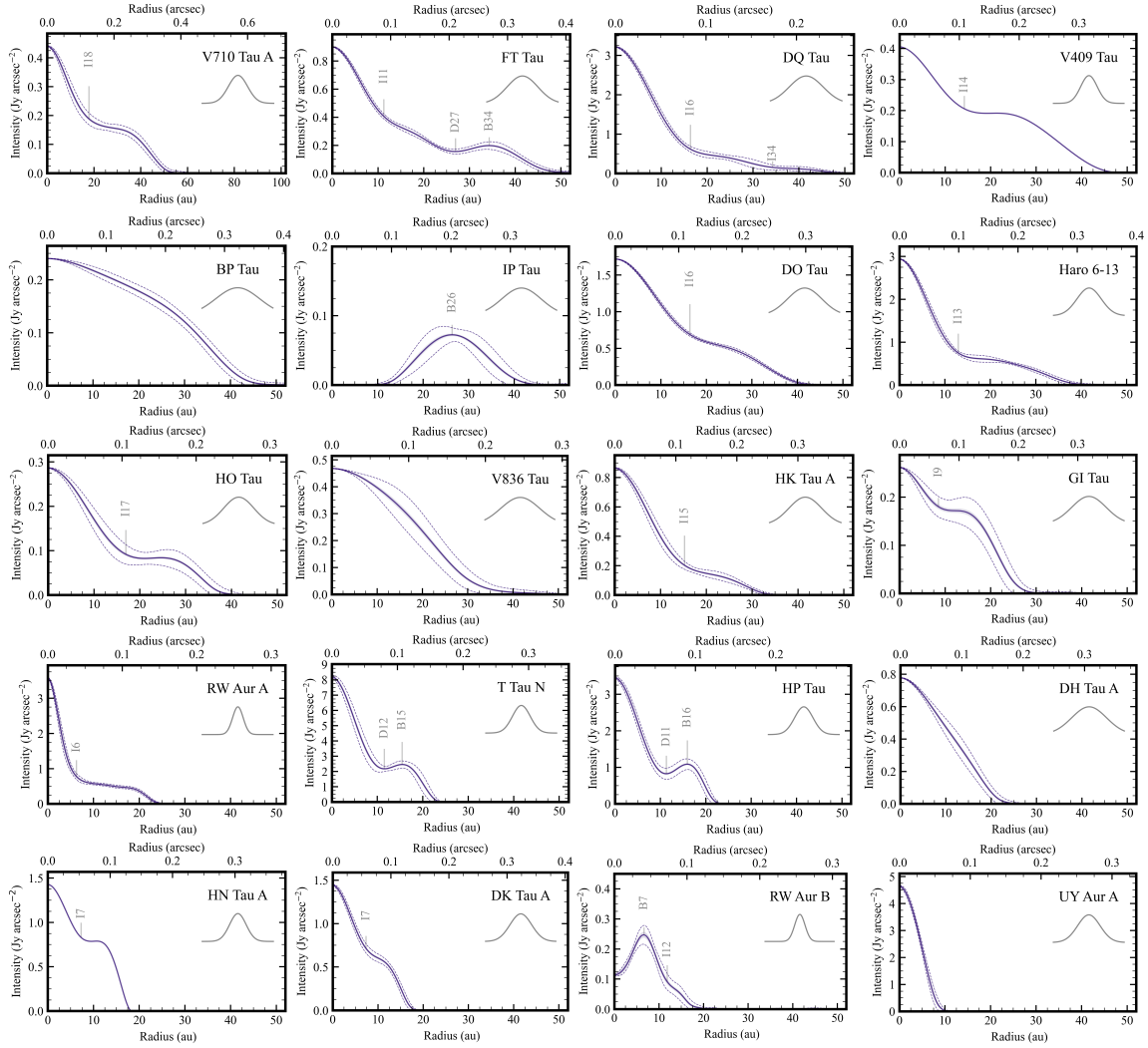
Figure 4.5.9: Continues from Figure 4.5.8.

Substructure Identification: Gaps, Rings, and Inflection Locations

We identified disk substructures (gaps, rings, and inflections) from the radial intensity profiles. Here, following Huang et al. (2018); Cieza et al. (2020), we label these features with a prefix "B" ("Bright" for rings) or "D" ("Dark" for gaps) followed by a number that indicates their location in au. We take a conservative approach and only identified gaps (r_{gap}) and rings (r_{ring}) as a clear local minimum ($I_{\nu,\mathrm{min}}(r)$) and local maximum ($I_{\nu,\mathrm{max}}(r)$), respectively, by calculating the radial intensity profile slope divided by the radial intensity, where $\frac{1}{I_\nu(r)}\frac{dI_\nu(r)}{dr} = 0$ (see Figure 4.5.7). Finally, the gap structures are confirmed in 80% of the large disks and 25% of the compact disks.

In addition to the gaps and rings, we also identified, as shown in Section 4.5.4, abrupt changes in the slopes of the radial profiles that are not identified as a local minimum. We refer to these as "inflection (r_{inf})" and label them with the "I" prefix. These features have previously been identified through visual inspection in Cieza et al. (2020); however, they are quantitatively identified in this study, as shown in Figure 4.5.7. When the slope $\frac{1}{I_\nu(r)}\frac{dI_\nu(r)}{dr}$ has both a local minimum and a local maximum but their values are less than zero, the inflection location, r_{inf}, can be identified by the position at which the maximum residual has been reached between the line connecting the two points and the profile. The procedure is, in part, performed using the `Kneed` python package to identify the inflection point of a line fit to the data. Note that these inflection points are not sufficiently spatially resolved. The origin of these inflections observed in each profile could have several cases, such as a non-identified gap with shallow width, a slope without a gap, and a shoulder due to inner-rim brightening in rings. Currently, the slope can be confirmed using the compact disk of RW Aur A (I6) with as high spatial resolution of $0''.02$. The identification of the shoulder due to inner-rim brightening in rings would also be an interesting point of study in terms of investigating the radial drift model, where the maximum grain size is smaller outside the shoulder and the dust opacity decreases at millimeter wavelengths (e.g., Pérez et al. 2019), or searching for pressure bumps produced by unseen planets orbiting inside the rings (e.g., Pinilla et al. 2019). Nine candidates can be identified by a visual inspection of the radial intensity profiles, e.g., CIDA 9A (I53), RW Aur B (I12), DM Tau (I41), LkCa 15 (I118), AA Tau (I110), RY Tau (I22), UZ Tau E (I25), CI Tau (I28), and GM Aur (I44,I99). However, this viewpoint is outside the scope of this study and will be covered separately in future work.

The locations of these features ("D", "B", and "I") are listed in Table 4.5.2. Note that because the disk around AB Aur has a larger gap, it was difficult to identify the local minimum from the radial intensity profile; hence, the gap location in this disk was ignored. As a result, we identified 23 gaps, 29 rings, and 36 inflections in the SpM images. In other words, the SpM images reveal 16 disks with annular gaps and rings, 30 disks with inflection points, and four disks with a ring alone.

Frequency of Substructures in Compact and Large Disks

SpM reveals annular gaps in seven disks: UZ Tau E (D69), RY Tau (D5, D46), DL Tau (D66, D94), DR Tau (D37), FT Tau (D27), T Tau N (D12), and HP Tau (D11), and a small inner-hole

Table 4.5.2.   Location of Gap, Ring, and Inflection
identified in Radial Intensity Profile.

Name	Gap ("D") r_{gap}: au (mas)	Ring ("B") r_{ring}: au (mas)	Inflection ("I") r_{inf}: au (mas)
(1)	(2)	(3)	(4)
AB Aur	$\cdots$	164.7(1011)	$\cdots$
GM Aur	16.1(101), 69.1(433)	38.8(243), 83.8(525)	44.0(276), 99.0(620)
CI Tau	130.9(825), 16.2(102), 49.0(309)	150.8(950), 25.1(158), 60.3(380)	28.2(178)
LkCa 15	87.2(549)	68.8(433)	117.7 (741)
DL Tau	66.4(417), 93.8(589)	115.2(723), 79.2(497)	25.6(161)
Haro 6-37 C	79.1(404)	109.2(558)	31.5(161)
AA Tau	18.0(131), 77.9(568)	44.2(322), 92.7(676)	110.4(805)
GO Tau	54.8(379), 95.4(660)	114.2(790), 71.4(494)	24.9(172)
MWC 480	78.3(484)	98.4(608)	19.7(122)
IQ Tau	$\cdots$	$\cdots$	35.5(270)
DM Tau	12.5(86)	25.1(173)	41.4(285), 58.0(400)
UZ Tau E	69.4(529)	10.4(79), 80.0(610)	24.9(190)
DS Tau	32.5(204)	55.7(350)	$\cdots$
CY Tau	$\cdots$	$\cdots$	24.5(190)
CIDA 9 A	$\cdots$	35.6(207)	53.3(310)
RY Tau	5.5(43), 45.9(358)	15.4(120), 52.3(408)	21.9(171)
DN Tau	$\cdots$	$\cdots$	20.9(163), 44.7(349)
DR Tau	37.2(190)	42.7(218)	14.7(75)
DG Tau	$\cdots$	$\cdots$	16.4(135), 25.6(211), 4.0(33)
UX Tau A	$\cdots$	34.8(249)	$\cdots$
V710 Tau A	$\cdots$	$\cdots$	18.0(126)
FT Tau	27.0(211)	34.4(269)	11.2(88)
DQ Tau	$\cdots$	$\cdots$	16.4(83), 34.4(174)
V409 Tau	$\cdots$	$\cdots$	14.2(108)
IP Tau	$\cdots$	26.4(202)	$\cdots$
DO Tau	$\cdots$	$\cdots$	16.4(118)
Haro 6-13	$\cdots$	$\cdots$	12.9(99)
HO Tau	$\cdots$	$\cdots$	16.9(105)
HK Tau A	$\cdots$	$\cdots$	15.2(114)
GI Tau	$\cdots$	$\cdots$	8.5(65)
RW Aur A	$\cdots$	$\cdots$	6.4(39)
T Tau N	11.6(81)	15.7(109)	$\cdots$
HP Tau	11.3(64)	15.9(90)	$\cdots$
HN Tau A	$\cdots$	$\cdots$	7.2(53)
DK Tau A	$\cdots$	$\cdots$	7.3(57)
RW Aur B	$\cdots$	6.7(41)	11.9(73)

Note. — Column description: (1) Name of host star. The names are ordered by the au-scale size of the dust disks from top to bottom. (2), (3), and (4) The position of the gap, ring, and inflection, which are calculated using the same method as in Section 4.5.4

Table 4.5.3:: Classification of Compact and Large Disks to Five Categories.

Disk Properties (1)	Compact Disks ($r_d < 45$ au) (2)	Large Disks ($r_d > 45$ au) (3)
Gap (or with inflection)	T Tau N, HP Tau, FT Tau	AB Aur, GM Aur, LkCa 15, DM Tau, DL Tau, Haro 6-37 C, RY Tau, DS Tau, DR Tau, AA Tau, GO Tau, MWC 480, UZ Tau E
Inflection alone: candidate gap	Haro 6-13, HO Tau, GI Tau DQ Tau, DK Tau	DG Tau, DN Tau, CY Tau
Inflection alone: no candidate gap	DO Tau, RW Aur A, HK Tau A, V710 Tau A, HN Tau (Edge-on), V409 Tau (Edge-on)	IQ Tau
Ring alone	IP Tau, RW Aur B	CIDA 9 A, UX Tau A
Smooth (or unresolved)	BP Tau, DH Tau A, V836 Tau, UY Tau A	None

Note. — Column description: (1) Disk properties. Gap, inflection, ring, and smooth are identified from the radial intensity profile in Section 4.5.4. In the inflections, candidate gaps are listed, which were selected by visual inspection. The selection criterion for gap candidates is that the concavity should be circular and not edge-on ($i \gtrsim 70°$) in the image. (2) and (3): Compact and large disks corresponding to each disk property.

($r < 7$ au) is found in the RW Aur B disk around low-mass stars ($M_* < 1.5$ $M_\odot$, M-K type stars), although the CLEAN image does not spatially resolve them. van der Marel & Mulders (2021) suggested that a ring/gap formation occurs in more massive stars ($M_* > 1.5$ $M_\odot$, G-F-A type stars); however, our study provides evidence that the gap/ring formation is common even in low-mass stars with a dust disk radius of $r_d > 15$ au. In Table 4.5.3, the observed 40 disks are classified into five categories: (1) Disks with the gap(s) with other inflection(s), (2) disks with inflections alone in its radial profile and candidate gap features selected by visual inspection of the image (these candidates are selected because the annular depression can be visually confirmed on the image, but did not reach the local minimum by azimuthal averaging onto the radial profile owing to a lack of spatial resolution. The locations of the gap candidate observed on the image and the inflection identified from the radial profile are confirmed to be the same within a few au), (3) disks with inflections alone but no gap candidate on the image, (4) disks with only a ring (i.e., an inner hole is identified), and (5) disks with smooth radial intensity profiles (or an unresolved case). The 40 sources are sorted into the five categories for compact and large disks, as shown in Table 4.5.3. In the large disks, most of the sources (16 sources out of 20) have substructures, such as gaps and rings, and inflections are identified in the remaining four. In IQ Tau, one inflection alone is identified, and its radial profile appears to be the smoothest among the large disks. However, the spatial resolution of the SpM image is still approximately $0''.1$, and a higher spatial resolution image will be necessary to search for substructures in detail.

Conversely, gaps and rings are identified in five sources out of 20 in the compact disks; their frequencies are considerably lower than in the large disks. However, inflections are identified for

11 sources; five out of 11 exhibit gap structures in their SpM images. Although a higher spatial
resolution is required to reveal the statistical frequencies of substructures in such compact disks,
it is clear that more than half of the 20 sources have substructures, such as gaps and rings, and
substructures are relatively common properties of Class-II disks in the Taurus region.
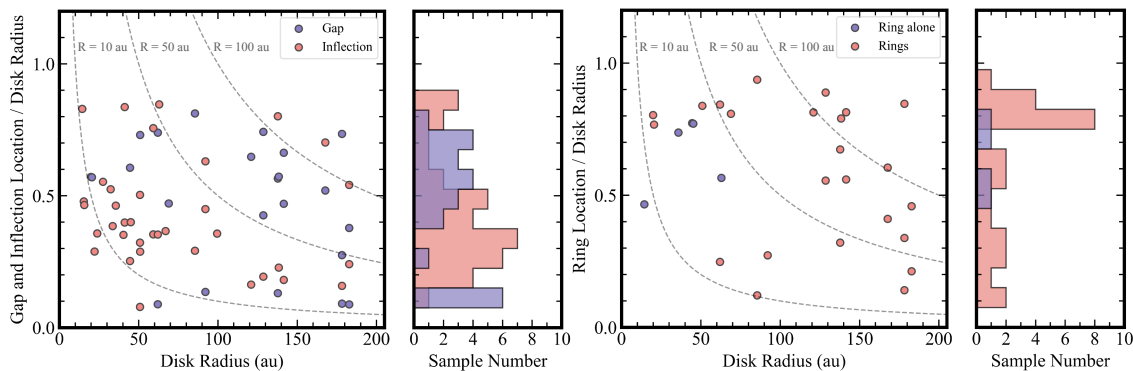
Radial Locations where Gaps are Formed

Figure 4.5.10: Left panel: The relationship between the disk radius and gap (or inflection)
location normalized by the disk radius, with its corresponding histogram. Right panel: Similar
to the left panel but for considering the ring location. The features of each disk are taken from
the SpM images. The images reveal 16 disks with annular gaps and rings, 30 disks with inflection
points (implying an unresolved gap or other features), and four disks with a ring alone.

Next, we explore the radial locations where gaps are generally formed in Taurus disks using
our samples (23 gaps in 16 disks). Figure 4.5.10 shows that the gap locations r_{gap} collected
from the disks are broadly distributed ($r_{gap} = 5.5 - 131$ au) and there is a tendency for gap
formation in the vicinity ($r_{gap}/r_d \simeq 0.1$) and the middle ($r_{gap}/r_d \simeq 0.4 - 0.7$) of the central
star. Because, by definition, rings (29 rings in 34 disks) are generally formed behind gaps, ring
locations are concentrated behind locations ($r_{ring}/r_d \simeq 0.8 - 0.9$) formed by the majority of gaps
($r_{gap}/r_d \simeq 0.4 - 0.7$).

Meanwhile, the inflection locations r_{inf} (36 inflections in 30 disks) are found to be behind
the gaps statistically described above; r_{inf}/r_d is approximately $0.2 - 0.5$ or 0.8. It would be
reasonable to suggest that the inflections are formed behind the gaps as shoulder candidates
(9 candidates in 36 inflections); however, if spatially unresolved gaps dominate the remaining
inflections, they form everywhere. These candidates can be especially identified in compact disks
imaged at resolutions of $0''.05 - 0''.10$, and their inflection locations are centrally distributed at
$r_{inf} = 10 - 20$ au (see Figure 4.5.9). The identified gaps in the compact disks, T Tau N (D12)
and HP Tau (D11), are imaged at higher resolutions ($0''.03 - 0''.04$). Hence, improving the
spatial resolution may reveal the nature of the observed inflections in the compact disks, and
we would be able to closely analyze where the gaps are definitely formed.

4.5.5   Width and Depth of Gaps

For each disk exhibiting a gap(s) presented in Section 4.5.4, we measured the gap depth $\delta_{\rm I}$, width $\Delta_{\rm I,unit}$, and normalized width $\Delta_{\rm I}$ using the same approach as Huang et al. (2018); Zhang et al. (2018). As shown in Figure 4.5.7, the gap depth is defined as $\delta_{\rm I} = I_\nu\left(r_{\rm ring}\right)/I_\nu\left(r_{\rm gap}\right)$. The gap and normalized widths are defined as $\Delta_{\rm I} = r_{\rm out} - r_{\rm in}$ and $\Delta_{\rm I} = \left(r_{\rm out} - r_{\rm in}\right)/r_{\rm out}$, respectively, where $r_{\rm out}$ and $r_{\rm in}$ are the inner edge of the outer ring and the outer edge of the inner disk, respectively. The relationship between $I_{\rm edge} \equiv 0.5\left\{I_\nu\left(r_{\rm ring}\right) + I_\nu\left(r_{\rm gap}\right)\right\}$ defines the edge locations. The edge location $r_{\rm in}$ is defined as the smallest value r satisfying the criteria $I_{\rm edge} = I_\nu(r_{\rm in})$ and $r < r_{\rm gap}$. Another edge location, $r_{\rm out}$, is defined as the largest value satisfying the criteria $I_{\rm edge} = I_\nu(r_{\rm out})$ and $r_{\rm gap} < r < r_{\rm ring}$. The uncertainties adopted for the gap width and depth are given by the error propagation, which is based on the standard deviation of the measurements on the azimuthally averaged intensity profiles (see Section 4.5.4). Overall, the majority of the errors are within 5% of the gap width and depth measurements. Given the 10% uncertainty on the absolute flux calibration for Band 6 (see ALMA technical handbook), these errors may be up to $\sim 15\%$ of the measurements.

AA Tau (D18) was excluded from the gap width and depth measurements because its inner disk to outer ring are misaligned, resulting in large uncertainties (Loomis et al. 2017). RY Tau (D5) and DM Tau (D13) were not measured for their gap widths with this metric because the intensity of their inner disks is smaller than that of their outer rings. Instead, we applied a Gaussian fit to these gap regions to derive each FWHM gap width using the least-squares method implemented in `optimize.leastsq` from `SciPy` (Jones et al. 2001). The uncertainties are the statistical uncertainties from the Gaussian fitting. Here, we assume that the FWHM gap width is approximate and taken from the above definition, as in Birnstiel et al. (2018). Finally, we obtained 22 gap features from 16 disks and investigated whether the measured gaps were spatially resolved by comparing $\Delta_{\rm I,unit}$ with the spatial resolution $\theta_{\rm eff}(= \sqrt{\theta_{\rm maj,eff} \times \theta_{\rm min,eff}})$. More than half of the total, 64% (14/22), were found to be spatially resolved. The verification results and the gap property measurements ($\delta_{\rm I}, \Delta_{\rm I,unit}$, and $\Delta_{\rm I}$) are summarized in Table 4.6.1.

Stellar Mass Dependence of Gap Properties

As described in Section 4.5.4, we reveal that gaps are commonly formed in disks with various sizes (small to large disks), regardless of the primary stellar masses. However, the relationship between the obtained gap size (i.e., $\Delta_{\rm I,unit} \times \delta_I$) and the primary stellar mass has been unexplored owing to the limited number of observed disks. As shown in Figure 4.3.1, Class II disks around more massive stars ($M_* > 1.5\ M_\odot$, A-F-G-type stars) in Taurus still have a limited population size, and the gap detected in our study is naturally limited to RY Tau (D5, D46) and MWC 480 (D78). To increase the number of samples, we added DSHARP disks (11 gaps in 8 disks) with clearly confirmed gaps (i.e., $\Delta_{\rm I} > 0.15$) from Zhang et al. (2018); Huang et al. (2018) and used their measured gap size for our study. Here, we obtained three DSHARP disks (HD14266, HD143006, and HD 163296) as categorized in the A-F-G-type stars (Andrews et al. 2018b). The
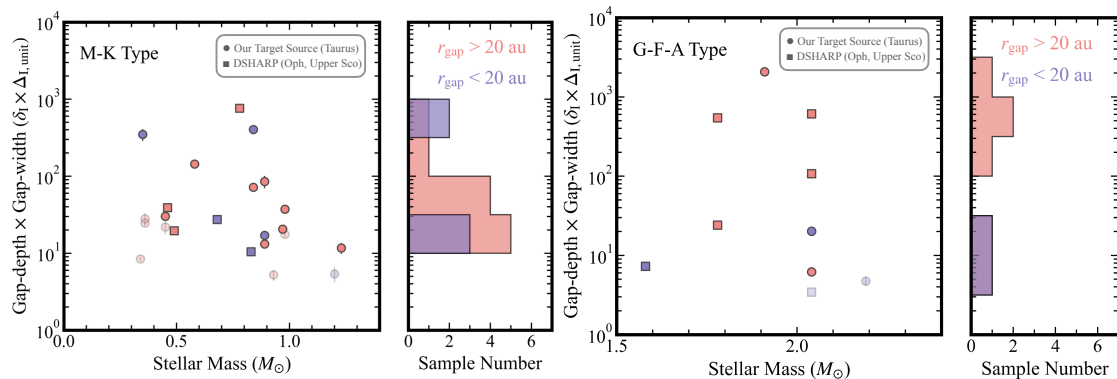
Figure 4.5.11: Relationship between stellar mass and the product ($\delta_{\mathrm{I}} \times \Delta_{\mathrm{unit,I}}$) of the width and depth of the disk gap. The circles indicate the Taurus disk sample, and the squares indicate the DSHARP disk sample given in Huang et al. (2018); Zhang et al. (2018). The color of the sample differs with the position of the gap (r_{gap}), with $r_{\mathrm{gap}} < 20$ au is indicated by blue, and $r_{\mathrm{gap}} < 20$ au is indicated by red. Left panel: Scatter diagram and histogram within the stellar mass range ($M_* = 0.3 - 1.5$ $M_\odot$), applicable to the M-K stellar spectral type. Right panel: Same as the left panel but within the stellar mass range ($M_* = 1.5 - 2.5$ $M_\odot$), applicable to the G-F-A stellar spectral type. Note that the lightly-colored markers indicate the spatially unresolved gaps compared with the spatial resolutions (i.e., $\theta > \Delta_{\mathrm{I,unit}}$). The samples are not counted in the histograms.

details of the DSHARP disks are presented in Table 4.6.1. Finally, we gathered 33 gaps in 24 disks.

Figure 4.5.11 suggests a tendency of the size of the gaps formed away from the central star ($r_{\mathrm{gap}} > 20$ au) to differ depending on the stellar mass (or the stellar spectral type). The distribution of the gap sizes $\Delta_{\mathrm{I,unit}} \times \delta_I \simeq 10^1 - 10^2$ for M-K-type stars and increases by one order of magnitude to $\Delta_{\mathrm{I,unit}} \times \delta_I \simeq 10^3$ for A-F-G-type stars. The AB Aur disk (A1.0-type star), whose large gap makes it difficult to measure its gap size (see Section 4.5.4), would also be included in the large gap-size distribution (right panel in Fig 4.5.11). This result is further investigated for planetary masses under the hypothesis of a planet-induced gap in Section 4.6.3.

4.6 Discussion

4.6.1 Possible Origins of the Gap and Ring Features

Our Taurus survey, along with large surveys by DSHARP (Andrews et al. 2018b) and the Ophiuchus DIsk Survey Employing ALMA (ODISIA; Cieza et al. 2020), suggests that disk substructures appear to be ubiquitous, and in particular, the most frequently observed structures are almost axisymmetric gaps and rings. Several theoretical explanations have been proposed for the origin of gaps. For instance, a planet inducing the formation of a gap (e.g., Lin & Papaloizou

1986; Takeuchi et al. 1996; Zhu et al. 2012; Pinilla et al. 2012), the effect of the snowlines of major volatiles (e.g., Zhang et al. 2015), sintering effects (Okuzumi et al. 2016), magneto-hydrodynamic effects (e.g., Flock et al. 2015), secular gravitational instability (e.g., Youdin 2011; Takahashi & Inutsuka 2014, 2016), disk-wind (Takahashi & Muto 2018), and thermal wave instability (e.g., Watanabe & Lin 2008; Siebenmorgen & Heymann 2012; Ueda et al. 2019, 2021). In certain disks, different mechanisms may interplay, while in others, a specific mechanism may be dominant in the disks. This section focuses on comparing the 33 gaps of the 24 disks identified in the Taurus and DSHARP disks using two major hypotheses: embedded planets and snowlines induced by volatile molecules. Note that other scenarios may play a role in gap formation in some disks.

4.6.2   Snowline Origin

We discuss the snowline origin to explain gap formation, that is, we perform a comparison of the various snowline locations (e.g., H_2O, CO_2, CO and N_2) and the gap locations. As the radius of the disk increases, the disk midplane temperature $T_{mid}(r)$ gradually decreases and major volatile molecules freeze into the dust grains. These phase transition regions, also known as condensation fronts or snowlines, are expected to change the dust opacity and its growth and fragmentation due to collisions, giving rise to the gap and ring-like features observed in continuum images (Zhang et al. 2015; Pinilla et al. 2017). To estimate the location of the snowlines, several physical parameters are required, such as the disk midplane temperature $T_{mid}(r)$ and the condensation temperature for each volatile molecule. Here, the disk midplane temperature $T_{mid}(r)$ is applied to the irradiated fired disk model (Chiang & Goldreich 1997; Dullemond et al. 2001), as expressed in

$$T_{mid}(r) = \left(\frac{\phi L_*}{8\pi r^2 \sigma_{SB}} \right)^{1/4}, \qquad (4.1)$$

where σ_{SB} is the Stefan-Boltzmann constant, L_* is the stellar luminosity (taken from Table 4.5.1), and ϕ is the flaring angle, which is settled at a constant of 0.02 (Huang et al. 2018). A higher value of $\phi = 0.05$ is selected for DR Tau and HP Tau because lower values reach dust temperature estimates below $T_{br}(r)$ of each inner disk. High ϕ results in snowline locations occurring outside that of the low ϕ. If the annular gap traces the locations of the various molecular snowlines, the relationship can be expressed using Equation 4.1 as $r_{gap} \propto T_{snline}^{-2} L_\star^{0.5}$. Figure 4.6.1 compares the expected locations of the snowlines to the gap locations in the $r_{gap} - \sqrt{L_*}$ plane. To verify whether the gap locations are consistent with those of the snowlines for each disk, the condensation temperature ranges have been shaded for the major volatile molecules, $H_2O(128 - 155\,\text{K})$, $CO_2(60 - 72\,\text{K})$, $CO(23 - 28\,\text{K})$, and $N_2(12\text{–}15\text{K})$, following the approach of Zhang et al. (2015).

Overall, no strong correlation can be observed between the snowline and the gap location. As for specific snowlines, approximately half of the gaps are located around the expected CO and N_2 snowlines. However, the possible locations of such snowlines are extending considerably in radius (e.g., $r_{snline} = 5 - 100$ au for CO and $r = 30 - 200$ au for N_2), and these snowlines appear
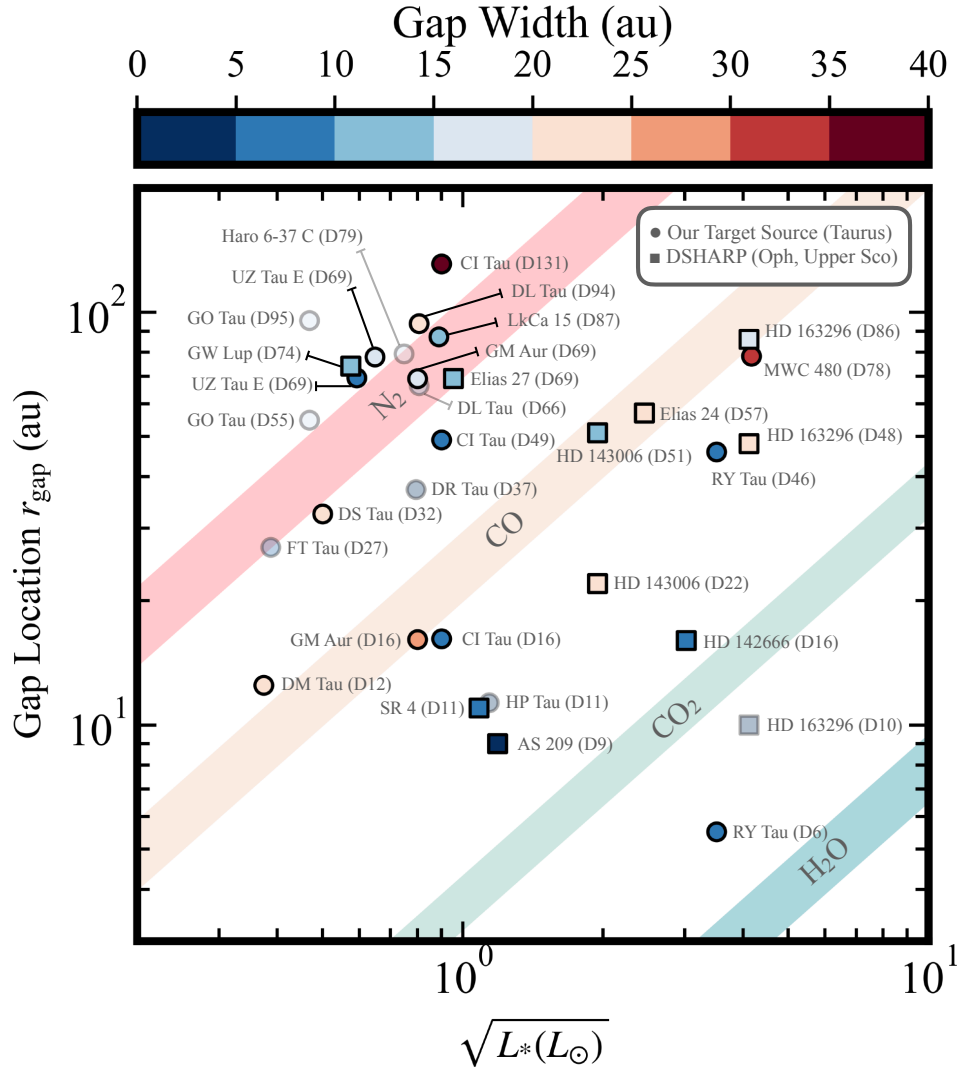
Figure 4.6.1: Relationship between the location of the gap (r_{gap}) and the square root of the
stellar luminosity ($\sqrt{L_*}$). In the disk mid-plane temperature $T_{\mathrm{mid}}(r)$, the flaring angle ϕ is settled
at a constant of 0.02. The color-coded regions represent the range of snowlines corresponding to
the volatile molecules N_2 (red), CO (pale orange), CO_2 (green), and H_2O (blue). Each snowline
range is determined from a combination of the condensation temperatures for volatile molecules
in Zhang et al. (2015) and disk dust temperatures in Equation 4.1. The circles indicate the
Taurus disk sample, and the squares show the DSHARP disk sample. For reference, the size of
the gap width ($\Delta_{\mathrm{unit,I}}$) for each sample is visualized with the color bar. Note that the lightly-
colored markers indicate the spatially unresolved gaps compared with the spatial resolutions
(i.e., $\theta > \Delta_{\mathrm{I,unit}}$).

to coincidentally correlate with the randomly-distributed gap locations in the $r_{\mathrm{gap}} - \sqrt{L_*}$ plane. The gap widths near the expected CO and N_2 snowline locations appear to be heterogeneous, that is, several gaps are narrow, whereas others are wide. This indicates no clear physical association between the snowline and gap location (Huang et al. 2018). The snowline locations are sensitive to the flaring angle of the given temperature model, and the flaring angle may differ disk to disk, although we assume a fixed value ($\phi = 0.02$). The lack of clear correlation would be due to the uncertainty in the mid-plane temperature introduced by the flaring angle.

We conclude that there is no strong evidence for the snowline origin of gaps, which agrees with previous studies on Class II disks in low-mass star-forming regions (van der Marel et al. 2019; Long et al. 2019; Huang et al. 2018).

4.6.3   Planetary Mass Estimate by Gap Properties

Another possible origin of the gaps is the clearing of the disk material by the planet (e.g., Lin & Papaloizou 1986; Takeuchi et al. 1996; Zhu et al. 2012; Pinilla et al. 2012). As described in Section 4.5.5, there appears to be a mutual dependence between the gap properties in a disk and the disk's primary stellar mass. In terms of a planet-disk interaction, the results motivate us to estimate a planetary mass by applying the method that connects the planetary mass and gap shape in Zhang et al. (2018). This approach defines the gap depth δ_{I} and width Δ_{I} in $I_\nu(r)$ without assuming a functional form for the substructures or an initial surface density; there are two relationships to derive the planetary mass from the measured δ_{I} and Δ_{I}, respectively. The planetary-mass derivation from the gap width δ_{I} can be formulated as (Eq. 24 in Zhang et al. 2018)

$$\frac{M_{\mathrm{p},\delta_{\mathrm{I}}}}{M_*} = 0.073 \left(\frac{\delta_{\mathrm{I}} - 1}{C} \right)^{1/D} \left(\frac{h_{\mathrm{gap}}}{r_{\mathrm{gap}}} \right)^{2.81} \left(\frac{\alpha_{\mathrm{vis}}}{10^{-3}} \right)^{0.38}. \tag{4.2}$$

The equation using the gap width Δ_{I} can be formulated as (Eq. 22 in Zhang et al. 2018)

$$\frac{M_{\mathrm{p},\Delta_{\mathrm{I}}}}{M_*} = 0.115 \left(\frac{\Delta_{\mathrm{I}}}{A} \right)^{1/B} \left(\frac{h_{\mathrm{gap}}}{r_{\mathrm{gap}}} \right)^{0.18} \left(\frac{\alpha_{\mathrm{vis}}}{10^{-3}} \right)^{0.31}. \tag{4.3}$$

By assuming $M_{\mathrm{p},\delta_{\mathrm{I}}} = M_{\mathrm{p},\Delta_{\mathrm{I}}}$ and eliminating the planetary mass in the two equations, Eq.4.2 and Eq.4.3, the relationship between Δ_{I} and δ_{I} can be obtained as follows.

$$\Delta_{\mathrm{I}} = A \left[0.635 \left(\frac{\delta_{\mathrm{I}} - 1}{C} \right)^{1/D} \left(\frac{h_{\mathrm{gap}}}{r_{\mathrm{gap}}} \right)^{2.63} \left(\frac{\alpha_{\mathrm{vis}}}{10^{-3}} \right)^{0.07} \right]^{B}, \tag{4.4}$$

where A, B, C, and D are fitting parameters introduced by Zhang et al. (2018), which can be obtained from the parameter list given by Zhang et al. (2018) that is constrained by three

Table 4.6.1:: Gap Properties and Inferred planetary mass.

Name	$r_{\rm gap}$ (au)	$\theta < \Delta_{\rm I,unit}$	$\Delta_{\rm I,unit}$ (au)	$\Delta_{\rm I}$	$\delta_{\rm I}$	$\Sigma_{\rm d}$ (g cm^{-2})	h/r	$\Sigma_{\rm gas}$ (g cm^{-2})	$M_{\rm planet}$ ($M_{\rm Jup}$)
(1)	(2)	(3)	(4)	(5)	(6)	(7)	(8)	(9)	(10)
Our Target disks (Taurus, 22 gaps in 16 disks).									
GM Aur	69	Yes	18.67 ± 0.16	0.24 ± 0.01	3.83 ± 0.09	0.51	0.07	30	$0.19 \pm 0.08,\ 0.45 \pm 0.22,\ 1.03 \pm 0.58$
GM Aur	16	Yes	26.49 ± 0.01	0.96 ± 0.01	15.23 ± 1.15	0.23	0.05	30	$13.55 \pm 13.12,\ 27.74 \pm 26.72,\ 56.83 \pm 54.37$
CI Tau	16	Yes	6.82 ± 0.48	0.34 ± 0.02	2.5 ± 0.16	0.62	0.05	100	$0.31 \pm 0.21,\ 0.65 \pm 0.41,\ 1.38 \pm 0.78$
CI Tau	49	Yes	9.2 ± 0.48	0.17 ± 0.01	1.43 ± 0.02	0.38	0.06	30	$0.03 \pm 0.0,\ 0.08 \pm 0.02,\ 0.17 \pm 0.05$
CI Tau	131	Yes	35.23 ± 6.19	0.25 ± 0.04	2.42 ± 0.11	0.07	0.08	10	$0.16 \pm 0.0,\ 0.36 \pm 0.04,\ 0.8 \pm 0.14$
LkCa 15	87	Yes	12.71 ± 0.48	0.14 ± 0.01	1.62 ± 0.02	0.26	0.07	30	$0.05 \pm 0.04,\ 0.12 \pm 0.09,\ 0.29 \pm 0.23$
DL Tau	66	No	10.35 ± 0.8	0.14 ± 0.01	1.7 ± 0.04	0.44	0.06	30	$0.04 \pm 0.02,\ 0.09 \pm 0.06,\ 0.22 \pm 0.16$
DL Tau	94	Yes	23.1 ± 1.59	0.22 ± 0.01	1.61 ± 0.03	0.10	0.06	10	$0.07 \pm 0.03,\ 0.16 \pm 0.06,\ 0.34 \pm 0.11$
Haro 6-37 C	79	No	17.42 ± 3.33	0.19 ± 0.03	1.26 ± 0.06	0.30	0.09	30	$0.03 \pm 0.01,\ 0.07 \pm 0.02,\ 0.17 \pm 0.06$
AA Tau	78	Yes	17.7 ± 1.65	0.21 ± 0.02	1.7 ± 0.06	0.12	0.09	10	$0.06 \pm 0.01,\ 0.12 \pm 0.03,\ 0.28 \pm 0.09$
GO Tau	55	No	15.33 ± 2.6	0.24 ± 0.04	1.83 ± 0.14	0.12	0.09	10	$0.06 \pm 0.01,\ 0.13 \pm 0.01,\ 0.29 \pm 0.05$
GO Tau	95	No	16.2 ± 0.01	0.16 ± 0.01	1.52 ± 0.08	0.05	0.10	10	$0.03 \pm 0.02,\ 0.08 \pm 0.05,\ 0.19 \pm 0.13$
MWC 480	78	Yes	32.85 ± 0.16	0.36 ± 0.01	63.21 ± 6.38	0.11	0.07	10	$3.34 \pm 2.18,\ 7.82 \pm 5.43,\ 18.32 \pm 13.46$
DM Tau	12	Yes	21.04 ± 0.01	0.58 ± 0.01	16.53 ± 2.89	0.98	0.06	100	$0.89 \pm 0.44,\ 1.9 \pm 0.81,\ 4.08 \pm 1.46$
UZ Tau E	69	Yes	9.84 ± 1.57	0.13 ± 0.02	1.19 ± 0.04	0.09	0.05	10	$0.02 \pm 0.0,\ 0.04 \pm 0.01,\ 0.08 \pm 0.01$
DS Tau	32	Yes	22.43 ± 0.64	0.54 ± 0.01	6.41 ± 0.46	0.28	0.06	30	$1.06 \pm 0.84,\ 2.2 \pm 1.68,\ 4.6 \pm 3.35$
RY Tau	6	Yes	6.92 ± 0.13	0.77 ± 0.01	2.92 ± 0.12	0.32	0.03	30	$12.25 \pm 12.21,\ 25.02 \pm 24.91,\ 51.11 \pm 50.85$
RY Tau	46	Yes	5.9 ± 0.64	0.12 ± 0.01	1.05 ± 0.01	0.15	0.06	10	$0.02 \pm 0.01,\ 0.04 \pm 0.02,\ 0.09 \pm 0.03$
DR Tau	37	No	4.89 ± 0.78	0.12 ± 0.02	1.07 ± 0.02	0.51	0.06	100	$0.02 \pm 0.0,\ 0.03 \pm 0.0,\ 0.08 \pm 0.01$
FT Tau	27	No	6.65 ± 0.38	0.22 ± 0.01	1.27 ± 0.02	0.92	0.07	100	$0.04 \pm 0.01,\ 0.08 \pm 0.02,\ 0.17 \pm 0.02$
T Tau N	12	No	3.88 ± 0.43	0.28 ± 0.02	1.22 ± 0.06	3.40	0.05	100	$0.35 \pm 0.3,\ 0.73 \pm 0.6,\ 1.52 \pm 1.21$
HP Tau	11	No	4.07 ± 0.89	0.3 ± 0.05	1.32 ± 0.03	2.02	0.04	100	$0.23 \pm 0.21,\ 0.47 \pm 0.42,\ 0.97 \pm 0.85$
DSHARP disks (Ophiuchus, Upper Scorpion, 11 gaps in 8 disks).									
AS 209	9	Yes	4.7 ± 0.2	0.42	$2.22^{+0.1}_{-0.09}$	1.23	0.04	100	$0.5 \pm 0.46,\ 1.04 \pm 0.93,\ 2.13 \pm 1.88$
Elias 24	57	Yes	22.8 ± 0.3	0.32	$33.33^{+16.67}_{-8.33}$	0.52	0.09	100	$3.08 \pm 2.67,\ 7.32 \pm 6.48,\ 17.4 \pm 15.69$
Elias 27	69	Yes	14.3 ± 1.1	0.18	$1.37^{+0.04}_{-0.04}$	0.48	0.09	100	$0.06 \pm 0.03,\ 0.15 \pm 0.08,\ 0.35 \pm 0.2$
GW Lup	74	Yes	12.1 ± 0.4	0.15	$3.23^{+0.35}_{-0.28}$	0.13	0.08	10	$0.07 \pm 0.06,\ 0.16 \pm 0.13,\ 0.38 \pm 0.33$
HD 142666	16	Yes	5.3 ± 1.4	0.2	$1.37^{+0.04}_{-0.04}$	1.63	0.05	100	$0.1 \pm 0.04,\ 0.22 \pm 0.08,\ 0.48 \pm 0.14$
HD 143006	22	Yes	21.7 ± 1.0	0.62	$25.0^{+25.0}_{-8.33}$	0.20	0.04	30	$5.1 \pm 4.35,\ 10.55 \pm 8.74,\ 21.86 \pm 17.53$
HD 143006	51	Yes	12.8 ± 1.4	0.22	$1.89^{+0.07}_{-0.07}$	0.14	0.05	30	$0.12 \pm 0.04,\ 0.26 \pm 0.06,\ 0.57 \pm 0.08$
HD 163296	10	No	3.2 ± 1.4	0.24	$1.08^{+0.04}_{-0.73}$	1.43	0.04	100	$0.18 \pm 0.17,\ 0.36 \pm 0.34,\ 0.75 \pm 0.68$
HD 163296	48	Yes	20.2 ± 1.0	0.34	$30.3^{+6.73}_{-4.66}$	0.41	0.06	30	$2.12 \pm 1.07,\ 4.9 \pm 2.75,\ 11.38 \pm 6.98$
HD 163296	86	Yes	16.2 ± 0.3	0.17	$6.62^{+0.37}_{-0.33}$	0.15	0.07	30	$0.64 \pm 0.57,\ 1.53 \pm 1.39,\ 3.64 \pm 3.35$
SR 4	11	Yes	6.3 ± 1.4	0.45	$4.35^{+0.04}_{-0.04}$	1.56	0.05	100	$0.6 \pm 0.44,\ 1.25 \pm 0.88,\ 2.61 \pm 1.74$

Note. — Column description: (1) Name of host star for our target disks and DSHARP disks taken from Huang et al. (2018); Zhang et al. (2018). For each sample set, the names are ordered according to the au-scale size of the dust disks from top to bottom. (2) Radial location of the gap $r_{\rm gap}$. (3) A judgment (Yes or No) of whether the size of the spatial resolution θ is smaller than the gap width $\Delta_{\rm I,unit}$. (4), (5), and (6) The gap width $\Delta_{\rm I,unit}$, normalized gap width $\Delta_{\rm I}$, and gap depth $\delta_{\rm I}$, which are calculated using the same method as in Section 4.5.5. The uncertainties adopted for the gap width and depth are given by the error propagation based on the standard deviation of the measurements on the azimuthally averaged intensity profiles. (7) The averaged dust surface density $\Sigma_{\rm d}$ from 1.1 $r_{\rm gap}$ to 2.0 $r_{\rm gap}$ on the radial intensity profiles, as shown in Figure 4.5.8 and 4.5.9. (8) The aspect ratio at the position of the gap. (9) The closest gas density found from Figure 18 in Zhang et al. (2018), given by the results of $\Sigma_{\rm d}$ and $h/r_{\rm gap}$. (10) The inferred planetary mass assuming $\alpha = 10^{-4}, 10^{-3}$, and 10^{-2} (left to right). The planetary mass is determined as an average value from the respective values obtained from the gap depth and width. The errors denote the upper and lower limits of the planetary masses given by the two methods.
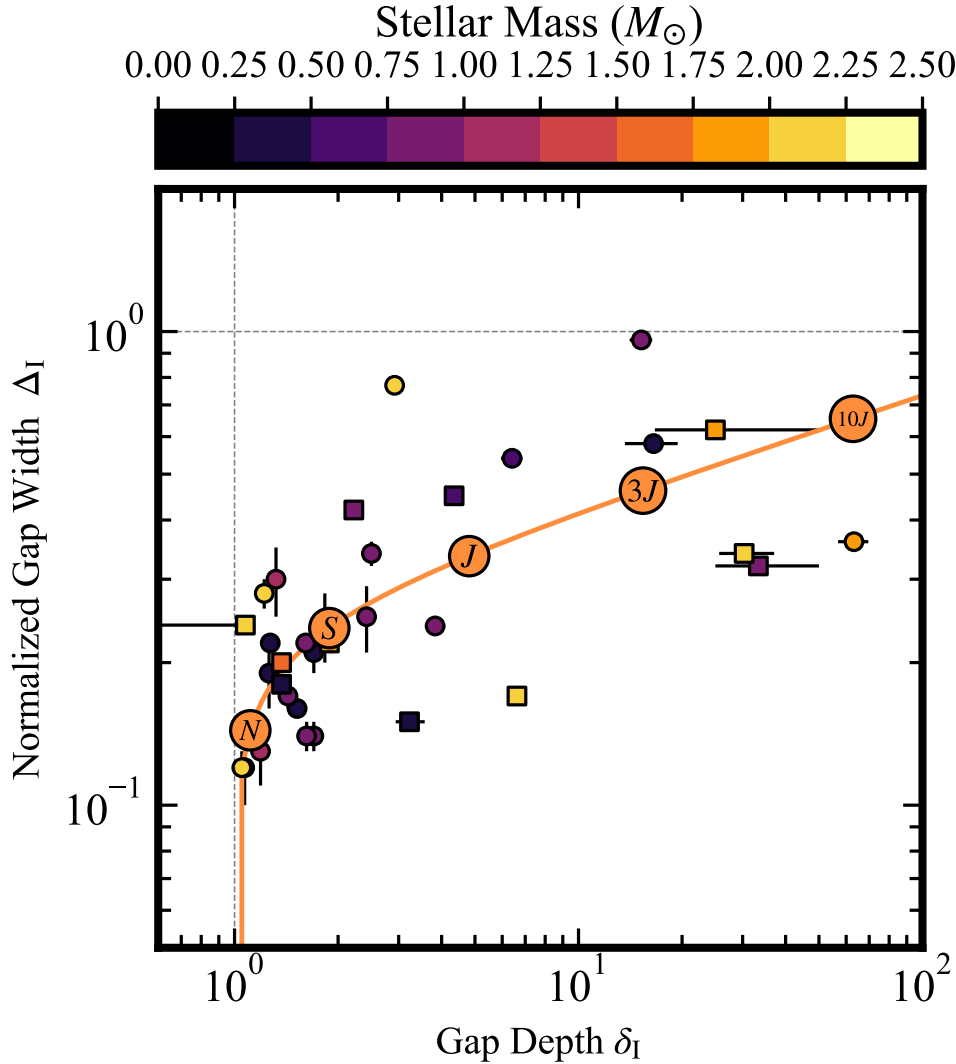
Figure 4.6.2: The measured gap size (δ_I, Δ_I) versus the inferred planetary mass. The circle
and square markers indicate Taurus disks and DSHARP disks, respectively. The primary stellar
masses give the color scales of each sample. The orange curve denotes the theoretical expression
derived from planet-disk interactions, following Equation 4.4. In this case, the viscous parameter
α_{vis} is set to 10^{-3}, and the scale height ratio h/r is set to 0.08. The fitting parameters (A =
1.18, B = 0.29, C = 0.135, D = 1.21) are applied, which were found by assuming that the gas
surface density is 10 g cm^{-2} and the maximum dust size is 0.1 mm. The light orange curve shows
the equation for the case where α_{vis} is applied for 10^{-2} to 10^{-4}; there is no significant error
compared to the case with $\alpha_{vis} = 10^{-3}$. The vertical and horizontal dashed lines indicate the
measurement limits of the gap depth and width, respectively. As a comparison, using Equations
4.2 and 4.3 with a stellar mass of 1 $M_\odot$, planetary masses in the solar system (Neptune: N,
Saturn: S, Jupiter: J, three times the Jupiter mass: $3J$, ten times the Jupiter mass: $10J$) are
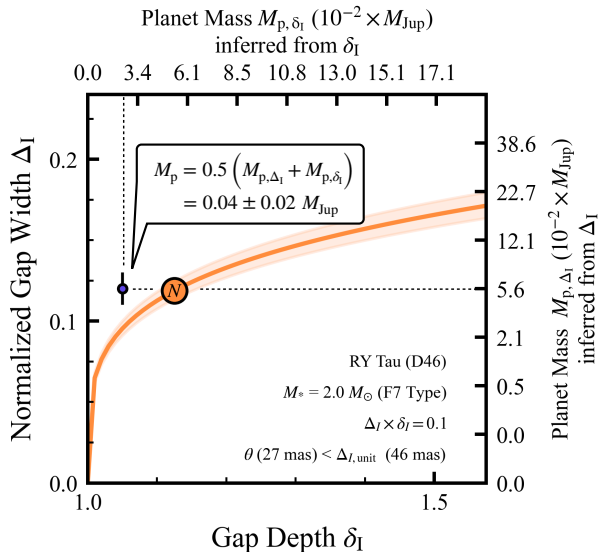overlaid on the relationship curve.

Figure 4.6.3: Estimate of planetary masses using the gap width $\Delta_{\rm I}$ and depth $\delta_{\rm I}$, taken from RY Tau (D46). The plot shows the measured gap size ($\delta_{\rm I}$, $\Delta_{\rm I}$) compared with the theoretical curve (orange) of the inferred planetary mass for $\alpha = 10^{-3}$ in Equation 4.4. The light orange ribbon shows the case with $\alpha_{\rm vis} = 10^{-2}$ to 10^{-4}, indicating that there is no significant error compared with the $\alpha_{\rm vis} = 10^{-3}$ case. The circle marker indicates the gap size measured from the radial intensity profile. The two masses $(M_{\rm p,\Delta_{\rm I}}, M_{\rm p,\delta_{\rm I}})$ of the inferred planet in the gap are derived from the width and depth of the gap, respectively. The average of the two masses is used as a representative planetary mass, that is, $M_{\rm p} = 0.5(M_{\rm p,\Delta_{\rm I}} + M_{\rm p,\delta_{\rm I}})$, and the original masses are set to be the upper and lower limits, respectively. The mass range of the inferred planet converges when the gap size is close to the theoretical curve. For reference, a planetary mass in the solar system (Neptune: N) is overlaid on the theoretical curve.

physical parameters (averaged gas surface density $\Sigma_{\rm g}$, the aspect ratio at the gap location $h/r_{\rm gap}$[1], and the maximum grain size $s_{\rm max}$ in the disk). Thus, the derivation of the planetary mass thus requires an estimation of the three parameters for each disk. $\Sigma_{\rm g}$ was estimated from the averaged dust surface density Σ_d using the relationship in Figure 18 from Zhang et al. (2018). Σ_d can be derived using radiative transfer calculations with a combination of the disk midplane temperature model $T_{\rm mid}(r)$ in Equation 4.1, the dust absorption opacity κ_ν, and the observed brightness temperature $T_{\rm br}(r)$ for each disk. Knowing $T_{\rm mid}(r)$, we can simply derive $h/r_{\rm gap}$ using the host stellar mass M_* and luminosity L_* (taken from Table 4.5.1). κ_ν is adopted from the DSHARP opacity model ($\kappa_\nu = 0.43$ cm^2 g^{-1}; Birnstiel et al. 2018) by assuming $s_{\rm max} = 0.1$ mm. The value of $s_{\rm max}$ is supported by recent (sub)mm polarization measurements of Class II PPDs in the Taurus region (Bacciotti et al. 2018). $T_{\rm mid}(r)$ is adopted for all sources except T Tan N. In Chapter 3, we noted that the inner disk around T Tan N appears to be optically thick in the 1.3-mm observations and cannot be applied to the irradiated flared disk model. Subsequently,

---

[1]The vertical disk scale height is given by $h = c_{\rm s}/\Omega$, where $c_{\rm s} = \sqrt{k_{\rm B}T_{\rm mid}(r)/\mu m_{\rm p}}$ is the insothermal sound speed and $\Omega = \sqrt{GM_*/r^3}$ is the Keplerian angular velocity. G is the gravitational constant, $k_{\rm B}$ is the Boltzmann constant, and μ is mean molecular weight in units of the proton mass $m_{\rm p}$. By substituting Equation 4.1 (with $\phi = 0.02$) into the scale height ratio h/r, we can obtain the following expression: $h/r \simeq 225 \times 10^{-4}(M_*/M_\odot)^{-0.5}(L_*/L_\odot)^{0.25}(r/1 \text{ au})^{0.25}$.

we used the compromised disk from the disk temperature model given in Chapter 3. From the
above procedure, the derived average densities of dust and gas and h/r_{gap} are presented in Table
4.5.2.

First, for an overview of the relationship between the measured gap size (i.e., $\delta_{\mathrm{I}} \times \Delta_{\mathrm{I}}$)
and a planet's mass, Figure 4.6.2 shows all of the measured gap sizes compared with a general
theoretical curve from Equation 4.4. The curve was derived from general physical parameters,
e.g., a viscous parameter α of 10^{-3}, a gas surface density of 10 g cm^{-2}, a maximum dust size
of 0.1 mm, and a stellar mass of 1 $M_{\odot}$. We adopted an averaged scale height ratio h/r of 0.08
calculated from the Taurus and DSHARP disks in Table 4.6.1. We found that most gaps with
M-K-type stars ($M_* < 1.0 \ M_{\odot}$) are centrally distributed in Neptune-Saturn-mass planets, while
the remaining gaps can be seen in Saturn-Jupiter-mass planets scattered around the center.
Meanwhile, gaps with G-F-A-type stars ($M_* > 1.5 \ M_{\odot}$) appear to be concentrated at 3–10
Jupiter masses. In addition, comparisons with the theoretical curve for each disk are shown in
Figure B.1 and B.2.

Subsequently, we calculated 22 planetary masses from 16 Taurus disks. Similarly, we recal-
culated 11 planetary masses from 8 DSHARP disks (δ_{I} and Δ_{I} of the DSHARP disks are taken
from Huang et al. (2018)) because they only estimate the planetary masses $M_{\mathrm{p},\Delta_{\mathrm{I}}}$ given by the
gap with Δ_{I}. Figure 4.6.3 provides a method of estimating planetary masses using the gap width
Δ_{I} and depth δ_{I}. From the measured width and depth of the gap, two inferred planet masses
$(M_{\mathrm{p},\Delta_{\mathrm{I}}}, M_{\mathrm{p},\delta_{\mathrm{I}}})$ can be derived by adopting Equation 4.2 and 4.3. We employed the average of
the two masses as a representative planetary mass, that is, $M_{\mathrm{p}} = 0.5(M_{\mathrm{p},\Delta_{\mathrm{I}}} + M_{\mathrm{p},\delta_{\mathrm{I}}})$ and set the
original masses to be the upper and lower limits, respectively. This method means that when
the measured δ_{I} and Δ_{I} are in good agreement with the theoretical curve in Equation 4.4, the
estimate converges to a specific planetary mass and decreases its mass range. This situation
suggests that the measured gap properties successfully explain a possible gap from a planet, as
derived by a hydrodynamic simulation. Although there are uncertainties of $\sim 15\%$ on the mea-
sured gap width and depth (see Section 4.5.5), recalculating these values with the uncertainties
reveals that the planetary mass estimates would diverge by up to a factor of two from the above
estimate. Such errors would not significantly change the tendency of the inferred planetary mass
populations, e.g., moving from a Saturn mass to Jupiter mass. The inferred planetary masses
over a wide range of $\alpha_{\mathrm{vis}} = 10^{-2} - 10^{-4}$ for each disk are listed in Table 4.6.1.

4.6.4   Classification of the Inferred Planets into Four Cases

To investigate how the derived 33 planet masses reconcile with the theoretical curves in Eq. 4.4,
we classify them into four cases by inspecting the relation between the location of the measured
gap properties and each theoretical curve on the $\delta_{\mathrm{I}} - \Delta_{\mathrm{I}}$ plane (see Figure B.1 and B.2). The
categorized planetary-mass features are summarized in Table 4.6.2.

Figure 4.6.4 shows the inferred planetary mass versus the planet's semi-major axis, including
the four categorized planetary-mass features in the histograms. Case 1 defines a large gap width

Table 4.6.2:: Classification of 33 Inferred Planets into Four Cases.

Cases	Names (gap location in au)
(1)	(2)
Case 1 (8/33)	AS 209 (D9), HD 143006 (D22), SR 4 (D11), CI Tau (D16), RY Tau (D6), DS Tau (D32), GM Aur (D16), DM Tau (D12)
Case 2 (5/33)	Elias 24 (D57), GW Lup (D74), HD 163296 (D48), HD 163296 (D86), MWC 480 (D78)
Case 3 (8/33)	HD 163296 (D10), T Tau N (D12), DR Tau (D37), GO Tau (D55), GO Tau (D95), HP Tau (D11), FT Tau (D27), Haro 6-37 C (D79)
Case 4 (12/33)	Elias 27 (D69), HD 142666 (D16), HD 143006 (D51), CI Tau (D49), CI Tau (D131), DL Tau (D66), DL Tau (D94), RY Tau (D46), UZ Tau E (D69), AA Tau (D78), LkCa 15 (D87), GM Aur (D69)

Note. — The 33 inferred planets located in the gaps are classified into four cases through a comparison of the measured gap size ($\delta_{\rm I}$, $\Delta_{\rm I}$) and the theoretical curve in Figure B.1 and B.2. The cases are quantitatively judged by the criterion that $d \lesssim 1$ for case 4 and otherwise for cases 1 and 2 on the $\delta_{\rm I} - \Delta_{\rm I}$ plane, where d is the shortest distance between the measured point and the theoretical curve. Column description: (1) Case 1: normalized gap width $\Delta_{\rm I}$ is larger than the theoretical curve. Case 2: gap depth $\delta_{\rm I}$ is larger than the theoretical curve. Case 3: gap width $\Delta_{\rm I,unit}$ is not sufficiently spatially resolved ($\theta > \Delta_{\rm I,unit}$). Case 4: the gap width and depth approximate the theoretical curve. (2) The 33 names/gaps of the sources taken from the 22 Taurus and 11 DSHARP disks.

in the disk in the vicinity of the primary star ($r_{\rm gap} = 10 - 30$ au), which implies a Jupiter-mass planet. By increasing h/r by approximately $2 - 3$ times our estimates, the measurements intersect the theoretical curve (i.e., $h/r \sim 0.1 - 0.3$ at $r_{\rm gap} = 10 - 30$ au; Figure B.1 and B.2). In this case, we must consider a vertically thick disk in the vicinity of the primary star within this region. The modified planetary mass approaches the upper limit of our original planet mass (estimated from the gap width) and increases to a few Jupiter masses. It should be noted that RY Tau (D6), GM Aur (D16), and HD 143006 (D22) have planetary masses above 20 $M_{\rm Jup}$. In this case, the theoretical curve itself is unsuitable, although another mechanism not of planetary origin may work.

Case 2 defines a large gap depth at the far side of the primary star ($r_{\rm gap} > 50$ au), and a planet of several Jupiter masses is inferred. For the measured and theoretical values to intersect, h/r must be $0.3 - 0.5$ times smaller than our original estimates (i.e., $h/r \sim 0.02 - 0.04$ at $r_{\rm gap} > 50$ au; ; Figure B.1 and B.2). In this case, a vertically thin disk must be considered in the region. The modified planetary masses are close to the lower limits of our original planetary masses (estimated from the gap width), which are approximately of Jupiter mass. Several disks that fit Case 2 may have an overestimated gap depth because the intensity at its gap location is in the vicinity of the noise level. In that case, the planetary masses estimated from the gap depth could be overestimated; hence, care must be taken when calculating its masses. With a few exceptions in cases 1 and 2, the planetary masses fitted to the theoretical curves are found to be within the error of our original planetary mass estimates; therefore, we adopt the original planetary masses to investigate the following sections.
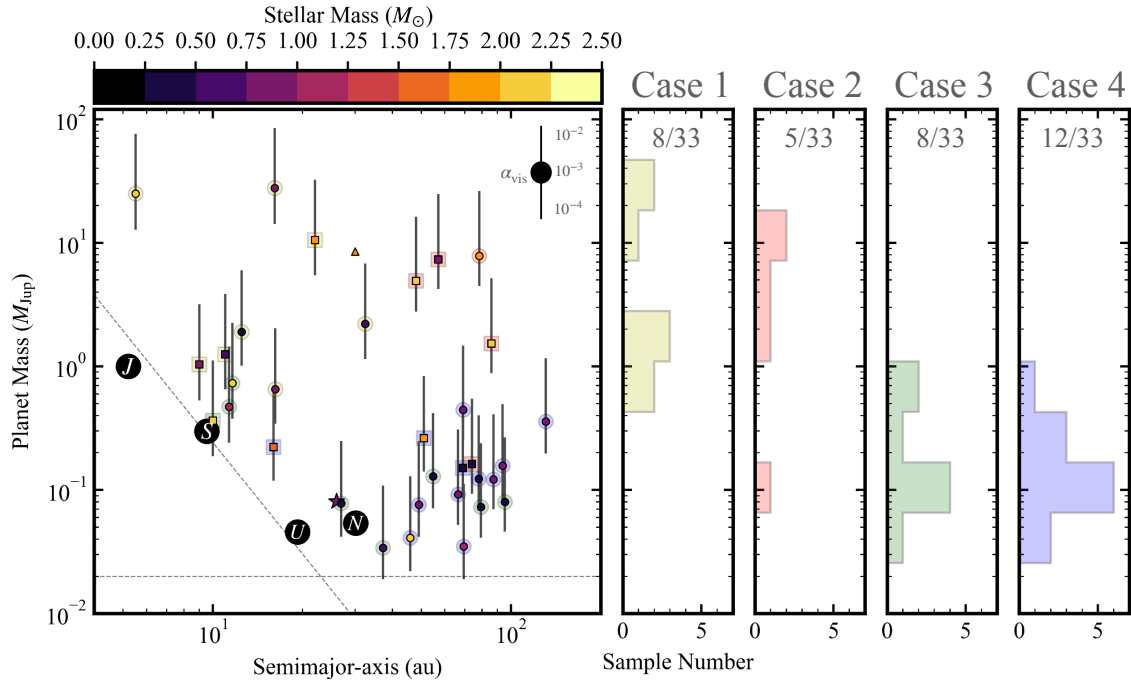
Figure 4.6.4: Left panel: Inferred planetary mass versus the planet's semi-major axis. The circle, square, and star markers indicate the planetary masses of Taurus disks, DSHARP disks, and TW Hya, respectively. The derivation of the planetary mass is based on the viscous parameter $\alpha_{\rm vis} = 10^{-3}$, including the error bars in the case of $\alpha_{\rm vis} = 10^{-4} - 10^{-2}$. For reference, the star and triangle indicate the inferred planets of the TW Hya and AB Aur disks taken from previous studies. The host stellar mass gives the color scale in each sample. For comparison, the four categories of planetary masses in Table 4.6.2 are colored around each sample. The yellow, red, green, and blue represent case 1, case 2, case 3, and case 4, respectively. The diagonal dotted line indicates the detection limit of the planet mass given by the Hill radius. The horizontal dotted line indicates the upper limit of the minimum planetary mass for reproducing the gap. Right panel: Histograms of planetary masses classified into four categories.

In case 3, the gap width $\Delta_{\rm I,unit}$ is not sufficiently spatially resolved ($\theta > \Delta_{\rm I,unit}$). Thus, it is not included in further discussions because of the indeterminacy of the spatially unresolved gap width. There is a method to infer the planetary mass from a spatially unresolved gap structure under the assumption that the gap size is conserved, as in Chapter 3; however, this method lacks verification that the gap size is correctly conserved. Another approach used by Kanagawa et al. (2015, 2016) demonstrates this conservation (Tsukagoshi et al. 2016, priv. comm) but requires a separate process to measure the gap size from the dust (gas) density profile.

For case 4, the gap width and depth approximate the theoretical curve. Case 4 is inferred for a Neptune-mass planet and is consistent with the planetary masses derived by the theoretical curve within the error range. 12 out of 33 sources (36%) are categorized as case 4.

4.6.5 Comparison between Our Estimates of Planet Mass and Values from Previous Studies

Four disks in our Taurus sample, MWC 480 (Liu et al. 2019), CI Tau (Clarke et al. 2018), DS Tau (Veronesi et al. 2020), and LkCa 15 (Facchini et al. 2020) have been previously investigated using detailed hydrodynamical simulations based on the a planet-disk interaction and the same ALMA data. We found that our planet-mass estimates agree with those from the simulations within the error.

We also compare our estimates with recent surveys searching for planetary-mass companions in Taurus and DSHARP. Wallace et al. (2020) surveyed 55 Taurus Class I/II disks using KECK II near-infrared observations and detected no Jupiter mass planets ($5-10$ M_{Jup}) at separations of $50-100$ au from the central star with $\sim 50\%$ probability. These observations place an upper limit on the mass of planets far from the central star ($r = 50-100$ au) and suggest that our estimates for viscous parameters α_{vis} of $10^{-4}-10^{-3}$ are within the upper limit of the planetary mass. Jorquera et al. (2021) surveyed 10 DSHARP disks using NaCo/VLT infrared observations, including the four disks we used in this study (i.e., AS 209, Elias 24, GW Lup, and HD 143006). The detection of a point-like source candidate was only reported in the disk gap of Elias 24 at r = 55 au ($0''.42$). Assuming it is a planetary companion, its mass was suggested to be in the range of $0.5-5.0$ M_{Jup}, which is in agreement with our estimate of 3.08 ± 2.67 M_{Jup} for $\alpha_{\mathrm{vis}} = 10^{-4}$. For all the remaining systems, the lack of detection suggests the presence of planetary companions with masses lower than 5 M_{Jup}, which reconciles with our estimates. It is worth noting that our estimate of the inferred planet around HD 143006 (D22) is of a few Jupiter masses; however, the Very Large Telescope (VLT) observations cannot confirm this candidate near the central star owing to an instrumental detection limit (see Fig 3 in Jorquera et al. 2021).

4.6.6 Nature of Gap-opening Planets in Disks

Figure 4.6.5 shows a planetary mass versus planet semi-major axis plot for exoplanets and gap-opening planets in the disks[1]. First, we investigated an observational bias as a limit of the detectable planetary mass in Appendix C and placed the limits in Figure 4.6.5. By considering the limits missing in our sample, planets with lower masses than a Saturn-Jupiter mass in inner disks ($r = 5-20$ au) appear to be affected by the bias due to limitations in the spatial resolution. For the outer region, the lower boundary of planet mass around the Neptune mass appears to be affected by the minimum planet mass for gap-opening. A void of Neptune-Saturn mass planets is found at $r = 20-40$ au; however, we consider that several disks with inflections will

---

[1]In Figure 4.6.5, we added two source candidates around AB Aur ($M_{\mathrm{p}} = 8.5 \pm 4.5$ M_{Jup}, $r = 30$ au; Boccaletti et al. 2020) and TW Hya ($M_{\mathrm{p}} \sim 0.08$ M_{Jup}, $r = 26$ au; Tsukagoshi et al. 2016). The SPHERE/VLT observations detected the candidate at r = 30 au around AB Aur, whose surrounding dust material forms a twist in the large disk gap. The twist can be reproduced with a planet-driven density wave model, translating into a Jupiter planet mass. ALMA dual-wavelength observations revealed the disk gaps at $r = 26$ au around TW Hya, indicating a deficit of dust grains within the gap owing to dust filtration caused by an unseen planet with a Neptune mass.
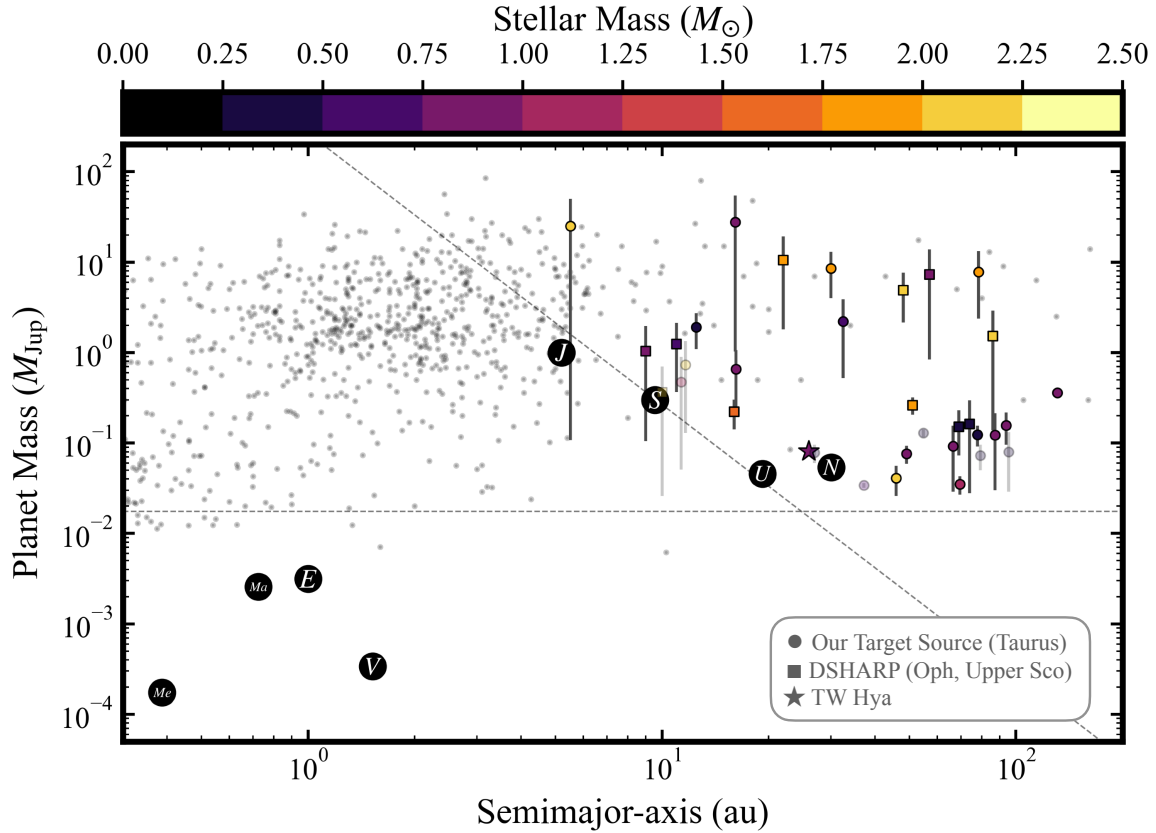
Figure 4.6.5: Inferred planetary mass versus the planet's semi-major axis. The circle, square, and star markers indicate the planetary masses of Taurus disks, DSHARP disks, and TW Hya, respectively. The derivation of the planetary mass is based on the viscous parameter $\alpha_{\rm vis} = 10^{-3}$. The host stellar mass gives the color scale in each sample. We note that the lightly-colored markers indicate the planet masses derived from the spatially unresolved gaps compared with the spatial resolutions (i.e., case 3: $\theta > \Delta_{\rm I,unit}$, in Table 4.6.2). The samples are not counted in the histogram. The diagonal dotted line indicates the detection limit of the planet mass given by the Hill radius. The horizontal dotted line indicates the upper limit of the minimum planetary mass for reproducing the gap. The black circles with white labels indicate planets of the solar system. For reference, the small black dots are exoplanets confirmed in the Open Exoplanet Catalogue (https://github.com/OpenExoplanetCatalogue/open_exoplanet_catalogue).
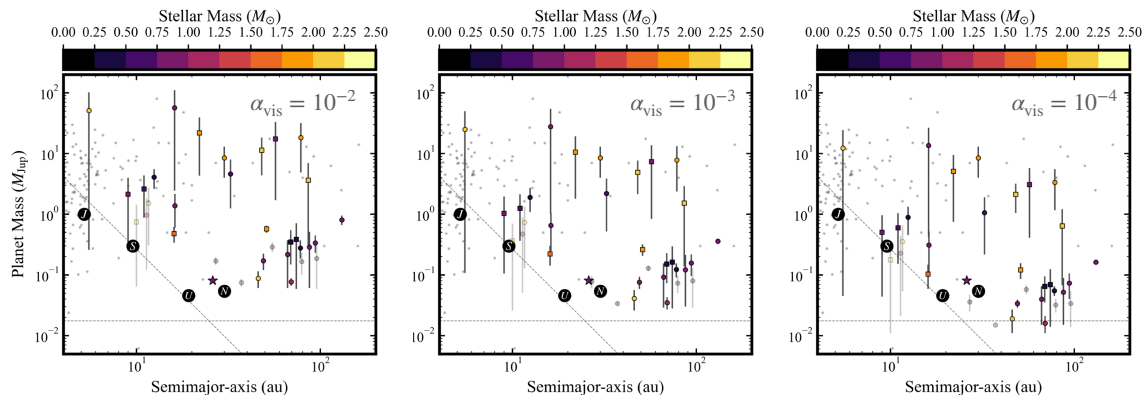
Figure 4.6.6: Close-up views of the inferred planetary mass versus the planet's semi-major axis. Both axes are the same as in Figure 4.6.5; however, the planetary mass varies in the viscous parameter α_{vis} ranging from 10^{-4} up to 10^{-2}. The left, center, and right panels represent the cases for $\alpha_{\mathrm{vis}} = 10^{-2}$, 10^{-3}, and 10^{-4}, respectively.

probably host smaller mass planets than those responsible for clear gaps. Several examples of such small-mass planets will be expected even at $r = 20 - 40$ au (see Table 4.5.2).

It is likely that stars with higher masses will host planets with higher masses; the majority of the outer planets of low mass stars (M-K-type: $M_* = 0.3 - 1.5 \ M_\odot$) are Neptune-mass planets, while more massive stars (G-F-A-type: $M_* = 1.5 - 2.5 \ M_\odot$) host Jupiter-mass outer planets. As shown in Figure 4.6.6, changing the viscous parameter α_{vis} from 10^{-4} to 10^{-2} does not break the stellar mass dependence of the inferred planet mass.

To explore this trend and dependence, Figure 4.6.7 presents the relation between the disk radius and inferred planetary mass. Each inferred planet is extracted only from the most massive planet (hereafter, the primary planet) in the 20 spatially-resolved gap disks for $\alpha_{\mathrm{vis}} = 10^{-3}$. The primary planets in the large disks ($r_d > 45$ au) are found to be located at a radius of 20 au from the primary star in 70% of cases. A correlation appears to have the primary planet mass depending on the stellar mass for the large disk. In regions far from the primary stars, Neptune-mass (or sub-Saturn-mass) planets are found only in the M-K-type stars (corresponding to case 4 in Section 4.6.4), whereas the G-F-A-type stars have Jupiter-mass planets (corresponding to case 2 in Section 4.6.4). However, because a few samples remain in the inferred planets of case 2, it is not sufficient to conclude that Jupiter-mass planets are robust. The Neptune-mass planets in case 4 account for 80%(8/10) of the primary planets around M-K-type stars, which instead supports this trend.

Recent exoplanet surveys have suggested that the occurrence of giant planets is positively correlated with the stellar mass (Johnson et al. 2010) and Neptune planets are more common around low-mass stars (Mulders et al. 2015; Mulders 2018). Our results appear to reconcile with these exoplanet properties, suggesting a possible link between exoplanets and forming planets in dust disks. In addition, the challenging detection of such planets directly should be a critical topic of investigation in observations using the James Webb Space Telescope (JWST) and other
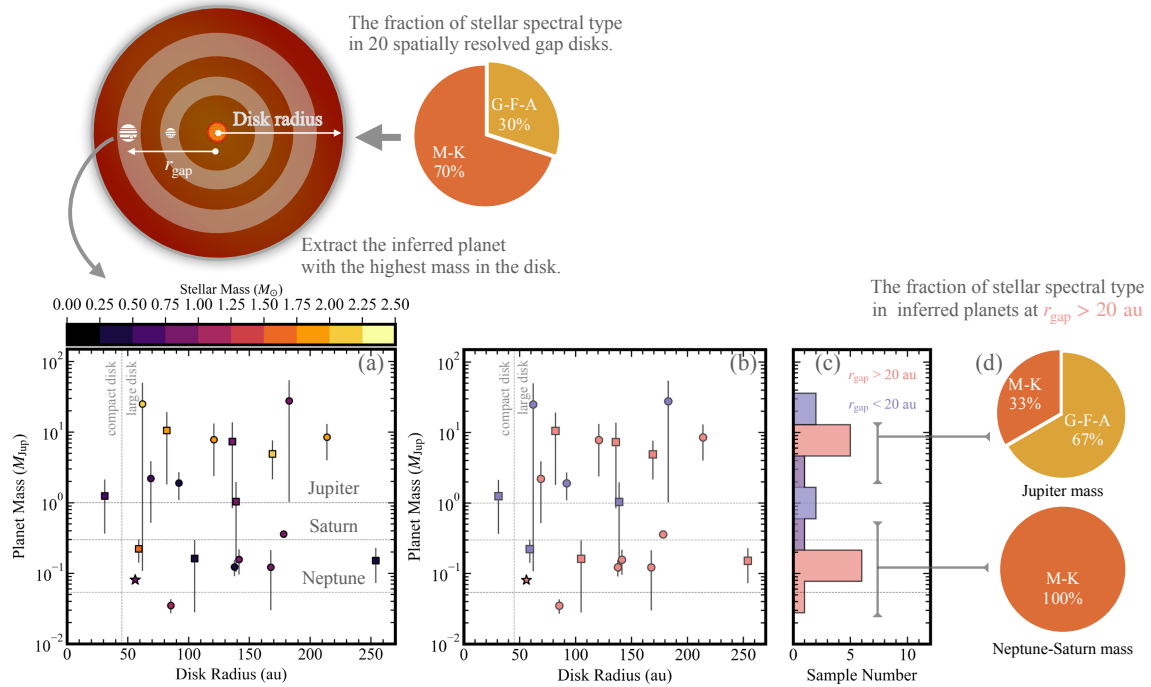
Figure 4.6.7: The relation between the disk radius and inferred planetary mass to explore the stellar mass dependence. (a) Disk radius versus inferred planet mass. As shown in the schematic view, each planetary mass is extracted only from the most massive planet in the spatially resolved gap disks ($\theta < \Delta_{I,unit}$) for $\alpha_{vis} = 10^{-3}$. The circle, square, and star markers indicate the planetary masses of Taurus disks, DSHARP disks, and TW Hya, respectively. (b) The same figure as (a), but color-coded according to the gap location r_{gap} at which the inferred planet forms. Red indicates $r_{gap} > 20$ au, and blue indicates $r_{gap} < 20$ au. (c) Histogram compiled from the scatter diagram in (b), color-coded according to the position of the gap, as in (b). (d) Pie chart of the planetary mass in the gap identified at $r_{gap} > 20$ au. The planetary mass is classified by the spectral type of the primary star. In large disks ($r_d > 45$ au), Neptune-mass planets are filled with M-K-type stars ($M_* = 0.3 - 1.5\ M_\odot$), whereas Jupiter-mass planets are dominated by G-F-A-type stars ($M_* = 1.5 - 2.5\ M_\odot$).

future large telescopes, such as the European Extremely Large Telescope (E-ELT) and Thirty
Meter Telescope (TMT).

4.7   Conclusions

Using super-resolution imaging with SpM, we investigated 40 Class-II protoplanetary disks in
the Taurus star-forming region. The dust disk radii r_d in our sample have a wide range of r_d to
8 au to 200 au. A summary of our findings is as follows:

1. The target disk sample is based on ALMA archival Band 6 (1.3 mm) data, which were
   observed with a nominal resolution of less than $0''.1 - 0''.2$ and a relatively high SNR. Using
   the SpM images of the 40 disk sources, the statistical nature of this method, including its
   achievable effective spatial resolution and the limitation on its applicability, was investi-
   gated, and we found that SpM achieves a better spatial resolution than the conventional
   CLEAN method (i.e., $\sim 30 - 50\%$ of the CLEAN beam in size for a half of the disk sample
   with a more compact size and higher SNR).

2. The imaging technique drastically improves the spatial resolution of the images. Our SpM
   images reveal 23 gaps, 29 rings, and 30 inflections in the radial intensity profiles. The gap
   locations r_gap of the collected disks are located at $r_\mathrm{gap} = 5.5$ to 131 au; $r_\mathrm{gap}/r_\mathrm{d}$, which is the
   gap location normalized by their disk radius, was found to be approximately 0.1 or 0.4–0.7.
   The almost inflections r_inf are behind the gaps. It would be reasonable to suggest that such
   inflections are formed behind the gaps as a shoulder; however, if the spatially unresolved
   gaps dominate the remaining inflections, they form everywhere. These candidates can be
   identified, especially in compact disks imaged at resolutions of $0''.05 - 0''.10$, and their
   inflection locations are centrally distributed at $r_\mathrm{inf} = 10 - 20$ au.

3. We investigated the stellar mass dependence of the gap properties, gathered from the
   33 gaps of 24 disks, including DSHARP disks. We found a tendency for the size of the
   gaps in the outer regions ($r_\mathrm{gap} > 20$ au) to differ depending on the stellar mass (or the
   stellar spectral type). The distribution of the spatially-resolved gap sizes is in the range
   of $10^1 - 10^2$ for M-K-type stars and increases by one order of magnitude to $\sim 10^3$ for
   A-F-G-type stars.

4. We estimate planetary masses assuming that the annular gaps are due to forming planets
   and apply the theoretical method of gap-formation, which connects the planetary mass
   and gap properties. Even though the viscous parameter is taken over the wide range
   $10^{-2} - 10^{-4}$, changes in the planet mass depending on the stellar mass is likely observed for
   large disks. The majority of the outer planets of low-mass stars (M-K-type) are Neptune-
   mass planets, whereas more massive stars (G-F-A-type) have Jupiter-mass outer planets.
   However, this is not yet sufficient to conclude that the trend of Jupiter-mass planets is
   robust because only four are counted by samples in the G-F-A-type stars. Neptune-mass

planets account for 80% (8/10) of the ten inferred planets around M-K-type stars, which
reasonably supports this trend.

5. Substructures, such as gaps and rings, were found to be common, even for compact/large
Class II disks in the Taurus region, and planetary masses inferred from gap properties
appear to be analogous to those of gas giants and intermediate planets in our solar system.

Software: AnalysisUtilities (`https://casaguides.nrao.edu/index.php?title=Analysis_Utilities`), Astropy (Astropy Collaboration et al. 2013), CASA (McMullin et al. 2007), DIFMAP
(Shepherd et al. 1994), Matplotlib (Hunter 2007), PRIISM (Nakazato & Ikeda 2020), SciPy
(Jones et al. 2001), least-squares fitting (Hammel & Sullivan-Molina 2020)

Appendix

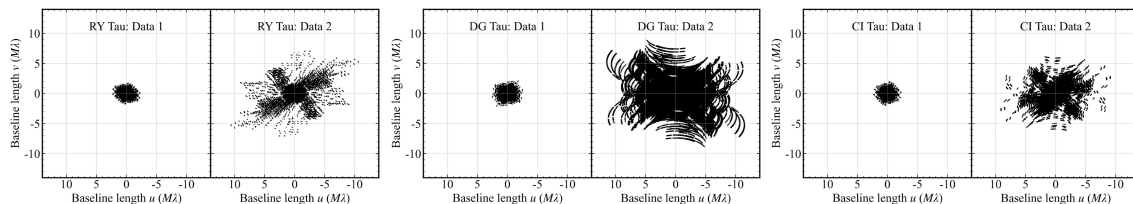## A   Evaluation of Sparse Modeling with Three Disks

Figure A.1: $uv-$coverage of six datasets from ALMA Band 6 (1.3 mm) observations. The left,
middle, and right panels show the cases of RY Tau, DG Tau, and CI Tau, respectively. Each
source is observed separately with a compact array configuration (labeled as Data 1) and a more
extended array configuration (labeled as Data 2). The baseline length between Data 1 and Data
2 differs by a factor of $3-4$.

In this section, the main objective is to evaluate the performance of SpM super-resolution
imaging using two datasets with different spatial resolutions in the same manner as in Chapter
2. The first uses a shorter-baseline dataset in each target source, and the second uses a longer-
baseline dataset. For simplicity, we refer to the short- and long-baseline datasets as Data 1 and
Data 2, respectively. Here, three Taurus disks, RY Tau, DG Tau, and CI Tau, are employed
in our investigation to evaluate the performance of SpM imaging. The RY Tau and DG Tau
disks have brighter distributions throughout but differ in the presence of gaps (Francis & van
der Marel 2020; Podio et al. 2020). The CI Tau disk has been confirmed to have a high-contrast
intensity distribution and multiple gaps (Clarke et al. 2018). Figure A.1 shows the $uv-$coverages
of each dataset. The maximum sizes of the baseline lengths differ by a factor of 3–4, indicating
the same difference in the size of the synthesized beams. The properties for each dataset are
presented in Table A.1. Data 2 was applied with the combined short-baseline and long-baseline
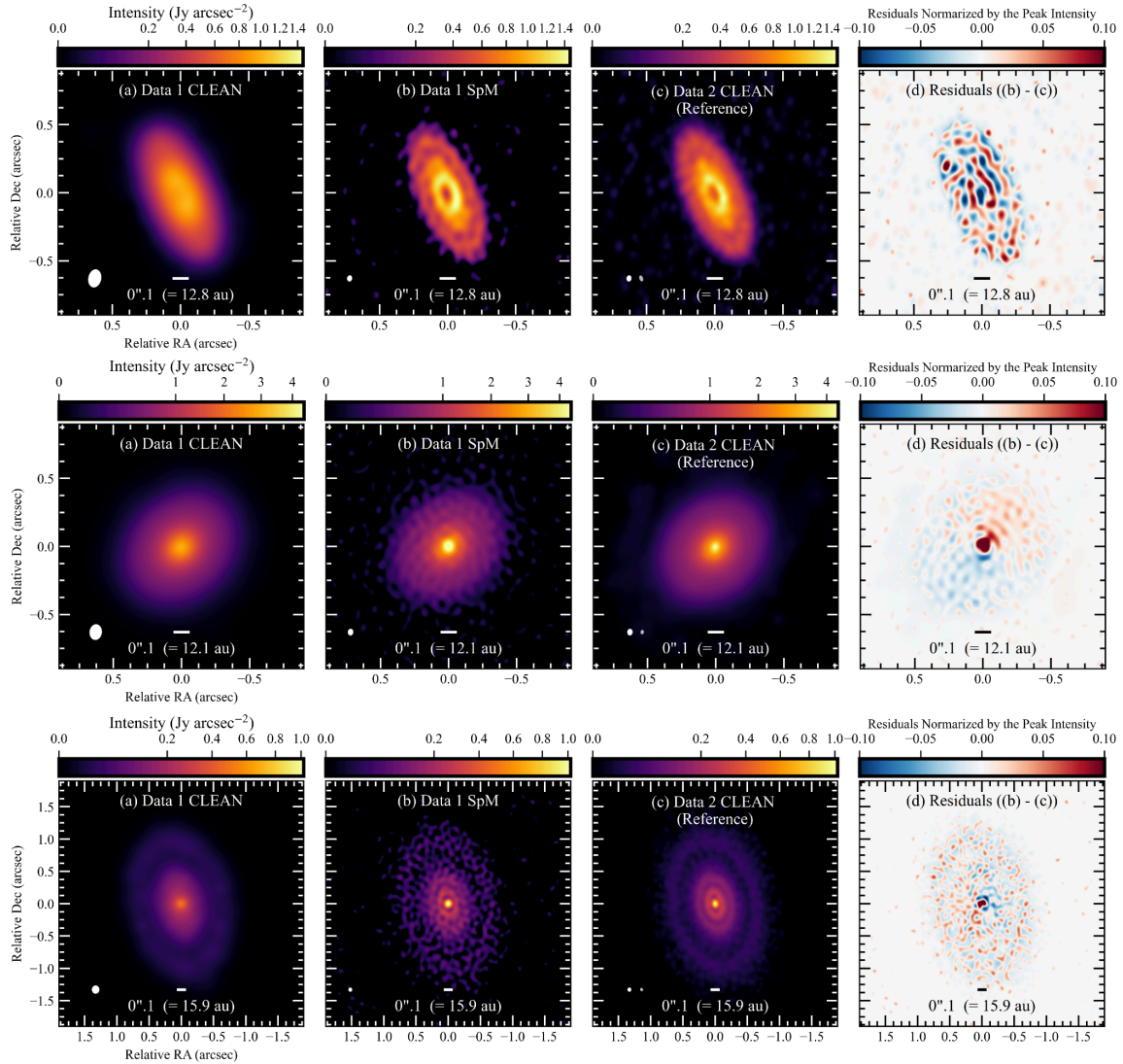data used in Section 4.5, achieving a spatial resolution of $0''.04 - 0.0''.5$. Data 1 was applied

Figure A.2: Images of three Taurus disks (top: RY Tau, middle: DG Tau, and bottom: CI Tau) constructed with datasets from ALMA 1.3-mm observations. The same color scale is applied to the power-law relationship (i.e., $y = x^\gamma$, where γ is the power and $\gamma = 0.5$ is adopted). (a) The CLEAN images of Data 1 with `Briggs robust` parameter of 0.5. (b) The SpM images of Data 1. (c) The CLEAN images of Data 2 with a `Briggs robust` parameter of 0.5. The images are regarded as reference images. Note that when comparing the same resolution of Data 1 and Data 2, each Data 2 CLEAN model is finally convolved with the beam size corresponding to the effective spatial resolution of the Data 1 SpM image. For reference, the white and gray filled ellipses in the bottom left corner denote the spatial resolution of Data 1 SpM and Data 2 CLEAN. (d) The residual map ((b) - (c)). The color scale is normalized by the peak intensity of the residual map. For reference, a white bar of $0''.1$ is provided to the angular scales. The total flux of the Data 1 SpM and CLEAN images are scaled to that of the Data 2 CLEAN image to minimize the effects of flux-calibration errors.

Figure A.3: Top panel: Deprojected and az-
imuthally averaged radial intensity profiles
taken from the three Taurus disks, RY Tau
(ref), DG Tau (purple), and CI Tau (yellow).
The solid lines denote the profile given by the
Data 2 CLEAN image (i.e., the reference),
while the dashed lines denote the profile given
by the Data 1 SpM image (i.e., evaluated).
For reference, each detection threshold I_{DT}
taken from the Data 1 SpM images shows the
horizontal dotted line on the profile. Bottom
panel: The residual profiles given by Data 1
and Data 2. The percentage of the residual
scale is calculated as (Data 1 - Data 2)/Data
2. The values below I_{DT} are represented by
the dotted line on the profile. All the Data
1 SpM show a residual within 20% compared
with the references. The total flux of the Data
1 SpM image is scaled to that of the Data 2
CLEAN image to minimize the effects of flux-
calibration errors.
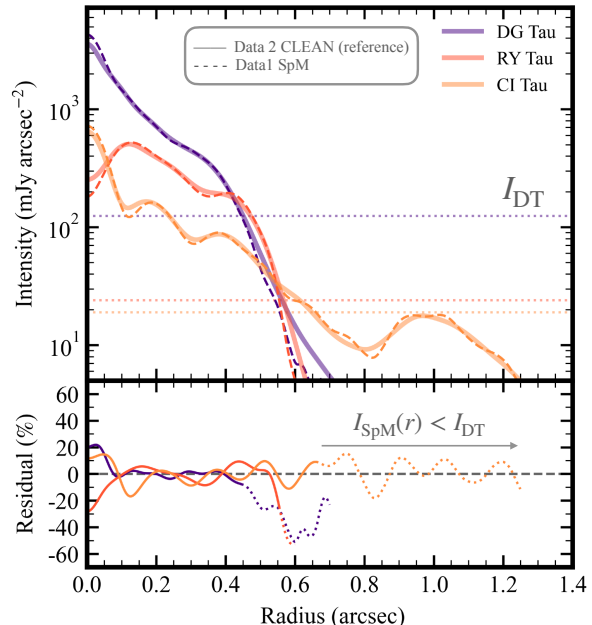
with Data 2 short-baseline data alone and calibrated, self-calibrated, and imaged using the same
procedure as in Section 4.4. First, we found that the Data 1 spatial resolution on the CLEAN
image is $0''.11 - 0.13$ and that on the SpM image is $0''.05 - 0''.07$, that is, SpM achieves $40 - 50\%$
of the beam size compared to the that of CLEAN.

Figure A.2 shows the resultant images of the three Taurus disks after various imaging with
different datasets. First, we compare the CLEAN and SpM images of Data 1. In the RY Tau
and CI Tau disks, SpM can reconstruct a substructure (i.e., a gap and inner hole) that CLEAN
could not reconstruct because its spatial resolution was improved by up to two times. SpM does
not erroneously reproduce gaps, as shown in the result of the DG Tau disk. As shown in Figure
A.3, compared to the reference of the high-resolution images of Data 2 CLEAN, SpM presents
good agreement in the gap and disk size within a 20% error on the area where the intensity
is above I_{DT} for all samples. On the 2-D image, SpM can reproduce the non-axisymmetric
structures of the RY Tau disk appearing as a bright ring at $r = 15$ au ($r = 0''.1$), representing
its imaging strength. In contrast, a good example of the disadvantages of this method is the
high-contrast intensity of the CI Tau disk structure. The CI Tau disk has a higher intensity
distribution around the central region, consistent with the reference. However, the lower intensity
distributions change the situation, especially for a faint ring ($I_\nu(r) < I_{DT}$) at $r > 150$ au (or
$r > 1''.0$). SpM reconstructs an artificial and sparsity structure around there. This behavior
can be explained by the fact that it works with a bias to weight higher intensity areas, whereas

the fitting weights are generally ignored in weaker areas. In other words, if the gradient of the disk intensity is relatively low on the image and its image has a high SNR, SpM should work well. This point would also demonstrate that the RY Tau and DG Tau disks are good sources for reconstructing high-fidelity images with SpM because of their low-contrast intensity distributions.

Table A.1.   Disks Sample and CLEAN/SpM Image Properties.

Name (1)	Freq (GHz) (2)	D_{max} (m) (3)	θ_{cl} (mas, PA) (4)	θ_{eff} (mas, PA) (5)	σ_{cl} (mJy asec^{-2}) (6)	I_{DT} (mJy asec^{-2}) (7)	CL F_ν (mJy) (8)	SpM F_ν (mJy) (9)	$\log \Lambda, \log \Lambda_{tsv}$ (10)
RY Tau									
Data 1	225	3638	$150 \times 106(-11.4°)$	$52 \times 41(-9.0°)$	2.7	72.1	208	204	(5,10)
Data 2	225	16196	$51 \times 30(20.5°)$	.	22.2	.	204	.	.
DG Tau									
Data 1	245	3697	$129 \times 101(-7.2°)$	$55 \times 45(-5.2°)$	2.5	51.4	388	347	(5,11)
Data 2	237	13815	$36 \times 27(-5.7°)$	.	11.3	.	360	.	.
CI Tau									
Data 1	225	3638	$136 \times 124(-1.7°)$	$69 \times 62(4.6°)$	2.8	49.7	131	138	(5,11)
Data 2	230	12145	$58 \times 45(14.1°)$	.	5.1	.	118	.	.

Note. — Column description: (1) Name of host star and dataset. (2) Observed frequency. All target sources are taken from ALMA Band 6 observations. (3) Maximum baseline length D_{max} of the observed visibilities. (4) CLEAN beam size θ_{cl}. **Briggssrobust** parameter is set to be 0.5. (5) SpM beam size θ_{eff}. The beam size (effective spatial resolution) of each image is taken from a point source simulation. (6) RMS noise σ_{cl} of the CLEAN image. The value is derived from the emission-free area. (7) Detection threshold I_{DT} of the SpM image. The value is derived from the peak value in the emission-free area. (8, 9) Total flux F_{nu} of each CLEAN and SpM image. The flux is taken from the total value above $5\sigma_{cl}$ for CLEAN or I_{DT} for SpM. (10) Two regularization parameters ($\log \Lambda_l, \log \Lambda_{tsv}$) adopted for each SpM image.

References. — ALMA project IDs.
RY Tau Data 1: 2016.1.01164.S, and Data2: 2016.1.01164.S, 2017.1.01460.S.
DG Tau Data 1: 2016.1.00846.S, and Data 2: 2015.1.00846.S, 2016.1.00846.S.
CI Tau Data 1: 2016.1.01164.S, and Data 2: 2016.1.01164.S, 2016.1.01370.S.

B Measured Gap Properties as Compared with Theoretical Curves

Figure B.1 and B.2 show the measured gap properties (δ_I, Δ_I) in the Taurus and DSHARP disks compared with the theoretical curves from Equation 4.4.

C Observational Bias

The mass estimate for the gap-opening planets should have an observational bias originating from limitations on the spatial resolution. Although it is difficult to estimate such an observational bias correctly, we attempted to investigate the bias as a limit of the detectable planetary mass M_p derived using the Hill radius r_H and an empirical upper limit taken by our samples. First, we used empirically determined scaling relations between the gap properties and the planetary mass. In particular, for low-viscosity disks ($\alpha_\mathrm{vis} = 10^{-3}$), the spatially-resolved gap width $\Delta_\mathrm{I,unit}$ is expected to scale with the planet Hill radius

$$r_\mathrm{H} = \left(\frac{M_\mathrm{p}}{3M_\star}\right)^{1/3} r_\mathrm{gap} \qquad (4.5)$$

Here, we assume that the location of the planet coincides with the gap location r_gap and that Equation 4.5 is compatible with the scaling relation $\Delta_\mathrm{I,unit} = kr_\mathrm{H}$ with a proportionality constant k. To determine the constant k, we used the inferred planetary masses inherent in the gap of each disk and its stellar mass. The median of k was found to be a common value; $k = 6.5$, 6.5, and 6.6 for Taurus, DSHARP, and all samples (Taurus + DSHARP), respectively. The constants are good agreements with previous values ranging from $4 - 8$, depending on the disk parameters (e.g., Rosotti et al. 2016; Lodato et al. 2019). Here, the minimum gap width $\Delta_\mathrm{I,unit}$ is assumed to correspond to the FWHM size of the spatial resolution; when a spatial resolution of $0''.03$ (corresponding to our higher-resolution data) can be achieved at a distance of 140 pc, the minimum $\Delta_\mathrm{I,unit}$ was derived to be 4.2 au. Adopting the minimum mass of the host star (0.3 $M_\odot$) taken from our samples, the constant $k = 6.6$, and the minimum gap width $\Delta = 4.2$ au, the first relationship of the planet's detection limit was established as $M_\mathrm{p} \simeq 243 M_\mathrm{Jup}(r_\mathrm{gap}/1\ \mathrm{au})^{-3}$.

Second, another bias would be the minimum planetary mass for reproducing the annular gap structure. We applied an au upper limit to the average ($M_\mathrm{p,mim} = 0.02\ M_\mathrm{Jup}$) of the two lowest-mass planets located farthest away from the primary stars in our sample; RY Tau (D46) and UZ Tau E (D69) for $\alpha = 10^{-4}$. The upper limit is generally consistent with the another minimum planetary mass of $\sim 0.02 - 0.05\ M_\mathrm{Jup}$, which perturbs the disk modeled in a numeral simulation, assuming that $h/r_\mathrm{gap} = 0.05$ and $M_* = 0.3 - 1.0\ M_\odot$ (Rosotti et al. 2016).
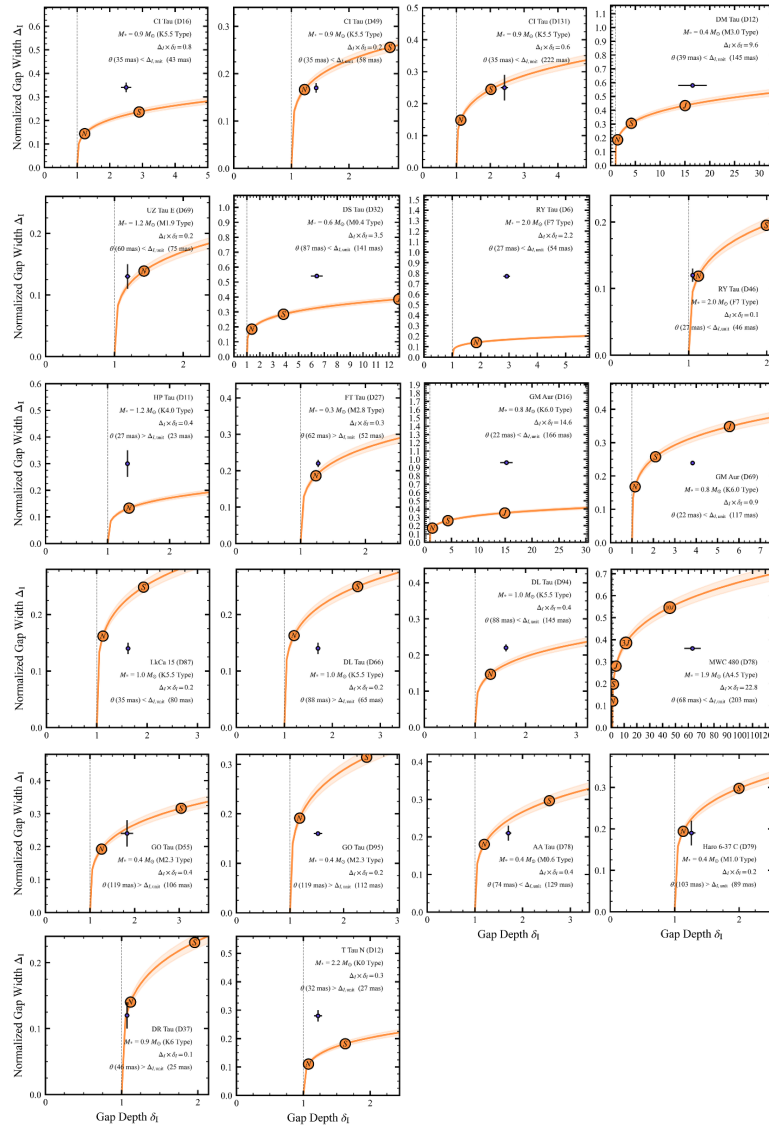
Figure B.1: The measured gap properties $(\delta_{\mathrm{I}},\ \Delta_{\mathrm{I}})$ in the Taurus disks compared with the theoretical curve of the inferred planetary mass from Equation 4.4. The circle marker indicates the gap properties measured from each Taurus disk. The orange curve denotes the theoretical expression derived from the planet-disk interaction, following Equation 4.4. The expression applies to each disk, with its physical parameters listed in Table 4.6.1. The light orange curve shows the theoretical curve in the case of the viscous parameter α of 10^{-3}. The light orange ribbon shows the case with $\alpha_{\mathrm{vis}} = 10^{-2}$ to 10^{-4}, indicating that there is no significant error compared to the case with $\alpha_{\mathrm{vis}} = 10^{-3}$. The vertical dashed line indicates the measurement limit on the gap depth. Applying Equations 4.2 and 4.3 with each stellar mass listed in Table 4.5.1, the planetary masses of the solar system (Neptune: N, Saturn: S, Jupiter: J, three times the Jupiter mass: $3J$, ten times the Jupiter mass: $10J$) are overlaid on the theoretical curve.
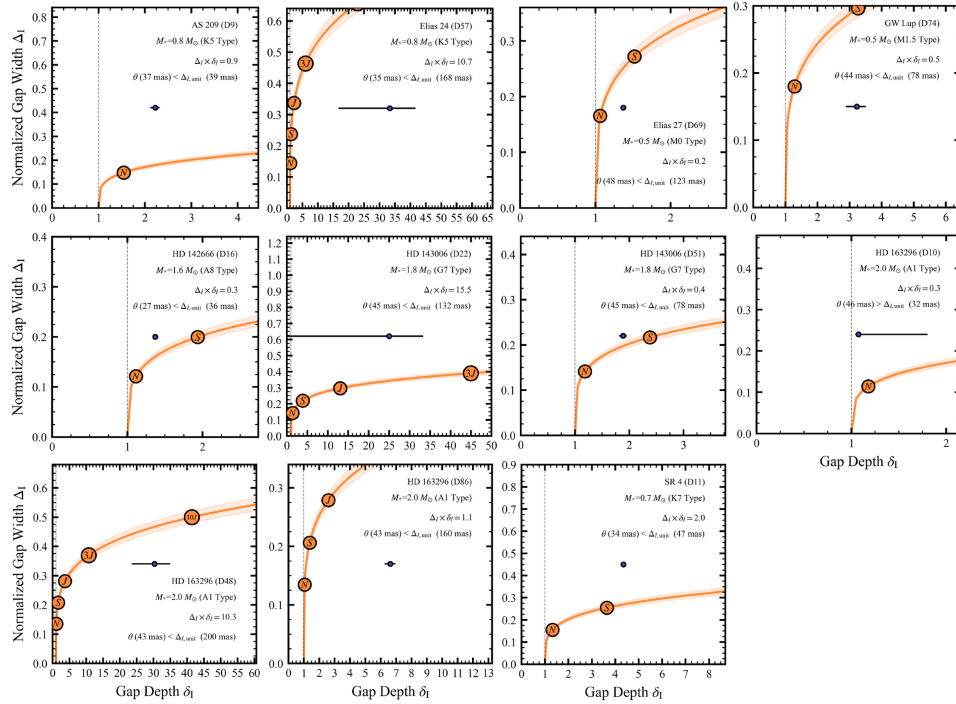
Figure B.2: The measured gap properties ($\delta_{\rm I}$, $\Delta_{\rm I}$) in the DSHARP disks compared with the theoretical curve of the inferred planetary mass in Equation 4.4. The description of the figures are same as in Figure B.1.

Chapter 5

Summary and Conclusions

With a wealth of ALMA observing data, I have investigated whether the new super-resolution imaging technique with sparse modeling (SpM) can achieve 2-3 times the higher spatial resolution than the conventional method (CLEAN) while maintaining a high image fidelity. Furthermore, I have applied the imaging technique to reveal the detailed structure of protoplanetary disks of the T Tau system, which has not been spatially resolved. I finally explored the statistical nature of disk substructures gathered from the Taurus disk survey reconstructed by super-resolution imaging. The main results are summarized below.

1. A protoplanetary disk around HD 142527 showing the lopsided structure was used as the validation source. ALMA has observed the disk in various antenna configurations. The data with different spatial resolutions (i.e., maximum baseline length) in the same frequency band makes it the most suitable for evaluating the performance of super-resolution imaging. As shown in Figure 5.0.1, the validation was performed as follows. (1): I prepared two data consisting of short-baseline configuration (Data 1) and three times longer-baseline one (Data 2). (2): Imaging of Data 2 was performed with the conventional method, CLEAN. (3): Imaging of Data 1 was performed with both SpM and CLEAN. I re-scaled the spatial resolution of Data 1 images into the super-resolution same as the Data 2 resolution. (4): I compared the reconstructed images of Data 1 and 2, respectively. Consequently, I demonstrated that the SpM successfully reconstructs the high-fidelity image even at about three times the spatial resolution of CLEAN (see Figure 5.0.1). In the super-resolution regime, CLEAN reproduces many artificial components on the Data 1 image. Conversely, SpM reconstructs the disk structure comparable to that on the Data 2 CLEAN image. The residual intensity between the SpM Data 1 image and the Data 2 CLEAN image (reference) is less than the flux-calibration errors. Following the successful experimental application of the SpM, I performed a super-resolution imaging of Data 2 with SpM. Figure 5.0.1 shows that the radial profile of the Data 2 SpM image only shows a double ridge-like structure at P.A.= $265° - 270°$, which might indicate the presence of substructure in the horseshoe dust distribution.
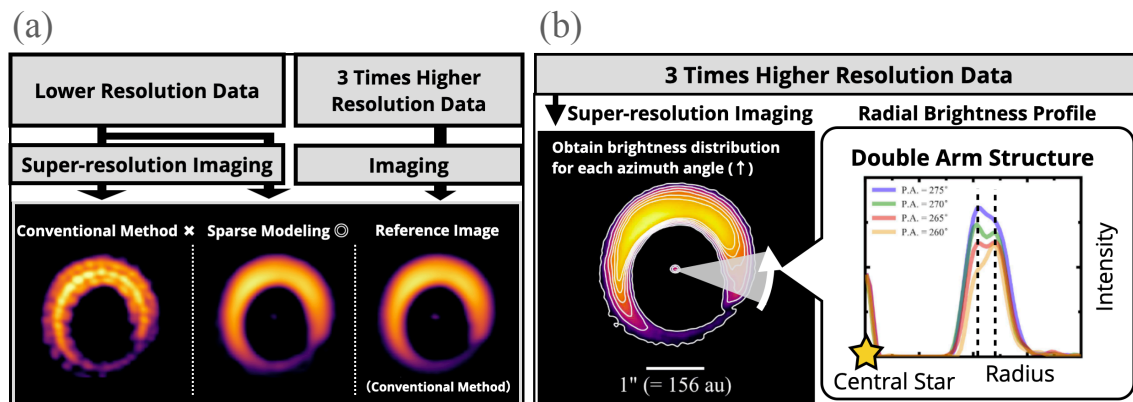
Figure 5.0.1: (a): comparison of reconstructed images between the conventional method (CLEAN) and the new method (SpM) in the super-resolution region. A lopsided disk around HD 142527 is employed in the evaluation with ALMA 0.8 mm (Band 7) observations. (b): the super-resolution image reconstructed by SpM, using high-resolution data. The radial profile of the SpM image only shows a double ridge-like structure at P.A. $= 265° - 270°$.

2. Following the successful experimental application of SpM, I employ the T Tau system. T Tau is a triple star that became an eponymous member of the class of low-mass, pre-main sequence stars. Figure 5.0.2 shows the dust continuum images of CLEAN and SpM at ALMA band 6 (1.3 mm) targeting the T Tau disks. SpM have achieved an effective spatial resolution of $\sim 30\%$ (5 au) compared with the conventional CLEAN beam size at a resolution of 17 au. The reconstructed image reveals a new annular gap structure at $r = 12$ au in the T Tau N compact disk with a dust radius of 24 au and resolves the T Tau Sa and Sb binary into two sources, while the CLEAN image does not resolve them. In the radial visibility profiles, SpM accurately traces the observed data with a null point at the $uv-$distance of~ 1.25 Mλ (suggesting a cavity or a gap structure), whereas the CLEAN profile represents a Gaussian-like profile and could not trace the observed visibilities. Each position of the separated two emissions around T Tau Sa and Sb is in good agreement within their uncertainties, with each one predicted by the stellar orbital model. The dust disk sizes of T Tau Sa and Sb are smaller than 6×4 au and 7×3 au, respectively. The total flux density of T Tau Sb is about seven times lower than T Tau Sa. This ratio implies that the actual disk size of T Tau Sb would be smaller than that of T Tau Sa when considering general scaling relations between disk properties. The T Tau N disk, despite being a small dust disk, would be regarded to be more massive than regular disks. Meanwhile, given the relatively high values of Toomre Q parameter ($Q > 3$) at the outer ring, it appears to be gravitationally stable. If the observed gap structure in the T Tau N disk is caused by an embedded planet, I estimate a Saturn-mass planet when the viscous parameter of the disk is 10^{-3}.

3. I next have studied 1.3 mm super-resolution images for 40 Class II protoplanetary disks in the Taurus star-forming region (see Figure 5.0.3), with following the successful demon-
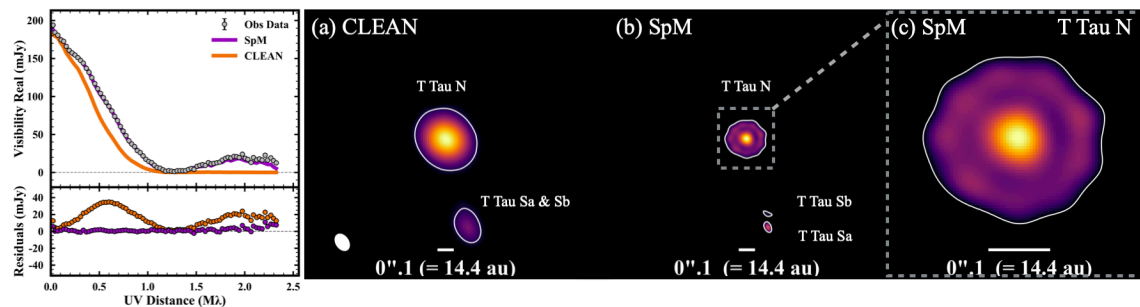
Figure 5.0.2: The left panel shows the azimuthally averaged visibility profiles for models (CLEAN and SpM) and the observation for the T Tau system at ALMA band 6 (240 GHz). Panel (a) shows the CLEAN continuum image. Panel (b) shows the SpM continuum image. Panel (c) shows a close up view of the T Tau N on the SpM image.

stration of SpM imaging applied to two disks (HD 142527 and T Tau). The target disks are based on the ALMA archival Band 6 (1.3 mm) data, which are observed with a nominal resolution less than $0''.1 - 0''.2$. Here I apply the SpM imaging technique to explore several au-scale substructures in the compact and large disks such as gap and ring, which are thought to be possible evidence for forming planets. The dust disk radius r_d is found to have a wide span of r_d from 8 up to 200 au with a median of 45 au. Using the SpM images of the 40 disk sources, statistical nature such as achievable effective spatial resolution and limitation of its applicability has been investigated, and I find that the SpM achieves better spatial resolution than the conventional CLEAN, i.e., $\sim 30 - 50\%$ of the CLEAN beam in size, for half of the disk sample with more compact size and higher SNR. The imaging drastically improves the spatial resolution of the images. SpM images reveal 23 gaps, 29 rings, and 30 inflection (suggesting unresolved gaps or other features), and four disks with a ring alone. The gap locations r_gap of the collected disks are located at $r_\mathrm{gap} = 5.5$ to 131 au; $r_\mathrm{gap}/r_\mathrm{d}$, gap location normalized by their disk radius, is found to be around 0.1 or 0.4-0.7. Including several disks of the Disk Substructures at High Angular Resolution Project (DSHARP), I find the stellar mass dependence of the gap size and then estimate planetary masses assuming the gaps are due to forming planets and by applying the theoretical method of gap-formation, which connects the planetary mass and gap properties. If viscous parameters are taken over a wide range of $10^{-2} - 10^{-4}$, the stellar mass dependence of planetary mass in the outer disk regions ($r > 20$ au) can be observed for large disks. The majority of the inferred planets with a low-mass star (M–K type) is found to be Neptune-mass planets.

This thesis concludes that the new imaging technique using SpM is an attractive choice to provide a high-fidelity super-resolution image with ALMA, substructures such as gap and ring are found to be common for Class II disks in the low mass star-forming regions, and host stellar masses depend on gap size of their disks, suggesting that planetary masses inferred from the gap properties are related to the host stellar mass.
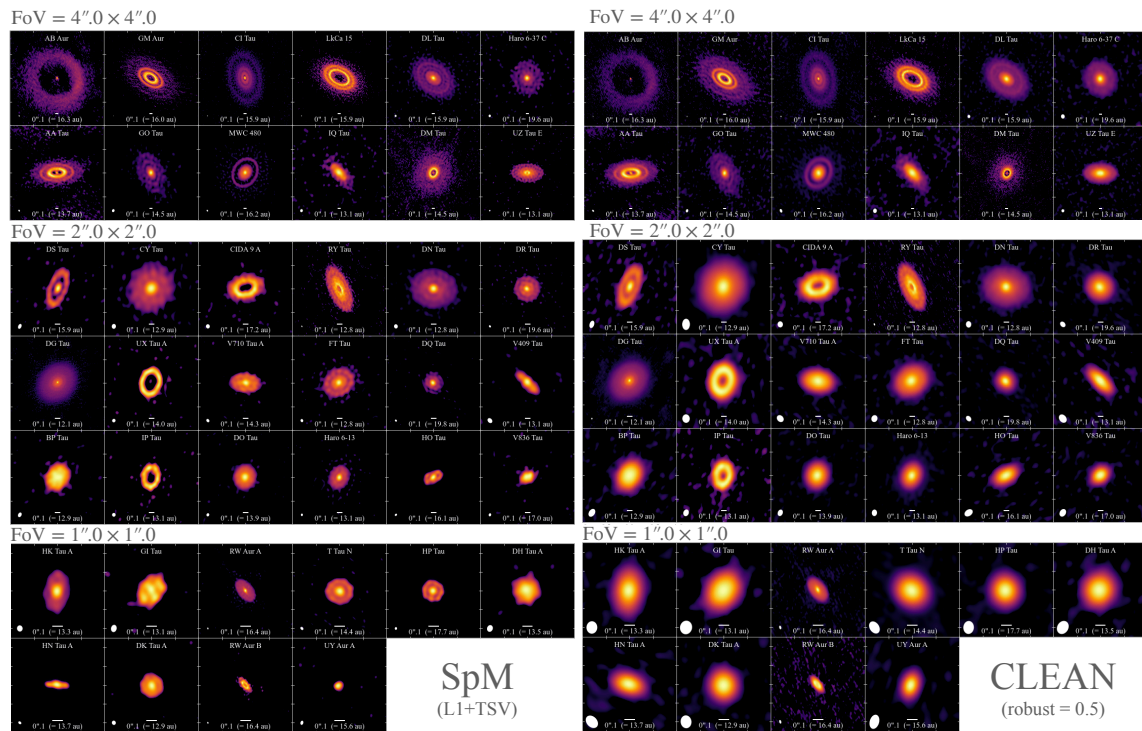
Figure 5.0.3: Gallery of SpM/CLEAN (left or right) images for 40 disks in our sample. Briggs weighting with a robust parameter of 0.5 is adopted for CLEAN images. These images are ordered by decreasing dust disk size from left to right and top to bottom. The same color scale given by a power law with a scaling exponent of $\gamma = 0.45$ is adopted. A white bar of $0.''1$ is provided for reference to the angular scales. A filled white ellipse denotes a spatial resolution in the bottom left corner

Acknowledgments

My interest in astronomy was sparked by the Leonid meteor shower in 2001 when I was in elementary school. At that time, I not only simply looked at the astronomical phenomenon but also asked myself "Why do meteor showers occur?", which led me to develop a deep interest in this field. What led me to strongly aspire to this field was my experience of a radio observation training course organized by the National Astronomical Observatory of Japan (NAOJ) when I was an undergraduate student. During this training, I was able to learn the process of observational research, including observations of a molecular cloud using the Nobeyama 45m radio telescope, analysis of the observed data, and discussion based on the results. This experience made me realize how interesting observational research can be, and made me want to answer the age-old questions in astronomy, for instance, "How did the various stars and planetary systems of the universe come into being?", and "Is there life on other planets?" I would also like to mention how I became interested in data visualization. I remember that my father gave me a computer (an Apple product) at an early age, and I used it to enjoy a variety of software, especially for drawing pictures. Working with computers was thus a natural thing for me, I began to be interested in data visualization through programming at a lecture during my undergraduate years. It is because the most effective way to intuitively understand the meaning of data. Such great opportunities have eventually got me to focus on data visualization of astronomical images using statistical mathematics as well as observational studies regarding circumstellar disks, a reservoirs of material out of which planets may form. I would like to express my sincere gratitude to many people for their support and cooperation in pursuing this research.

I would like to first thank Prof Dr. Ryohei Kawabe, my supervisor, for allowing me to conduct outstanding research. He guided me on how to proceed with this research from a broad perspective. He gave me valuable discussions and advice daily. I have learned the logical thinking and the attitude toward research required for astronomers. I would like to express my sincere gratitude to him for providing me with many opportunities and experiences to develop valuable skills.

I would like to thank Dr. Kazunori Akiyama. He is my mentor for the research in my master's course. Even though I had limited knowledge and understanding, he kindly guided me many times until I could understand. Even with a time difference of almost half a day because of the difference in our living locations (Japan to United States of America), he spent much time discussing me through this research via e-mail and video meetings. He taught me the importance of discerning the essence of research for surviving as astronomers. Even when my circumstances interfered with my research, he was willing to support me with my research plan. I am deeply grateful to him.

I would like to thank Dr. Takeshi Nakazato, Dr. Shiro Ikeda, Dr. Mareki Honma, and Dr. Fumie Tazaki of the Interferometry Imaging Development Group for their advice on applying a new imaging technique to ALMA observational data in this research. I would like to thank Dr. Takashi Tsukagoshi for his guidance on the analysis of ALMA observational data. I would

like to thank Dr. Takayuki Muto, Dr. Hideko Nomura, Dr. Misato Fukagawa, Dr. Motohide Tamura, and Dr. Fumitaka Nakamura for all comments and advice that helped improve the manuscript and contents of this study. I would like to thank East Asian ALMA staff members at NAOJ for their kind support.

I would like to thank my colleagues, Hiroyuki Ishikawa, Jinshi Sai, Ko Hosokawa, and Noriharu Watanabe for their support in my research and personal life. We have often shared hardships in our research, and spending a period as a graduate student at NAOJ should be one of the most precious memories in my life. I would like to express my gratitude to all of them and look forward to working with them in the future.

I appreciate the great support by Asuka. No matter how hard my research is, the valuable time with you always makes me happy and emotional support. I would like to express my gratitude to her. Last but not least, I appreciate my family. In particular, I would like to express my deepest gratitude to my father, the mainstay of the family, who passed away due to illness while I was a graduate student. After my father's death, I was asking myself if I should continue with my graduate research for my curiosity alone. However, I could have accomplished the research as a driving force of what my mother said as "He hoped you would obtain the degree". I again give thanks to him living in heaven.

References

Abod, C. P., Simon, J. B., Li, R., et al. 2019, ApJ, 883, 192

Adams, F. C., Lada, C. J., & Shu, F. H. 1987, ApJ, 312, 788

Akeson, R. L., & Jensen, E. L. N. 2014, ApJ, 784, 62

Akeson, R. L., Jensen, E. L. N., Carpenter, J., et al. 2019, ApJ, 872, 158

Akeson, R. L., Koerner, D. W., & Jensen, E. L. N. 1998, ApJ, 505, 358

Akiyama, K., Akahori, T., Miyashita, Y., et al. 2018, arXiv e-prints, arXiv:1811.10610

Akiyama, K., Kuramochi, K., Ikeda, S., et al. 2017a, ApJ, 838, 1

Akiyama, K., Ikeda, S., Pleau, M., et al. 2017b, AJ, 153, 159

ALMA Partnership, Brogan, C. L., Pérez, L. M., et al. 2015, ApJ, 808, L3

Andre, P., Ward-Thompson, D., & Barsony, M. 1993, ApJ, 406, 122

Andrews, S. M. 2015, PASP, 127, 961

—. 2020, ARA&A, 58, 483

Andrews, S. M., Rosenfeld, K. A., Kraus, A. L., & Wilner, D. J. 2013, ApJ, 771, 129

Andrews, S. M., Terrell, M., Tripathi, A., et al. 2018a, ApJ, 865, 157

Andrews, S. M., & Williams, J. P. 2005, ApJ, 631, 1134

—. 2007, ApJ, 671, 1800

Andrews, S. M., Wilner, D. J., Zhu, Z., et al. 2016, ApJ, 820, L40

Andrews, S. M., Huang, J., Pérez, L. M., et al. 2018b, ApJ, 869, L41

—. 2018c, ApJ, 869, L41

Ansdell, M., Williams, J. P., van der Marel, N., et al. 2016, ApJ, 828, 46

Ansdell, M., Williams, J. P., Trapman, L., et al. 2018, ApJ, 859, 21

Armitage, P. J. 2011, ARA&A, 49, 195

Aso, Y., Ohashi, N., Saigo, K., et al. 2015, ApJ, 812, 27

Astropy Collaboration, Robitaille, T. P., Tollerud, E. J., et al. 2013, A&A, 558, A33

Avenhaus, H., Quanz, S. P., Garufi, A., et al. 2018, ApJ, 863, 44

Bacciotti, F., Girart, J. M., Padovani, M., et al. 2018, ApJ, 865, L12

Bally, J., Sutherland, R. S., Devine, D., & Johnstone, D. 1998, AJ, 116, 293

Bate, M. R. 2018, MNRAS, 475, 5618

Beck, A., & Teboulle, M. 2009a, Image Processing, IEEE Transactions on, 18, 2419

—. 2009b, SIAM journal on imaging sciences, 2, 183

Beck, T. L., Schaefer, G. H., Guilloteau, S., et al. 2020, arXiv e-prints, arXiv:2009.03861

Beckwith, S. V. W., & Sargent, A. I. 1991, ApJ, 381, 250

Beckwith, S. V. W., Sargent, A. I., Chini, R. S., & Guesten, R. 1990, AJ, 99, 924

Biller, B., Lacour, S., Juhász, A., et al. 2012, ApJ, 753, L38

Birnstiel, T., Dullemond, C. P., Zhu, Z., et al. 2018, ApJ, 869, L45

Boccaletti, A., Di Folco, E., Pantin, E., et al. 2020, A&A, 637, L5

Boehler, Y., Weaver, E., Isella, A., et al. 2017, ApJ, 840, 60

Bohlin, R. C., Savage, B. D., & Drake, J. F. 1978, ApJ, 224, 132

Booth, A. S., & Ilee, J. D. 2020, MNRAS, 493, L108

Boss, A. P. 1998, ApJ, 503, 923

Cameron, A. G. W. 1978, Moon and Planets, 18, 5

Cárcamo, M., Román, P. E., Casassus, S., Moral, V., & Rannou, F. R. 2018, Astronomy and Computing, 22, 16

Carrasco-González, C., Sierra, A., Flock, M., et al. 2019, ApJ, 883, 71

Carrera, D., Johansen, A., & Davies, M. B. 2015, A&A, 579, A43

Casassus, S., van der Plas, G., M, S. P., et al. 2013, Nature, 493, 191

Casassus, S., Wright, C. M., Marino, S., et al. 2015, ApJ, 812, 126

Casassus, S., Avenhaus, H., Pérez, S., et al. 2018, MNRAS, 477, 5104

Casassus, S., Marino, S., Lyra, W., et al. 2019, MNRAS, 483, 3278

Cazzoletti, P., van Dishoeck, E. F., Pinilla, P., et al. 2018, A&A, 619, A161

Chael, A. A., Johnson, M. D., Bouman, K. L., et al. 2018, ApJ, 857, 23

Chael, A. A., Johnson, M. D., Narayan, R., et al. 2016, ApJ, 829, 11

Chiang, E., & Youdin, A. N. 2010, Annual Review of Earth and Planetary Sciences, 38, 493

Chiang, E. I., & Goldreich, P. 1997, ApJ, 490, 368

Cieza, L. A., Casassus, S., Pérez, S., et al. 2017, ApJ, 851, L23

Cieza, L. A., Ruíz-Rodríguez, D., Hales, A., et al. 2019, MNRAS, 482, 698

Cieza, L. A., González-Ruilova, C., Hales, A. S., et al. 2020, arXiv e-prints, arXiv:2012.00189

Clark, B. G. 1980, A&A, 89, 377

Clarke, C. J., Tazzari, M., Juhasz, A., et al. 2018, ApJ, 866, L6

Condon, J. J. 1997, PASP, 109, 166

Cornwell, T., Braun, R., & Briggs, D. 1999, GB Taylor, CL Carilli, & RA Perley (San Francisco, CA: ASP), 151

Cornwell, T. J. 2008, IEEE Journal of Selected Topics in Signal Processing, 2, 793

Cornwell, T. J., & Evans, K. F. 1985, A&A, 143, 77

Dubrulle, B., Morfill, G., & Sterzik, M. 1995, Icarus, 114, 237

Dullemond, C. P., Dominik, C., & Natta, A. 2001, ApJ, 560, 957

Dullemond, C. P., Hollenbach, D., Kamp, I., & D'Alessio, P. 2007, in Protostars and Planets V, ed. B. Reipurth, D. Jewitt, & K. Keil, 555

Dunham, M. M., Stutz, A. M., Allen, L. E., et al. 2014, in Protostars and Planets VI, ed. H. Beuther, R. S. Klessen, C. P. Dullemond, & T. Henning, 195

Dyck, H. M., Simon, T., & Zuckerman, B. 1982, ApJ, 255, L103

Evans, Neal J., I., Dunham, M. M., Jørgensen, J. K., et al. 2009, ApJS, 181, 321

Event Horizon Telescope Collaboration, Akiyama, K., Alberdi, A., et al. 2019, ApJ, 875, L4

Facchini, S., van Dishoeck, E. F., Manara, C. F., et al. 2019, A&A, 626, L2

Facchini, S., Benisty, M., Bae, J., et al. 2020, A&A, 639, A121

Flock, M., Ruge, J. P., Dzyurkevich, N., et al. 2015, A&A, 574, A68

Francis, L., & van der Marel, N. 2020, ApJ, 892, 111

Fukagawa, M., Tsukagoshi, T., Momose, M., et al. 2013, PASJ, 65, L14

Furlan, E., Hartmann, L., Calvet, N., et al. 2006, ApJS, 165, 568

Gaia Collaboration, Prusti, T., de Bruijne, J. H. J., et al. 2016a, A&A, 595, A1

—. 2016b, A&A, 595, A1

Gaia Collaboration, Brown, A. G. A., Vallenari, A., et al. 2018, A&A, 616, A1

Garufi, A., Avenhaus, H., Pérez, S., et al. 2020, A&A, 633, A82

Geisser, S. 1975, Journal of the American Statistical Association, 70, 320

Gulick, H. C., Sadavoy, S., Matrà, L., Sheehan, P., & van der Marel, N. 2021, ApJ, 922, 150

Hammel, B., & Sullivan-Molina, N. 2020, bdhammel/least-squares-ellipse-fitting: v2.0.0

Hashimoto, J., Dong, R., & Muto, T. 2021a, arXiv e-prints, arXiv:2103.16731

Hashimoto, J., Muto, T., Dong, R., et al. 2021b, arXiv e-prints, arXiv:2102.05905

Hayashi, C. 1981, Progress of Theoretical Physics Supplement, 70, 35

Hayashi, C., Nakazawa, K., & Nakagawa, Y. 1985, in Protostars and Planets II, ed. D. C. Black & M. S. Matthews, 1100–1153

Helled, R., Bodenheimer, P., Podolak, M., et al. 2014, in Protostars and Planets VI, ed. H. Beuther, R. S. Klessen, C. P. Dullemond, & T. Henning, 643

Hendler, N., Pascucci, I., Pinilla, P., et al. 2020, ApJ, 895, 126

Herbig, G. H. 1960, ApJS, 4, 337

Herczeg, G. J., & Hillenbrand, L. A. 2014, ApJ, 786, 97

Hernández, J., Hartmann, L., Megeath, T., et al. 2007, ApJ, 662, 1067

Högbom, J. A. 1974, A&AS, 15, 417

Honma, M., Akiyama, K., Uemura, M., & Ikeda, S. 2014, PASJ, 66, 95

Huang, J., Andrews, S. M., Dullemond, C. P., et al. 2018, ApJ, 869, L42

Hughes, A. M., Duchêne, G., & Matthews, B. C. 2018, ARA&A, 56, 541

Hunter, J. D. 2007, Computing in science & engineering, 9, 90

Ida, S., Lin, D. N. C., & Nagasawa, M. 2013, ApJ, 775, 42

Jennings, J., Booth, R. A., Tazzari, M., Rosotti, G. P., & Clarke, C. J. 2020, MNRAS, 495, 3209

Johansen, A., Blum, J., Tanaka, H., et al. 2014, in Protostars and Planets VI, ed. H. Beuther, R. S. Klessen, C. P. Dullemond, & T. Henning, 547

Johansen, A., Oishi, J. S., Mac Low, M.-M., et al. 2007, Nature, 448, 1022

Johnson, J. A., Aller, K. M., Howard, A. W., & Crepp, J. R. 2010, PASP, 122, 905

Jones, E., Oliphant, T., Peterson, P., et al. 2001, SciPy: Open source scientific tools for Python, [Online; accessed ¡today¿]

Jorquera, S., Pérez, L. M., Chauvin, G., et al. 2021, AJ, 161, 146

Joy, A. H. 1945, ApJ, 102, 168

Kanagawa, K. D., Muto, T., Tanaka, H., et al. 2015, ApJ, 806, L15

—. 2016, PASJ, 68, 43

Kant, I. 1755, Allgemeine Naturgeschichte und Theorie des Himmels

Kataoka, A., Tsukagoshi, T., Momose, M., et al. 2016, ApJ, 831, L12

Kawabe, R., Hara, C., Nakamura, F., et al. 2018, ApJ, 866, 141

Kenyon, S. J., & Hartmann, L. 1987, ApJ, 323, 714

Kitamura, Y., Momose, M., Yokogawa, S., et al. 2002, ApJ, 581, 357

Koepferl, C. M., Ercolano, B., Dale, J., et al. 2013, MNRAS, 428, 3327

Köhler, R., Kasper, M., Herbst, T. M., Ratzka, T., & Bertrang, G. H. M. 2016, A&A, 587, A35

Koresko, C. D. 2000, ApJ, 531, L147

Kratter, K., & Lodato, G. 2016, ARA&A, 54, 271

Kudo, T., Hashimoto, J., Muto, T., et al. 2018, ApJ, 868, L5

Kuramochi, K., Akiyama, K., Ikeda, S., et al. 2018, ApJ, 858, 56

Kurtovic, N. T., Pinilla, P., Long, F., et al. 2021, A&A, 645, A139

Kwon, W., Looney, L. W., & Mundy, L. G. 2011, ApJ, 741, 3

Lambrechts, M., & Johansen, A. 2012, A&A, 544, A32

Laughlin, G., & Bodenheimer, P. 1994, ApJ, 436, 335

Li, F., Cornwell, T. J., & de Hoog, F. 2011, A&A, 528, A31

Lin, D. N. C., & Papaloizou, J. 1986, ApJ, 309, 846

Lin, Z.-Y. D., Lee, C.-F., Li, Z.-Y., Tobin, J. J., & Turner, N. J. 2021, MNRAS, 501, 1316

Liu, H. B. 2019, ApJ, 877, L22

Liu, Y., Dipierro, G., Ragusa, E., et al. 2019, A&A, 622, A75

Lodato, G., Dipierro, G., Ragusa, E., et al. 2019, MNRAS, 486, 453

Long, D. E., Zhang, K., Teague, R., & Bergin, E. A. 2020, ApJ, 895, L46

Long, F., Pinilla, P., Herczeg, G. J., et al. 2018, ApJ, 869, 17

Long, F., Herczeg, G. J., Harsono, D., et al. 2019, ApJ, 882, 49

Long, F., Andrews, S. M., Vega, J., et al. 2021, ApJ, 915, 131

Loomis, R. A., Öberg, K. I., Andrews, S. M., & MacGregor, M. A. 2017, ApJ, 840, 23

Luhman, K. L., Allen, P. R., Espaillat, C., Hartmann, L., & Calvet, N. 2010, ApJS, 186, 111

Machida, M. N., Tomisaka, K., Matsumoto, T., & Inutsuka, S.-i. 2008, ApJ, 677, 327

Macías, E., Guerra-Alvarado, O., Carrasco-González, C., et al. 2021, A&A, 648, A33

Manara, C. F., Tazzari, M., Long, F., et al. 2019, A&A, 628, A95

Mannings, V., & Emerson, J. P. 1994, MNRAS, 267, 361

Mathis, J. S., Rumpl, W., & Nordsieck, K. H. 1977, ApJ, 217, 425

McMullin, J. P., Waters, B., Schiebel, D., Young, W., & Golap, K. 2007, in Astronomical Data Analysis Software and Systems XVI, ed. R. A. Shaw, F. Hill, & D. J. Bell, Vol. 376, 127

Mizuno, H. 1980, Progress of Theoretical Physics, 64, 544

Momose, M., Ohashi, N., Kawabe, R., Hayashi, M., & Nakano, T. 1996, ApJ, 470, 1001

Mulders, G. D. 2018, Planet Populations as a Function of Stellar Properties, ed. H. J. Deeg & J. A. Belmonte, 153

Mulders, G. D., Pascucci, I., & Apai, D. 2015, ApJ, 814, 130

Muto, T., Grady, C. A., Hashimoto, J., et al. 2012, ApJ, 748, L22

Nakazato, T., & Ikeda, S. 2020, PRIISM: Python module for Radio Interferometry Imaging with Sparse Modeling, ascl:2006.002

Nakazato, T., Ikeda, S., Akiyama, K., et al. 2019, in Astronomical Society of the Pacific Conference Series, Vol. 523, Astronomical Data Analysis Software and Systems XXVII, ed. P. J. Teuben, M. W. Pound, B. A. Thomas, & E. M. Warner, 143

Narayan, R., & Nityananda, R. 1986, ARA&A, 24, 127

Nomura, H., Tsukagoshi, T., Kawabe, R., et al. 2016, ApJ, 819, L7

Offner, S. S. R., & Arce, H. G. 2014, ApJ, 784, 61

Ohashi, N., Saigo, K., Aso, Y., et al. 2014, ApJ, 796, 131

Ohashi, S., Kataoka, A., Nagai, H., et al. 2018, ApJ, 864, 81

Okuzumi, S., Momose, M., Sirono, S.-i., Kobayashi, H., & Tanaka, H. 2016, ApJ, 821, 82

Osorio, M., Macías, E., Anglada, G., et al. 2016, ApJ, 825, L10

Pérez, L. M., Carpenter, J. M., Andrews, S. M., et al. 2016, Science, 353, 1519

Pérez, S., Casassus, S., Baruteau, C., et al. 2019, AJ, 158, 15

Pérez, S., Casassus, S., Hales, A., et al. 2020, ApJ, 889, L24

Persson, M. V. 2014, Current view of protostellar evolution (ENG), `https://doi.org/10.6084/m9.figshare.654555.v7`

Pinilla, P., Benisty, M., Cazzoletti, P., et al. 2019, ApJ, 878, 16

Pinilla, P., Birnstiel, T., Ricci, L., et al. 2012, A&A, 538, A114

Pinilla, P., Pohl, A., Stammler, S. M., & Birnstiel, T. 2017, ApJ, 845, 68

Pinilla, P., Benisty, M., Birnstiel, T., et al. 2014, A&A, 564, A51

Pinilla, P., Tazzari, M., Pascucci, I., et al. 2018, ApJ, 859, 32

Pinilla, P., Kurtovic, N. T., Benisty, M., et al. 2021, A&A, 649, A122

Podio, L., Garufi, A., Codella, C., et al. 2020, A&A, 644, A119

Pollack, J. B., Hubickyj, O., Bodenheimer, P., et al. 1996, Icarus, 124, 62

Prato, L., Simon, M., Mazeh, T., Zucker, S., & McLean, I. S. 2002, ApJ, 579, L99

Rafikov, R. R. 2011, ApJ, 727, 86

Ratzka, T., Schegerer, A. A., Leinert, C., et al. 2009, A&A, 502, 623

Rau, U., & Cornwell, T. J. 2011, A&A, 532, A71

Rebull, L. M., Padgett, D. L., McCabe, C. E., et al. 2010, ApJS, 186, 259

Ribas, Á., Espaillat, C. C., Macías, E., et al. 2017, ApJ, 849, 63

Ricci, L., Testi, L., Natta, A., et al. 2010, A&A, 512, A15

Rosotti, G. P., Juhasz, A., Booth, R. A., & Clarke, C. J. 2016, MNRAS, 459, 2790

Rybicki, G. B., & Lightman, A. P. 1979, Radiative processes in astrophysics

Sanchis, E., Testi, L., Natta, A., et al. 2021, A&A, 649, A19

Schaefer, G. H., Beck, T. L., Prato, L., & Simon, M. 2020, AJ, 160, 35

Schwab, F. R. 1984, AJ, 89, 1076

Segura-Cox, D. M., Schmiedeke, A., Pineda, J. E., et al. 2020, Nature, 586, 228

Shakura, N. I., & Sunyaev, R. A. 1973, A&A, 500, 33

Sheehan, P. D., Tobin, J. J., Federman, S., Megeath, S. T., & Looney, L. W. 2020, ApJ, 902, 141

Shepherd, M. C., Pearson, T. J., & Taylor, G. B. 1994, in Bulletin of the American Astronomical Society, Vol. 26, 987–989

Siebenmorgen, R., & Heymann, F. 2012, A&A, 539, A20

Simon, J. B., Armitage, P. J., Li, R., & Youdin, A. N. 2016, ApJ, 822, 55

Simon, M., Guilloteau, S., Di Folco, E., et al. 2017, ApJ, 844, 158

Soon, K.-L., Momose, M., Muto, T., et al. 2019, PASJ, 71, 124

Stapper, L., Hogerheijde, M. R., van Dishoeck, E. F., & Mentel, R. 2021, arXiv e-prints, arXiv:2112.03297

Takahashi, S. Z., & Inutsuka, S.-i. 2014, ApJ, 794, 55

—. 2016, AJ, 152, 184

Takahashi, S. Z., & Muto, T. 2018, ApJ, 865, 102

Takeuchi, T., Miyama, S. M., & Lin, D. N. C. 1996, ApJ, 460, 832

Tang, Y.-W., Guilloteau, S., Dutrey, A., et al. 2017, ApJ, 840, 32

Tazzari, M., Testi, L., Natta, A., et al. 2017, A&A, 606, A88

Terebey, S., Shu, F. H., & Cassen, P. 1984, ApJ, 286, 529

Thompson, A. R., Moran, J. M., & Swenson, Jr., G. W. 2017, Interferometry and Synthesis in Radio Astronomy, 3rd Edition, doi:10.1007/978-3-319-44431-4

Tibshirani, R. 1996, Journal of the Royal Statistical Society. Series B (Methodological), 58, 267

Tobin, J. J., Sheehan, P. D., Megeath, S. T., et al. 2020, ApJ, 890, 130

Tofflemire, B. M., Mathieu, R. D., Ardila, D. R., et al. 2017, ApJ, 835, 8

Toomre, A. 1964, ApJ, 139, 1217

Trapman, L., Facchini, S., Hogerheijde, M. R., van Dishoeck, E. F., & Bruderer, S. 2019, A&A, 629, A79

Tripathi, A., Andrews, S. M., Birnstiel, T., & Wilner, D. J. 2017, ApJ, 845, 44

Tsukagoshi, T., Nomura, H., Muto, T., et al. 2016, ApJ, 829, L35

Ueda, T., Flock, M., & Birnstiel, T. 2021, arXiv e-prints, arXiv:2105.13852

Ueda, T., Flock, M., & Okuzumi, S. 2019, ApJ, 871, 10

van der Marel, N., Dong, R., di Francesco, J., Williams, J. P., & Tobin, J. 2019, ApJ, 872, 112

van der Marel, N., & Mulders, G. D. 2021, AJ, 162, 28

van der Marel, N., van Dishoeck, E. F., Bruderer, S., et al. 2013, Science, 340, 1199

van der Marel, N., Birnstiel, T., Garufi, A., et al. 2021, AJ, 161, 33

van der Plas, G., Ménard, F., Ward-Duong, K., et al. 2016, ApJ, 819, 102

Verhoeff, A. P., Min, M., Pantin, E., et al. 2011, A&A, 528, A91

Veronesi, B., Ragusa, E., Lodato, G., et al. 2020, MNRAS, 495, 1913

Villenave, M., Ménard, F., Dent, W. R. F., et al. 2020, A&A, 642, A164

Wallace, A. L., Kammerer, J., Ireland, M. J., et al. 2020, MNRAS, 498, 1382

Ward-Thompson, D., & Whitworth, A. P. 2011, An Introduction to Star Formation

Watanabe, S.-i., & Lin, D. N. C. 2008, ApJ, 672, 1183

Waters, L. B. F. M., & Waelkens, C. 1998, ARA&A, 36, 233

Weidenschilling, S. J. 1977, MNRAS, 180, 57

White, R. J., & Ghez, A. M. 2001, ApJ, 556, 265

Wiaux, Y., Jacques, L., Puy, G., Scaife, A. M. M., & Vandergheynst, P. 2009, MNRAS, 395, 1733

Williams, J. P., & Cieza, L. A. 2011, ARA&A, 49, 67

Wu, Y.-L., Sheehan, P. D., Males, J. R., et al. 2017, ApJ, 836, 223

Yamaguchi, M., Tsukagoshi, T., Muto, T., et al. 2021, ApJ, 923, 121

Yamaguchi, M., Akiyama, K., Tsukagoshi, T., et al. 2020, ApJ, 895, 84

Yang, C.-C., Johansen, A., & Carrera, D. 2017, A&A, 606, A80

Yang, Y., Mayama, S., Hayashi, S. S., et al. 2018, ApJ, 861, 133

Yen, H.-W., Gu, P.-G., Hirano, N., et al. 2019, ApJ, 880, 69

Youdin, A. N. 2011, ApJ, 731, 99

Youdin, A. N., & Goodman, J. 2005, ApJ, 620, 459

Zagaria, F., Rosotti, G. P., & Lodato, G. 2021, arXiv e-prints, arXiv:2107.05268

Zhang, K., Blake, G. A., & Bergin, E. A. 2015, ApJ, 806, L7

Zhang, L., Xu, L., & Zhang, M. 2020, PASP, 132, 041001

Zhang, S., Zhu, Z., Huang, J., et al. 2018, ApJ, 869, L47

Zhu, Z., Nelson, R. P., Dong, R., Espaillat, C., & Hartmann, L. 2012, ApJ, 755, 6

Zhu, Z., Zhang, S., Jiang, Y.-F., et al. 2019, ApJ, 877, L18